TECHNISCHE UNIVERSITÄT MÜNCHEN

Physik-Department

Lehrstuhl für Funktionelle Materialien (Experimentalphysik IV)

Hydrogen dynamics in complex borohydrides

Luca Silvi

Vollständiger Abdruck der von der Fakultät für Physik der Technischen Universität München zur Erlangung des akademischen Grades eines

Doktors der Naturwissenschaften (Dr. rer. nat.)

genehmigten Dissertation.

Vorsitzender:	Prof. Dr. Martin Zacharias
Prüfer der Dissertation:	1. Prof. Dr. Winfried Petry
	2. Prof. Alessandro Paciaroni

Die Dissertation wurde am 18.01.2017 bei der Technischen Universität München eingereicht und durch die Fakultät für Physik am 06.02.2017 angenommen.

Hydrogen Dynamics in Complex Borohydrides

Abstract

Hydrogen dynamics in complex borohydrides, $LiBH_4$ and $Mg(BH_4)_2$, was studied on the picosecond time scale in a wide range of temperatures and in different structural phases using neutron spectroscopy at the instrument TOFTOF (Heinz Maier-Leibnitz Zentrum). A global analysis of the quasi-elastic and inelastic contributions to the scattering function was developed, to identify local reorientations of hydrogen atoms and low energy vibrations, and to evaluate the influence of the different cations (Li^+, Mg^{2+}) on the dynamics in borohydrides.

Wasserstoffdynamik in komplexen Bohrydriden

Zusammenfassung

Die Wasserstoffdynamik in den Borhydriden $LiBH_4$ und $Mg(BH_4)_2$ wurde auf der Pikosekundenzeitskala in einem großen Temperaturbereich und in unterschiedlichen strukturellen Phasen mit Neutronenspektroskopie am Instrument TOFTOF (Heinz Maier-Leibnitz Zentrum) untersucht. Eine globale Analyse der quasielastischen und inelastischen Beiträge zur Streufunktion wurde entwickelt, um die lokale Reorientierung der Wasserstoffatome und die Schwingungsanregungen zu identifizieren, und den Einfluß der unterschiedlichen Kationen (Li^+, Mg^{2+}) auf die Dynamik zu untersuchen.

Table of Contents

Part I

Introduction and theoretical background

Chapter 1

Introduction

Contents

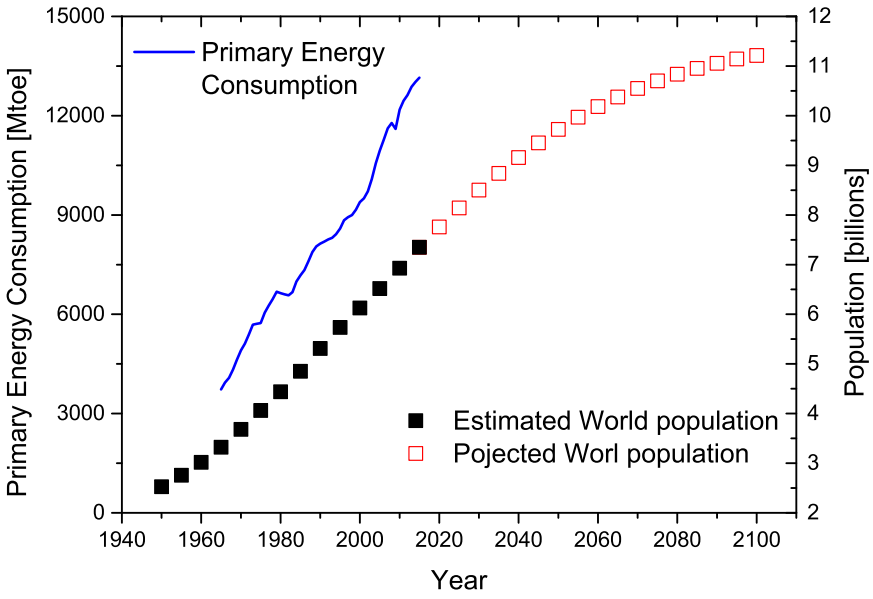

Figure 1.1: Estimated and projected world population (squares), together with Primary Energy Consumption. The strong correlation between increasing population and energy consumption is evident. Data from [1] and [2].

1.1 Energy demand and energy supply

The increase in world population, which is estimated to be 9.8 billion in 2050 [1], leads consequently to an increase of energy demand [2]. Fig. 1.1 shows a strong correlation between population growth and primary energy consumption. Energy demand continue to increase in the future, especially due to emergent countries' energy demand (Asia). Conventional energy sources (like fossils or nuclear fission) suffer from limited availability and from environment pollution. Fossil fuels produce carbon dioxide (CO_2) and a big effort has been done in the last 20 years, in order to reduce carbon dioxide emissions [3]. On the other hand, nuclear fission energy is not directly polluting the environment, but a big (unsolved) problem is related to the nuclear waste management.
While new oil reserves are still discovered, the rise in energy demand continues at a higher rate. Fossil fuels resources are finite even if their longevity of supply is under debate. Since not all nations are independent from fossil fuels, some countries are dependent on others. As a consequence, this creates inevitably political and economical tensions.

In this scenario, renewable energy sources (like solar, wind, geothermal, etc.) could satisfy the growing energy demand. The main issue, about renewable energy sources, is the reliability: these are intermittent, depending on time (like day-night shift, seasonal shift, weather conditions) and on geological parameters (wind absence/presence). Sun light is in principle a great energy source, but as stated before, it is insufficiently reliable to satisfy the

Isotope	**Hydrogen** [H]	**Deuterium** [D]	**Tritium** [T]
Atomic mass [u]	1.007825	2.0140	3.01605
Abundance [%]	99.985	0.015	$\simeq 10^{-18}$
Half life time [yr]	–	–	12.26
Spin [$\hbar$]	+1/2	+1	+1/2
Nuclear magnetic moment [μ_N]	2.79285	0.85744	2.97896

Table 1.1: Hydrogen isotopes. Table taken from the review on hydrogen properties [6].

whole energy demand, especially from industry and transportation. Furthermore, the production sites of renewable energies are usually far away from usage locations (e.g. off-shore wind farms, [4]): this also poses a problem for the infrastructure of energy transportation and, subsequently, for its storage. A typical example is the solar energy production: on sunny days, a large amount of energy is produced and might not be used for many reasons. This excess energy needs to be stored in order to satisfy the energy demand during the non-production time such as during the night.
Alternatives to fossil fuels have been explored and still are under investigations, such electrochemical storage (batteries or hydrogen based devices), compressed air, etc.

Hydrogen is always found in a bonded form, especially with carbon or oxygen, the latter in the form of water. The use of hydrogen as an energy carrier can form one part of the cycle: it can be produced from water, using a renewable energy source (for example solar) to dissociate a water molecule and obtain hydrogen in a free form. As a second step it can be stored either chemically (for example bonded in a metal or adsorbed in a porous material) or compressed in a high pressure tank. Finally it can be transported and used where it is necessary, to produce energy for automotive purposes in a fuel cell or in an internal combustion engine. The only waste product is water, and therefore the cycle is closed [5].

Briefly, the three processes involved in the hydrogen cycle will be explained. Before going into the details of the aforementioned cycle, a brief introduction about hydrogen properties is given.

1.2 Hydrogen properties

Hydrogen is the lightest and most abundant element in the periodic table of elements. The most common isotope of hydrogen is composed of one proton and one electron, giving an atomic weight of 1.0078 u. Different isotopes have been discovered in the last century, namely Deuterium (D = ^{2}H) and Tritium (T = ^{3}H). Among all isotopes, ^{1}H abundance is 99.985%. Deuterium is 0.015 % abundant, whereas Tritium is only present in $\simeq 10^{-18}$% of all isotopes.

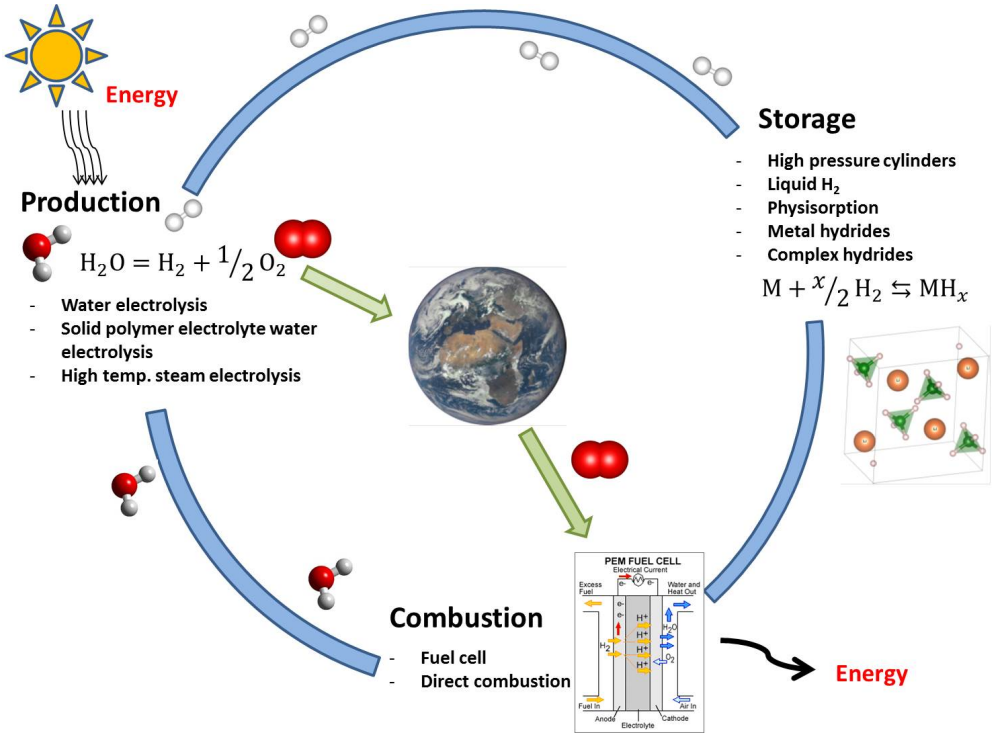

Figure 1.2: Hydrogen cycle. Using renewable energy, free molecular hydrogen can be produced by water electrolysis. Later, it can be stored using high pressure vessels or chemically bounded in materials. The combustion process uses hydrogen to produce electrical work, and the waste product is simply water.

	Property	Value + Unit
	molar mass	$2.016\,\mathrm{kg\,mol^{-1}}$
	(gravimetric) calorific value H_u	$120\,\mathrm{MJ\,kg^{-1}} = 33.33\,\mathrm{kWh\,kg^{-1}}$
at triple point	temperature	$13.80\,\mathrm{K}$
	pressure	0.07 bar
	density (g)	$0.125\,\mathrm{kg\,m^{-3}}$
	density (l)	$77\,\mathrm{kg\,m^{-3}}$
liquid phase	density	$70.8\,\mathrm{kg\,m^{-3}}$
	(volumetric) calorific value	$2.36\,\mathrm{kWh\,kg^{-1}}$
gaseous phase	density	$1.34\,\mathrm{kg\,m^{-3}}$
	(volumetric) calorific value	$0.044\,\mathrm{kWh\,dm^{-3}}$
at critical point	temperature	$33.20\,\mathrm{K}$
	density	$31.4\,\mathrm{kg\,m^{-3}}$
at 293.15 K and 1.01325 bar	density	$0.09\,\mathrm{kg\,m^{-3}}$
	(volumetric) calorific value	$2.8\,\mathrm{Wh\,dm^{-3}}$
	diffusion coefficient	$0.61\,\mathrm{cm^2 s^{-1}}$
	specific heat capacity c_p	$14.32\,\mathrm{kJ\,kg^{-1}\,K^{-1}}$
	specific heat capacity c_v	$10.17\,\mathrm{kJ\,kg^{-1}\,K^{-1}}$
	thermal conductivity	$0.184\,\mathrm{W\,m^{-1}\,K^{-1}}$

Table 1.2: Some of the hydrogen properties, taken from [7].

A list of basic properties of hydrogen (including isotopes) is briefly given in tables 1.1 and 1.2. All the above cited isotopes form diatomic molecules. The interaction of two hydrogen atoms involves the interaction of the two electrons, and therefore the combination of spin involves the formation of singlet and triplet states. Consequently, hydrogen exists in two forms: ortho-hydrogen (o-H_2, symmetric state with parallel nuclear spins) and para-hydrogen (p-H_2, antisymmetric state with anti-parallel nuclear spins). Depending on the temperature and on the rotational states, normal hydrogen is a mixture of para- and ortho-hydrogen. At room temperature, the mixture is composed by 25 mol% p-H_2 and 75 mol% o-H_2.
Some of the hydrogen properties are listed in table 1.2 [7].

At normal temperature, hydrogen is colourless and odourless. It is the element with the lowest density and high diffusion coefficient. Moreover it is also highly inflammable with a low ignition energy.

1.2.1 Equation of State

Thermodynamic properties of hydrogen can be derived once the equation of state can be formulated:

$$f(p, V, T) = 0. \tag{1.1}$$

If hydrogen is considered as a perfect gas, the above equation becomes:

$$PV = nRT, \tag{1.2}$$

where P is the pressure, V the volume, n number of moles, R is the gas constant ($8.314\,\mathrm{J\,mol^{-1}\,K^{-1}}$) and T is the temperature. All thermodynamics quantities can be calculated from the equation of state, for example the Gibbs energy and entropy:

$$G(pT) = G(p_0, T) + \int_{p_0}^{p} V \mathrm{d}P = G(p_0, T) + nRT \ln\left(\frac{p}{p_0}\right) \tag{1.3}$$

$$S(p, T) = S(p_0, T) - \int_{p_0}^{p} \left(\frac{\partial V}{\partial T}\right)_p \mathrm{d}p. \tag{1.4}$$

The enthalpy can be calculated:

$$H(p, T) = G(p, T) + TS(p, T). \tag{1.5}$$

The total enthalpy can not be measured directly. Instead, any change ΔH can be measured and related to the chemical processes in the system. This quantity will be relevant later in this work in order to characterize hydrogenation and dehydrogenation properties of different materials.

1.2.2 Temperature-entropy diagrams

Using a $T - S$ diagram, any changes of states and heat or work absorbed or released can be illustrated. The entropy S is related to the reversible heat through the equation

$$\mathrm{d}S = \frac{\mathrm{d}Q_{\mathrm{rev}}}{T}, \tag{1.6}$$

and it corresponds to the area under the curve in the T-S graph. Using the definition of the reversible heat, for a process at constant pressure ($\mathrm{d}p = 0$), the area represents the change of enthalpy

$$\mathrm{d}Q_{\mathrm{rev}} = \mathrm{d}H - V\mathrm{d}p. \tag{1.7}$$

1.3 Hydrogen cycle

H_2 production Using renewable energy sources (solar, wind, etc.), hydrogen can be directly produced using water dissociation. In order to electrolyse water, a minimum voltage is required. The hydrolysis reaction reads:

$$\mathrm{H_2O} = \mathrm{H_2} + \frac{1}{2}\,\mathrm{O_2}. \tag{1.8}$$

the enthalpy change is $285\,\mathrm{kJ\,mol^{-1}}$ and entropy change $70\,\mathrm{J\,K^{-1}\,mol^{-1}}$ (at $25\,^\circ\mathrm{C}$ and atmospheric pressure), leading to a minimum decomposition voltage of $1.23\,\mathrm{V}$ [6, 8]. Electrolyse cells consist of a cathode, an anode, a separator and an electrolyte. Various electrolytic processes are implemented, depending on the electrolyte, pressure and operating temperature. The most widespread system used is the alkaline electrolysis, using potassium hydroxide (KOH). The electrodes are separated by a diaphragm that allows the transportation of ions. The theoretical efficiency of eq. 1.8 is about 83%, under isothermal conditions. Real conditions, using slightly higher input voltages, are in the range 70-75%. Another possibility is to use polymer electrolyte membranes (PEM). They operate at a temperature between 30 and $100\,^\circ\mathrm{C}$, with slightly higher efficiencies (80-90%).

Storage Once molecular hydrogen is produced, it has to be transported and stored. Two main possibilities can be considered: physical based and material based hydrogen storage.

- **Physical based**
  - **Gas cylinders**: Hydrogen can be compressed in reinforced stainless steel cylinders, up to a pressure of 800 bar. Using carbon fibres gas cylinders, the pressure can be lowered to 700 bar. At room temperature, about 13 mass% can be reached, with a volumetric density of 33 kg $H_2 \cdot m^{-3}$.
  - **Liquid hydrogen**: At 21 K, liquid molecular hydrogen can be stored with a volumetric density of $71\,\mathrm{kg\,H_2 \cdot m^{-3}}$.
- **Material based**
  - **Physisorption**: Materials with large specific surface (carbon or Metal Organic Framework) can adsorb hydrogen molecules at low temperature using van der Waals forces (e.g. MOF-5).
  - **Liquid organic**: hydrogen can be bonded in a liquid carrier via catalytic reactions (e.g. N-ethylcarbazole) [9].
  - **Interstitial or metal hydride**: metals and alloys can form interstitial hydride. Hydrogen atoms diffuse into metal/alloy lattice structure, forming metallic bonds with lattice atoms.
  - **Complex Hydrides**: these are materials composed of a metal cation (usually an alkali metal) and a complex anion containing the hydride, usually with a strong covalent character. Examples are sodium alanate ($NaAlH_4$), lithium borohydride ($LiBH_4$), etc.

Conversion Once hydrogen is stored, it can be used for energy production. The conversion into electric and thermal energies involves the use of fuels cells, combustion engines,

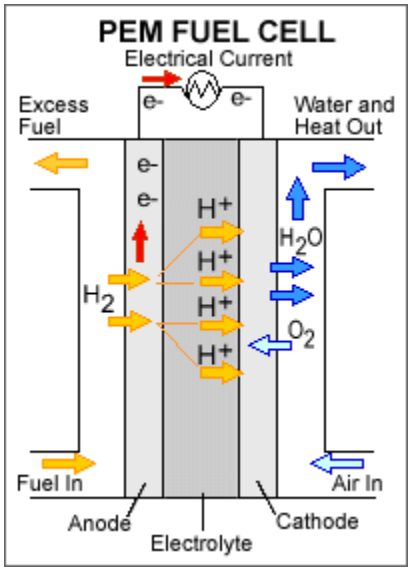

Figure 1.3: Schematic representation of a PEM fuel cell. [10]

turbines. the most promising method is the use of proton exchange membrane (PEM) fuel cells. A PEM fuel cell is formed by a thin layer of a proton conduction polymer between an anode and a cathode, schematically represented in fig. 1.3 [10]. Electrodes are usually made of porous carbon containing platinum or platinum alloy catalyst and the whole system operates at around 80 °C. The platinum catalyst used to separate H_2 molecules in protons and electrons is usually expensive and sensitive to carbon monoxide, therefore additional purification systems might be required in order to prolong the fuel cell lifetime. In general, the only products of the fuel cell are electricity, water and heat, and in that respect, the hydrogen cycle can be considered closed.

1.4 Hydrogen storage

As briefly introduced in the previous section, hydrogen can be stored in different ways, each one with advantages and disadvantages.
Among material-based storage of hydrogen, complex hydrides are a novel class of materials with potential use in stationary and mobile applications.

1.4.1 Gravimetric and volumetric capacities

In order to quantify the amount of hydrogen that a material can absorb, two useful definitions are given: gravimetric and volumetric storage capacities.

- **gravimetric storage capacity**: it is the amount of hydrogen stored per unit mass of material. It is defined as the ratio of the mass of hydrogen stored in the metal

Property	Units	DOE Ultimate	2006 IEA
Gravimetric density	wt.% H_2	7.5	–
Volumetric density	kg H_2/m^3	70	–
System cost	US$/kg H_2	266	–
Refuelling time	minutes	2.5	–
Medium density	wt.% H_2	5.5	5.0
H_2 liberation temperature	°C	60	80

Table 1.3: Selected H_2-storage systems and media targets for fuel cell vehicles [14] [13].

compound to the mass of whole system (host + absorbed hydrogen). Usually it is indicated as a [wt.%], and the expression is given by:

$$c_{\text{wt.\%}} = \left(\frac{(\text{H/M}) M_{\text{H}}}{M_{\text{Host}} + (\text{H/M}) M_{\text{H}}} \times 100 \right) \%. \tag{1.9}$$

where H/M is the hydrogen-to-metal or material host atom ratio, M_H is the molar mass of hydrogen, and M_{Host} is the molar mass of the host material or metal.

- **volumetric storage capacity**: it defines the amount of hydrogen stored per unit volume of material. It is defined as the number of hydrogen moles absorbed in the unit cell volume, assuming that during hydrogen uptake process the crystal lattice does not expand considerably. In reality, this additional effect should be taken into account in the calculation of the volumetric density.

Both quantities can be measured by gravimetric and volumetric techniques. A more detailed explanation of these two methods is given in [11].

1.4.2 Storage target requirements

In order to make hydrogen a safe a reliable fuel for on-board applications, some requirements have to be satisfied in order to become a commercial alternative to fossil fuels.
Some requirements have been set by the IEA (International Energy Agency) in the "IEA-HIA Task 32/17 - Hydrogen-Based Energy Storage" in 2006 [12, 13]. Also, the Department of Energy of United States (DOE) set some system targets, which have been revised in 2015 [14]. Some values are reported in table 1.3.

1.4.3 Hydrides

Hydrides are promising candidates for many stationary and mobile hydrogen storage applications. Current applications vary from nickel-metal hydrides rechargeable batteries, aircraft

fire-detectors, isotope separation, synthesis of magnetic materials, switchable mirrors [7].
Hydrogen can be either adsorbed at the surface of the materials or chemically bonded with the host material. In metal hydrides the hydrogen is bounded with the structure of the material with a chemical bond.
The first metal hydride was discovered by Graham, who observed a large hydrogen uptake from palladium. Formation of metal hydrides is a chemical process, therefore the thermodynamics of this process will be shortly presented.
The reaction can be described by the following expression:

$$\mathrm{M} + \frac{x}{2}\mathrm{H_2} \longleftrightarrow \mathrm{MH}_x + Q, \tag{1.10}$$

where M is the hydride-forming metal and Q is the heat of reaction in the formation process.
The uptake process of hydrogen at a constant temperature can be better visualized in the Pressure-Composition Isotherms (PCI) plot.
For each (constant) temperature, the pressure is plotted as a function of the hydrogen uptake (or concentration).
Three different regions can be identified:

- α**-phase**: at low H_2 concentrations x , hydrogen molecules dissociate at the surface of the metal and start to form a solid solution.
  At this stage, the thermodynamic equilibrium conditions is given by:

  $$\frac{1}{2}\mu_{\mathrm{H_2}}\left(p, T\right) = \mu_{\mathrm{H}}\left(p, T, c_{\mathrm{H}}\right), \tag{1.11}$$

  where $\mu_{\mathrm{H_2}}$ and μ_{H} are the chemical potentials of molecular and atomic hydrogen, respectively. c_{H} is the hydrogen concentration.

- $\alpha + \beta$ **phase**: as the hydrogen concentration increases, hydrogen atoms start to diffuse inside the lattice and the interaction H–H starts to be significant. In this region, a new phase nucleation takes place, characterized by high concentration, called β phase. During this nucleation, the pressure does not increase with increasing H_2 concentration. In this region, the equilibrium pressure P_{eq} at the $\alpha \rightarrow \beta$ transformation is given by the van't Hoff equation:

  $$\ln p_{\mathrm{eq}} = \frac{\Delta H}{RT} - \frac{\Delta S}{R}, \tag{1.12}$$

  where ΔH and ΔS are, respectively, the enthalpy and entropy changes. Plotting the plateau pressure as a function of the inverse of the temperature, the van't Hoff plot is obtained. A linear fit of the values leads to a slope and an intercept that are, respectively, proportional to the enthalpy and entropy changes. Therefore, these two values can be obtained and they characterize the reaction thermodynamics.

- β **phase**: once the phase transformation is completed, the α phase disappears and the pressure rises as the hydrogen concentration increases.

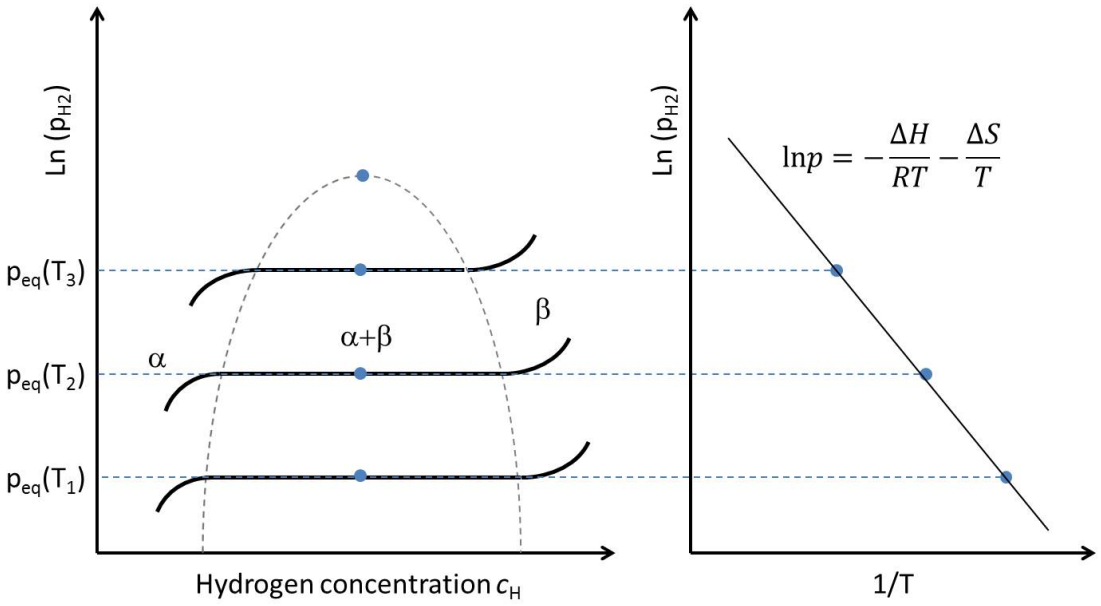

Figure 1.4: Left: PCI measurements. **Right**: van't Hoff plot of the plateau values as a function of inverse of the temperature. The straight line is a linear fit in order to extract the enthalpy (slope) and entropy (intercept) changes.

The three phases above described are strictly valid for interstitial metal hydrides, e.g. palladium hydride or LaNi compounds. However, PCI measurements can be performed also in other hydrides.

Different hydrides can be formed, depending on the metal-hydrogen bond. They can be grouped in three different categories: Ionic Hydrides, Covalent Hydrides and Metallic Hydrides. The division made in three categories is not strict. In fact, most of metal hydrides don't have a precise bonding type, but they might exhibit a mixture of different bondings. For example, lithium hydride (LiH) is not a pure ionic hydride, since it shows significant covalent bonding. For the same reason, in magnesium hydride (MgH_2), the interaction with magnesium and hydrogen is partly ionic partly covalent.

1.4.3.1 Ionic Hydrides

Ionic hydrides are characterized by an ionic bond between hydrogen and the host metal. Usually alkali and alkaline earth metals are forming ionic hydrides. Examples are sodium hydride (NaH) or calcium hydride (CaH_2). These compounds show a quite high decomposition temperature, and therefore they are not suitable for hydrogen storage applications.

1.4.3.2 Covalent Hydrides

Covalent hydrides are formed by hydrogen and a non-metal. The bonding between hydrogen and the non-metal is covalent. Most covalent hydrides are liquid or gaseous at room temperature. In fact, they are characterized by low melting and boiling points. Examples are hydrogen sulfide (H_2S), methane (CH_4), water (H_2O).

1.4.3.3 Metallic Hydrides

These compounds are formed by transition metals, including rare earth and actinide series. The nature of the bonding between hydrogen and host lattice is metallic. Metallic hydrides have a wide variety of stoichiometric and non-stoichiometric compounds. Examples are palladium or neodymium hydrides.

1.4.4 Complex hydrides

A promising category of hydrides that are characterised by high volumetric and gravimetric density are the so-called complex hydrides. The general form of complex hydrides is

$$A_xMe_yH_z, \tag{1.13}$$

where A is usually an element of the first or second group of the periodic table and Me is boron or aluminium. Complex hydrides are well known in chemistry: sodium or potassium borohydrides are used as reduction agents in organic chemistry syntheses. The interest of these materials as possible hydrogen storage materials became important when in 1997 Bogdanović and Schwickardi [15] reported a strong enhancement of sodium alanate ($NaAlH_4$) kinetics, adding a small amount of Ti catalyst. Also, the reversibility of this material in hydrogen cycling became possible at moderate temperatures and pressures (100 °C and 100 bar). Since then, complex hydrides became object of intense scientific studies. An extensive literature exists and some reviews are available [16, 17, 18, 19, 20, 21, 22].
Most of complex hydrides exhibit high gravimetric and volumetric densities. At the same time, they show high thermal stability and thus an obstacle in hydrogen liberation at moderate temperatures. In this thesis, only complex borohydrides are discussed, and therefore the next section will be dedicated to this category of complex hydrides.

1.4.4.1 Complex borohydrides

Borohydrides have the highest gravimetric hydrogen storage capacities compared to all other complex hydrides. The complex anion is composed by the central boron atom an four hydrogen covalently bonded, forming a tetrahedra. The nature of the bonding between tetrahedra and the cation is usually ionic, although some of the borohydrides exhibits some

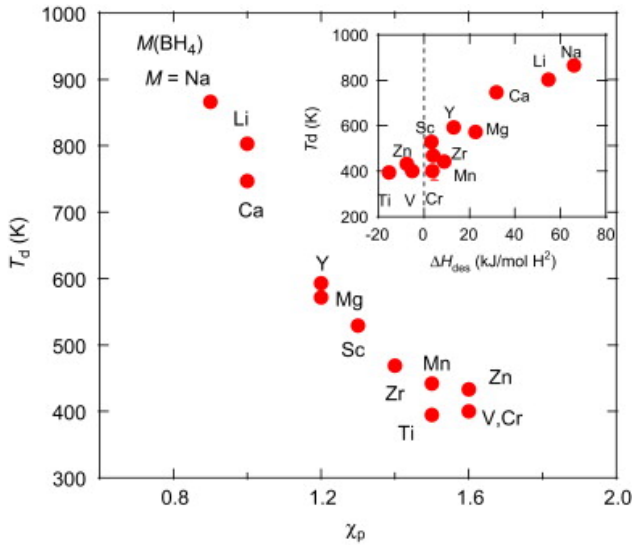

Figure 1.5: Decomposition temperature of selected borohydrides as a function of Pauling electronegativity. The inset shows the decomposition temperature as a function of decomposition enthalpy. [Reprinted from Journal of Physics and Chemistry of Solids, Volume 69 , Issue 9, Y. Nakamori *et. al.* , Development of metal borohydrides for hydrogen storage, 2292-2296, 2007, with permission from Elsevier].

covalent bonding behaviour.
The chemical formula is:

$$\mathrm{Me(BH_4)}_n, \tag{1.14}$$

where Me is an element of the first or second group of the periodic table.
They are characterized by high thermodynamic stability, and studies have been done in order to understand the origin. *Ab initio* calculations have been performed on a series of borohydrides and a correlation between thermodynamical stabilities and cation electronegativities has been found [23]. Boron atoms have a Pauling electronegatity (χ_P) of 2.04. With increasing the cation χ_P the decomposition temperature decreases, as shown in fig. 1.5. Also, first-principle calculation have been performed to calculate the heat of formation (fig. 1.6). Calculations show that the charge transfer between the anion and cation regulates the stability of the metal borohydrides [24]. Also, light weight borohydrides have the highest heat of formation and decomposition temperatures, and a the same time high gravimetric H_2 densities.
Upon heating, the decomposition of borohydrides can take place in different pathways, differing from material to material and from external conditions (pressure).
If the complex borohydride decomposes liberating the whole amount of hydrogen, the reaction is expressed by [23]:

$$\mathrm{Me(BH_4)}_n \rightarrow \mathrm{Me} + n\mathrm{B} + 2n\mathrm{H_2}. \tag{1.15}$$

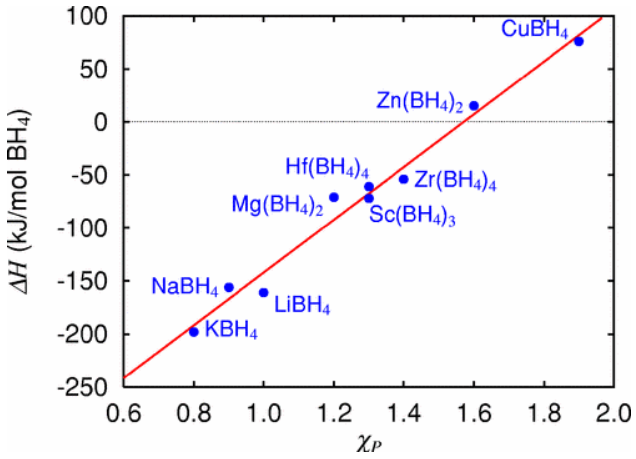

Figure 1.6: Heats of formation ΔH_{boro} of selected borohydrides as a function of Pauling electronegativity of the cation. [Reprinted from Journal of Physics and Chemistry of Solids, Volume 69 , Issue 9, Y. Nakamori *et. al.* , Development of metal borohydrides for hydrogen storage, 2292-2296, 2007, with permission from Elsevier].

Instead, if the complex borohydrides decomposes into a metal hydride,

$$\mathrm{Me(BH_4)}_n \rightarrow \mathrm{MeH}_m + n\mathrm{B} + \frac{4n-m}{2}\mathrm{H_2}. \tag{1.16}$$

Intermediate steps involving the release of boranes or metal boride can take place when involving alkaline earth borohydrides [7]. The release of boranes ($\mathrm{B}_x\mathrm{H}_y$) is an unwanted process, since these products are toxic and gaseous, and therefore having a two fold negative effect: a) these gases are toxic for PEM fuel cell membranes, reducing the fuel cell life-time; b) loss of hydrogen in gaseous form and therefore reducing the storage capacity over time. The stability of borohydrides is given by the enthalpy and entropy differences between the pure complex hydride and the first stable desorption products [16], that might differ from pure elements: this is shown in the two reaction schemes 1.15 and 1.16.

Hydrogen sorption in borohydrides involves, most of the time, processes with formation of intermediate compounds. At a given decomposition temperature, these compounds might prevent a full dehydrogenation, and thus reducing the theoretical gravimetric $\mathrm{H_2}$ density and making heat management more difficult.

1.4.4.2 Destabilization of hydrides

As briefly introduced before, the thermodynamics of $\mathrm{H_2}$ desorption from known borohydrides is not compatible with working condition of fuel cells, in terms of pressure and temperature (100 °C). Experimental and theoretical works have been done to find strategies to destabilize the materials, and therefore facilitating $\mathrm{H_2}$ sorption conditions. In fact, *ab initio* calculations have been performed in order explore destabilization procedures [25, 26]. Usually two

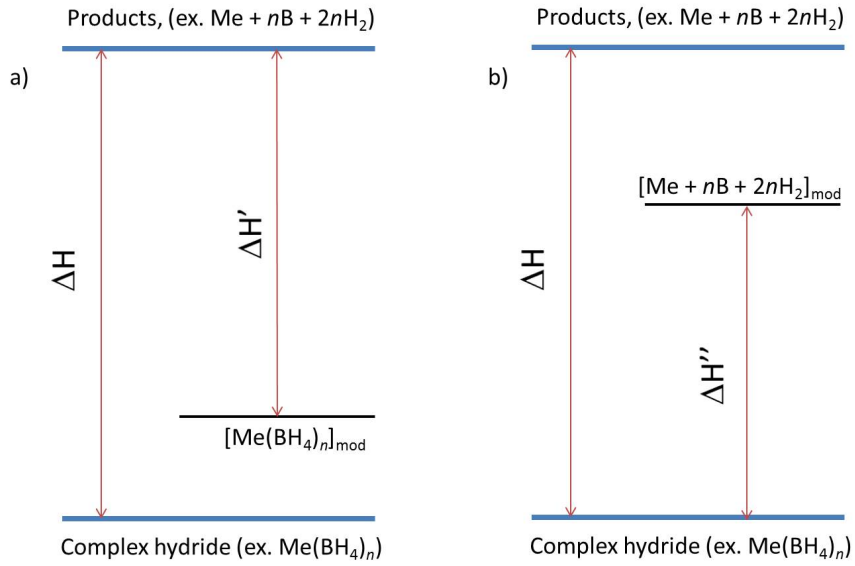

Figure 1.7: Strategies to facilitate hydrogen sorption conditions. In a) the destabilization of the complex hydride, lowering the reaction enthalpy. In b) stabilization of reaction products.

strategies are considered: a) destabilization of the complex hydride or b) stabilization of dehydrogenation products. These two possibilities are shown in fig. 1.7. (De)stabilization can be achieved mixing the complex hydride with additives, with metal hydrides or with other complex hydrides. Also, the formation of binary complex borohydrides

$$\mathrm{MM'(BH_4)_n} \tag{1.17}$$

has been proved as a method to lower the decomposition temperature. This relies on the fact that the other cation M' has a different Pauling electronegativity, lower than the cation M. In fact, since the charge transfer regulates the stability of the complex borohydrides [23, 24], the overall effect is a destabilization of the complex hydride. Physical mixture of borohydrides have been studied, for example $\mathrm{LiBH_4 + Mg(BH_4)_2}$ [27, 28, 29] or $\mathrm{LiBH_4 + Ca(BH_4)_2}$ [30], also in porous carbon materials. The melting point is generally lowered compared to the isolated materials, and also the (de)hydrogenation processes are enhanced. Extensive literature can be found for destabilization strategies and materials [18, 31]

Among the borohydrides, lithium ($\mathrm{LiBH_4}$) and magnesium ($\mathrm{Mg(BH_4)_2}$) borohydrides have the highest gravimetric and volumetric densities. The only compound that exceeds $\mathrm{LiBH_4}$ is beryllium borohydride, but, due to its toxicity, is not considered a safe and practical storage material. In this work, only $\mathrm{LiBH_4}$, $\mathrm{Mg(BH_4)_2}$ and the mixture of $\mathrm{LiBH_4}$ and $\mathrm{Mg(BH_4)_2}$ are studied, and therefore the next three sections will be dedicated to lithium, magnesium and their mixture, respectively.

This work is investigating mostly fundamental properties of hydrogen, in particular its dynamics on the picosecond time scale, in lithium and magnesium borohydrides. The harsh conditions of hydrogen sorptions make these materials still not suitable for storage applications. Nevertheless, basic studies on structure and dynamics properties of hydrogen in these materials are of fundamental importance for a complete material characterization, and therefore improving theoretical calculations (i.e. DFT) and possible destabilization pathways. Neutron scattering is of fundamental importance in these studies, due to the high neutron incoherent cross section of hydrogen, thus allowing the study of structure and dynamics.

1.4.5 Lithium Borohydride ($LiBH_4$)

Lithium borohydride is a chemical compound synthesized for the first time in 1940, with a direct reaction of ethyl lithium with diborane (B_2H_6) [32] . Other reaction strategies are implemented to synthesize $LiBH_4$, i.e. reactions of sodium borohydride ($NaBH_4$) with Li halide or chloride, and with a direct synthesis with Li, B and H_2 at elevated temperatures and gas pressures [33]. It is characterized by high gravimetric and volumetric H_2 densities, 18.4 wt.% and 121 kg/m^3, respectively. These two features made this material a possible candidate for automotive applications [34]. The decomposition starts around 380 °C and at 500 °C half of the H_2 content is released. The enthalpy ΔH and entropy ΔS of dehydrogenation are, respectively, 74 $kJ\,mol^{-1}\,H_2$ and 115 $J\,K^{-1}\,mol^{-1}\,H_2$, based on the pressure-concentration isotherm measurements [35]. However, the sluggish sorption kinetics and the high temperatures required for (de)-hydrogenation are still the major obstacles to large scale applications. The limited reversibility is also a major obstacle to overcome in order to make the material ready for portable applications. A full reversibility is possible only above 870 K (600 °C) and 15–35 MPa of H_2 [35, 36], and therefore it is not practical.
$LiBH_4$ decomposes using two reaction schemes:

$$LiBH_4 \longrightarrow LiH + B + \frac{3}{2}H_2 \longrightarrow Li + B + 2H_2. \tag{1.18}$$

In the first reaction, a partial hydrogen amount is still retained in lithium hydride, and therefore the liberated mass is 13.5 wt.% H_2. In the second reaction scheme, the whole H_2 content is released, i.e. 18.4 wt.% H_2. Also, intermediate compounds were reported during the decomposition process, e.g. the monoclinic $Li_{12}B_{12}H_{12}$. This compound were identified by Raman measurements [37] and NMR spectroscopy [38]. Alternatively, the $Li_{12}B_{12}H_{12}$ is not a direct product of $LiBH_4$ decomposition, but a side-product of the interaction between boranes (B_2H_6) and $LiBH_4$ itself.

Various strategies have been pursued to overcome (de)hydrogenation barriers, e.g. mixing $LiBH_4$ with binary hydrides, such as MgH_2 [39, 40, 41, 42, 43] or with CaH_2 [44, 45]. An

alternative approach to improve the sorption kinetics is to add various additives that act as a catalyst [46, 47]. A third method that improves hydrogen sorption properties is the use of nanoengineering: for example, the confinement of $LiBH_4$ in mesoporous scaffolds, nanotubes or with nano-particles included in a matrix [48, 49, 50, 51, 52, 53]. Extensive reviews of the catalysts and nanoporous scaffolds incorporation can be found in [54, 16].

Despite numerous studies, the structure and the binding in $LiBH_4$ is still not well understood and density functional theory (DFT) simulations have difficulties to reproduce the experimentally found crystal structure as the lowest energy ones [55, 56]. Entropy might play an important role and the understanding of dynamic properties is thus essential.

1.4.5.1 Structure

At low temperature (LT), three different crystal structures of $LiBH_4$ have been found: one orthorhombic $Pnma$ [57] one at 1.2-10 GPa pressure with a pseudo-tetragonal $Ama2$ structure [58] and one above 10 GPa with $Fm\text{-}3m$ structure. At around 381 K and at ambient pressure, a first order structural phase transition occurs to a hexagonal high temperature (HT) phase $P6_3mc$. A simplified phase diagram is shown in fig. 1.10. The four hydrogen atoms are covalently bound to the central boron atom in a tetrahedra complex. After some controversy, it was concluded that the $[BH_4]$ tetrahedra are close to ideal in both modifications [59]. From synchrotron experiments, the distance between H and B, $d_{\text{B-H}}$, was estimated to be 1.16–1.26 Å in the HT-phase. Neutron diffraction data show distances between 1.18-1.20 Å at 302 K [60]. The cell parameters of the LT crystal structure display a highly anisotropic temperature dependence and it was suggested that the structural phase transition is driven by these anharmonic effects [61].

1.4.5.2 Dynamics

The dynamics of $LiBH_4$ was investigated by nuclear magnetic resonance [62] and by neutron scattering experiments. Quasi-elastic neutron scattering experiments was performed on $LiBH_4$ with the aim to investigate the hydrogen reorientational dynamics [53, 63]. In the LT-phase, $[BH_4]$ tetrahedra undergo predominantly 120° rotations around the C_3 symmetry axis. At high temperatures, instead, the large thermal ellipsoids detected from X-ray diffraction measurements suggested a disordered rotational mechanism, and Verdal *et al.* concluded that the hydrogen motions can be described by quasi-free rotations of atoms around the C_3 axis, superimposed on a tumbling motion of the axial hydrogen. The diffusion coefficient of the $[BH_4]$ units was also measured at temperatures above the melting point [64]. Using quasi-elastic neutron scattering experiments, the apparent diffusion coefficient at 573 K is

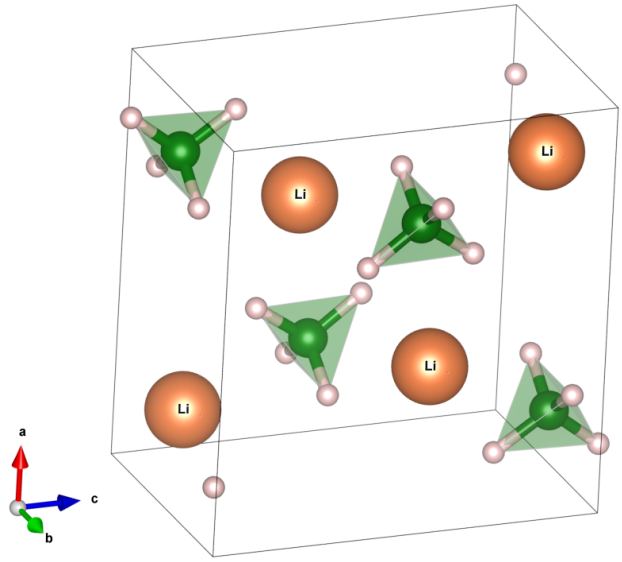

Figure 1.8: Low temperature $LiBH_4$ orthorhombic crystal structure ($Pnma$) [59]. Big orange spheres: lithium, green spheres: boron, small grey spheres: hydrogen. Structure parameters: $a = 7.141$ Å, $b = 4.431$ Å and $c = 6.748$ Å. The angle between H-B-H is in the range $108.8° - 109.9°$.

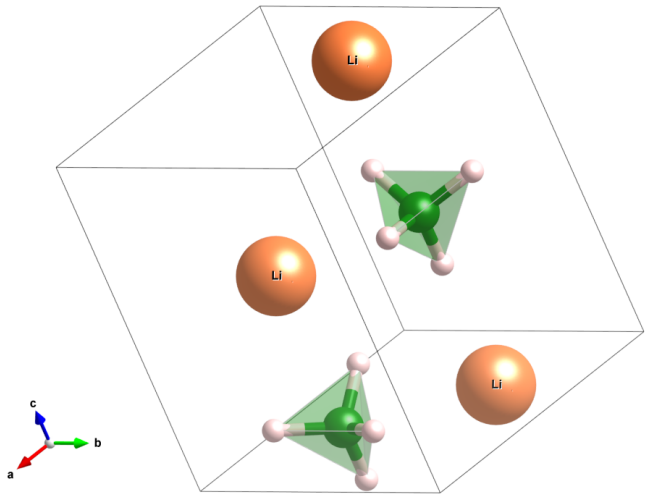

Figure 1.9: High temperature $LiBH_4$ hexagonal crystal structure ($P6_3mc$) [57]. Big orange spheres: lithium, green spheres: boron, small grey spheres: hydrogen. Structure parameters: $a = 4.27631$ Å and $c = 6.94844$ Å. The angle between H-B-H is in the range $106° - 112°$.

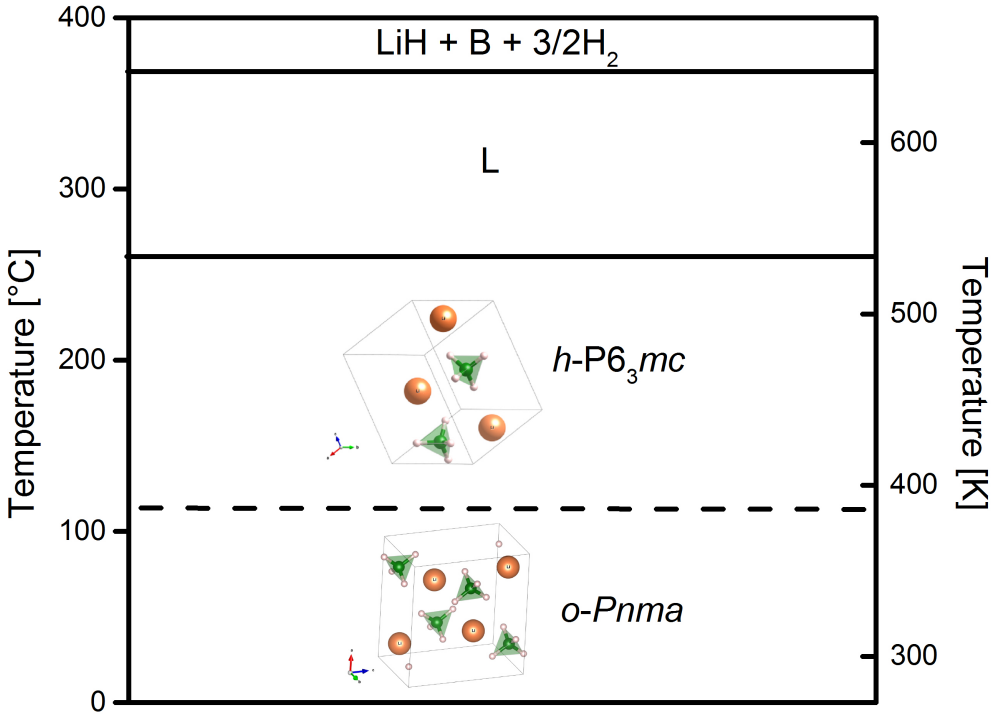

Figure 1.10: Simplified phase diagram of $LiBH_4$: a reversible phase transition takes place at 108 °C (381 K), from an orthorhombic to an hexagonal crystal structure. At $\sim$ 268 °C ($\sim$ 541 K), $LiBH_4$ melts (L), and the decomposition starts above $\sim$ 380 °C ($\sim$ 650 K).

$D_s = 5.3 \cdot 10^{-5}\,\mathrm{cm}^2/\mathrm{s}$, increasing to $D_s = 7.9 \cdot 10^{-5}\,\mathrm{cm}^2/\mathrm{s}$ at 753 K.

Recently, it was shown that $LiBH_4$ exhibits a high Li^+ - ion conductivity in the HT crystal modification and in solid solution with LiI [65]. The superionic transition is thought to be coupled with order/disorder transition which is characteristic for $LiBH_4$ [66, 60].

Most experimental studies of hydrogen sorption properties require intensive ball milled materials. It is a usual procedure in order to increase the material active surface, and therefore improving gas sorption properties. As shown in previous work [67], ball milling is shown to affect the structural phase transition, altering the endothermic peak in the LT $\rightarrow$ HT crystal phase transition and the lattice parameters in the LT crystal modification.

In this work, a quasi-elastic experiment has been performed on different ball milled samples to elucidate the hydrogen dynamics across the crystal phase transition, and the possible influence of mechanical treatment on the microscopic hydrogen dynamics (see chapter 4).

1.4.6 Magnesium Borohydride ($Mg(BH_4)_2$)

Magnesium borohydride was first synthesized in the 1950s, but the interest in hydrogen energy made it a possible candidate for hydrogen storage. It is characterised by a gravimetric and volumetric storage density of 14.9 wt% and 90 $\mathrm{kg/m^3}$ H_2, [23, 68]. Moreover the material is interesting due to its overall reaction enthalpy ΔH, reported values (for desorption to MgH_2) are in the range -40 to $-57\,\mathrm{kJ/mol\,H_2}$ [69, 70] which is in the range suitable for storage applications. However, reaction kinetics is sluggish, and $Mg(BH_4)_2$ decomposes above $\sim 300\,^\circ\mathrm{C}$ (573 K) in a multi step process [71, 72] and its limited reversibility [73] makes it unsuitable for practical application, so far.
Magnesium borohydride exists in various crystalline forms, as recently discovered and characterized by X-ray and neutron scattering techniques [74, 75, 76]. Among the observed polymorphs of $Mg(BH_4)_2$, namely α, β, γ and δ-phase, the low-temperature (LT) α-phase and the high-temperature (HT) β-phase are the most commonly investigated for hydrogen storage applications [73].

1.4.6.1 Structure

The first low- temperature (LT) and high- temperature (HT) crystal phases were identified by Her *et al.* [77]. In that work, a LT α phase was identified with an hexagonal structure and space group $P6_1$. Later, this phase was refined using a combination of X-ray diffraction on single crystal and neutron diffraction on powder, yielding a lower symmetry space group $P6_122$ [78]. The hexagonal crystal structure is characterized by a unit cell volume of 3434 $\mathrm{Å}^3$

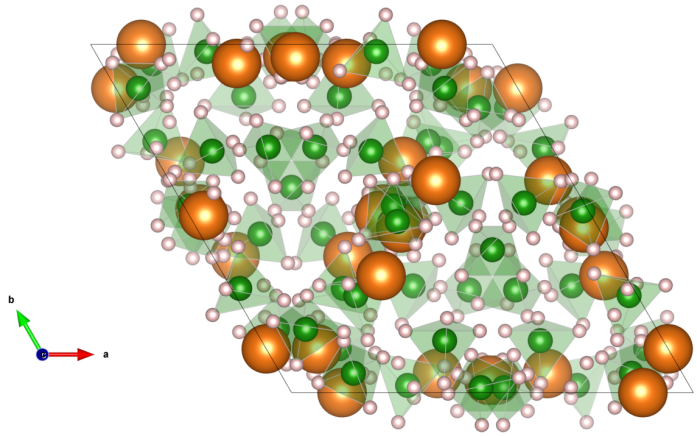

Figure 1.11: Crystal structure of α−-$Mg(BH_4)_2$ along the c axis: magnesium atoms are represented by orange spheres, boron by green and hydrogen by grey spheres.

and the lattice parameters show a non-linear thermal expansion over a wide range of temperatures. The structure is also characterized by six non-equivalent positions of the $[BH_4]$ units, giving a strongly anisotropic environment for the tetrahedron. The α-$Mg(BH_4)_2$ is also characterized by unoccupied voids ($37\,\text{Å}^3$) along the $(00z)$ direction which are not present in the β-polymorph.

The LT α-phase transforms into a HT β-phase at 490 K, and the β-phase is metastable when it is cooled to room temperature. It is characterized by an orthorhombic crystal structure with a $Fddd$ symmetry. The unit volume cell is double of the α-phase, $7543\,\text{Å}^3$, and the crystal structure does not contain any voids. The structure is characterized by five non-equivalent positions of the $[BH_4]$ units, yielding as well to a strongly anisotropic environment. X-ray and neutron diffraction on both polymorphs showed a non linear thermal expansion of lattice parameters [78], but the effect is more pronounced in β-$Mg(BH_4)_2$. Indeed, lattice parameters show maxima and minima in the thermal range 100 - 500 K, leading to a strong anharmonicity of the system even at low temperature. This may be related to the change in the free energy profile and therefore a possible reason for the non-reversibility of the $\alpha \rightarrow \beta$ transition.

In both phases, Mg atoms are surrounded by four $[BH_4]$ tetrahedra leading to a strongly distorted tetrahedral environment, and at local level, the $[BH_4]$ groups are facing the Mg atoms via two opposite edges of the tetrahedra, leading to an almost linear configuration Mg-B-Mg and a bidentate orientation of the Mg with respect to the bridging hydrogens [78, 77] (see fig. 1.14). Fig. 1.13 shows a simplified phase diagram of $Mg(BH_4)_2$ at atmospheric pressure.

Despite the numerous studies, a full understanding of the ground state structures, hydrogen bonding and gas release is still missing. Extensive theoretical calculations show that

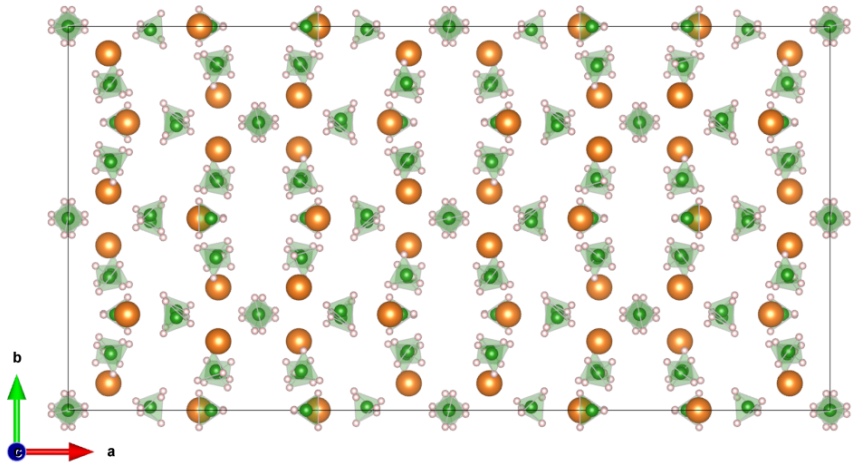

Figure 1.12: Crystal structure of $\beta-$.$Mg(BH_4)_2$ along the c axis: magnesium atoms are represented by orange spheres, boron by green and hydrogen by grey spheres.

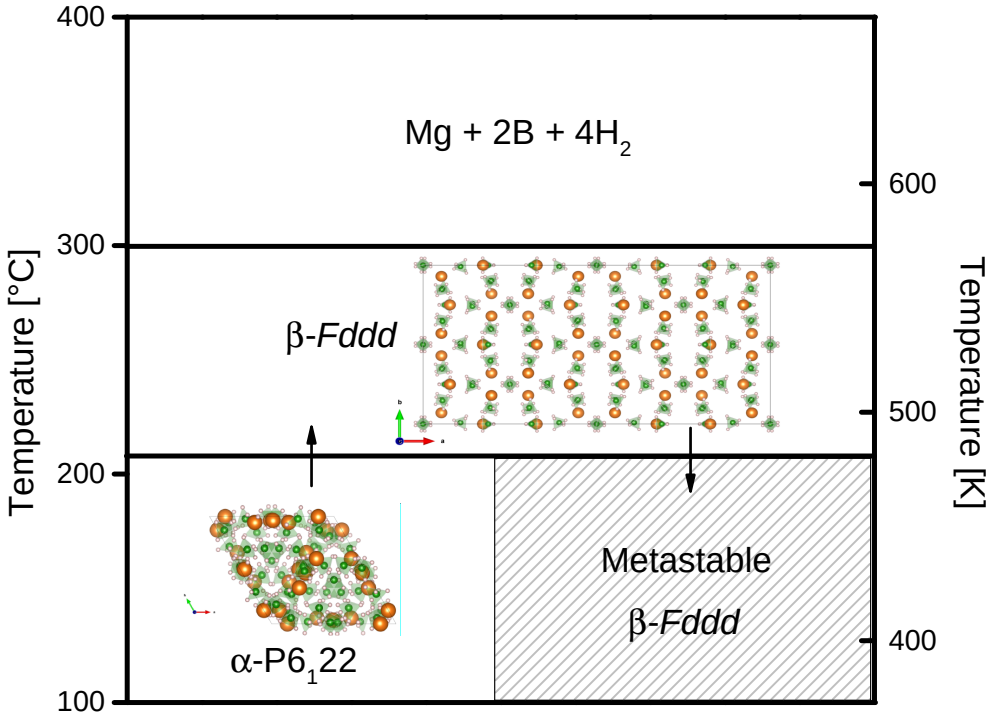

Figure 1.13: Simplified phase diagram of $Mg(BH_4)_2$. The LT α-$Mg(BH_4)_2$ transforms into β-$Mg(BH_4)_2$ at $\sim$ 210 °C ($\sim$ 480 K). The β-polymorph is then metastable at room temperature, and the shaded area represents the metastable region. Above 300 °C (573 K), the decomposition process starts.

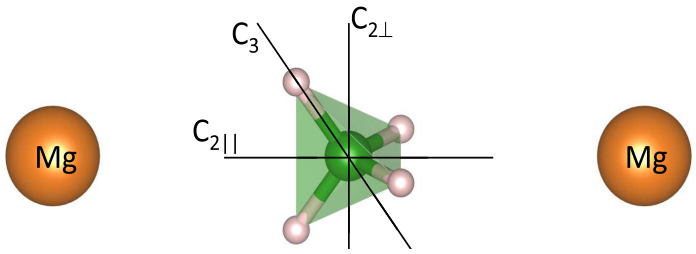

Figure 1.14: Idealized configuration of the $[BH_4]$ units in the Mg environment. The $[BH_4]$ unit lies almost in the line between two Mg atoms in a linear configuration. The three rotation axis are shown: the 3-fold 120° rotation axis C_3, and the 2-fold 180° rotation axes ($C_{2||}$ and $C_{2\perp}$). (large orange sphere) magnesium, (green spheres) boron, (small grey spheres) hydrogen.

the ground state is energetically almost degenerate and a variety of different structures that are very close in energy have been proposed, among the experimentally found α-phase [79]. A recent work [80], showed that, including van der Waals interactions, the lowest energy structure is the experimentally observed α-phase. Conversely, Caputo *et al.* [81], using computational methodology combining cluster optimization, simulated annealing based crystal structure prediction, periodic DFT total energy calculations and Symmetry Group Relations analysis, found other crystal structures with lower energies. The rich polymorphism of $Mg(BH_4)_2$ could be partially attributed to the partial covalent bonding between Mg^{2+} and $[BH_4]^-$ [75]. Still, the question about theoretical predicted and experimentally observed structures is open. The β-phase is energetically less favourable than the α-phase, as shown by DFT calculations [82, 83, 84], but the origin for the non-reversibility of the structural phase transition is not clear yet.

1.4.6.2 Decomposition

The decomposition of β-$Mg(BH_4)_2$ was studied extensively for hydrogen storage applications and various pathways were observed both experimentally and theoretically, depending on the applied hydrogen pressure and temperature conditions [68, 72, 85]. The decomposition temperature is fairly low (around 500 K) and mostly pure hydrogen is released.
DTF calculations have been performed also to predict reaction pathways. For example, in α-$Mg(BH_4)_2$, the reaction pathway was predicted to be

$$Mg(BH_4)_2 \longrightarrow MgB_2 + 4\,H_2, \tag{1.19}$$

with a reaction enthalpy between -38 and $-54\,\mathrm{kJ\,mol^{-1}H_2^{-1}}$ in the temperature range of 293-348 K [86]. Unfortunately, this was not experimentally confirmed and the measurements show at least two or more intermediate steps in the decomposition pathways, with formation of intermediate compounds, such as $MgB_{12}H_{12}$ [87] and polyboranes [71]. In order to improve

the slow kinetics, $Mg(BH_4)_2$ has been mixed with additives [88], mainly metal salts such as CaF_2, ZnF_2 and TiF_3 [89], $ScCl_3$ [90] or NbF_5. The use of transition-metal additives lowers significantly the desorption temperature, although it was shown that no significant improvements were detected on the rehydrogenation.
Another possibility to enhance hydrogen sorption properties is the dispersion on porous matrix or with reactive hydride composites [91, 92, 93]. The effect is an overall reduction of the decomposition temperature, possibly due to surface effects, thus reducing the overall reaction enthalpy. A review of the several decomposition schemes proposed and additives used to improve the kinetics can be found in this work [94].

1.4.6.3 Dynamics

The dynamics $[BH_4]$ anion has been studied with vibrational spectroscopy techniques, mainly involving Raman and Infrared (IR) spectroscopy, Nuclear Magnetic Resonance (NMR), as well as inelastic neutron scattering. The anions have high structural symmetry (being an almost perfect tetrahedra) and four normal modes of vibrations: symmetric stretching (ν_1) and bending (ν_2), asymmetric stretching and bending ν_3 and ν_4, respectively. Some of these modes can be Raman or IR-active, as well as double or more degenerate. Raman, IR and inelastic neutron scattering measurements have been performed to establish a possible link between compound stability and vibrational dynamics. Raman measurements on α-$Mg(BH_4)_2$ and β-$Mg(BH_4)_2$ phases show quite different features, especially in the region of lattice modes $150-900\,cm^{-1}$ [$18-110\,meV$]) and in the B-H stretching ($1100-1500\,cm^{-1}$ [$130-180\,meV$]) [95, 96]. Inelastic neutron scattering measurements have been performed in order to confirm Raman calculations and measurements, due to the absence of any selection rules. In β-$Mg(BH_4)_2$, a broad inelastic band is present ($3-38\,meV$), is possibly ascribed to lattice phonon. A band around ($355-661\,cm^{-1}$ [$40-82\,meV$]) was found and attributed to rigid librations of the $[BH_4]$ tetrahedron; in Raman measurements, this band is completely absent.

In $Mg(BH_4)_2$, nuclear magnetic resonance (NMR) experiments [97, 98] revealed a complex reorientational dynamics involving at least three jump processes in $\alpha-Mg(BH_4)_2$, and a variety of thermally activated processes in $\beta-Mg(BH_4)_2$, with a distribution of activation energies. The difference in these compounds could be attributed to the intrinsic orientational disorder, where the potential walls between different reorientational motions are lowered and therefore resulting in a broad distribution of activation energy. Among all the $Mg(BH_4)_2$ polymorphs, the β-phase shows the fastest reorientational motions [98].

Quasi-elastic neutron scattering (QENS) experiments, performed on $\beta-Mg(BH_4)_2$, studied the reorientation of the $[BH_4]$ tetrahedra on two different characteristic timescales, using

backscattering and indirect geometry time-of-flight spectroscopy [99] . From the analysis of the elastic incoherent structure factor (EISF) (which correlates to the spatial distribution of the hydrogen atoms in the long time average), it was suggested that the [BH_4] units exhibit hindered rotations around the 2-fold C_2 and 3-fold C_3 symmetry axis of the [BH_4] units, respectively (see fig. 1.14) on a time scale of hundreds of picoseconds.

1.4.7 Lithium and Magnesium Borohydride mixture

In the section 1.4.4.2, several destabilization methods were introduced, in order to lower the decomposition enthalpy, and hence the decomposition temperature. Among these methods, mixing borohydrides with different cation Pauling electronegativities has been proved to be a successful strategy. In particular, $LiBH_4$ and $Mg(BH_4)_2$ were investigated in different mixing ratios in order to study:

1. the formation of double cation compounds, e.g. $LiMg(BH_4)_3$;
2. the decomposition conditions and compare them with the ones of single constituent.

Moreover, mixtures of $Mg(BH_4)_2$ and $LiBH_4$ in nanoconfined carbon materials were also investigated [27, 28, 100, 101, 102]. This particular system is interesting due to the overall H_2 content that can be extracted from the decomposition scheme:

$$LiBH_4 + Mg(BH_4)_2 \quad \longrightarrow \quad LiH + B + MgB_2 + \frac{11}{2}H_2 \quad 14.6 \text{ wt. } \%H_2 \tag{1.20}$$

The initial study on the 1:1 $LiBH_4/Mg(BH_4)_2$ mix, conducted by Fang. *et. al.* [27], showed a lower overall decomposition temperature compared with the constituent phases. It was also speculated the formation of a double cation system $LiMg(BH_4)_3$, which was refuted, successively, in the work of Bardají *et al.* [28].
In this work, a mixture of $Mg(BH_4)_2$ and $LiBH_4$ with different mixing ratios was studied, focusing on the possible decomposition steps and structure evolutions, using thermogravimetry, differential scanning calorimetry, mass spectroscopy and X-ray diffraction. The mixtures

$$x LiBH_4 + (1-x)Mg(BH_4)_2, \text{ with } x = 0, ..., 1, \tag{1.21}$$

were investigated and a tentative phase diagram was proposed. The eutectic composition was found in the $x \sim 0.5$ mixture, showing a melting temperature around 180 °C (453 K) (see fig. 1.16). Further DSC-TG-MS measurements (at 5 bar H_2) showed that, for $0.5LiBH_4 + 0.5Mg(BH_4)_2$ mixture, the main decomposition takes place between 170 and 400 °C, with 12.6 mass % loss.

In DSC measurements, four distinct peaks are observable (fig. 1.15): the first one at 108 °C is attributed to the crystal phase transition of the lithium borohydride (o-$LiBH_4$ →

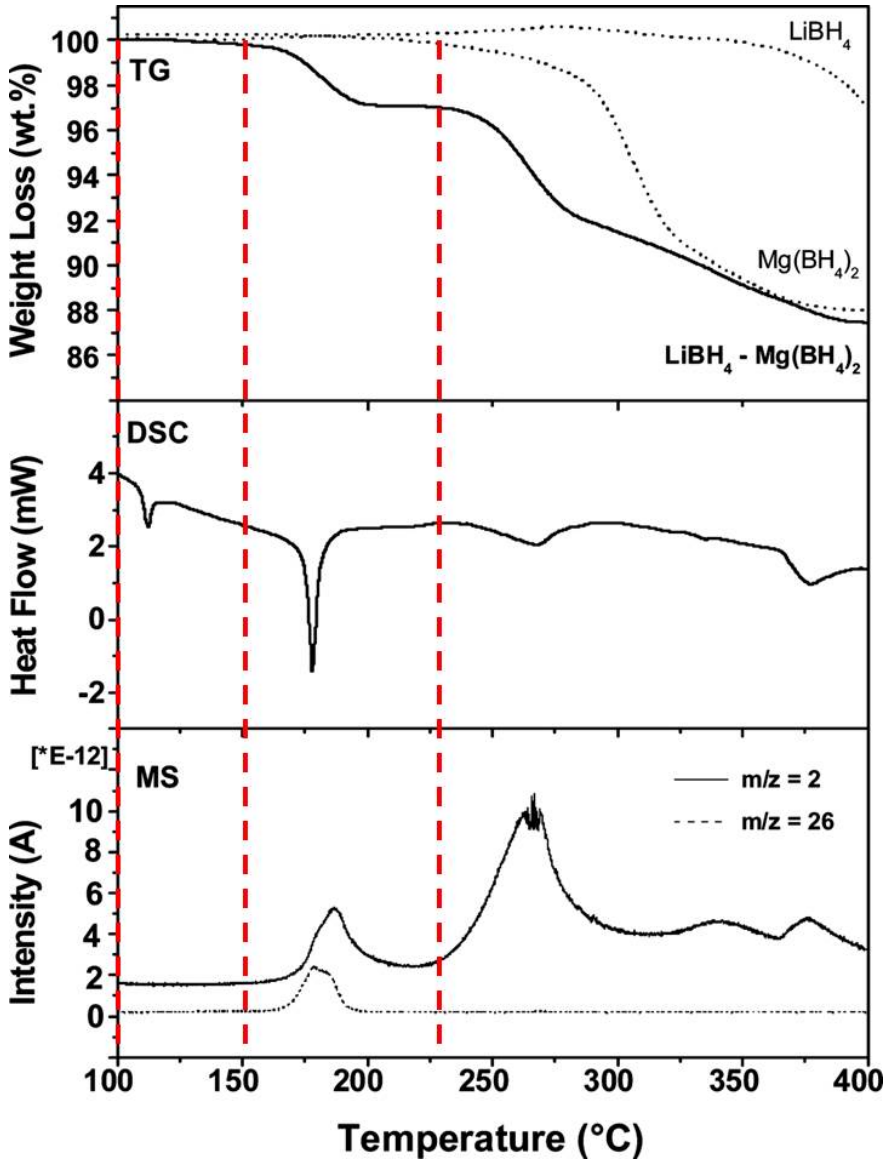

Figure 1.15: DSC-TG-MS performed on $0.5LiBH_4 + 0.5Mg(BH_4)_2$. Vertical dashed red lines correspond to the temperatures of neutron scattering measurements: 100 °C (373 K), 150 °C (423 K), 227 °C (500 K) (see chapter 6). Reprinted (adapted) with permission from E. G. Bardají *et. al.*, *J. Phys. Chem. C*, **2011**, 115 (13), pp 6095-6101. Copyright 2011 American Chemical Society.

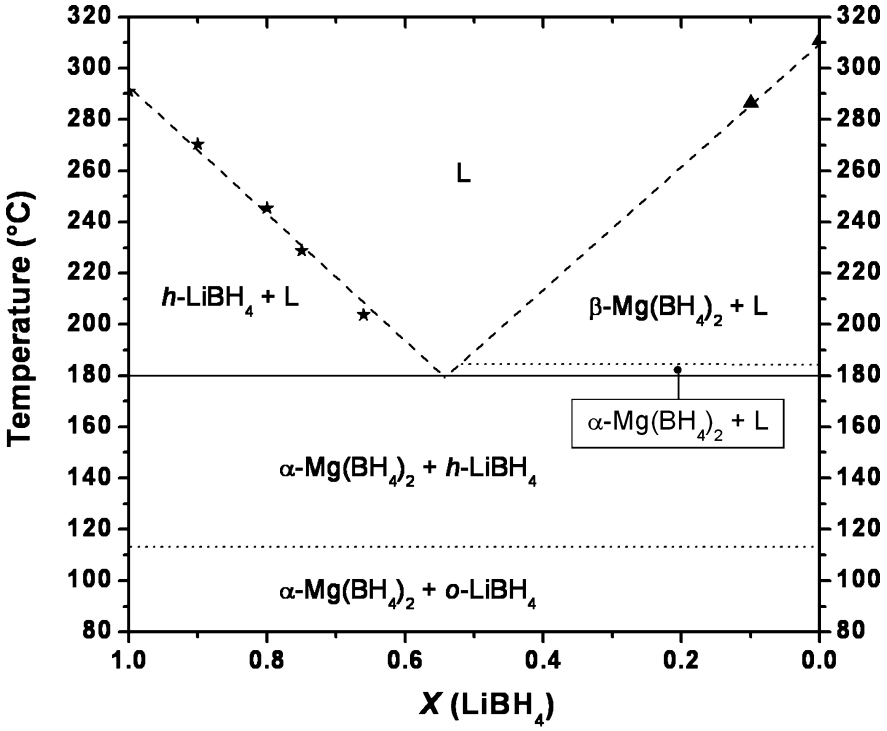

Figure 1.16: Tentative phase diagram of the $x\mathrm{LiBH_4} + (1-x)\mathrm{Mg(BH_4)_2}$. Reprinted (adapted) with permission from E. G. Bardají *et. al.*, *J. Phys. Chem. C*, **2011**, 115 (13), pp 6095-6101. Copyright 2011 American Chemical Society.

h-$LiBH_4$). The second peak, at 175 °C, coincides with the first decomposition step observed in the TG measurement, and it is attributed to the $Mg(BH_4)_2$ crystal phase $\alpha \rightarrow \beta$ transformation. Both crystal phase transition temperatures are slightly lower than in the pure compounds. The last two peaks correspond to decomposition steps releasing the highest amount of hydrogen: the total H_2 amount released was 12.6 wt.% at 435 °C, compared to the theoretical estimated of 14.6 wt.% H_2.

Since the material is a physical mixture, the decomposition temperature should be an average of the single phases' temperature. Instead, the decomposition temperature is lower than the pure materials (see TG measurement in fig.1.15). Moreover, X-ray measurements show that the α crystal phase in $Mg(BH_4)_2$ is recovered upon cooling the material below the crystal phase transition around 175 °C. Already a small amount of $LiBH_4$ destabilizes $Mg(BH_4)_2$, making possible the transformation from orthorhombic to hexagonal crystal phase.

1.5 Scope of the thesis

In complex borohydrides, there is a correlation between the cation electronegativity χ_P and the thermodynamic stability of different compounds, thus the desorption temperatures. The bonding between the cations (Li^+, Mg^{2+}, Ca^{2+}) and the $[BH_4]^-$ units plays then a crucial role.
In the alkaline borohydrides $LiBH_4$ or $NaBH_4$, the cation$\cdots[BH_4]^-$ bond is almost ionic [103, 104], while for alkaline earth borohydrides the bond also has some covalent character [105, 75]. Borohydrides exist in different crystalline structures, and many structure phase transitions depend on thermodynamic conditions (e.g. temperature and/or pressure). Moreover, it has been observed that some crystal phases are metastable, depending on the material synthesis procedure. Usually, these structural phase transitions are accompanied with a change in the dynamics of the $[BH_4]^-$ units.

In ionic bonded borohydrides ($LiBH_4$, $NaBH_4$, KBH_4), the structure show an order/disorder transition, most likely triggered by the enhanced rotational dynamics at high temperatures. In more covalently bonded compounds (e.g. $Mg(BH_4)_2$ and $Ca(BH_4)_2$), hydrogen dynamics across different crystal phases is scarcely investigated and poorly understood, and some fundamental questions are still open, especially regarding the non-reversibility of crystal phases transitions. In $Ca(BH_4)_2$, the rich polymorphism influences the decomposition reactions and the formation of different reaction products. Moreover, in $Ca(BH_4)_2$, the vibrational dynamics seems to drive the crystal phase transition from the α- to β-phase. Instead, in $Mg(BH_4)_2$, the mechanism responsible for the transition and for its non-reversibility is not totally clear.
The main goal in this thesis is the investigation of the hydrogen dynamics on the picosecond time scale with the use of quasi-elastic neutron scattering (QENS) experiments, exploring the dynamics of low energy vibrations and self diffusion mechanisms.
The materials chosen, lithium and magnesium borohydrides, are the ones with the highest hydrogen content, and thus candidates for on-board hydrogen storage applications.
Starting from this, the present work is addressing some fundamental questions:

1. How the localized dynamics of the $[BH_4]$ units is correlated with different anion/cation bonding?
2. Is the low energy lattice dynamics of the $[BH_4]$ units connected with different crystal structure transitions?
3. How the different dynamics might influence the crystal phase transitions and their metastability?

In chapter 2, inelastic neutron scattering is introduced from the theoretical point of view, with focus on quasi-elastic neutron scattering technique. In chapter 3, the instrument

TOFTOF will be described, also focussing on energy resolution and dynamical range. Chapter 4, 5 and 6 will be dedicated to results and analysis of $LiBH_4$, $Mg(BH_4)_2$ and $LiBH_4$ + $Mg(BH_4)_2$, respectively. In chapter 7, conclusions and future perspectives are presented.

Chapter 2

Techniques

Contents

Different techniques are used for studying hydrogen storage materials, especially in complex hydrides. Among them, the dynamics is investigated using neutron scattering experiments, Nuclear Magnetic Resonance (NMR), Raman and Infra-Red (IR) spectroscopy. In this work, only neutron scattering will be briefly described.

2.1 Neutron Scattering

One of the most suitable technique to provide information where atoms are and how they move is neutron scattering [106, 107]. Neutrons are not charged and therefore the interaction between matter is not driven by Coulomb forces, but their principal means of interaction is through the strong force with nuclei: these forces act on an effective distance of 10^{-15} m, and therefore the interaction between neutrons and atoms can be considered as a point-like interaction. This will have a consequence in the derivation of some important equation characterizing the neutron scattering. Neutrons are weakly absorbed by most of materials, and thus they can easily penetrate inside the matter, making them suitable for studying

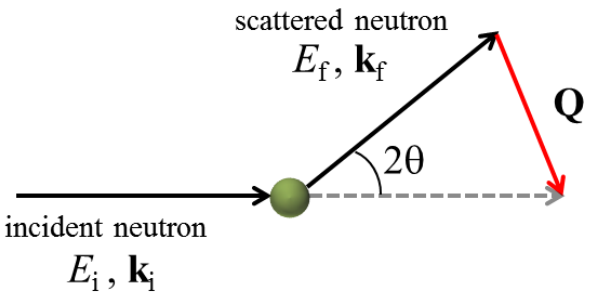

Figure 2.1: 2D representation of a scattering process in the reciprocal space. The incident neutron is characterized by an incident energy E_i and momentum $\mathbf{p}_\mathrm{i} = \hbar\mathbf{k}_\mathrm{i}$. The outgoing neutron characterized by an final energy E_f and momentum $\mathbf{p}_\mathrm{f} = \hbar\mathbf{k}_\mathrm{f}$. The momentum transfer is defined as $\hbar\mathbf{Q} = \hbar\mathbf{k}_\mathrm{i} - \hbar\mathbf{k}_\mathrm{if}$.

condensed matter properties in the atomic scale.
Due to the low interaction with matter, a neutron scattering experiment provides information on the physical and chemical properties of the sample, which is not perturbed by the presence of the neutron. In this approximation, the neutron measures the undistorted properties of the sample. A neutron can be described, in a non relativistic description, as a particle and a wave, respectively characterized by a kinetic energy E and a wave vector $\mathbf{k}$:

$$E = \frac{\hbar^2 k^2}{2m}, \quad |\mathbf{k}| = k = \frac{2\pi}{\lambda}, \tag{2.1}$$

with $m = 1.67 \cdot 10^{-27}$ kg the mass, k is the magnitude of the wave vector $\mathbf{k}$, λ the wavelength.

A typical scattering experiment is depicted in fig. 2.1. In an simplified scheme, a neutron with an incident energy E_i and a wave-vector $\mathbf{k}_i$ is impinging on a sample. The neutron interacts with the sample and a scattering event takes place. After this interaction, the neutron emerges from the sample with an outgoing wave vector $\mathbf{k}_f$ and energy E_f. The task of the experiment is to detect any changes in energy and in wave vector of the scattered neutron, after the interaction with a sample. Therefore it is useful to define two quantities that will used to characterize the experiment:

- Energy transfer: $\hbar\omega = E_i - E_f = \frac{\hbar^2}{2m}\left(|\mathbf{k_i}|^2 - |\mathbf{k_f}|^2\right)$
- Momentum transfer: $\hbar\mathbf{Q} = \hbar\left(\mathbf{k_i} - \mathbf{k_f}\right)$.

Usually the energy and wave vector transfers are measured in [meV] and [$\mathrm{\AA}^{-1}$], respectively.

It is important to underline that motions of atoms and their correlations are revealed by neutron scattering only if energy and momentum transfers match excitation energies and distances in the sample. Nowadays, neutrons in science span quite a large interval in energy

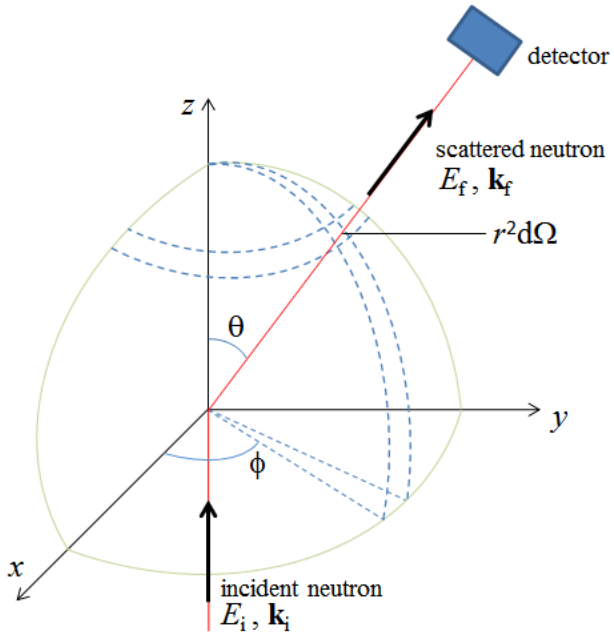

Figure 2.2: 3D schematic representation of the scattering process. The area delimited by dashed lines represent a surface at a certain distance r from the sample and in a solid angle $d\Omega$.

and momentum transfers, ranging from $10^{-5}\text{meV} < \hbar\omega < 1\,\text{eV}$ and $10^{-3} < Q < 30\,\text{Å}^{-1}$, allowing the study of structural and dynamical properties in a variety of systems.

In the scattering experiment depicted in fig. 2.1, three processes can take place:

- Absorption: the incident neutron is absorbed in the sample by nuclear capture.
- Elastic scattering: the magnitude of the incident wave vector does not change after the interaction with sample, $k_i = k_f$
- Inelastic scattering: the neutron loses or gains energy, $k_i > k_f$ or $k_i < k_f$ respectively
- Transmission: the incident neutron does not interact with the sample.

After being scattered by the sample, the neutron is registered by using a detector. Depending on the scope of the experiment, time and position of the arrival can be registered, and thus analysed.

2.1.1 Neutron cross section

The basic quantity to be measured in the scattering process is the partial (or double) differential cross-section, which gives the number of incident neutrons with energy E_i scattered into a solid angle $d\Omega$, with an energy in the interval $[E', E' + dE']$. This quantity is denoted by

$$\frac{d^2\sigma}{d\Omega dE'}. \tag{2.2}$$

The complete derivation of double differential scattering cross section can be simplified assuming the scattering from single bound nuclei. As mentioned before, the neutron is a weak probe and it does not interact strongly with solids (except for strong absorbing materials). Thus, the total scattering amplitude of a sample containing N scatterers is the sum of single scattering amplitudes. The expression is given first for the elastic case, then will be generalized for the inelastic one.

Denoting the initial state of the incident neutron as $\psi_{\mathbf{k}}$ and the final state of the scattered neutron as $\psi_{\mathbf{k}'}$, the differential cross-section is calculated starting from the probability of a transition between the state $|\mathbf{k}\rangle$ and $|\mathbf{k}'\rangle$, with the same energy E. The probability follows the Fermi's Golden rule,

$$W_{k\to k'} = \frac{2\pi}{\hbar}\left|\int d\mathbf{r}\psi^{\star}_{\mathbf{k}'}\hat{\mathbf{V}}\psi_{\mathbf{k}}\right|^2 \rho_{\mathbf{k}'}(E)\,. \tag{2.3}$$

The potential $\hat{V}$ describes the interaction that allows a transition from a state $|\mathbf{k}\rangle$ to a state $|\mathbf{k}'\rangle$, and $\rho_{\mathbf{k}'}(E)$ is the density of final states. The final expression for the scattering cross section becomes:

$$\left(\frac{\mathrm{d}\sigma}{\mathrm{d}\Omega}\right) = \left|\frac{m}{2\pi\hbar^2}\int \mathrm{d}\mathbf{r}\exp(-i\mathbf{k}'\cdot\mathbf{r})\hat{V}\exp(i\mathbf{k}\cdot\mathbf{r})\right|^2 = \left|\langle\mathbf{k}'|\,\hat{V}\,|\mathbf{k}\rangle\right|^2. \tag{2.4}$$

In order to get the partial differential cross-section, we must consider inelastic events. In case of inelastic scattering, the neutron energy change is a quanta of $\hbar\omega$, given or taken by the sample in the scattering process. Assuming the target in a state $|\alpha\rangle$, the state describing the incident neutron and the initial state of target is the product of the two ket vectors, namely $|\mathbf{k},\alpha\rangle$.The target energy is denoted by the eigenvector E_α. In case there is an energy transfer between target and neutron, the conservation of energy in this process leads to

$$\hbar\omega = E_\alpha - E_{\alpha'}, \tag{2.5}$$

and the cross section reads

$$\left(\frac{\mathrm{d}\sigma}{\mathrm{d}\Omega}\right)^{\alpha}_{\alpha'} = \frac{k'}{k}\left|\langle\mathbf{k}'\alpha'|\,\hat{V}\,|\mathbf{k}\alpha\rangle\right|^2. \tag{2.6}$$

The partial differential cross section is obtained from the conservation of energy equation as written above:

$$\left(\frac{\mathrm{d}\sigma}{\mathrm{d}\Omega\mathrm{d}E'}\right)^{\alpha}_{\alpha'} = \frac{k'}{k}\left|\langle\mathbf{k}'\alpha'|\,\hat{V}\,|\mathbf{k}\alpha\rangle\right|^2\delta\left(\hbar\omega + E_\alpha - E_{\alpha'}\right). \tag{2.7}$$

The previous equation relates the scattering process from a state $|\alpha\rangle$ to a final state $|\alpha'\rangle$. Depending on the target, only certain states can be accessible; therefore it is necessary to include a weight p_α in the double differential cross-section:

$$\left(\frac{\mathrm{d}\sigma}{\mathrm{d}\Omega\mathrm{d}E'}\right)^{\alpha}_{\alpha'} = \frac{k'}{k}\overline{\sum_{\alpha,\alpha'} p_\alpha\left|\langle\mathbf{k}'\alpha'|\,\hat{V}\,|\mathbf{k}\alpha\rangle\right|^2\delta\left(\hbar\omega + E_\alpha - E_{\alpha'}\right)}, \tag{2.8}$$

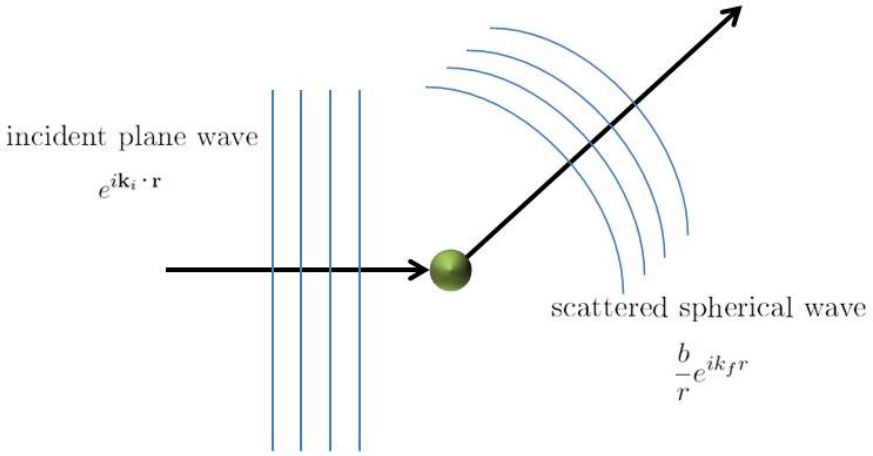

Figure 2.3: Scattering of a incident plane wave into a target (green sphere). The outgoing wave is spherical (s-wave).

where the average is performed on all possible and accessible states. The expression for the differential cross section 2.8 is obtained in the first Born approximation (or first perturbation series), under the hypothesis that the interaction neutron-target is weak. In all previous expressions for differential and partial differential cross-sections the unknown variable is the potential $\hat{V}$. The interaction between neutrons and nuclei is in the order 10^{-15} m, at least four orders of magnitude smaller than the typical wavelength for slow neutrons ($\sim 10^{-10}$ m), and therefore the neutron-nuclei scattering is isotropic and contains only plane waves. The outgoing wave is characterized by a parameter b, called scattering length. This quantity can be complex and depends on the energy of incident neutron, on the isotope and on the relative orientation between the incident neutron spin and the nuclei spin.

If the scattering potential $\hat{V}$ is a δ-function (i.e. a point-like interaction), the outgoing wave is spherical. Fermi's pseudo-potential satisfies the requirement. Assuming a rigid array of N nuclei fixed in positions denoted by $\mathbf{R}_l$ and scattering length b_l, the expression of $\hat{V}$ is

$$\hat{V}(\mathbf{r}) = \frac{2\pi\hbar^2}{m} \sum_l b_l \delta\left(\mathbf{r} - \mathbf{R}_l\right). \tag{2.9}$$

The length b_l can be interpreted as a radius of an impenetrable sphere centred at the nuclei l and it has dimensions of a [length]. Given this expression for the Fermi's potential, it is possible, in eq. 2.8, to evaluate:

$$\langle \mathbf{k}' | \hat{V} | \mathbf{k} \rangle = \sum_l b_l \exp(i\mathbf{Q} \cdot \mathbf{R}_l) \tag{2.10}$$

and then the eq. 2.6 becomes:

$$\left(\frac{\mathrm{d}\sigma}{\mathrm{d}\Omega}\right) = \overline{\left| \sum_l b_l \exp(i\mathbf{Q} \cdot \mathbf{R}_l) \right|^2} = \sum_{l,l'} \exp(i\mathbf{Q} \cdot (\mathbf{R}_l - \mathbf{R}_{l'})) \overline{b_{l'}^* b_l}. \tag{2.11}$$

In the last equation, the scattering length (that in general is a complex number) has to be averaged all over random nuclear spin orientations and random isotope distributions, and it is generally dependent on the position $\mathbf{R}_l$. Assuming that there is no correlation between different sites l and l', then

$$\overline{b_{l'}^* b_l} = \left|\overline{b}\right|^2 + \delta_{l,l'}\left(\overline{|b|^2} - \left|\overline{b}\right|^2\right) \tag{2.12}$$

In this way the contribution in the average has been separated in two terms, one coming from different pair of atoms, and one from the same atoms. Therefore, the scattering cross-section can be written as

$$\left(\frac{\mathrm{d}\sigma}{\mathrm{d}\Omega}\right) = \left(\frac{\mathrm{d}\sigma}{\mathrm{d}\Omega}\right)_{\mathrm{coh}} + \left(\frac{\mathrm{d}\sigma}{\mathrm{d}\Omega}\right)_{\mathrm{inc}}, \tag{2.13}$$

where

$$\left(\frac{\mathrm{d}\sigma}{\mathrm{d}\Omega}\right)_{\mathrm{coh}} = \left|\overline{b}\right|^2 \left|\sum_l b_l \exp(i\mathbf{Q}\cdot\mathbf{R}_l)\right|^2 \tag{2.14}$$

is the coherent cross-section, and

$$\left(\frac{\mathrm{d}\sigma}{\mathrm{d}\Omega}\right)_{\mathrm{inc}} = N\left[\overline{|b|^2} - \left|\overline{b}\right|^2\right] = N\overline{\left|b-\overline{b}\right|^2} \tag{2.15}$$

is the incoherent cross-section.

The first one, the coherent cross-section, is dependent on the interference between waves scattered from different lattice sites and it is weighted with an average scattering length. The incoherent cross-section, instead, is lattice independent and it is weighted with a mean-square scattering length deviation. In a scattering experiment, both contributions are detected: the coherent cross-section is angle (or momentum transfer) dependent, whereas the incoherent one does not depend on $\mathbf{Q}$ and therefore leads to an isotropic signal.
The scattering cross-sections are given usually in units of area, 1 barn = $10^{-24}\,\mathrm{cm}^2$, and they vary randomly from element to element, and from isotope to isotope. The most extreme case is the scattering cross-section of hydrogen: the most abundant isotope, ^{1}H, has a coherent cross section of 1.8 barn, whereas the incoherent cross-section is 81.7 barn. Deuterium, instead, has σ_i= 2.05 barn and σ_c = 5.59 barn. A list of all scattering lengths and cross sections can be found in literature [108]. The next section will deal with the formalism of inelastic neutron scattering and how it is related with positions of particles in space and time.

2.1.2 Inelastic neutron scattering

The difference between coherent and incoherent scattering has been shown above for the elastic case, calculating the differential cross-section. For the inelastic case, the double dif-

ferential cross section can still be divided into coherent and incoherent. Both give information about spatial- and time-correlations of atoms in a sample.
In eq. 2.8, the δ-function can be replaced by its integral representation and it leads to a separation of the incoherent and coherent parts:

$$\left(\frac{\mathrm{d}^2\sigma}{\mathrm{d}\Omega \mathrm{d}E'}\right) = \left(\frac{\mathrm{d}^2\sigma}{\mathrm{d}\Omega \mathrm{d}E'}\right)_{\mathrm{coh}} + \left(\frac{\mathrm{d}^2\sigma}{\mathrm{d}\Omega \mathrm{d}E'}\right)_{\mathrm{inc}}, \tag{2.16}$$

where

$$\left(\frac{\mathrm{d}\sigma}{\mathrm{d}\Omega \mathrm{d}E'}\right)_{\mathrm{coh}} = |b|^2 \frac{k'}{k} N S_{\mathrm{coh}}(\mathbf{Q},\omega) \tag{2.17}$$

and

$$\left(\frac{\mathrm{d}\sigma}{\mathrm{d}\Omega \mathrm{d}E'}\right)_{\mathrm{inc}} = \left[\overline{|b|^2} - \left|\overline{b}\right|^2\right] \frac{k'}{k} N S_{\mathrm{inc}}(\mathbf{Q},\omega). \tag{2.18}$$

The two terms $S_{\mathrm{coh}}(\mathbf{Q},\omega)$ and $S_{inc}(\mathbf{Q},\omega)$ are defined as

$$S_{\mathrm{coh}}(\mathbf{Q},\omega) = \frac{1}{2\pi\hbar}\int_{-\infty}^{+\infty} \mathrm{d}t \exp(-i\omega t) \sum_{l,l'}^{N} \langle \exp(-i\mathbf{Q}\cdot\mathbf{R}_l) \exp(i\mathbf{Q}\cdot\mathbf{R}_{l'}(t))\rangle \tag{2.19}$$

and

$$S_{\mathrm{inc}}(\mathbf{Q},\omega) = \frac{1}{2\pi\hbar}\int_{-\infty}^{+\infty} \mathrm{d}t \exp(-i\omega t) \sum_{l}^{N} \langle \exp(-i\mathbf{Q}\cdot\mathbf{R}_l) \exp(i\mathbf{Q}\cdot\mathbf{R}_{l}(t))\rangle. \tag{2.20}$$

The term $S_{\mathrm{coh|inc}}(\mathbf{Q},\omega)$ is called *dynamic structure factor*, *response function* or *scattering function*, and this is what is measured in a neutron scattering experiment. $S_{\mathrm{coh|inc}}(\mathbf{Q},\omega)$ is directly related to the spectrum of spontaneous fluctuation in the system and, since the neutron is weakly interacting with nuclei, it measures the undistorted properties of the sample. The scattering function can be related to physical properties in the sample, like correlation in space and time $(\mathbf{r},t)$. The link between $(\mathbf{Q},\omega)$- and $(\mathbf{r},t)$-space has been formulated by Léon Van Hove [109].

Pair- and self-correlation functions It is useful to define two kinds of functions: the pair correlation function

$$G(\mathbf{r},t) = \frac{1}{N}\sum_{l,l'}\int \mathrm{d}\mathbf{R}' \langle \delta(\mathbf{r}-\mathbf{R}'+\mathbf{R}_l(0))\delta(\mathbf{R}'-\mathbf{R}_{l'}(t))\rangle, \tag{2.21}$$

and the self correlation function

$$G_s(\mathbf{r},t) = \frac{1}{N}\sum_l \int \mathrm{d}\mathbf{R}' \langle \delta(\mathbf{r}-\mathbf{R}'+\mathbf{R}_l(0))\delta(\mathbf{R}'-\mathbf{R}_l(t))\rangle. \tag{2.22}$$

Having defined these two quantities, it is possible to express the scattering functions (coherent and incoherent) as the double Fourier transform (in time and space) of the pair and self correlation functions:

$$S_{\mathrm{coh}}(\mathbf{Q},\omega) = \frac{1}{2\pi\hbar}\int_{-\infty}^{+\infty} \mathrm{d}t \exp(-i\omega t)\int \mathrm{d}\mathbf{r}\exp(i\mathbf{Q}\cdot\mathbf{r})G(\mathbf{r},t) \tag{2.23}$$

$$S_{\mathrm{inc}}(\mathbf{Q},\omega) = \frac{1}{2\pi\hbar}\int_{-\infty}^{+\infty} \mathrm{d}t \exp(-i\omega t)\int \mathrm{d}\mathbf{r}\exp(i\mathbf{Q}\cdot\mathbf{r})G_s(\mathbf{r},t) \tag{2.24}$$

Usually pair correlation functions have complex values due to fact that the quantities in $\langle ... \rangle$ do not commute at different times. If the system can be considered classical (meaning that the particles are widely separated in space and no quantum effect can be detected), the expressions for pair- and self correlation functions become:

$$G^{cl}(\mathbf{r},t) = \frac{1}{N}\sum_l \langle \delta(\mathbf{r}-\mathbf{R}_l(t)+\mathbf{R}_k(0))\rangle \tag{2.25}$$

and

$$G_s^{cl}(\mathbf{r},t) = \langle \delta(\mathbf{r}-\mathbf{R}_k(t)+\mathbf{R}_k(0))\rangle \tag{2.26}$$

The averaging now is performed, being a classical system, all over the possible configuration of the initial state. The sum in eq. 2.25 is performed all over the N particles, and the position of particle k has been taken at t. Both eqs. 2.25 and 2.26 can be interpreted as a probability density. The first one, $G^{cl}(\mathbf{r},t)$ represents a probability that, given a particle k in a position $\mathbf{R}$ at time $t=0$, *another one* (including the same particle) can be found at a distance $\mathbf{r}$ and at a time t. Differently, $G_s^{cl}(\mathbf{r},t)$ represents a probability that, given a particle k in a position $\mathbf{R}$ at time $t=0$, the *same* particle can be found at a distance $\mathbf{r}$ and at a time t.

From the previous two equations and from eqs. 2.17-2.18, we can directly access the correlation functions by measuring the scattering cross-section. It is intuitive that an integration of these two quantities over the total spaces leads to:

$$\int G^{cl}(\mathbf{r},t)\mathrm{d}\mathbf{r} = N \quad \text{and} \quad \int G_s^{cl}(\mathbf{r},t)\mathrm{d}\mathbf{r} = 1. \tag{2.27}$$

In many complex problems, sometimes it is more convenient to deal with the spatial Fourier transform of the pair correlation function. This is generally known as Intermediate scattering

function, denoted with $I(\mathbf{Q},t)$. Similar to the scattering function, it is possible to distinguish a coherent and incoherent one:

$$I_{\rm coh}(\mathbf{Q},t)=\frac{1}{N}\sum_{l,l'}^{N}\langle\exp(-i\mathbf{Q}\cdot\mathbf{R}_l)\exp(i\mathbf{Q}\cdot\mathbf{R}_{l'}(t))\rangle=\int G(\mathbf{r},t)\exp(i\mathbf{Q}\cdot\mathbf{r})\mathrm{d}\mathbf{r}, \tag{2.28}$$

and

$$I_{\rm inc}(\mathbf{Q},t)=\frac{1}{N}\sum_{l}^{N}\langle\exp(-i\mathbf{Q}\cdot\mathbf{R}_l)\exp(i\mathbf{Q}\cdot\mathbf{R}_{l}(t))\rangle=\int G_{\rm s}(\mathbf{r},t)\exp(i\mathbf{Q}\cdot\mathbf{r})\mathrm{d}\mathbf{r}. \tag{2.29}$$

General properties of correlation functions In general, the scattering functions $S(\mathbf{Q},\omega)$ are proportional to the double differential cross-section, thus implying that they are real functions. The correlation functions then satisfy

$$G(\mathbf{r},t)=G^{*}(-\mathbf{r},t), \tag{2.30}$$

and this leads to the a general principle on the scattering function $S(\mathbf{Q},\omega)$, called detailed balance condition

$$S(\mathbf{Q},\omega)=\exp\left(\frac{\hbar\omega}{k_BT}\right)S(-\mathbf{Q},-\omega), \tag{2.31}$$

where k_B is the Boltzmann constant and T is the temperature. The previous equation requires that the scattering function is real, and it gives the relationship between the intensity in the energy loss and energy gain of the scattering function. It can be read as the probability that a neutron loses an energy $\hbar\omega$ is equal to the probability that gains and energy $\hbar\omega$, multiplied by a factor $\exp\left(\frac{\hbar\omega}{k_BT}\right)$. At low temperature only the lower energy states in the sample are populated, and therefore the probability of a transition in to the higher states is greater than the inverse. As soon the temperature rises, the difference is reduced, since both higher and lower states are equally populated.

In the definition of pair and self correlation functions, quantum operators do not commute at different times, whereas they do at equal times. Two extreme cases can be considered $t=0$ and $t\to\infty$: these two cases will be useful in the interpretation of the quasi-elastic scattering experiments. In general these functions are characterized by a pronounced structure at $t=0$, whereas, in the opposite limit, the function is not depending any more on $\mathbf{r}$. It is useful then, to divide the correlation functions in two parts,

$$G_{(s)}(\mathbf{r},t)=G_{(s)}(\mathbf{r},\infty)+G'_{(s)}(\mathbf{r},t),\quad\text{with}\quad\lim_{t\to\infty}G'_{(s)}(\mathbf{r},t)=0. \tag{2.32}$$

and finally write the double differential cross-sections as a sum of the two terms, one elastic and one inelastic:

$$\left(\frac{\mathrm{d}\sigma}{\mathrm{d}\Omega\mathrm{d}E'}\right)_{\rm coh}=\left(\frac{\mathrm{d}\sigma}{\mathrm{d}\Omega\mathrm{d}E'}\right)^{\rm el}_{\rm coh}+\left(\frac{\mathrm{d}\sigma}{\mathrm{d}\Omega\mathrm{d}E'}\right)^{\rm inel}_{\rm coh}, \tag{2.33}$$

and

$$\left(\frac{\mathrm{d}\sigma}{\mathrm{d}\Omega\mathrm{d}E'}\right)_{\mathrm{inc}} = \left(\frac{\mathrm{d}\sigma}{\mathrm{d}\Omega\mathrm{d}E'}\right)_{\mathrm{inc}}^{\mathrm{el}} + \left(\frac{\mathrm{d}\sigma}{\mathrm{d}\Omega\mathrm{d}E'}\right)_{\mathrm{inc}}^{\mathrm{inel}}. \tag{2.34}$$

Using eq. 2.32, it is possible to write, for the coherent part:

$$\left(\frac{\mathrm{d}\sigma}{\mathrm{d}\Omega\mathrm{d}E'}\right)_{\mathrm{coh}}^{\mathrm{el}} = \left(\frac{\mathrm{d}\sigma}{\mathrm{d}\Omega}\right)_{\mathrm{coh}}^{\mathrm{el}} = N\frac{\sigma_c}{4\pi}\delta(\hbar\omega)\int \exp(i\mathbf{q}\cdot\mathbf{r})G(\mathbf{r},\infty)\mathrm{d}\mathbf{r} \tag{2.35}$$

and

$$\left(\frac{\mathrm{d}\sigma}{\mathrm{d}\Omega\mathrm{d}E'}\right)_{\mathrm{coh}}^{\mathrm{inel}} = \frac{N\sigma_c}{4\pi}\frac{k'}{k}\frac{1}{2\pi\hbar}\int_{-\infty}^{+\infty}\mathrm{d}t\exp(-i\omega t)\int \mathrm{d}\mathbf{r}\exp(-i\mathbf{q}\cdot\mathbf{r})G'(\mathbf{r},t). \tag{2.36}$$

The same can be done for the incoherent one:

$$\left(\frac{\mathrm{d}\sigma}{\mathrm{d}\Omega\mathrm{d}E'}\right)_{\mathrm{inc}}^{\mathrm{el}} = \left(\frac{\mathrm{d}\sigma}{\mathrm{d}\Omega}\right)_{\mathrm{inc}}^{\mathrm{el}} = N\frac{\sigma_i}{4\pi}\delta(\hbar\omega)\int \exp(i\mathbf{q}\cdot\mathbf{r})G_s(\mathbf{r},\infty)\mathrm{d}\mathbf{r}, \tag{2.37}$$

and

$$\left(\frac{\mathrm{d}\sigma}{\mathrm{d}\Omega\mathrm{d}E'}\right)_{\mathrm{inc}}^{\mathrm{inel}} = \frac{N\sigma_i}{4\pi}\frac{k'}{k}\frac{1}{2\pi\hbar}\int_{-\infty}^{+\infty}\mathrm{d}t\exp(-i\omega t)\int \mathrm{d}\mathbf{r}\exp(-i\mathbf{q}\cdot\mathbf{r})G'_s(\mathbf{r},t). \tag{2.38}$$

These equations are valid for any system, and correlate (double) differential scattering cross-section to pair and self correlation functions.

2.1.2.1 Vibrations of atoms

In hydrogenous compounds (i.e. complex hydrides), the incoherent cross-section of hydrogen exceeds by an order of magnitude all the coherent cross-sections of other atoms. Therefore, in inelastic neutron scattering on hydrogenous materials, only hydrogen contributes to the double differential cross section. In the next two sections the scattering functions of atomic vibrations and stochastic motions, considering only the incoherent signal, will be summarized.

The pair and self-correlation functions, defined in the previous section, are derived in a general scheme. When it comes to solids or liquid, an appropriate model has to be derived for the scattering function. The simplest model for taking account vibrations of atoms is to consider harmonics lattice vibrations. Given N atoms in a Bravais lattice, each atom can be described by lattice vectors $\mathbf{a}_1, \mathbf{a}_2, \mathbf{a}_3$,

$$\mathbf{l} = l_1\mathbf{a}_1 + l_2\mathbf{a}_2 + l_3\mathbf{a}_3. \tag{2.39}$$

Since atoms are vibrating in their equilibrium positions, the position of each atoms can be described by

$$\mathbf{R}_l = \mathbf{l} + \mathbf{u}(l). \tag{2.40}$$

If the potential is harmonic, the displacement can be expanded in Taylor series and the scattering cross sections for vibrating atoms can be calculated. Without going into the details, the general expression for the incoherent cross section of one phonon scattering is given:

$$\left(\frac{\mathrm{d}\sigma}{\mathrm{d}\Omega \mathrm{d}E'}\right)_{\mathrm{inc}} = \frac{N\sigma_i}{8\pi M}\frac{k'}{k}Q^2 \exp(-2W(\mathbf{Q}))\frac{Z(\omega)}{\omega}\left[n(\omega)+1\right], \tag{2.41}$$

where $n(\omega) = [\exp(\hbar\omega/k_BT)-1]^{-1}$ is the Bose-Einstein factor. In this expression

- $\exp(-2W(\mathbf{Q}))$ is the Debye-Waller factor (DWF)
- $Z(\omega)$ is the normalized density of states

Debye-Waller factor (DWF) The quantity in the exponent is defined as the expectation value of the mean square displacement of atom along the momentum transfer $\mathbf{Q}$:

$$\exp(-2W(\mathbf{Q})) = \langle\{\mathbf{Q}\cdot\mathbf{u}(l)\}^2\rangle. \tag{2.42}$$

The information about scattering is averaged all over the possible directions of the momentum transfer, and therefore eq. 2.42 becomes:

$$2W(Q) = \frac{1}{3}Q^2\langle u^2\rangle. \tag{2.43}$$

Density of states $Z(\omega)$ is called density of states and it reflects the density distribution of the vibration frequencies. It is defined in such a way that the fraction of vibration modes ω_q in an energy interval $[\omega, \omega+\mathrm{d}\omega]$ is $Z(\omega)\mathrm{d}\omega$. It is related to the Debye-Waller factor through

$$W(Q) = \frac{\hbar Q^2}{4M}\int_0^\infty \mathrm{d}\omega \frac{Z(\omega)}{\omega}\coth\left(\frac{1}{2}\frac{\hbar\omega}{k_BT}\right) \tag{2.44}$$

Therefore, the Debye-Waller factor itself contains information on the vibrational density of states. A simple approximation, valid at relatively low energies, is derived by Debye, where $Z(\omega)$ is:

$$Z(\omega) = \begin{cases} 3\frac{\omega^2}{\omega_D^3}, & \text{if } \omega < \omega_D \\ 0, & \text{otherwise.} \end{cases} \tag{2.45}$$

The Debye frequency ω_D is associated to a Debye temperature T_D, $k_BT_D = \hbar\omega_D$. The DWF can be then evaluated in two different extreme cases:

$$W(Q) = \begin{cases} 3\frac{\hbar^2Q^2}{2M}\frac{T}{\hbar\omega_D T_D} & \text{if } T \gg T_D \\ \frac{3}{4}\frac{\hbar^2Q^2}{2M}\frac{1}{\hbar\omega_D} & \text{if } T \to 0. \end{cases} \tag{2.46}$$

One phonon scattering In a harmonic system, vibrations of nuclei give a scattering cross-section

$$\left(\frac{\mathrm{d}^2\sigma}{\mathrm{d}\Omega \mathrm{d}E'}\right)_{\mathrm{inc}}^{\mathrm{inel}} = \frac{k'}{k}\frac{\sigma_{\mathrm{inc}}}{4M}\exp(-2W(\mathbf{Q}))\sum_{j,\mathbf{q}}|\mathbf{Q}\cdot\sigma^j(\mathbf{q})|^2 S_j(\mathbf{q},\omega) \tag{2.47}$$

with

$$S_j(\mathbf{q},\omega) = \frac{1}{2\omega_j(\mathbf{q})}\left[n_j(\mathbf{q})\delta(\omega+\omega_j(\mathbf{q})) + (n_j(\mathbf{q})+1)\delta(\omega-\omega_j(\mathbf{q}))\right]. \tag{2.48}$$

$\mathbf{Q} = \kappa \pm \mathbf{q}$, being κ a reciprocal lattice vector. The two terms in the square brackets represent annihilation and creation of one phonon quantum, and the two δ-functions are in agreement with the energy conservation principle. This is only true in a perfect harmonic crystal. In presence of anharmonic effects, the scattering function is slightly modified, taking into account anharmonic forces. These are originating from third- and higher-order terms in the Hamiltonian describing nuclei motions, and are responsible for thermal expansion, difference in specific heat at constant pressure and volume, finite thermal conductivity [106]. Due to this additional term, the phonon frequency is slightly shifted respect the nominal dispersion value $\omega_j(\mathbf{q})$. The scattering function can be calculated from the linear response theory [106, 110]

$$S_j(\mathbf{Q},\omega) = [n(\omega)+1]\frac{Z(Q)}{\pi}\frac{4\omega\Gamma_q}{\left[(\omega-\omega_q)^2+\Gamma_q^2\right]\left[(\omega+\omega_q)^2+\Gamma_q^2\right]}, \tag{2.49}$$

The expression is usually known as a damped harmonic oscillator (DHO). The term Γ_q is the damping factor and represents a decay constant of the phonon-lifetime and it is proportional to the anharmonic forces; It is also related to the peaks width, centred at $\pm\omega_q$. The prefactor $Z(Q)$ is the DHO strength. Two damping regimes can be distinguished: under-damped, with $\Gamma_q < \omega_q$, and over-damped with $\Gamma_q \geq \omega_q$. In the latter case, the function assumes a single peak shape, centred at $\omega_q = 0$, indistinguishable from a Lorentzian shape (see fig. 2.4) [111]. The transition from a damped to an over-damped DHO can be dependent on the temperature and on structural phase transition (usually also dependent on temperature).

2.1.2.2 Stochastic motions, EISF and QISF

Localized or diffusive motions are not originating from a quantized process, for example phonon creation or destruction, but rather from stochastic motions. Therefore the energy transfer is not a quantum of $\hbar\omega$, but a distribution of energies around the elastic line ($\hbar\omega = 0$). The neutron gains energy from the sample and gives energy to the sample in a continuous way, without defined energy transfer quanta. These motions give rise to the Quasi-Elastic Neutron Scattering (QENS).

For a localized motion (e.g. molecular jump rotations), the probability of finding a particle in a certain volume and time interval is finite. With increasing time, the particle moves and if the motion is spatially restricted (for example rotations around a lattice point) or

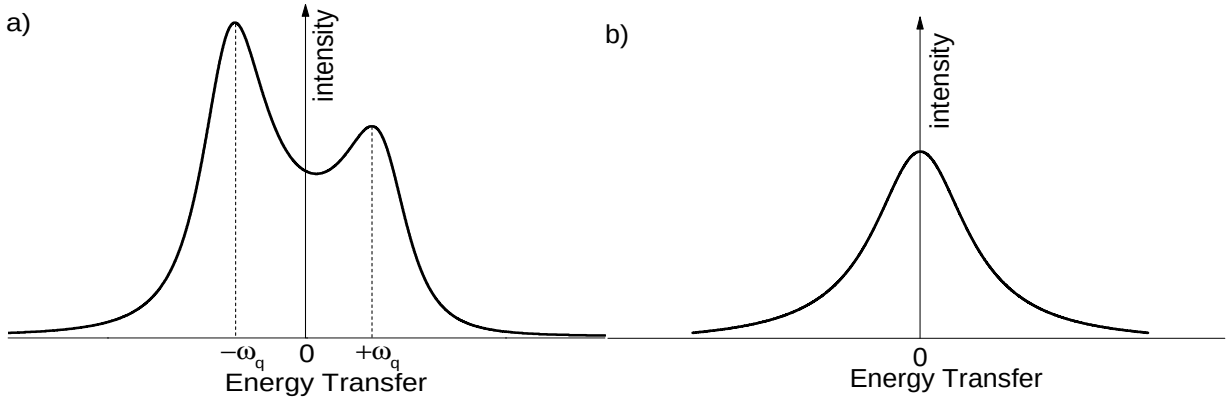

Figure 2.4: Schematic representation of the scattering of the DHO, in the classical limit. a) under-damped harmonic oscillator, $\Gamma_q < \omega_q$. b) over-damped harmonic oscillator, $\Gamma_q \gg \omega_q$.

diffusion in a cage, the probability tends to a finite value. Conversely, a free diffusive motion is characterized by a probability of finding the particle that decays in time and reaches zero in the long time limit.

In terms of the intermediate self-scattering function $I_s(\mathbf{Q}, t)$ (defined as the space Fourier transform of $G_s(\mathbf{R}, t)$), the evolution in times can be described in this way: at $t = 0$, the probability of finding the particle in a position $\mathbf{R}$ is one. As soon as time increases, the probability exponentially decays and, depending whether the motion is localized or not, tends to a finite value or goes to zero. In the case of a freely diffusing particle, the probability tends to zero and the Fourier transform of it is a Lorentzian. If the particle is performing a localized motion, instead, after some time the probability of finding a particle approaches a constant value. Since the Fourier transform of a constant value is a δ-function (i.e an elastic line), the scattering function is a sum of a Lorentzian and an elastic components. Both cases are shown in figs. 2.5 and 2.6, where the functions have been schematically drawn for a selected $\mathbf{Q}$.

Translational diffusive processes These processes involve the diffusion of a particle in a medium, in which there are no restrictions in terms of explored space. A particle starts in a staring position $\mathbf{R}$ and its centre of mass moves in the lattice space available, without any restrictions to fixed volume. According to the second Fick's law, the self correlation function obeys the differential equation:

$$\frac{\partial}{\partial t} G_s(r,t) = D_s \Delta G_s(r,t), \quad \text{with} \quad G_s(r, t=0) = \delta(r), \tag{2.50}$$

where D_s is the diffusion coefficient. The solution for the previous equation is:

$$G_s(r,t) = \frac{1}{\sqrt{(4\pi D_s |t|)^3}} \exp\left(-\frac{r^2}{4D_s|t|}\right), \tag{2.51}$$

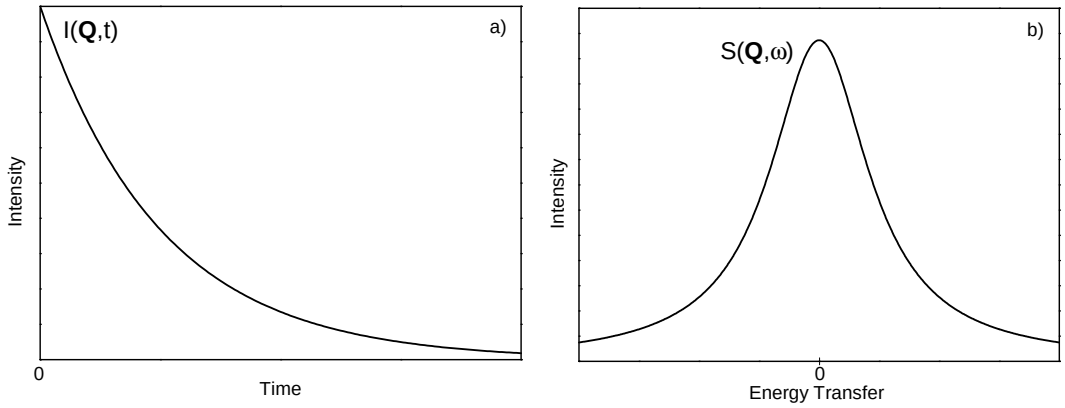

Figure 2.5: a) Intermediate scattering function $I_s(\mathbf{Q}, t)$ for a freely diffusing process. b) Fourier transform of the intermediate scattering function, $S_{\text{diff}}(\mathbf{Q}, \omega)$. In the scattering function there is any elastic component, but only a broad quasi-elastic one.

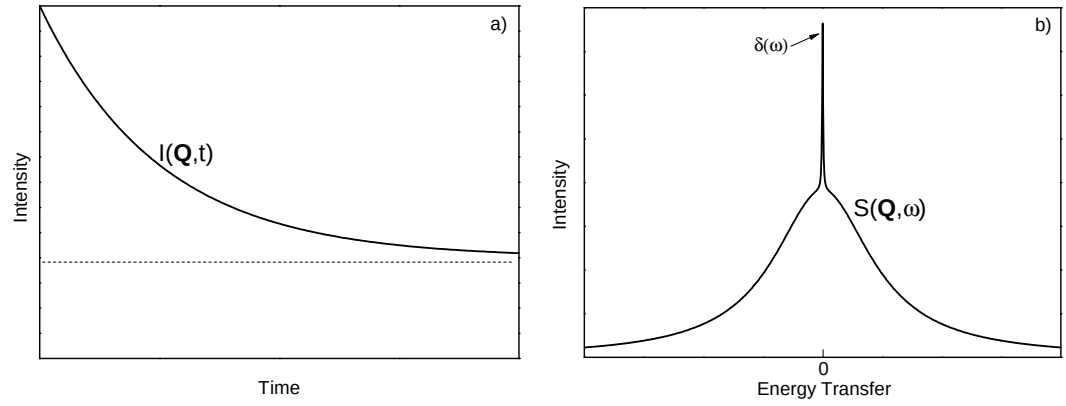

Figure 2.6: a) Intermediate scattering function $I_s(\mathbf{Q}, t)$ for a localized motion. b) Fourier transform of the intermediate scattering function, $S_{\text{diff}}(\mathbf{Q}, \omega)$. In the scattering function a $\delta(\omega)$ is representing the elastic scattered neutrons.

which transforms into the intermediate scattering function $I_s(Q,t)$

$$I_s(Q,t) = \exp\big(-Q^2 D_s|t|\big). \tag{2.52}$$

We can notice that, with increasing time, the intermediate scattering function approaches zero (see fig. 2.5). Performing a spatial Fourier transform, the incoherent scattering function is obtained:

$$S_{\text{inc}}(Q,\omega) = \frac{1}{\pi}\frac{D_s Q^2}{(D_s Q^2)^2 + \omega^2}. \tag{2.53}$$

The scattering function is then a Lorentzian characterized by a half width at half maximum (HWHM)

$$\Gamma_D = \hbar D_s Q^2. \tag{2.54}$$

As soon as the momentum transfer increases, the width of quasi-elastic signal increases with a quadratic dependence.

Rotational diffusive processes, EISF and QISF In solids and molecules, particles are subject to reorientational motions but the volume where these processes take place is spatially limited. For example, the $[BH_4]$ tetrahedra units in complex borohydride are fixed in the crystallographic positions, but they are able to reorient around one of the possible symmetry axis. In this case, hydrogen atoms are performing jump rotations. The probability of finding an atom in a certain position is then finite, and the intermediate scattering function resembles the one depicted in fig. 2.6. The intermediate scattering function can be divided in two, terms, one in the limit of long times, and another one that decays to zero with increasing time:

$$I_{\text{rot}}(Q,t) = I_{\text{rot}}(Q, t\to\infty) + I'_{\text{rot}}(Q,t), \quad \text{with } \lim_{t\to\infty} I'_{\text{rot}}(Q,t) = 0. \tag{2.55}$$

Taking the time-Fourier transform, the scattering function is still a Lorentzian, but additionally there is an elastic component $\delta(\omega)$:

$$S_{\text{rot}}(Q,\omega) = I_{\text{rot}}(Q,t\to\infty)\delta(\omega) + S^{\text{QE}}_{\text{rot}}(Q,\omega) = A_0(Q)\delta(\omega) + \sum_j A_j(Q)\frac{1}{\pi}\frac{\Gamma_j}{\Gamma_j^2+\omega^2}. \tag{2.56}$$

In this case, Γ_j are not characterized by any momentum transfer dependence, and this is the main difference between localized and diffusive motions.
The factors $A_0(Q)$ and $A_j(Q)$ are indeed dependent on the momentum Q. This dependence is related to the geometry of the reorientational motions. The factor $A_0(Q)$ is is called Elastic Incoherent Structure Factor (EISF). The EISF is the spatial Fourier transform of the probability function of finding an atom at a given position, hence its functional dependence on the momentum transfer reflects the spatial distribution of the atoms in the long time average. This quantity is represented by the asymptotic value at $t\to\infty$ of the intermediate

scattering function schematically shown in fig. 2.6. The EISF can be calculated, according to the definition

$$\mathrm{EISF} = \frac{1}{N^2}\left|\sum_{\text{sites } j} \mathrm{e}^{i\mathbf{Q}\cdot\mathbf{R}_j}\right|^2 . \tag{2.57}$$

The terms $A_j(Q)$ are called Quasi Incoherent Structure Factors (QISFs) and the following relation holds with the EISF:

$$A_0(Q) + \sum_{j>0} A_j(Q) = 1. \tag{2.58}$$

This equality is simply derived from the fact that the integral all over the reciprocal space of the scattering function has to be one by definition. The EISF (and therefore the QISFs) can be evaluated from the experimental data as the ratio between the elastic intensity and the sum of the quasielastic and elastic ones:

$$\mathrm{EISF} = \frac{I_{\mathrm{el}}}{I_{\mathrm{el}} + I_{\mathrm{qe}}}. \tag{2.59}$$

The HWHM Γ_j are related to the jump rates between different sites of rotational process. In case of N sites located on a circle of radius r, an exact expression can be given in the crystalline powder average [112]:

$$S_{\mathrm{circ}}(Q,\omega) = A_0(Q)\delta(\omega) + \sum_{j=1}^{N} A_j(Q)\frac{1}{\pi}\frac{\hbar/\tau_j}{(\hbar/\tau_j)^2 + \omega^2} \tag{2.60}$$

where

$$A_j(Q) = \frac{1}{N}\sum_{n=1}^{N} j_0(Qr_n)\cos\left(\frac{2jn\pi}{N}\right). \tag{2.61}$$

The quantities r_n and τ_j are respectively the jump distances in the rotation motions and the medium residential time of the particle in a specific site j. The inverse of the last quantity is the jump rate among the N sites. Both of them can be calculated:

$$r_n = 2r\sin\left(\frac{n\pi}{N}\right) \quad \text{and} \quad \tau_j^{-1} = 2\tau^{-1}\sin^2\left(\frac{\pi j}{N}\right). \tag{2.62}$$

In this work, some EISF are used to describe possible reorientations of the hydrogen bonded in the tetrahedra, as shown in fig. 2.7. Jump rotations around the symmetry axis C_3 involve one fixed hydrogen atom and the other 3 rotating between 3 equidistant positions on a circle. The rotations around the C_2 axis involve 180° rotations of the $[BH_4]$ unit. The EISFs for both reorientations, accidentally, have the same expression:

$$\mathrm{EISF}_{C_3} = \mathrm{EISF}_{C_2} = \frac{1}{2}\left[1 + j_0\left(\frac{2\sqrt{2}}{\sqrt{3}}Qd_{\text{B-H}}\right)\right], \tag{2.63}$$

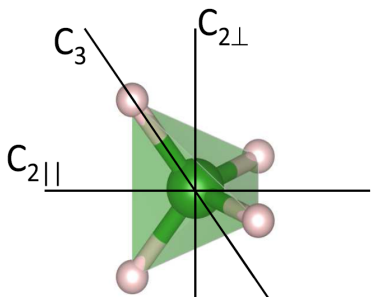

Figure 2.7: $[BH_4]$ tetrahedra in complex borohydrides: (large green sphere) boron, (small grey spheres) hydrogen. $C_{2\perp}$, $C_{2||}$ and C_3 are symmetry axes of the $[BH_4]$ unit.

with $d_{\text{B-H}}$ the distance between boron and hydrogen atoms. Another possible reorientation on the $[BH_4]$ units is involving jump reorienting around all four tetrahedral C_3-axes. The EISF is described by:

$$\text{EISF}_{\text{tumbling}} = \frac{1}{4}\left[1 + 3j_0\left(\frac{2\sqrt{2}}{\sqrt{3}}Qd_{\text{B-H}}\right)\right]. \tag{2.64}$$

In a liquid, the continuous diffusion of a particle can take place also in a confined space. In this case, the scattering function contains an elastic line, because the movement of the particle is still restricted, but the quasi-elastic part is expressed by an infinite sum Lorentzians. The model has been developed by Volino et. al. [113], and the scattering function reads:

$$S_{\text{diff}}(Q,\omega) = A_0^0(Q)\,\delta(\omega) + \sum_{(l,n)\neq(0,0)} (2l+1)\,A_n^l(Q)\,\frac{1}{\pi}\frac{\left(x_n^l\right)^2 D/a^2}{\left[\left(x_n^l\right)^2 D/a^2\right]^2 + \omega^2}. \tag{2.65}$$

Lorentzian are characterized by a HWHM of $\left(x_n^l\right)^2 D/a^2$, where D is the diffusion coefficient and a is the radius of an hypothetical sphere, in which space the diffusion takes place. A_0^0 and A_n^l are the EISF and QISFs, respectively:

$$\text{EISF} = A_0^0(Q) = \left[\frac{3j_1(Qa)}{Qa}\right]^2, \tag{2.66}$$

and

$$\text{QISFs} = A_n^l(Q) = \begin{cases} \frac{6\left(x_n^l\right)^2}{\left(x_n^l\right)^2 + l(l+1)}\left[\frac{Qaj_{l+1}(Qa) - lj_l(Qa)}{(Qa)^2 - \left(x_n^l\right)^2}\right] & \text{with } Qa \neq x_n^l, \{l,n\} \neq \{0,0\} \\ \frac{3}{2}j_l^2\left(x_n^l\right)\frac{\left(x_n^l\right)^2 - l(l+1)}{\left(x_n^l\right)^2} & \text{with } Qa = x_n^l, \{l,n\} \neq \{0,0\} \end{cases}. \tag{2.67}$$

Values of x_n^l are the root of the boundary condition equations, imposed on the scattering functions.

The Elastic Incoherent Structure Factors can be, as pointed out earlier, calculated in a general way knowing the possible sites explored by the atoms, and general expressions are given in the literature [112, 107]. In the calculation of the expressions of EISFs, it is evident that the different reorientational motions are distinguishable only if sufficiently momentum transfer Q is probed. This requirement will have consequences on the experimental settings required for studying reorientational motions of hydrogen atoms.

2.1.2.3 Superposition of motions

In case different reorientational processes occur at the same time, it is necessary to calculate the correlation functions (and therefore the scattering functions) of the global motion. In the bulk, possible motions are considered to be vibrations, rotational diffusion and translational diffusion. In the hypothesis of independence of the different motions, the intermediate scattering law will be the product of the single intermediate scattering functions:

$$I_{\mathrm{tot}}(Q,t) = I_{\mathrm{trans}}(Q,t) \cdot I_{\mathrm{rot}}(Q,t) \cdot I_{\mathrm{vib}}(Q,t). \tag{2.68}$$

Using the Fourier transform theorem, the total scattering function is derived as a convolution between the three motions:

$$S_{\mathrm{tot}}\left(Q,\omega\right) = S_{\mathrm{trans}}\left(Q,\omega\right) \otimes S_{\mathrm{rot}}\left(Q,\omega\right) \otimes S_{\mathrm{vib}}\left(Q,\omega\right), \tag{2.69}$$

If atoms are undergoing rotational diffusion motions and vibrations, (but not undergoing translational diffusive motions), the scattering function is

$$S_{\mathrm{tot}}\left(Q,\omega\right) = S_{\mathrm{rot}}\left(Q,\omega\right) \otimes S_{\mathrm{vib}}\left(Q,\omega\right). \tag{2.70}$$

Generally, the vibrational scattering function can be separated in two terms, an elastic and inelastic:

$$S_{\mathrm{vib}}\left(Q,\omega\right) = D(Q)\delta\left(\omega\right) + \left[1 - D(Q)\right] S_{\mathrm{vib}}^{\mathrm{inel}}\left(Q,\omega\right), \tag{2.71}$$

being $D(Q) = \exp[-2W(Q)]$ the Debye-Waller Factor [1]. The expression for $D(Q)$ is strictly true in the harmonic approximation, although it has been observed that it is also valid in presence of anharmonic effects [114]. In case the vibrational intensity is very well separated from the rotational diffusion processes, we can approximate the scattering function as a

$$S_{\mathrm{tot}}\left(Q,\omega\right) = D(Q)S_{\mathrm{rot}}(Q,\omega) + \left[1 - D(Q)\right] S_{\mathrm{vib}}^{\mathrm{inel}}\left(Q,\omega\right) \otimes S_{\mathrm{rot}}(Q,\omega). \tag{2.72}$$

If the vibrational motions are fast enough, compared to the time scales of the diffusive processes, the second term in the last equations appears as a flat background in the experimental measurement, and therefore can be disregarded in the calculation of the EISF. Thus,

[1] The expression of S_{vib} might differ from text books. See appendix A for a detailed explanation.

the EISF calculation and analysis is somehow easier because the Debye-Waller factor cancels out in eq. 2.59.

In case of low energy vibrational modes, a clear separation between quasi-elastic and inelastic signals is not possible, and the data analysis is more complicated. In this situation, the approximation 2.72 is not any more valid, and a convolution between localized and vibrational motion in required.
If the quasi-elastic scattering function is involving a free diffusive motion, the total scattering function will be characterized by the absence of an elastic line, since the convolution between the elastic $\delta(\omega)$- and Lorentzian function is again a Lorentzian function. Conversely, in purely localized motions, the convolution between eq. 2.56 and eq. 2.71 ensures the presence of an elastic line.

Considering a single reorientational motion (eq. 2.56 with $j = 1$), a convolution can be performed:

$$\begin{aligned} S(Q,\omega) &= \{A_0(Q)\delta(\omega) + [1 - A_0(Q)]\, L_1(Q,\omega)\} \otimes \left\{D(Q)\delta(\omega) + [1 - D(Q)]\, S^{\text{inel}}_{\text{vib}}(Q,\omega)\right\} = \\ &= A_0(Q)D(Q)\delta(\omega) + D(Q)\,[1 - A_0(Q)]\, L_1(Q,\omega) + \\ &+ A_0(Q)\,[1 - D(Q)]\, S^{\text{inel}}_{\text{vib}}(Q,\omega) + [1 - A_0(Q)]\,[1 - D(Q)]\, L_1(Q,\omega) \otimes S^{\text{inel}}_{\text{vib}}(Q,\omega)\,. \end{aligned}$$

All scattering functions are normalized, and the total scattering function $S(Q,\omega)$ is still a normalized function. The factor in front of the elastic line is, by definition, the EISF. The factors in front of all other terms are the QISFs. These quantities, in principle, can be evaluated from the data analysis, since the double differential cross-section is proportional to the scattering functions. Therefore:

$$\text{EISF} = A_0(Q)D(Q) \tag{2.73}$$

$$\text{QISF}_{L_1} = D(Q)\,[1 - A_0(Q)] \tag{2.74}$$

$$\text{QISF}_{\text{S}^{\text{inel}}_{\text{vib}}} = A_0(Q)\,[1 - D(Q)] \tag{2.75}$$

$$\text{QISF}_{\text{S}^{\text{inel}}_{\text{vib}} \otimes L_1} = [1 - A_0(Q)]\,[1 - D(Q)]\,. \tag{2.76}$$

All rotational diffusive processes are temperature dependent and, especially at low temperature, not all atoms are undergoing in reorientational processes. In this case some "hindered motions" are occurring, part of the scattering units (p) is contributing with an extra elastic intensity, and therefore the scattering function S_{rot} can be written as:

$$S^{\text{hind}}_{\text{rot}}(Q,\omega) = p\delta(\omega) + (1 - p)\, S_{\text{rot}}(Q,\omega)\,. \tag{2.77}$$

Inserting eq. 2.56 (with $j = 1$) in $S_{\text{rot}}(Q,\omega)$ and rearranging the $\delta(\omega)$ terms, we obtain:

$$S^{\text{hind}}_{\text{rot}}(Q,\omega) = [p + (1 - p)\, A_0(Q)]\delta(\omega) + (1 - p)\,[1 - A_0(Q)]\, L_1(Q,\omega). \tag{2.78}$$

Performing the convolution with the vibrational scattering function (eq. 2.71), we obtain the EISF and QISFs expressions in the case of hindered localized motions:

$$\mathrm{EISF}^{\mathrm{hind}} = D(Q)\,[p + (1-p)\,A_0(Q)] \tag{2.79}$$

$$\mathrm{QISF}^{\mathrm{hind}}_{L_1} = D(Q)\,[1 - A_0(Q)]\,(1-p) \tag{2.80}$$

$$\mathrm{QISF}^{\mathrm{hind}}_{\mathrm{S}^{\mathrm{inel}}_{\mathrm{vib}}} = A_0(Q)\,[1 - D(Q)]\,(1-p) \tag{2.81}$$

$$\mathrm{QISF}^{\mathrm{hind}}_{\mathrm{S}^{\mathrm{inel}}_{\mathrm{vib}}\otimes L_1} = [1 - A_0(Q)]\,[1 - D(Q)]\,(1-p)\,. \tag{2.82}$$

This procedure can be generalized in case of more than one reorientation processes.

These equations can be globally fitted to the experimental EISF and QISFs. In this way, not only the EISF can be evaluated, but also the other quasielastic and inelastic contributions. This procedure is believed to give more support in the choice between different reorientational motions.

Part II

Experimental Methods

Chapter 3

Quasi-elastic Neutron Scattering at TOFTOF

Contents

3.1 Introduction

Theoretical aspects of inelastic and quasi-elastic are given in the previous chapter. The situation depicted in a single scattering event shows an incident neutron with an exact energy E_i and wave vector $\mathbf{k}_\mathrm{i}$, as well as an outgoing neutron with a defined energy E_f and wave vector $\mathbf{k}_\mathrm{f}$. Unfortunately, reality is a bit different.

- Neutrons impinging on the sample have not all the same energy E_i, but rather a distribution of energies centred around the desired incident energy. The flux produced by a source is energy dependent (usually a Maxwellian distribution), and the selection process of a particular energy is also affecting the distribution of energies at the sample position.

- Neutrons don't have all the same direction $\hat{\mathbf{k}}_i$, being $\hat{\mathbf{k}}_i$ the versus of the incident wave vector. Neutrons are transported from the source to the sample position using neutron guides, through a total reflection mechanisms. This introduces undesired divergence of the beam, resulting in a non-perfect beam collimation.

- A real sample has finite dimensions and the neutrons might be scattered more than one time before leaving the sample and being detected. As a result, the scattering vector $\mathbf{Q}$ can not be uniquely defined and registered. Also, the finite sample dimensions introduce uncertainty in the flight path through the sample, depending also on the scattering angle 2θ.

In general the first two contributions can not be separable, and therefore the resulting distribution is a convolution of the energy and divergence distributions. Plus, a path uncertainty inside the sample influences the final energy determination of the outgoing neutrons. All these deviations from the idealized situation will be discussed and taken into account to determine and extract the final scattering function $S(\mathbf{Q}, \omega)$. In the following, a description of the instrument where all the measurements were performed is given.

3.2 Energy resolution and time scale

If a particle performs oscillatory or stochastic motions with a characteristic time τ, then an energy transfer (δE) occurs between the particle and the incident neutron. The Heisenberg uncertainty principle relates these quantities:

$$\delta E \cdot \tau \geq \hbar. \tag{3.1}$$

If a motion takes place on a long time scale, the energy transfer associated to this motion is small. Vice versa, fast motions (such vibrations) shows a large energy transfer. In a spectrometer, the smallest energy transfer that can be measured is represented by the energy resolution δE, and corresponds to the response of the spectrometer to a $\delta(\hbar\omega)$ function peak in the double-differential neutron cross section [115]. In a multi-chopper time-of-flight spectrometer, the beam is monochromatized using the time that a neutron uses to travel between one chopper disc to another chopper disc. In a simplified scheme, the first disc is called pulsing chopper (P) and the second one is the monochromating chopper (M). The time-distance diagram can be used to visualize the pulse duration and propagation in space. On the x-axis there is the time and on the y-axis the distances. The opening time of the choppers are represented by a segment in the x-axis, and the lines are the flight path of the neutron as a function of time. In general, a neutron with wavelength λ travels over a distance L in a time

$$t_{\text{tof}} = \alpha L \lambda, \tag{3.2}$$

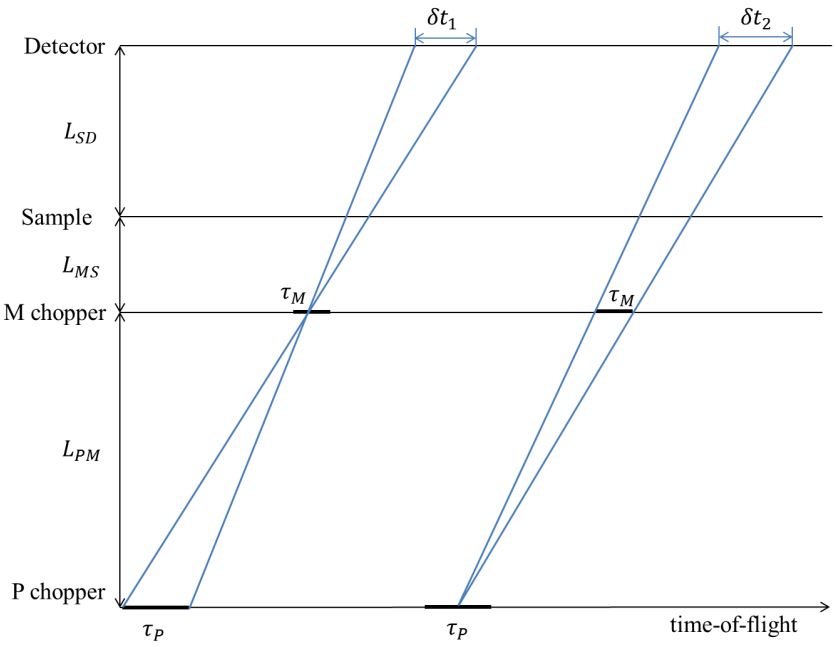

Figure 3.1: Time-of-flight diagram showing the contributions of the time spread at the detector positions. On the left, the contribution δt_1 and on the right δt_2. These contributions stem from two different effects and have to be summed up in order to obtain the total time spread at the detectors. See text for details.

where $\alpha = \frac{m_n}{h}$ is a constant. Given the distance L in units of m and the wavelength λ in units of Å, then

$$\alpha = 252.77 \frac{\mu\text{s}}{\text{m} \cdot \text{Å}}. \tag{3.3}$$

As represented in fig. 3.1, the P chopper produces a burst of τ_P length. The M chopper opens for a time τ_M, centred at the desired wavelength arrival time. The time spread of a neutron pulse arriving at the sample position is a sum of two different contributions (see fig. 3.1):

- the neutron that have passed the M chopper at a given instant within the interval τ_M after having passed the P chopper at any instant (δt_1).
- the time spread of neutron passing the M chopper in the time interval τ_M, coming from the P chopper at the middle of its burst (δt_2).

If these contributions are independent, the total time spread at the sample position is just the square root of the quadratic sum of the contribution.

Considering the time spread at the detector position, another contribution has to be taken into account. All deviations from the ideal conditions (divergence of the beam, finite sample size, detector thickness, etc. etc.) produce a flight path uncertainty δL, that translates into

a time uncertainty. Considering all these contributions, it is obtained:

$$\Delta t = \frac{1}{L_{\mathrm{PM}}}\sqrt{(\alpha\lambda_f L_{\mathrm{PM}}\cdot\delta L)^2 + \tau_P^2\left(L_{\mathrm{MS}} + L_{\mathrm{SD}}\frac{\lambda_f^3}{\lambda_i^3}\right)^2 + \tau_M^2\left(L_{\mathrm{PM}} + L_{\mathrm{MS}} + L_{\mathrm{SD}}\frac{\lambda_f^3}{\lambda_i^3}\right)^2}, \quad (3.4)$$

where λ_i is the wavelength of an elastically scattered neutron, and λ_f is the one corresponding to an inelastic scattered neutron. Converting time into energy, it is possible to obtain the effective resolution function full-width-half-maximum [FWHM]:

$$\delta E[\mathrm{meV}] = \frac{k}{\lambda_f^3 L_{\mathrm{PM}} L_{\mathrm{SD}}}\sqrt{A^2 + B^2 + C^2}, \quad (3.5)$$

with

$$\begin{aligned} k &= 0.6472\frac{\mathrm{meV}\cdot\mathrm{\AA}^3\cdot\mathrm{m}}{\mu\mathrm{s}} \\ A &= \alpha\lambda_f L_{\mathrm{PM}}\cdot\delta L \\ B &= \tau_P\left(L_{\mathrm{MS}} + L_{\mathrm{SD}}\frac{\lambda_f^3}{\lambda_i^3}\right) \\ C &= \tau_M\left(L_{\mathrm{PM}} + L_{\mathrm{MS}} + L_{\mathrm{SD}}\frac{\lambda_f^3}{\lambda_i^3}\right). \end{aligned} \quad (3.6)$$

Some considerations can be done concerning the analytical form of the energy resolution. First of all, in the ideal case, the quantity L_{MS} should be as small as possible since it is only increasing the time spread at the sample position (and therefore at the detector). On real experimental conditions, the sample has to be mounted in a sample environment, such as a cryostat or a high temperature furnace. Therefore this term can not be set to zero, but it has to be as small as possible, taking into account experimental requirements. Secondly, to minimize the energy resolution contributions, the quantities A, B and C should be approximately the same: in this case, the spectrometer is in the so-called "balanced conditions".

The contributions B and C are depending on two quantities, namely the opening times of the two choppers, τ_P and τ_M. All the other parameters are fixed by construction. The time openings of the choppers can be tuned using the chopper rotation frequency: higher rotation frequencies lead to smaller openings τ and therefore the resolution gets better. The contribution A in the above expression is determined, in first approximation, by the sample size. Thus, the term A should not be exceeding the contribution B and C. In case of elastic scattering, $\lambda_i = \lambda_f$ and therefore the expression of the resolution energy function is proportional to λ_i^{-3}, i.e. the resolution increases with the increase of thje incident neutron wavelength.

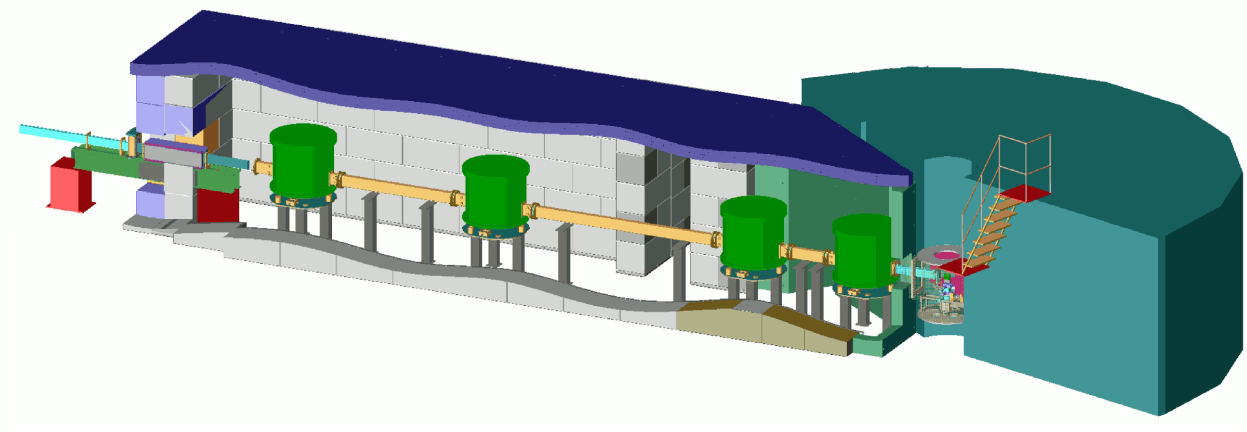

Figure 3.2: 3D-drawing of the time-of-flight spectrometer TOFTOF. Both primary and secondary spectrometers are visible, as well the sample and the flight chamber [116].

3.3 The time-of-flight spectrometer TOFTOF

The neutron time-of-flight spectrometer TOFTOF at the Forschungs-Neutronenquelle Heinz Maier-Leibnitz (FRM II) is shown in fig. 3.2 [116]. The spectrometer is fed with neutrons coming from the cold moderator of the FRM II. The moderator is a tank filled with liquid deuterium at a constant temperature of 25 K, shifting the thermal neutron spectrum towards lower energies. As a results, the cold spectrum flux has a maximum around energies corresponding to $\lambda = 1.4$ Å [117].
Neutrons are transported to the spectrometer through a 60 m long guide: it has a section of $44 \times 100\,\mathrm{mm}^2$ (width $\times$ height) and it is coated with a Ni/Ti supermirror with $m = 2$. The guide is composed by a double curved guide, resulting in an S-shape, with a curvature radius of 2000 m for both benders. Using this particular shape, it is achieved not only a strong suppression of the γ radiation, but also a sharp cut-off in intensity at short wavelengths [118]. At TOFTOF, the S-shape guide acts as neutron velocity filter with the suppression of neutrons with wavelengths shorter than $\lambda = 1.38$ Å. After the double bender guide, the TOFTOF instrument starts. It is divided in two parts: the primary spectrometer and the secondary spectrometer. The primary spectrometer is composed of guide and choppers systems, the secondary spectrometer of sample and flight chamber, and detectors. Each of the components will be briefly explained.

Guide system After the double bender guide, the focusing secondary guide starts. It is 12.2065 m long and it reduces the beam cross-section from $44 \times 100\,\mathrm{mm}^2$ to $23 \times 46.8\,\mathrm{mm}^2$. The coating was optimized in order to achieve best transmission values in the wavelength range between 1.4 Å and 12 Å: it starts with a $m = 2$, and ends with a $m = 3.6$ in the last convergent section. The guide ends at a distance of 20 cm before the sample position, and

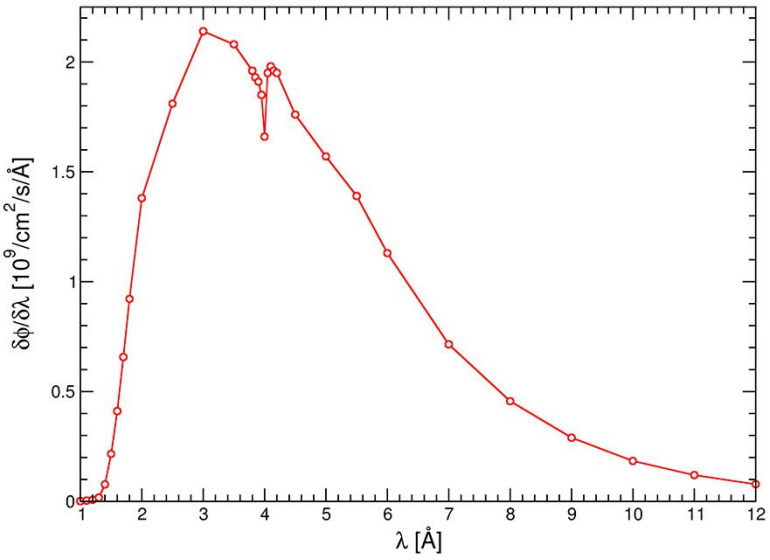

Figure 3.3: Measured flux at the sample position [116]. It has a Maxwellian distribution and the sharp cut-off at 1.38 Å is due to the double bender guide. The dip in the intensity at $\lambda = 4$ Å is due to the Bragg scattering of the various Aluminium windows positioned between the guide sections.

the integrated flux at the sample position is the order of 10^{10} neutrons/$(s \cdot cm^2)$ (see fig. 3.3). The cut-off at $\lambda = 1.38$ Å is clearly visible.

Chopper system At TOFTOF, neutrons are monochromatised through a time-of-flight technique using seven chopper discs, placed in evacuated vessels. They are made from carbon-fibre-reinforced plastic, coated with ^{10}B for neutron absorption, and they can rotate with frequencies ν_P up to 22000 rpm. The distance between the first and the last chopper is $L_{PM} = 10$ m, and all the other choppers are placed in special positions in order to obtain a monochromatic beam with the desired resolution.

The pulsing chopper is made of two counter-rotating discs (PCRC) that chop the continuous neutron beam, creating equidistant pulses of length τ_P. At a distance L_{PM} another pair of discs (MCRC), monochromatises the beam selecting a small wavelength range out of each pulse, with a time extension of τ_M.
Further two choppers (High Order Removal Choppers, HORC) are suppressing neutrons with higher order wavelengths, i.e. $\lambda/2$, $\lambda/4$, etc. The Frame Overlap Chopper (FOC), reduces the neutron pulse frequency at the sample position in order to avoid the overlap of energy loss and energy gain of the neutrons in two subsequent pulses. All choppers operate in synchronous mode, thus at the same frequency ν_P, except the frame overlap chopper that

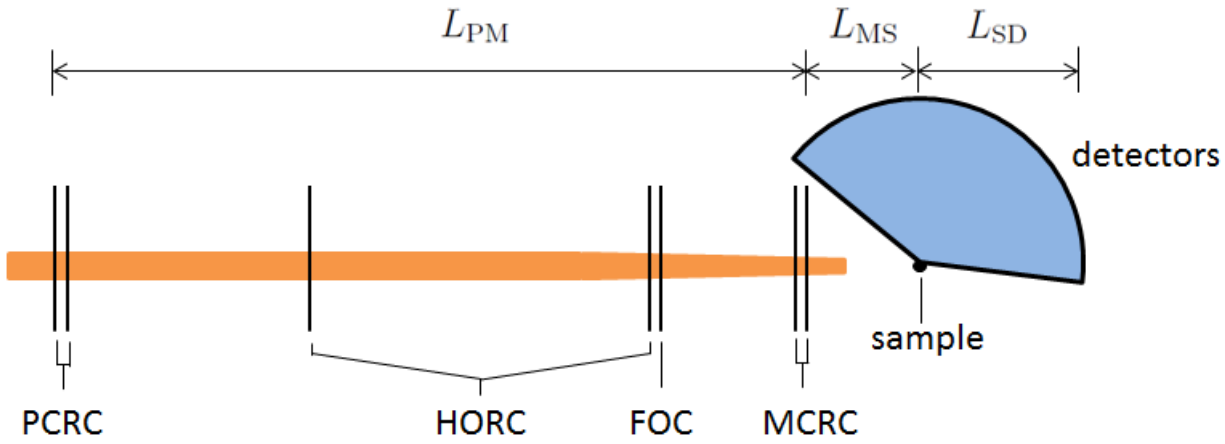

Figure 3.4: Schematic view of TOFTOF from the top. In orange the neutron guide, with the last focusing section reducing the beam cross-section. Choppers are represented by vertical black lines: (PCRC) Pulsing Counter Rotating Choppers, (HORC) High Order Removal Choppers, (FOC) Frame Overlap Chopper, (MCRC) Monochromating Counter Rotating Choppers. $L_{PM} = 10\,\text{m}$, $L_{MS} = 1.4\,\text{m}$ and $L_{SD} = 4\,\text{m}$.

rotates with a frequency

$$\nu_{\text{FOC}} = \frac{R-1}{R}\nu_{\text{P}}. \quad \text{with} \quad R = 2, 3, 4, 5, ... \tag{3.7}$$

In this way, only 1 over R pulses coming from the pulsing chopper is retained and allowed to arrive at the sample position.

The distance between the monochromating chopper pair and the sample is $L_{\text{MS}} = 1.4\,\text{m}$, and, beyond the sample, detectors are placed at a distance $L_{\text{SD}} = 4\,\text{m}$. In general scattering conditions, neutrons gain and loose energy, thus they are faster or slower than the elastically scattered neutrons. When the next pulse arrives at the sample position, not all the down scattered neutrons have arrived at the detector position, and therefore there is an overlap (in time) of neutrons. If the incident wavelength is λ_i, a good compromise is to allow neutrons with a wavelength longer than $\lambda_f = 1.5\lambda_i$ to overlap. The maximum time-of-flight allowed is then

$$t_{\text{max}} = 1.5\alpha L_{\text{SD}}\lambda_i. \tag{3.8}$$

Using this condition, a relation holds between the frequency ν_P and the ratio R and the incident wavelength.

$$\nu_P(\text{rpm}) = \frac{R}{2t_{\text{max}}} = \frac{R}{\lambda_i(\text{Å})} \times 19780.8\frac{\text{Å}}{\text{min}} \tag{3.9}$$

The factor 2 in the previous equation stems from the fact that the chopper discs at TOFTOF have two diametrically opposite slits, thus generating two pulses for each disc rotation. Eq. 3.9 describes the frame overlap ratio R, depending on the wavelength λ_i and the chopper frequency ν_P.

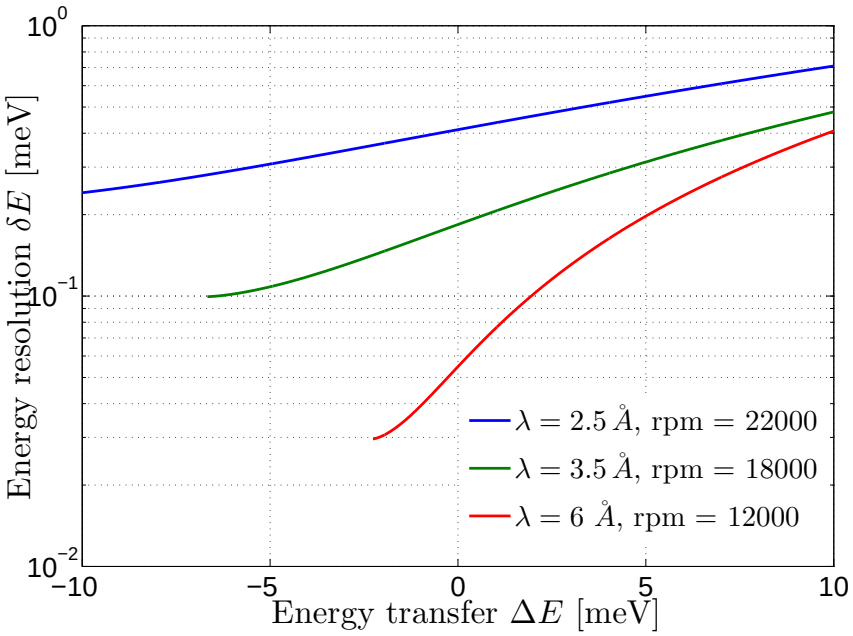

Figure 3.5: Energy resolution δE as a function of the energy transfer ΔE, for three different settings: (blue) 2.5 Å and 22000 rpm, (green) 3.5 Å and 18000 rpm, (red) 6 Å and 12000 rpm.

In fig. 3.5, a plot of the energy resolution δE as a function of the energy transfer ΔE, for three different settings. The energy resolution changes as a function of the final energy of the neutron. With respect to the elastic line ($\Delta E = 0$), the resolution is decreasing on the neutron energy loss side, and vice versa.

In fig. 3.7, it is shown the elastic resolution δE as a function of λ_i at different chopper frequencies.

Therefore, at TOFTOF, the energy resolution can be tuned adjusting the choppers rotation speed and the wavelength at the same time, resulting in a great versatility of the instrument.

Sample chamber The sample chamber is placed right after the last monochromating chopper pair and the neutron guide extends up to 20 cm before the sample position. The distance between the chopper and the sample is $L_{\mathrm{MS}} = 1.4\,\mathrm{m}$: this value is a good compromise between space available for sample environment, shielding of the monochromating choppers and good energy resolution. Typical measurements at TOFTOF are performed under sample conditions depending on an external quantity, e.g. temperature, pressure, magnetic field. Therefore, the distance of 1.4 m allows to have space for the sample environment. The sample chamber is also equipped with a radial collimator and it is isolated from the flight chamber through a thin Aluminum foil. It can be also flushed with Argon in order to decrease the scattering coming from the air, thus reducing the background.

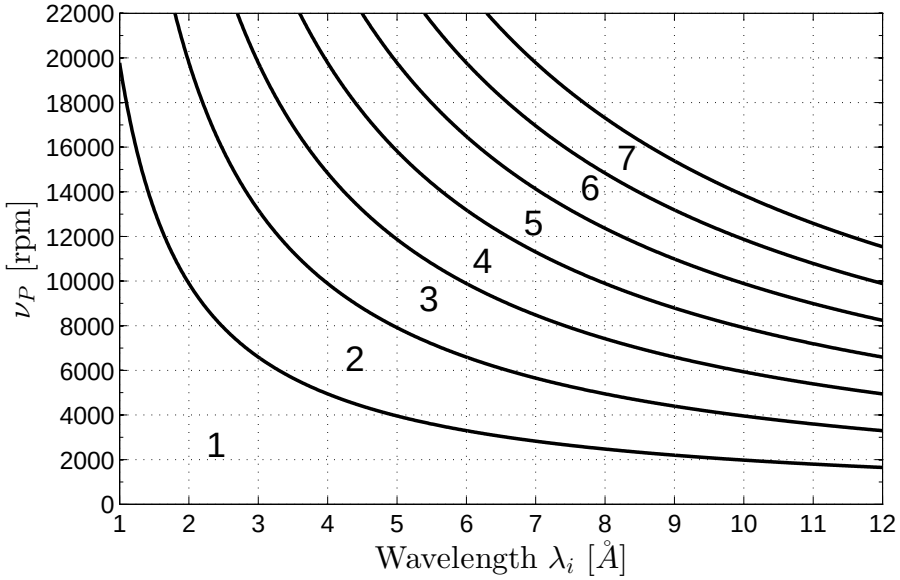

Figure 3.6: Frame overlap ratio R, indicated in the plot, as a function of wavelength λ_i and chopper frequency ν_P in units of [rpm]. Once the incident wavelength and the chopper speed are chosen, the chopper ratio will affect the speed of the FO chopper according to eq. 3.7.

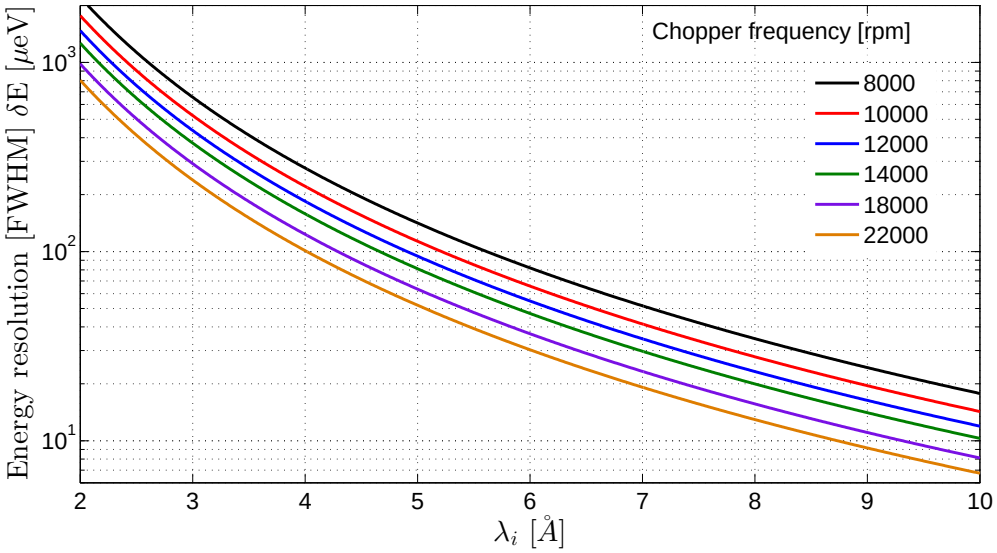

Figure 3.7: Elastic resolution (FWHM) δE in [μeV] as a function of the incident wavelength λ_i and at different chopper frequencies. Curves are obtained from eq. 3.4 setting $\lambda_f = \lambda_i$.

Flight chamber and detectors The detector banks are placed at a distance $L_{SD} = 4\,\text{m}$, from the sample position, and cover an angular range $2\theta = [-15°, -7.5°] \cup [7.5°, 140°]$. The flight path from the sample to the detectors is in Argon gas, in order to minimise any neutron loss due to air scattering. The whole flight chamber is shielded with polyethylene and B_4C, and coated with cadmium in order to minimise the scattering of neutrons that not hit the detectors surface.

In total, 987 detectors are mounted in the above described angular range. The detectors at TOFTOF are ^{3}He gas tubes, with an active surface of $30 \times 400\,\text{mm}^2$ each. Along the vertical axis, an anode wire is placed and kept at a high voltage (1500 V), whereas the outer wall of the tube is held at earth potential. The gas is a mixture of 97% of ^{3}He and 3% of CF_4 gas, operated at a pressure of 10 bar. Neutrons are measured via an indirect nuclear reaction, since they don't cause ionization. In case of ^{3}He gas, the nuclear reaction takes place in the detector gas

$$^3\text{He} + \text{n} \quad \longrightarrow \quad ^3\text{H} +^1 \text{H} + 0.764\,\text{MeV}. \tag{3.10}$$

The two particles produced are accelerated in the gas using the electric field. This leads to an ionization in the gas, later collected by an anode wire at high voltage. The energies carried by the individual fragments can be calculated using the energy and momentum conservation. Neglecting the energies and momentum of the incoming neutron, approximatively 193 keV are taken by the tritium and 577 keV by the proton. To enhance the spatial resolution, usually a small amount of stopping gas is added, in this case CF_4.

In general the gas is also sensitive to γ radiation, i.e. the signal produced by a neutron might be disturbed by external radiation. Usually the signal originated by a neutron is energetically distinguishable from the one originated by γ radiation, therefore a discriminator is able to reject the signals originating from the latter ones. After the discriminator, the signal is sent to the electronic cards, connected with a computer. The detector efficiency is taken into account during the data treatment. Not all the detectors have the same efficiency: it depends on the manufacturer and varies also as a function of time. Therefore a calibration of the detector has to be taken into account using a Vanadium standard: this will be explained later. One other contribution stems from the neutron loss due to the detector wall thickness, as well as from the incomplete absorption of the neutron by the detector gas. This contribution is energy dependent, and, in the case of TOFTOF, is expressed by the following:

$$\phi(E) = \exp\left(\frac{C_1}{\sqrt{E}}\right)\left[1 - \exp\left(\frac{C_2}{\sqrt{E}}\right)\right], \tag{3.11}$$

where $C_1 = -0.31\sqrt{\text{meV}}$ and $C_2 = -9.3518\sqrt{\text{meV}}$. [116].

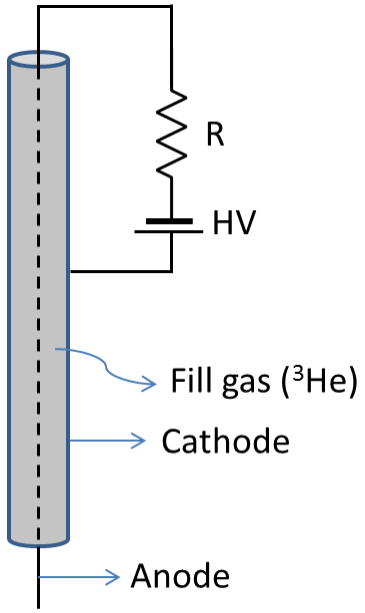

Figure 3.8: Proportional counter detector. The cylinder is filled with gas, in this case ^{3}He. The high voltage (HV) allows the collection of the charged particles produced during the interaction of the neutrons with the gas.

3.4 Dynamical range

In a spectrometer, two quantities are registered indirectly: the momentum transfer $\mathbf{Q}$ and the energy transfer $\hbar\omega$. Both quantities are related to the incident and final neutron energies, by

$$\hbar\mathbf{Q} = \hbar\mathbf{k}_\mathrm{i} - \hbar\mathbf{k}_\mathrm{f} \quad \text{momentum conservation} \tag{3.12}$$

$$\Delta E = \hbar\omega = E_\mathrm{i} - E_\mathrm{f} = \frac{\hbar^2}{2m_\mathrm{n}}\left(k_\mathrm{i}^2 - k_\mathrm{f}^2\right) \quad \text{energy conservation} \tag{3.13}$$

The scattering triangle is already sketched in fig. 2.1.

Using these two quantities, a relationship holds for a fixed scattering angle 2θ and incident neutron energy E_i:

$$Q = \sqrt{\frac{2m_\mathrm{n}}{\hbar^2}\left[2E_i - \hbar\omega - 2\sqrt{E_i\left(E_i - \hbar\omega\right)}\cos 2\theta\right]}. \tag{3.14}$$

The momentum transfer Q, accessible in an experiment, as a function of the energy transfer is called dynamical range, shown in fig. 3.9. The incident neutron energy can be varied in a continuous way and the final energy of the neutron can be registered without limitations. The limits are given, in this case, by the scattering angles: the detectors pose a limit in the dynamical range, since at angles higher than 140° there are no detector tubes. Therefore, the instrument is able to register only neutrons with a momentum Q and energy transfer $\hbar\omega$

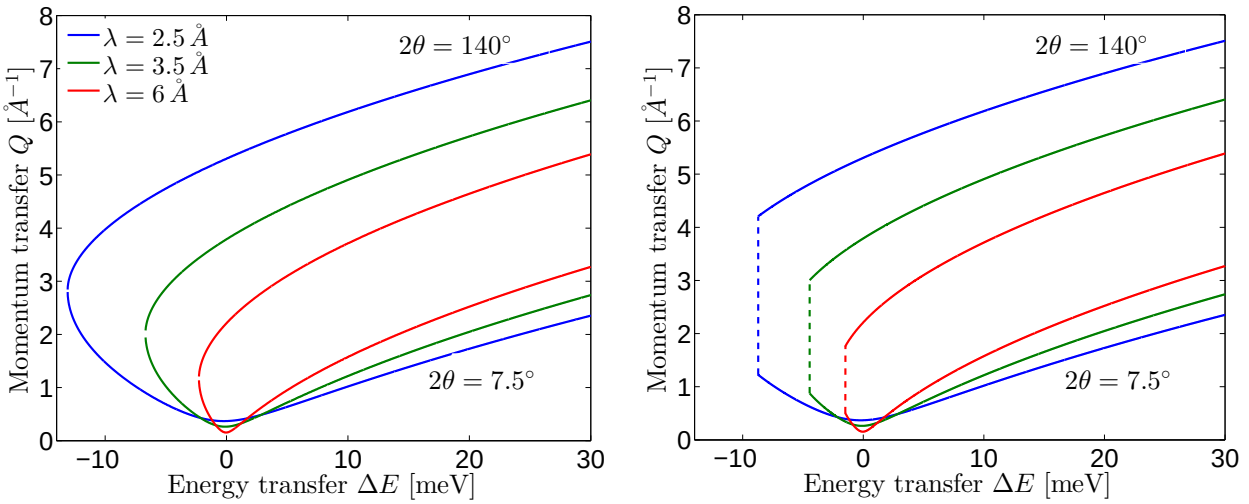

Figure 3.9: (Left): dynamical range of a time of flight spectrometer. The three curves represent the momentum transfer as a function of $\hbar\omega$, for two fixed angles, 7.5° and 140° , the lowest and highest detectors angle. (right): dynamical range of TOFTOF. In fact, the energy loss side is not totally accessible, due to the restriction imposed by the FO chopper. Only neutrons up to 1.5 times the incident wavelength are measured and slower neutrons are moved to the next pulse frame. This results in a vertical cut in the $(Q, \Delta E)$ space marked by vertical dashed lines.

in the region between the lines corresponding to $2\theta = 7.5°$ and $2\theta = 140°$.

The area of negative energy transfer is called "energy loss" side (with the respect to the neutron), whereas the one with positive energy transfer is the "energy gain" side. The loss side is physically limited from the energy of the incoming neutron: no energies larger than its energy can be transferred to the sample. Instead, no limitation is given on the gain side. In the experiments, the slowest neutrons registered are the ones that lost energy till they have a final wavelength ~ 1.5 times the incident wavelength λ. This is related to the frequency of chopper 5, the frame overlap chopper.

As noticeable in fig. 3.9, the (Q, ω)-space shrinks with decreasing the energy of the incoming neutron, i.e. with increasing wavelength λ_i. In this work, the momentum transfer Q plays a crucial role. In the analysis of local reorientation, the intensity as a function of Q reflects the geometry of the reorientational dynamics. Therefore, a large Q space is necessary and shorter wavelengths are required.

On the other hand, short wavelengths lead to a poor energy resolution and therefore the reorientational dynamics might not enter in the time scale set by the resolution, but will be inside the elastic line.

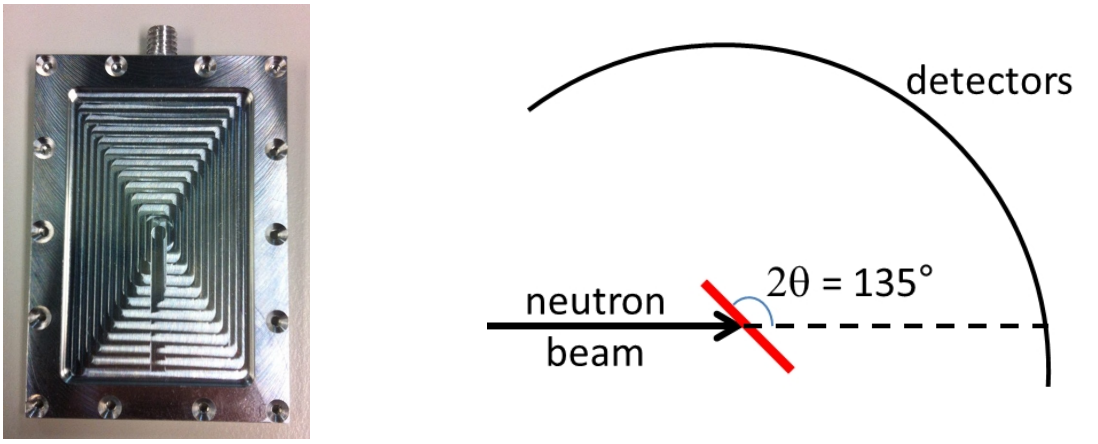

Figure 3.10: (Left): aluminium empty container used in the experiments. The borders hosting screw holes are shielded by borated aluminium, thus only the central surface is illuminated by the neutron beam. (Right): orientation of the flat cell with the respect of the incoming neutrons. The shadow produced by the cell will affect detectors around 135° .

3.5 Sample environment and measurements

Measurements at TOFTOF are usually performed as a function of an external parameter, such as the temperature. Therefore, the sample needs to be kept at a certain temperature T and kept constant for the measurement time. In this work, temperatures range from 10 K to 500 K, and therefore a closed cycle cryostat (CCR) was chosen. Using He gas expansions, the TOFTOF cryostat is able to cool the sample to about 3.5 K. In order to measure the sample at a desired temperature, a resistance is mounted at the bottom of the stick holding the sample cell. Using a current flow, the sample is heated up to the chosen temperature; the amount of current going through the resistance is regulated by the temperature controller.

In this work, all samples are reacting strongly with water and oxygen. All materials have been handled in a glove box, with air and oxygen levels below 10 ppm. Samples were mounted in flat aluminium cells, sealed with aluminium wires. Since all measurements were performed in transmission mode, samples were oriented in a way that the sample produces a shadow in the direction of detectors around 135° (see fig. 3.10). Therefore, detectors around this angle have been excluded in the data analysis.

3.6 Data handling and treatment

At TOFTOF, neutrons are registered and counted as a function of the time arrival at the detector and of the angle 2θ, $N(2\theta, \text{tof})$. Therefore, in order to obtain the scattering function $S(Q, \omega)$ some data treatment is necessary.
Usually, samples are held in the beam using a containaer. Thus, extra measurements of the

empty container are necessary in order to obtain the signal coming from the sample itself. When a sample (characterized by a finite thickness) is placed in the beam, the interior of the sample is exposed to a lower neutron flux than the exterior: this effect is known as self-shielding factor. Following the procedure from [119, 120, 107], the scattered intensity of the sample is:

$$I_{\text{sample}} = \frac{1}{f_{\text{s,s+c}}} \left[I^{\text{m}}_{\text{s+c}} - I^{\text{m}}_{\text{c}} \cdot \frac{f_{\text{c,s+c}}}{f_{\text{c,c}}} \right]. \tag{3.15}$$

The quantities involved in the previous equation are:

- $I^{\text{m}}_{\text{s+c}}$: measured intensity of the sample in the container
- I^{m}_{c}: measured intensity of the empty container
- $f_{\text{s,s+c}}$: self-shielding factor by the sample in container
- $f_{\text{c,s+c}}$: self-shielding of the container when measuring sample in the container
- $f_{\text{c,c}}$: self-shielding of the container when measuring the empty container

In some particular geometries, like "thin slab" or "hollow cylinder", these factors can be calculated analytically and therefore the corrected scattering intensity can be obtained.

Moreover, the thickness of the sample has to be adjusted in order to minimize the possibility that a neutron is scattered more than one time in the sample. When the neutron beam impinges on a sample with an intensity I_0, the transmitted intensity (I) follows the Lambert-Beer law:

$$I = I_0 \mathrm{e}^{-\Sigma d}, \quad \Sigma = \Sigma_a + \Sigma_s \quad \text{and} \quad \Sigma_{a|s} = N\sigma_{a|s}, \tag{3.16}$$

where Σ is the macroscopic cross-section, d the thickness of the sample, σ_a and σ_s the microscopic absorption and scattering cross-sections, respectively. The number of atoms per cm^3, N, is calculated by

$$N = \frac{\rho}{A} N_A. \tag{3.17}$$

where $N_A = 6.022 \cdot 10^{23}\,\text{mol}^{-1}$ is the Avogadro number, ρ is the material density in units of $[\text{g}\,\text{cm}^{-3}]$, A the atomic weight in units of $[\text{g}\,\text{mol}^{-1}]$. The sample must be as thick as possible without the effects of multiple scattering. A general rule of thumb is that the sample should have a transmission of 90%, i.e. it should scatter only 10% of the incident neutron intensity. Therefore, the thickness has to be adjusted in a way that $I = 0.9 I_0$:

$$\mathrm{e}^{-\Sigma d} = 0.9. \tag{3.18}$$

3.6.1 Data Reduction

As a first step, measurements of the sample and of the empty container are normalized to the incoming flux, using the counts obtained by the monitor placed in front of the sample chamber. Right after, the correction for self-shielding and self-attenuation factors are performed, detector by detector and subsequently the subtraction of the empty container is performed using eq. 3.15.

Afterwards, the time of flight is converted into energy transfer: this is done using a measurement of a Vanadium standard with the same geometry of the sample. Vanadium is an almost pure incoherent elastic scatterer ($\sigma_{\text{coh}} = 0.0184\,\text{barn}$, $\sigma_{\text{inc}} = 5.08\,\text{barn}$). Therefore, the arrival time of elastically scattered neutrons can be measured for each detector, which defines the time t_{el} of energy transfer $\Delta E = 0$. Slower or faster neutrons are scattered inelastically with a certain energy transfer $\Delta E \neq 0$.

The detector efficiency correction is also performed using the Vanadium standard: since it scatters only incoherently, the scattering is isotropic and the detectors should record the same intensity at all angles (corrected for the Debye-Waller factor of Vanadium). If some detectors are counting less or more than the average intensity registered, the correction can be performed. Moreover, detectors that are disturbed by a noisy electronic can be taken into account at this step, and excluded in the data analysis. Furthermore, a correction of the energy loss factor described in eq. 3.11 is performed.

After the conversion of time-of-flight into energy transfer, the momentum transfer Q is calculated. The scattering function $S(Q, \omega)$ is obtained after correcting the spectra for the factor $\frac{k_i}{k_f}$.

In order to analyse the spectra, data are binned in a regular grid of energy transfer (ΔE) and momentum transfer (ΔQ).

Part III

Results

Chapter 4

Lithium Borohydride

Contents

In this work, a quasi-elastic experiment has been performed on different ball milled samples across the crystal phase transition, in order to elucidate the hydrogen dynamics in the picosecond timescale and the possible influence of mechanical treatment.

4.1 Samples

$LiBH_4$ was purchased at Alpha Aesar, with 95% nominal purity. The material was used without further purification and three different batches were prepared: the first, "as received" without any mechanical treatment, the second and third were ball milled (b.m.) using a high energy planetary ball mill with stainless steel vials and balls.

- 1st batch: no ball milling, used "as received"
- 2nd batch: Fritsch Pulverisette P7, 2 h, ball-to-powder ratio 40 : 1
- 3rd batch: Retsch PM400, 27 h, ball-to-powder ratio 48 : 1

All handling of materials took place under inert atmosphere in an argon filled glove-box, avoiding contact with oxygen and moisture. X-ray diffraction was performed on all sample batches to check the quality after intensive ball milling times.

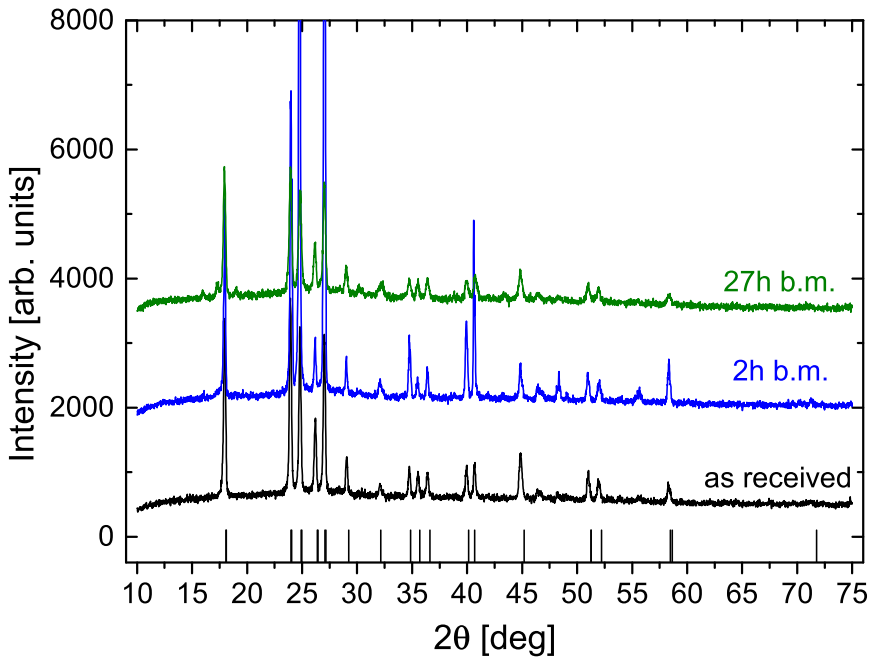

Figure 4.1: X-ray diffraction pattern of different $LiBH_4$ powder samples in the P*nma* crystal phase. From bottom to top: black - as received, blue - 2h b.m., green - 27h b.mm. At the bottom, vertical bars are the *o*-$LiBH_4$ calculated Bragg reflections. Graphs are shifted for clarity.

4.1.1 X-ray diffraction

The three samples (as received, 2h b.m, 27h b.m.) were investigated using X-ray diffraction. Samples were kept under Kapton (polyimide) protective films and mounted in a diffractometer (XPERT-PRO). The incident radiation was Cu-K_α, corresponding to $\lambda = 1.544\,\text{Å}$, and the diffractograms were recorded between 10° and 75°. Results are shown in fig. 4.1.

Although no Rietveld powder refinement was performed, no detectable changes in peak position can be detected between the "as received" sample and the different b.m. samples. This ensured that the crystal structure is retained even after several ball milling hours.

4.2 Quasi-elastic neutron scattering measurements

4.2.1 Experimental

For the neutron experiments, about 70 mg of $LiBH_4$ were packed in an aluminium thin foil and mounted into an aluminium flat cells, yielding to a theoretical neutron transmission $T = 0.85$. This transmission value ensures a low multiple scattering effect, and therefore it was not taken into account in the analysis. In all samples, the natural boron B was used: natural boron is composed by 80 % of the isotope ^{10}B, which is a strong neutron absorber, and therefore data were corrected for the self-shielding effect (see section 3.6). The flat cell was

T [K]	Fit functions
343, 373	$\delta + L_1 + L_2 +$ DHO
403	$\delta + L_1 + L_2$

Table 4.1: Table summarizing the fit functions used to describe experimental data at different temperatures.

mounted with an angle of $2\theta = 135°$ with respect to the incident neutron flux direction. The wavelength of the incoming neutron was $\lambda = 2.5\,\text{Å}$ and the chopper speed was 22000 r.p.m., resulting in an energy resolution of 440 μeV (FWHM of the elastic line). Measurements were performed in a range of temperatures from 11 K to 403 K, i.e. below and above the crystal phase transition occurring at 381 K. Data were corrected as described in section 3.6 and the scattering function $S(Q,\omega)$ was extracted; the available Q range is $0.5 - 4.2\,\text{Å}^{-1}$, which is a suitable range for discriminating different reorientation motions.

4.2.2 Results and discussions

Some results of measurements are shown in fig. 4.2, taken at different temperatures. It is evident, thatata show two quasi-elastic components, plus an inelastic peak around 9 meV at temperatures below the crystal phase transition. The scattering data obtained from different ball milling time are qualitatively similar, and all samples were analysed in the same manner. With increasing temperature, the scattering signal is increasing and a big jump in quasi-elastic intensity is noticeable at 403 K, above the phase transition temperature (381 K).
Due to the large incoherent scattering cross-section of hydrogen, the experiment probes only the hydrogen dynamics. In general, for independent motions the scattering function can be described by a convolution of three different motions, i.e. translational, rotational a vibrational (see eq. 2.69). In the obtained data sets, no indication for translational diffusion was found, but only vibrational and rotational motions were considered in the analysis.

At temperatures below the phase transition, i.e. 343 K and 373 K, data are modelled with an elastic line (δ-function), a narrow and a broad Lorentzian, plus a damped harmonic oscillator (DHO) (see table 4.1). Although the energy loss side of the spectra is not enough extended to catch the other (symmetric) inelastic peak, a DHO is still able to model the inelastic feature. At 403 K, instead, no visible inelastic peaks are detected and therefore data are modelled without damped harmonic oscillator.

In fig. 4.3 is presented how data are analysed at 343 K and 403 K. In the following, a detailed analysis of the various component is given.

The first narrow Lorentzian, $L_1(Q,\omega)$, is characterized by a constant width over the probed Q range, and therefore representing the quasi-elastic signal associated with a localized dynamics, most probably a reorientation mechanism of the entire $[BH_4]$ unit. In the temperature range explored, Γ_1 is smaller than 1.6 meV, at temperatures below and above

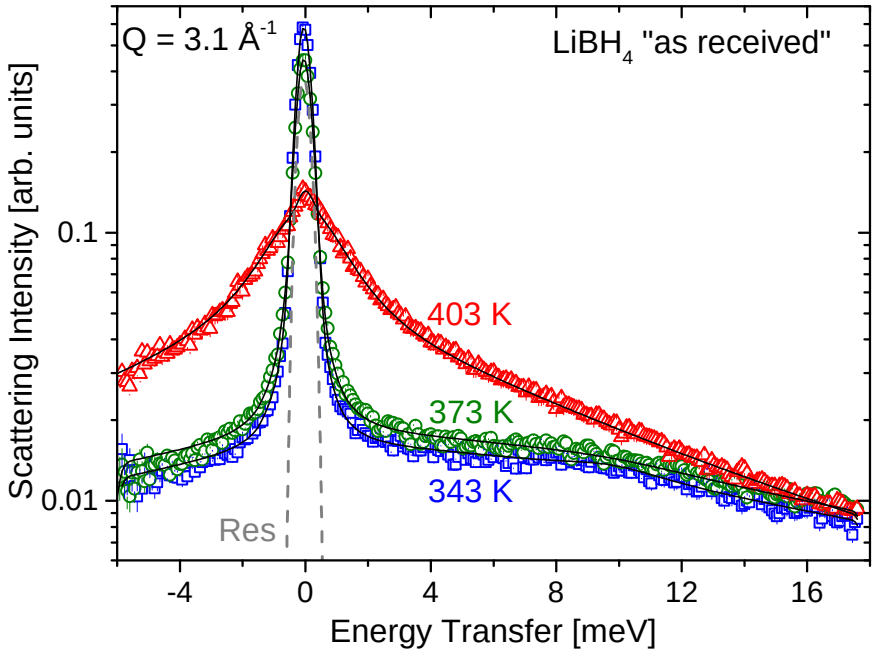

Figure 4.2: $S(Q,\omega)$ of "as received" $LiBH_4$ at $Q = 3.1\,\text{Å}^{-1}$ and at 343 K, 373 K and 403 K. (blue squares) 343 K, (green circles) 373 K and (red triangles) 403 K. The dashed line is the resolution function measured with a vanadium standard. The solid black lines represent the data fits, according to table 4.1.

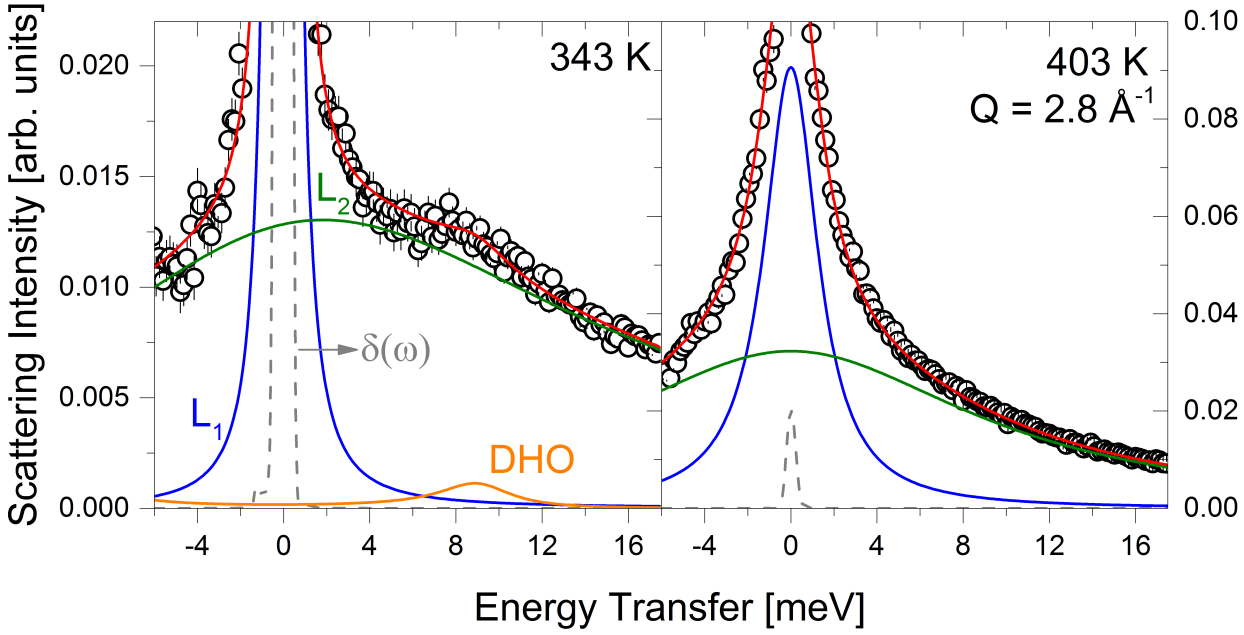

Figure 4.3: $S(Q,\omega)$ of $LiBH_4$ "as received" at $Q = 3.12\,\text{Å}^{-1}$ at 343 K (left panel) and 403 K (right panel). Solid red lines represent the fit. At 343 K data are successfully described by a δ-line, two Lorentzian (L_1 and L_2) and a DHO. At 403 K data are modelled by a δ-line and two Lorentzians.

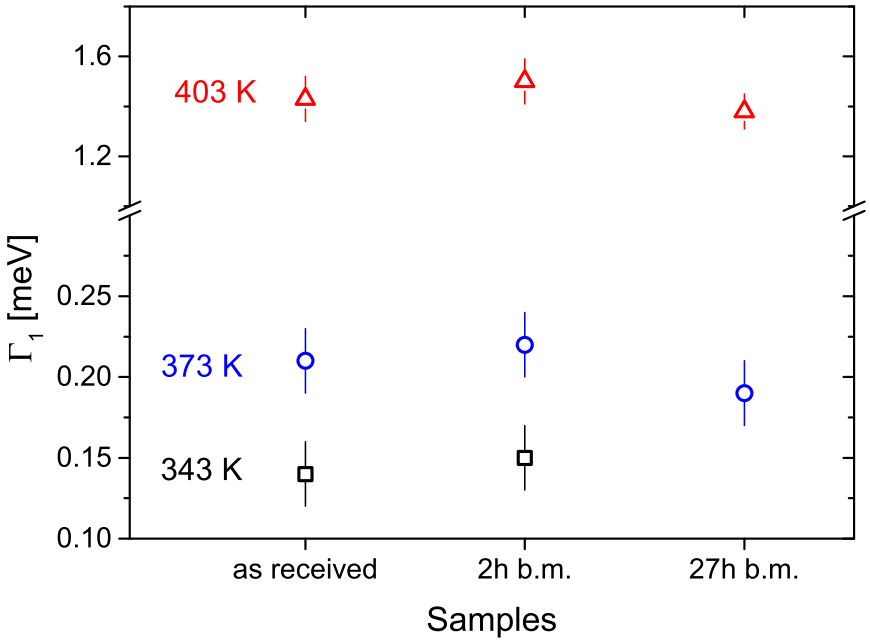

Figure 4.4: Half-widths-half-maximum Γ_1 at 343 K, 373 K and 403 K, and for different samples. Vertical error bars denote $\pm 1\sigma$.

381 K. An estimation of the characteristic time scales from $\tau = \frac{\hbar}{\Gamma_1}$ yields $\tau = 3 - 5$ ps at 343 K and 373 K, and 0.5 ps at 403 K.
In fig. 4.4, the different widths Γ_1 are reported for the samples with different ball milling times: it is noticeable that, within the experimental errors, the widths are identical.

The width of the quasi-elastic feature increases with temperature and typically exhibits an Arrhenius behaviour, with the following relation between widths and temperature

$$\Gamma = \Gamma_0 \exp\left(-\frac{E_A}{k_B T}\right). \tag{4.1}$$

Γ_0 is a pre-factor, k_B is the Boltzmann's constant and E_A the activation energy of the reorientational process. Plotting the logarithm of the widths Γ_1 against the inverse of temperature, we can tentatively extract the activation energy of the process. In figure 4.5, a linear fit was done to extract E_A from the LT-data. An activation energy of $E_A = 14.4$ kJ/mol $= 148.8$ meV was obtained. Verdal *et. al* obtained, using quasi-elastic measurements, an activation energy of 19.1 ± 0.2 kJ/mol [53].
NMR experiments were performed on the low temperature phase of $LiBH_4$, revealing two distinct reorientational dynamics, with two different activation energies (24.2 kJ/mol and 17.6 kJ/mol) [121]. These motions were attributed to reorientation around the 2-fold C_2 and 3-fold C_3 axes of the $[BH_4]$ tetrahedra. In this work, only one value is detected and it is close to the lower E_A reported.

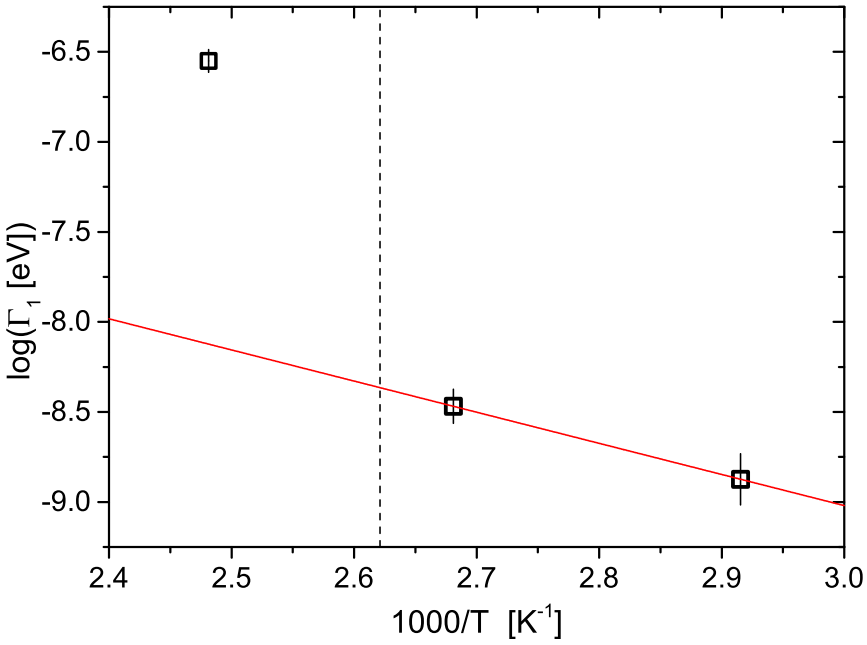

Figure 4.5: Arrhenius plot of $LiBH_4$ L_1 quasi-elastic widths, as a function of the inverse of the temperature. The red solid line is a fit to the LT-data with a linear function. The slope is proportional to the activation energy $E_A = 14.4\,kJ/mol$. Vertical dashed line indicates the crystal phase transition temperature. Vertical error bars denote $\pm 1\sigma$.

The second broader Lorentzian, $L_2(Q,\omega)$, is, instead, characterized by a HWHM depending on the momentum transfer Q, with $\Gamma_2 > 6\,meV$. Results are shown in fig. 4.6 and 4.7.

The widths is Q-dependent, indicating that the quasi-elastic component does not originate from simple rotations of the $[BH_4]$ tetrahedra; in fact, its increasing intensity and widths might be originated from low energy vibrational dynamics, close to the quasi-elastic region. Therefore, it is reasonable to assume that L_2 is representative of the fast vibrational dynamics. In fig. 4.7, the width Γ_2 shows the same trend for all the different samples. In the low temperature phase, L_2 is quite broad, with Γ_2 very well distinct from Γ_1. Conversely, in the HT-phase, Γ_2 is in the same order of magnitude of Γ_1, and shows a more pronounced Q-dependence. This is shown for the "as received" sample in fig. 4.6.

The inelastic peak, centred around 9 meV, is visible in the LT-phase measurement, whereas, in the HT-phase, is not any more observable. A damped harmonic oscillator (DHO, see eq. 2.49) is used to model the peak (see fig. 4.3, left panel) at 343 K and 373 K. ω_q is extracted from the fit at 343 K, and shown in fig. 4.8. At 373 K, the vibration frequency does not show any change, within the experimental uncertainty (not shown in figure).

The inelastic peak in this work can be also assigned to low energy lattice vibrations, and thus it is modelled using a DHO [111]. With increasing temperature, the DHO signal

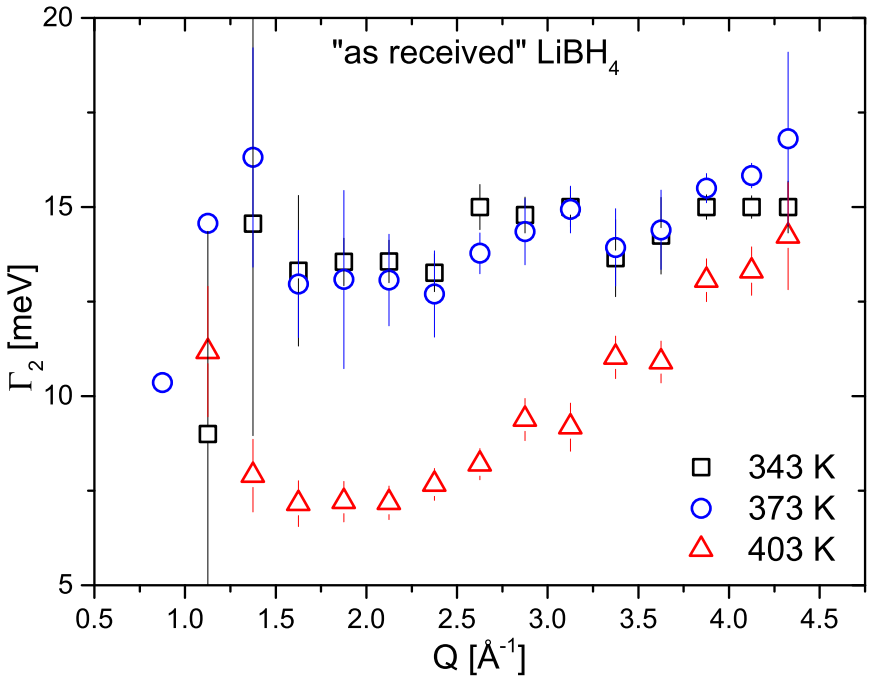

Figure 4.6: Half widths at half maximum Γ_2 at 343 K, 373 K and 403 K, of the "as received" sample. Vertical error bars denote $\pm 1\sigma$.

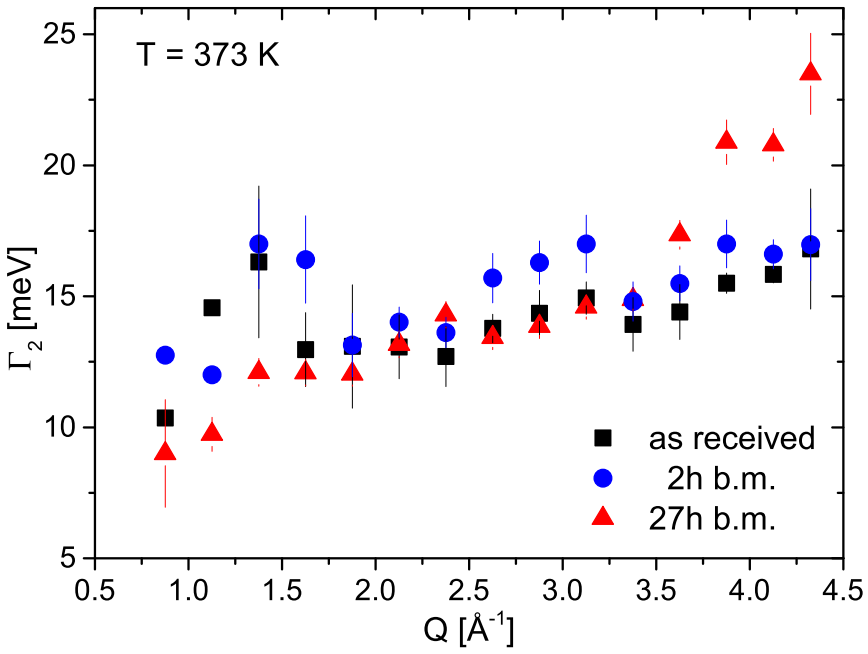

Figure 4.7: Half widths at half maximum Γ_2 at 373 K for different ball milled samples. Vertical error bars denote $\pm 1\sigma$.

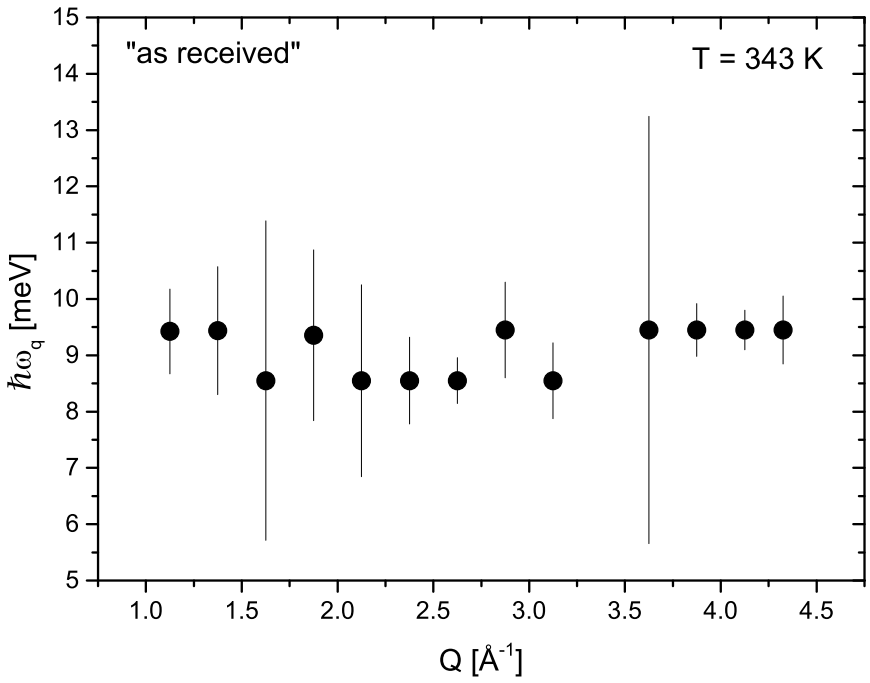

Figure 4.8: DHO vibrational energy $\hbar\omega_q$ extracted from data at 343 K and for the "as received" sample. At 373 K, the vibration frequency does not show any change, within the experimental uncertainty (not shown in the graph). Vertical error bars denote $\pm 1\sigma$.

becomes relatively weaker, till it is not any more visible in the HT crystal phase. In this case, an over-damped DHO (indistinguishable from a Lorentzian shape function) is assumed: in fact, Γ_2 at 403 K shows a completely different Q-dependence compared to Γ_2 at 343 and 373 K.

Several inelastic neutron scattering (INS) experiments were performed on $LiBH_4$ [122, 123, 124, 53, 61]. The energy range probed in these experiments is quite large, up to energies where libration or bending motions of the $[BH_4]$ units are visible. In the work of Gremaud *et al.*, the INS experiment was able to probe hydrogen vibrations below 20 meV at low temperature (15 K). A low energy band is found already at 10 meV, extending up to 25 meV: this was assigned to translational lattice vibrations, where the whole $[BH_4]$ moves against the lithium ion. In the same work, *ab initio* calculations of the single phonon scattering function confirm the presence of low energy lattice vibrations.

Raman and INS experiments [125, 124] showed a change in the external modes (the inelastic peak at 25 meV vanishes), due to a change in the crystal symmetry and an increased rotational disorder.

The evaluation of the EISF and QISF contributes to clarify the hydrogen mobility in $[LiBH_4]$, and therefore the next section will be dedicated to a detailed analysis of these quantities.

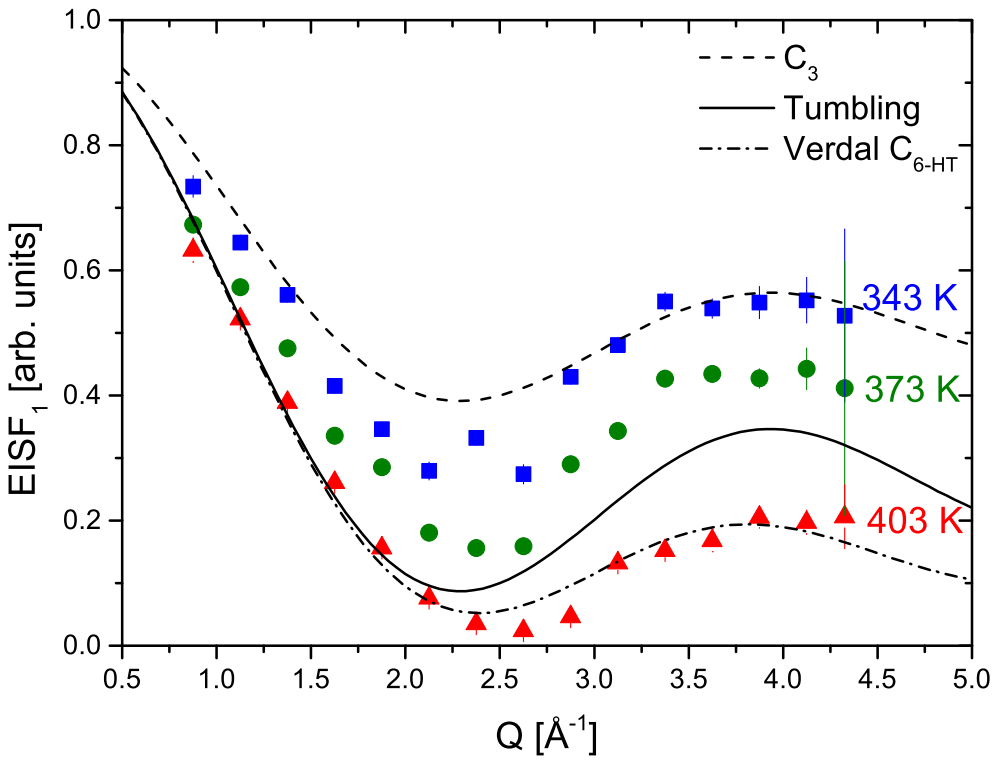

Figure 4.9: Elastic Incoherent Structure Factor of the "as received" sample at different temperatures, using only the quasi-elastic contribution $L_1(Q,\omega)$, eq. 4.2. Lines represent different reorientational models, with $d_{\text{B-H}} = 1.21$ Å (see text). The agreement is not satisfactory at 343 K and 373 K. Vertical error bars denote $\pm 1\sigma$.

4.2.2.1 EISF

The EISF is spatial Fourier transform of the probability function to find a hydrogen atom at a given position, averaged over the time. Its Q-dependence reflects the reorientational geometry.

As first approach, we consider in the EISF calculation only the relevant quasi-elastic component of the localized motion, the Lorentzian $L_1(Q,\omega)$ intensity:

$$\text{EISF}_1 = \frac{I_{\text{el}}}{I_{\text{el}} + I_{L_1}}. \tag{4.2}$$

The results are shown in fig. 4.9, together with simple model function reorientations.

In the LT modification of $LiBH_4$, data are somehow in disagreement with previous measurements on bulk $LiBH_4$ [53]: the EISFs calculated only with the narrow quasi-elastic component (eq. 4.2) are not represented by any simple reorientational motions, like C_3 reorientations or tumbling motions (see fig. 4.9). At 403 K, the experimental data are fairly in agreement with the model proposed by Verdal *et al.* [126, 127]. This model allows 3 trigonal H atoms to occupy 6 position on a circle (approaching a quasi-free rotation). In addition, any of these three orbiting H atoms can exchange position with the remaining axial atom (see fig. 4.10).

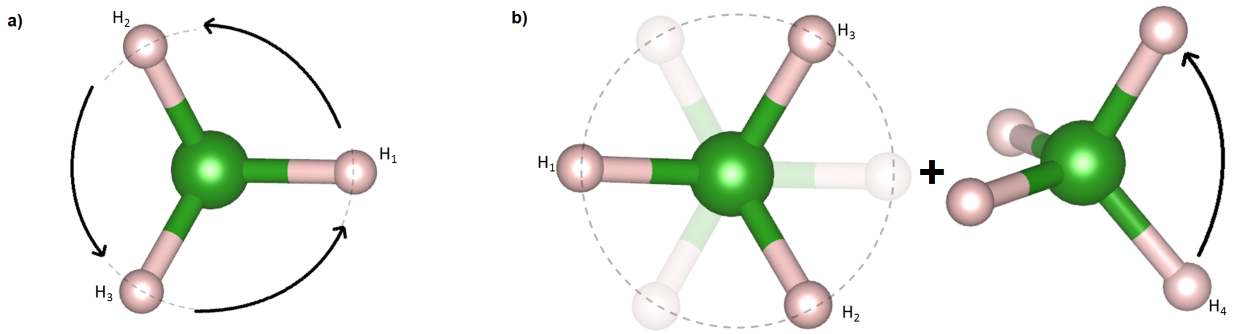

Figure 4.10: a) $[BH_4]$ tetrahedra C_3 rotations: one hydrogen is fixed (perpendicular to the plane) and the other three rotate with 120° rotations. b) Verdal high temperature model, C_6-HT. (see text for details).

In this case, the crystal symmetry is retained, as suggested in the work of Soulié *et al.* [57], and the model assumes this expression [126]:

$$\mathrm{EISF}_{\mathrm{C_6\text{-}HT}} = A_{\mathrm{0\text{-}C6\text{-}HT}} = \frac{1}{8}\left[\frac{5}{4} + \frac{9}{2}j_0\left(Qr\sqrt{3}\right) + \frac{3}{2}j_0\left(Qr\right) + \frac{3}{4}j_0\left(2Qr\right)\right], \tag{4.3}$$

where $r = \frac{2\sqrt{2}}{3}d_{\mathrm{B\text{-}H}}$, with $d_{\mathrm{B\text{-}H}}$ the distance between boron and hydrogen atoms (see fig. 4.10).

Therefore, a general approach is taken into account, including the vibrational part in the calculation of the EISF. The quasi-elastic and vibrational signals can not really be separated, especially at 403 K where the inelastic peak is not any more visible. In the analysis, vibrational and rotational contributions are considered, and the total scattering functions is (see section 2.1.2.3):

$$S_{\mathrm{tot}}(Q,\omega) = [A_0\delta(\omega) + (1-A_0)L_1(Q,\omega)] \otimes [D\delta(\omega) + (1-D)S^{\mathrm{inel}}_{\mathrm{vib}}(Q,\omega)]. \tag{4.4}$$

From the scattering function, we can calculate the EISF and the various QISFs, for $L_1(Q,\omega)$ and the inelastic functions ($L_2(Q,\omega)$ and DHO). The integrated intensities from the DHO and L_2 are summed up and identified with the inelastic scattering function $S^{\mathrm{inel}}_{\mathrm{vib}}(Q,\omega)$. Following the procedure described in section 2.1.2.3, the equation describing the EISF and QISFs are:

$$\begin{aligned} \mathrm{EISF} &= A_0(Q)D(Q) && (4.5)\\ \mathrm{QISF}_{L_1} &= D(Q)\left[1 - A_0(Q)\right] && (4.6)\\ \mathrm{QISF}_{\mathrm{vib}} &= 1 - D(Q). && (4.7) \end{aligned}$$

The factors $A_0(Q)$ and $D_0(Q)$ represent, respectively, the EISFs of localized motions. In the above expressions, the term $A_0(Q)$ is the EISF of localized motions (C_3 rotations, tumbling, etc.), whereas $D_0(Q)$ is the Debye-Waller factor $\exp\left(-\frac{\langle u^2\rangle Q^2}{3}\right)$.

Experimentally, the EISF and QISFs are calculated taking into account all contributions:

$$\text{EISF} = \frac{I_{\text{el}}}{I_{\text{el}} + I_{L_1} + I_{\text{vib}}} \tag{4.8}$$

$$\text{QISF}_{L_1} = \frac{I_{L_1}}{I_{\text{el}} + I_{L_1} + I_{\text{vib}}} \tag{4.9}$$

$$\text{QISF}_{\text{vib}} = \frac{I_{\text{vib}}}{I_{\text{el}} + I_{L_1} + I_{\text{vib}}}, \tag{4.10}$$

being I_{vib} the sum of the integrated intensity of the DHO and the broader Lorentzian $L_2(Q,\omega)$. The different data sets were fitted with aforementioned equations, for each sample and temperature. The fit was performed simultaneously, since parameters involved (mean square displacement $\langle u^2 \rangle$ and the distance $d_{\text{B-H}}$) are shared in the three expressions and these equations are valid simultaneously.
Results are shown in figs. 4.11-4.13 for the "as received", 2h b.m. and 27h b.m. samples, together with fits to eqs. 4.5-4.7.
X-ray and neutron diffraction experiments confirmed that the $[BH_4]$ units have an almost perfect tetrahedron shape, also in the HT-crystal structure. Therefore the distance is kept fixed at 1.21 Å [59].

The mean square displacement $\langle u^2 \rangle$ extracted from the fit is shown in fig. 4.14, for different samples and temperatures. At 343 K, far from the phase transition temperature, data are fairly well described using the C_3 rotation model (see fig. 4.10),

$$A_0(Q) = \text{EISF}_{C_3} = \frac{1}{2}\left[1 + j_0\left(\frac{2\sqrt{2}}{\sqrt{3}} Q d_{\text{B-H}}\right)\right]. \tag{4.11}$$

At 373 K, approaching the phase transition, the best agreement with the data was found with tumbling motion:

$$A_0(Q) = \text{EISF}_{\text{tumbling}} = \frac{1}{4}\left[1 + 3j_0\left(\frac{2\sqrt{2}}{\sqrt{3}} Q d_{\text{B-H}}\right)\right]. \tag{4.12}$$

At 403 K, in the HT crystal phase, the model that best fits the normalized intensities is the C_6-HT "orbit exchange", eq. 4.3 and fig. 4.10. Data could be also described as continuous rotations on a surface of a sphere of radius $d_{\text{B-H}}$, but X-ray experiments showed that the crystal order is still retained at high temperature, and thus this model is less likely to be applied.

The mean square displacement $\langle u^2 \rangle$ increases with increasing temperature, as shown in fig 4.14, and a big jump is seen from LT– to HT–crystal modification, independent from the mechanical treatment.

Effect of different ball milling times One of the key points of this experiment was to study the effects of ball milling time on the hydrogen dynamics on a microscopic level. The slow

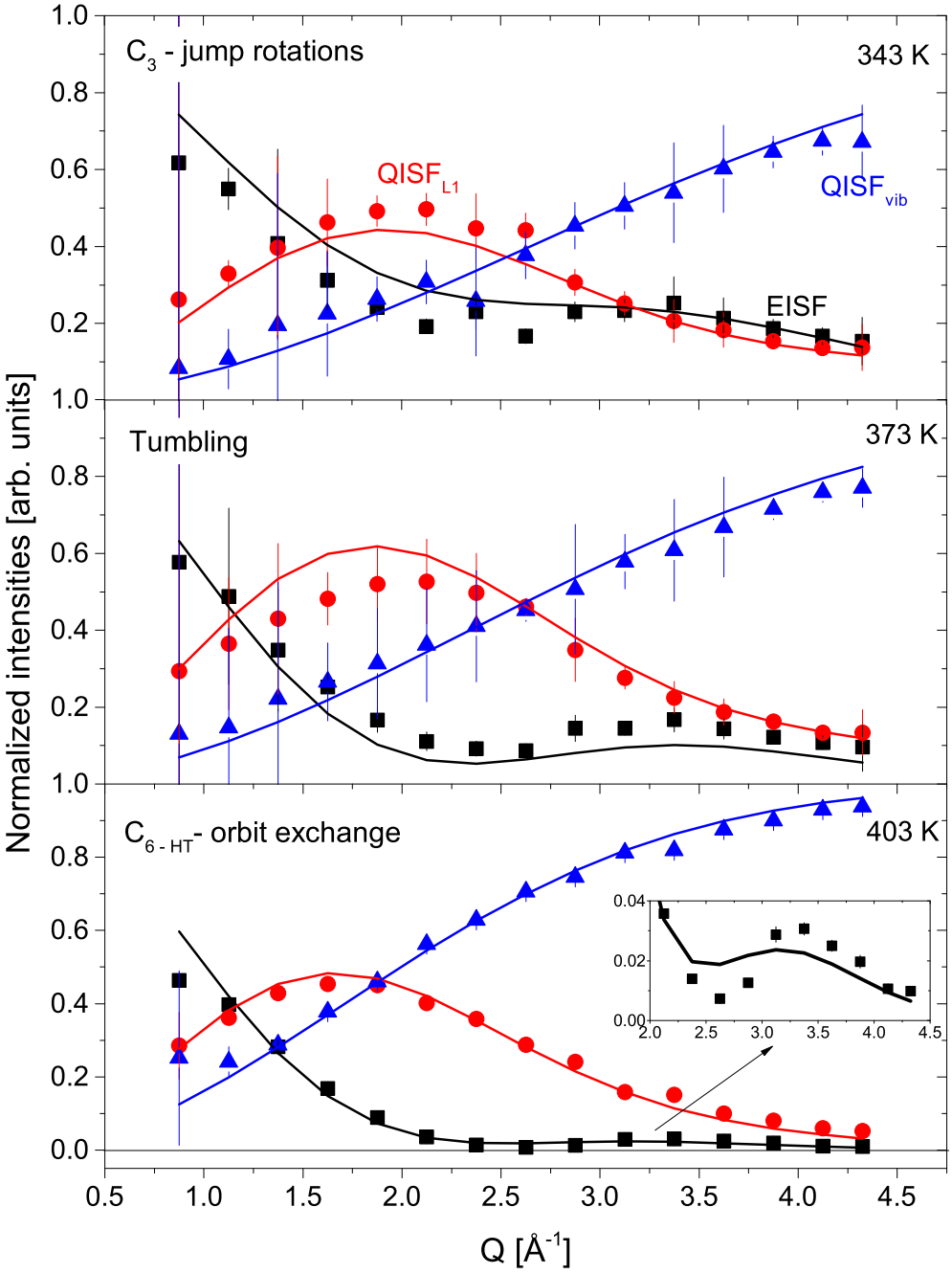

Figure 4.11: Normalized intensities of $LiBH_4$ "as received", at different temperatures (from top to bottom): (black squares) EISF (eq. 4.8), (red circles) $QISF_{L_1}$ (eq. 4.9), (blue triangles) $QISF_{Vib}$ (eq. 4.10). Solid black lines represent the fit to the data according to different $A_0(Q)$. Vertical error bars denote $\pm 1\sigma$.

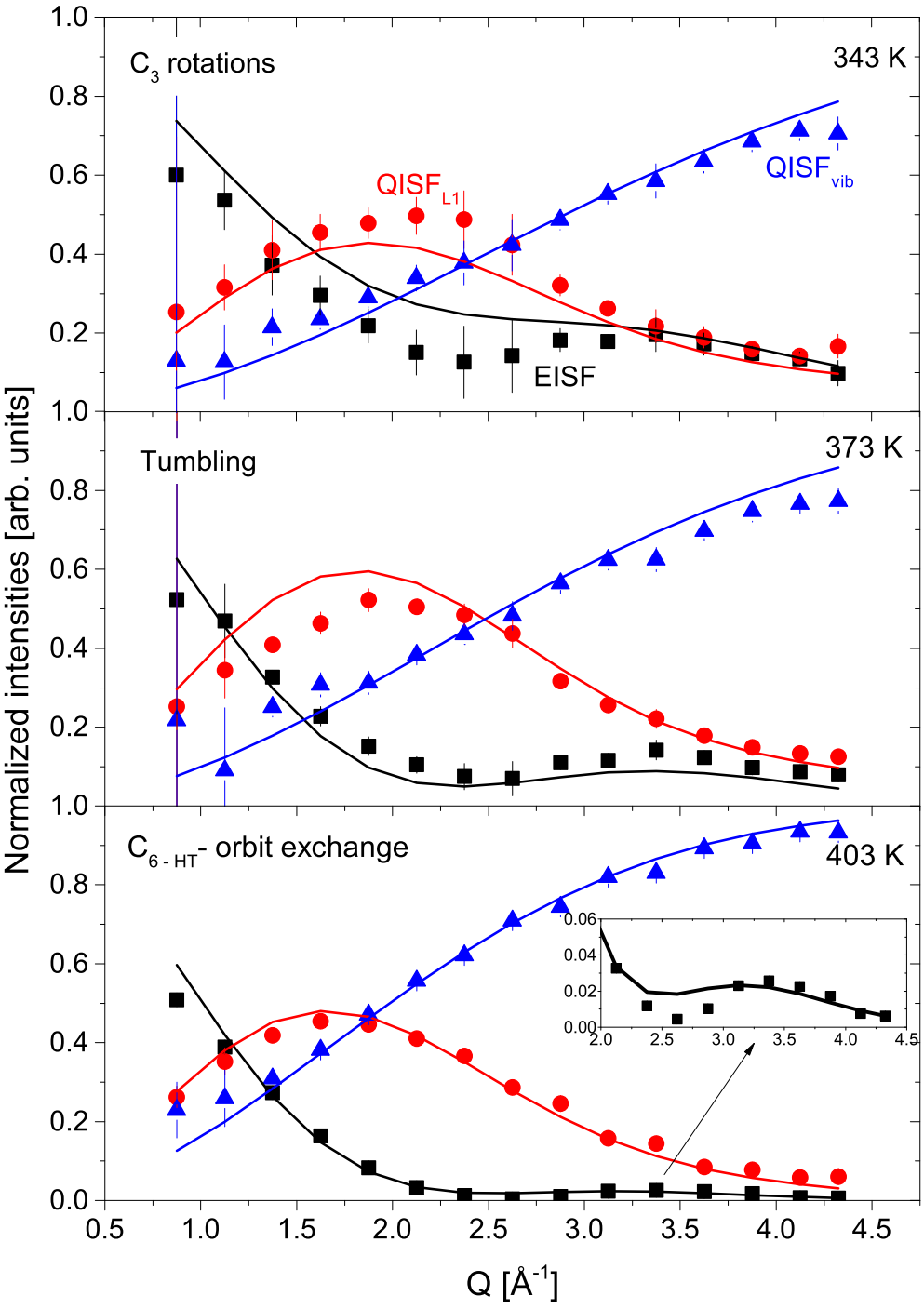

Figure 4.12: Normalized intensities of $LiBH_4$ 2h b.m., at different temperatures (from top to bottom): (black squares) EISF (eq. 4.8), (red circles) $QISF_{L_1}$ (eq. 4.9), (blue triangles) $QISF_{Vib}$ (eq. 4.10). Solid black lines represent the fit to the data according to different $A_0(Q)$. Vertical error bars denote $\pm 1\sigma$.

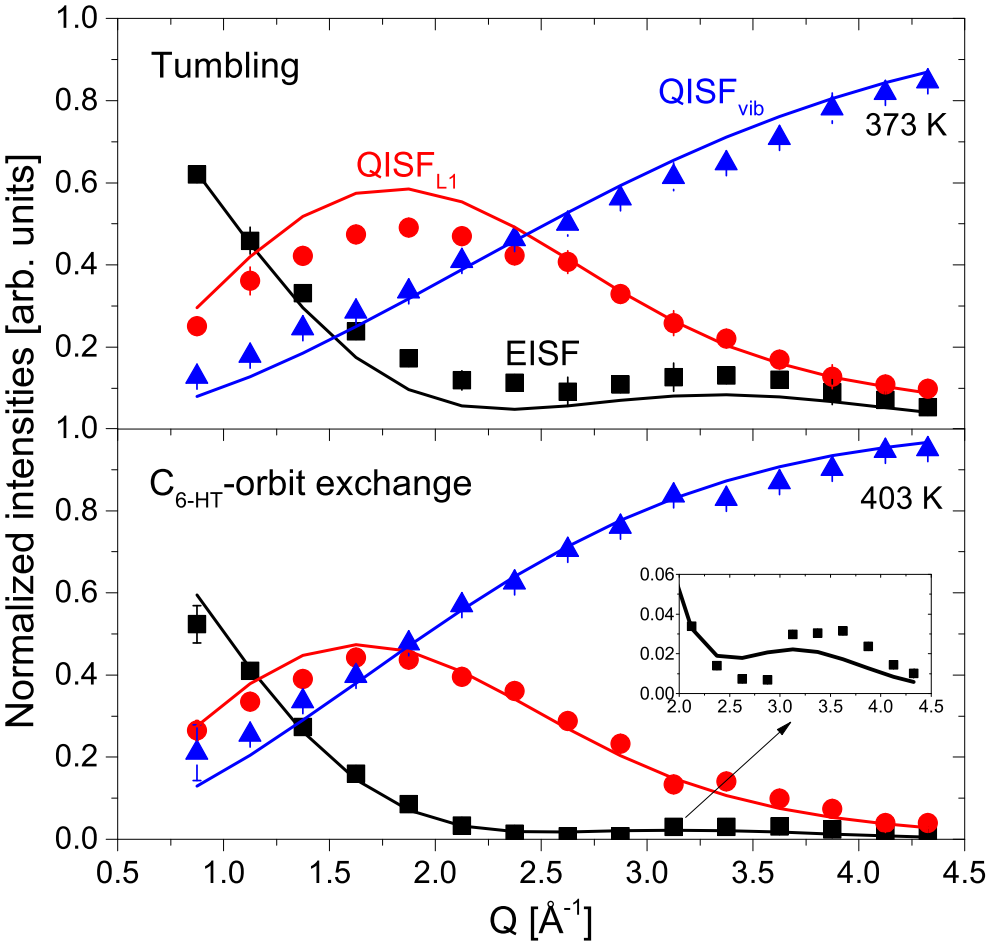

Figure 4.13: Normalized intensities of $LiBH_4$ 27h b.m., at different temperatures : (black squares) EISF (eq. 4.8), (red circles) $QISF_{L_1}$ (eq. 4.9), (blue triangles) $QISF_{Vib}$ (eq. 4.10). Solid black lines represent the fit to the data according to different $A_0(Q)$. Vertical error bars denote $\pm 1\sigma$.

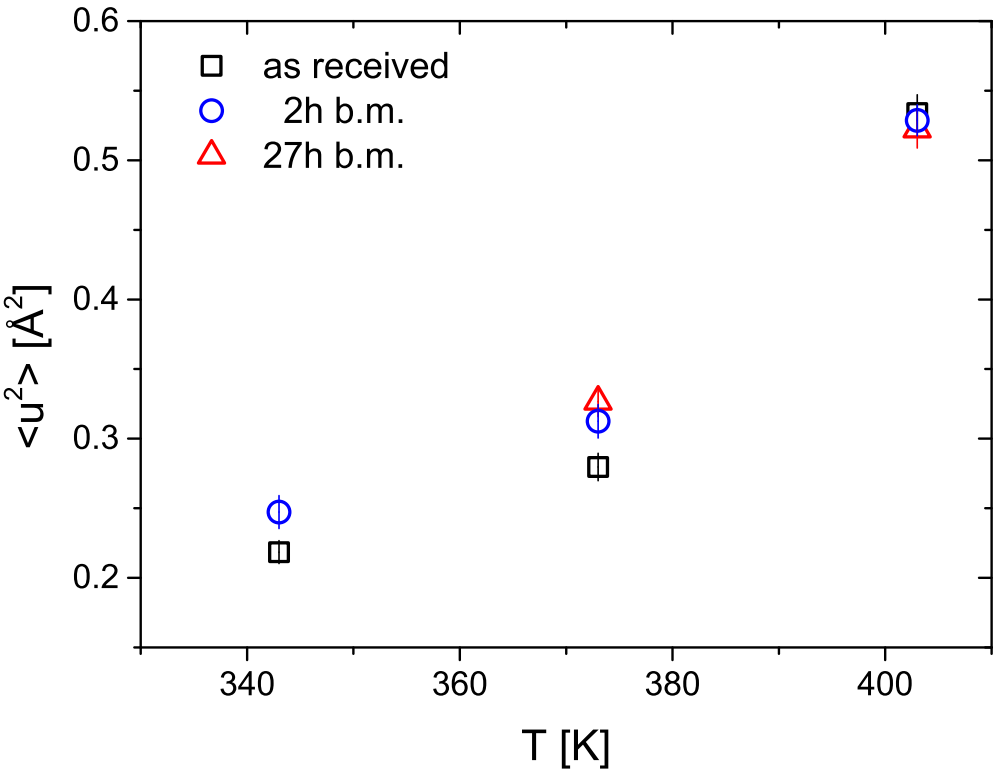

Figure 4.14: Mean square displacement $\langle u^2 \rangle$, obtained from the Debye-Waller factor $D_0(Q)$, of different ball milled samples and temperatures. A big step is evident from the LT- to the HT- crystal modification. Mechanical treatments enhance the mean square displacement in the LT crystal structure phase.

dynamics, identified with $L_1(Q,\omega)$, seems not being affected by the extensive ball milling time: in fig. 4.4, the widths are, within the experimental accuracy, the same.
Conversely, the fast dynamics, identified by $L_2(Q,\omega)$ and DHO, seems to be influenced: in fig. 4.7 it is shown the widths Γ_2 for different samples at 373 K, where the Q–dependence of Γ_2 is modified by increasing ball milling time, although the data scatter is quite large.
Also, the mean square displacement $\langle u^2 \rangle$ tends to increase in the LT–phase (although data of the 27h b.m. sample are available only at 373 K and above), whereas, in the HT–phase, the mechanical treatment seems do not affect the MSD.
Therefore, we can tentatively conclude that, extensive ball milling times favour the fast (vibrational) dynamics, without affecting the rotational one.

4.2.3 Conclusions

QENS experiments was performed on different ball milled $LiBH_4$ samples and on a range of temperature including the crystal phase transition. The above results show that vibrations in the low energy transfer might play an important role in understanding the reorientational dynamics of the $[BH_4]$ units. Anharmonic effects increase dramatically as soon as the phase transition is approached [128, 129]. In this work, a transition in the inelastic signal is found: at 343 K, spectra show a clear inelastic peak at 9 meV, whereas, at 403 K, the inelastic dynamic merges in the quasi-elastic region, superimposing to the localized reorientation dynamics.

Already at 373 K, the elastic signal is reduced, and at the same time the reorientation dynamics become more disordered. From an uni-axial C_3 rotations at 343 K, to a tumbling motion at 373 K, where all the H atoms are reorientating in time. Above the crystal phase transition temperature, an almost free rotation is approached with the C_{6-HT} "orbit exchange" model. This was also confirmed from MD simulation [129], where reorientations occur when hydrogen atoms move, on average, with 120° rotational jumps around the C_3-axis, repositioning all four hydrogen atoms of a $[BH_4]$ unit.

Taking into account the underlying vibrations, it was possible to extract the mean square displacement of H atoms. With increasing ball milling time the fast vibrational dynamic is enhanced, resulting in an increased hydrogen mobility.
This general approach, considering a convolution of the rotational and vibrational motions, allowed a comprehensive analysis of quasi-elastic and inelastic signal.

Chapter 5

Magnesium Borohydride

Contents

In this chapter, quasi-elastic neutron scattering experiments at different time scales and on α-$Mg(BH_4)_2$ and on β-$Mg(BH_4)_2$ are described, in order to elucidate the dynamics on both crystal species.

5.1 Sample characterization

Both samples were prepared as described in [68] at the Karlsruher Institut für Technologie, Karlsruhe, Germany.
Natural Boron contains roughly 80 % of ^{10}B, which is a great absorber for neutrons. In order to avoid absorption of neutrons inside the sample, isotope enriched ^{11}B was used. After the synthesis, X-ray diffraction (XRD), thermo-gravimetric (TG), differential scanning calorimetry (DSC) and mass spectroscopy (MS) measurements were performed in order to check the quality and crystal phases of the samples.

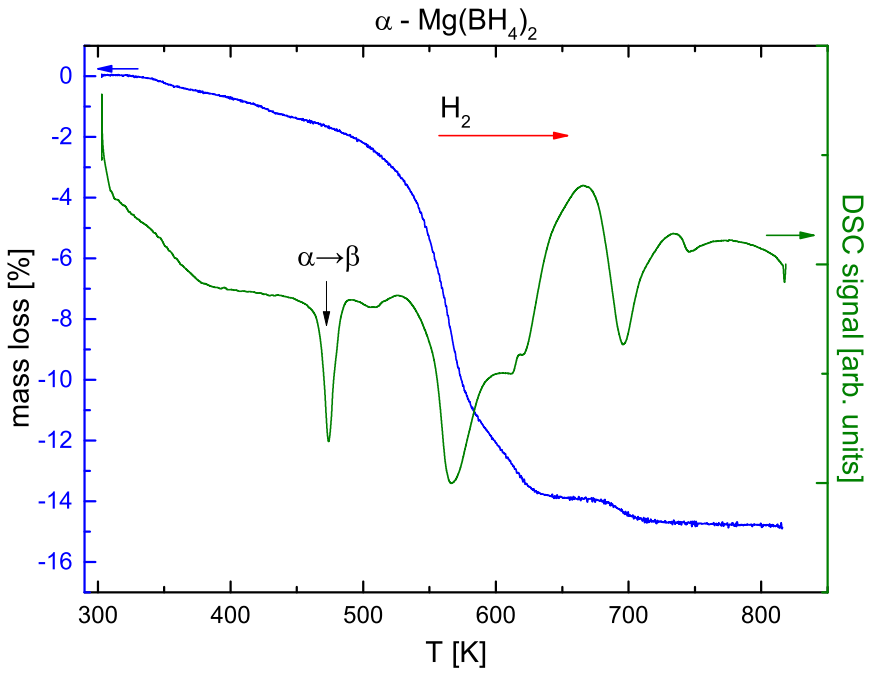

Figure 5.1: TG (blue and left axis) and DSC (green and right axis) measurement on α-$Mg(BH_4)_2$.

For α-$Mg(BH_4)_2$, 4.57 mg of sample were used in the measurements, whereas for the β-phase 17.71 mg. All DSC, TG and MS measurements were performed at the same time under inert (He) gas flow at a heating rate of $5\,K\,min^{-1}$, and results are shown in figs. 5.1, 5.2 and 5.3. The α-phase shows an endothermic peak around 470 K (fig. 5.1), where the material transforms into the β-phase: the peak is quite narrow, indicating that the transformation is completed in few Kelvins. The crystal phase transition is not accompanied by any significant hydrogen release. Both samples decompose and start to release hydrogen above 550 K, as it can be observed from the TG curve, where the major release of hydrogen takes place between 550 and 600 K. This is also confirmed by MS measurements (fig. 5.3), where the three peaks indicate the intensity of H_2 signal. The second endothermic peak corresponds to the first decomposition step of $Mg(BH_4)_2$, where ca. 10% wt.H_2 is released.
Above 670 K, a successive H_2 release is confirmed by the third DSC peak: this is interpreted as the decomposition of MgH_2 into Mg, as described in literature [72]. The total amount of hydrogen released is in good agreement with theoretical values of 14.9 wt.% H_2.
DSC measurements on β-$Mg(BH_4)_2$ show a different behaviour compared to the α-phase (fig. 5.2): the absence of the peak at 470 K confirms that the material is already in the β-phase. The MS measurements of H_2 shows at least four intensity peaks (fig. 5.3): the first three in the region between 550 K and 600 K, where the TG measurements show the most amount of hydrogen release, and the fourth around 700 K, where a successive H_2 release takes place.
As can be observed, hydrogen release does not happen in a single step decomposition. In-

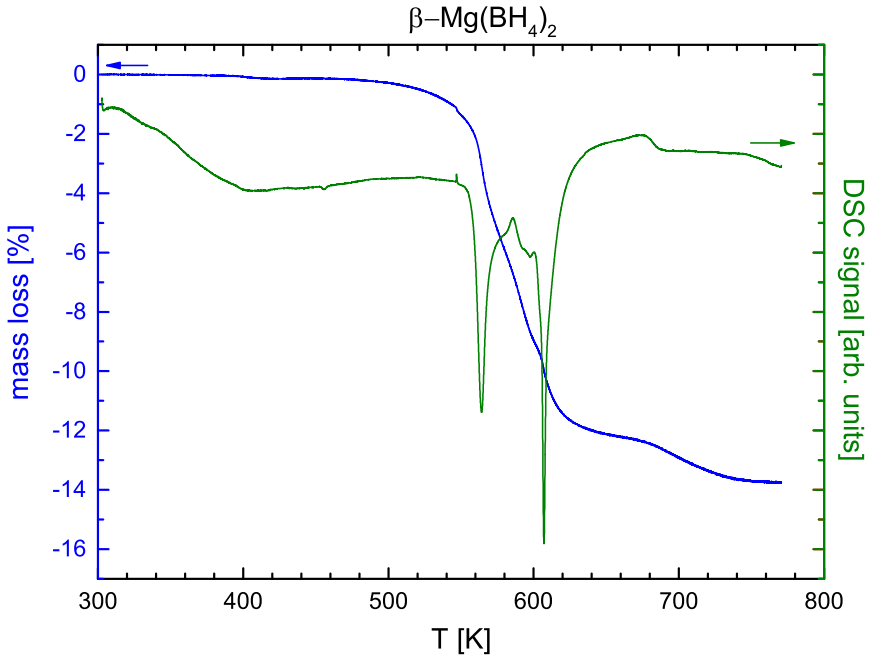

Figure 5.2: TG (green and right axis) and DSC (orange and left axis) measurement on β-$Mg(BH_4)_2$.

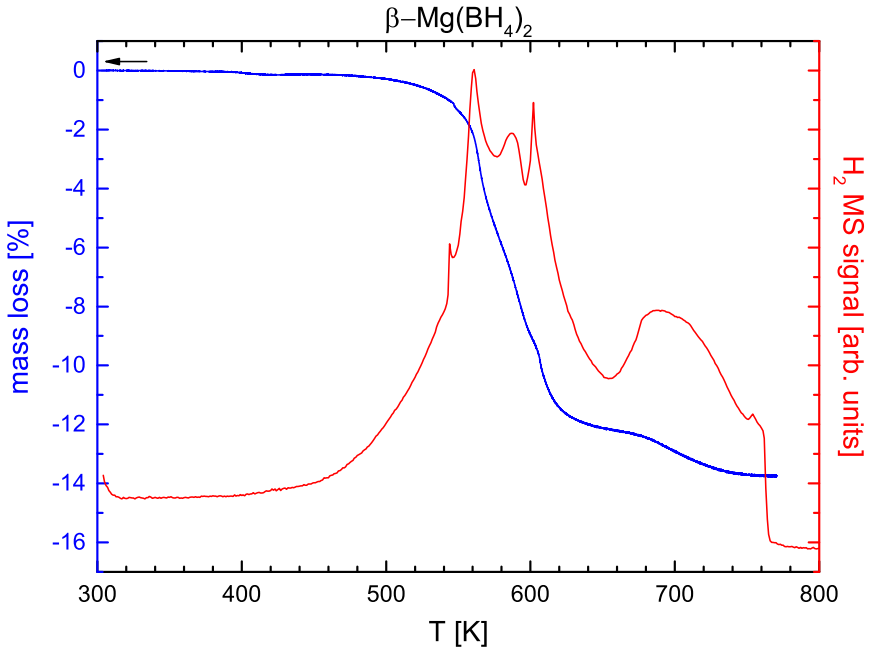

Figure 5.3: TG (blue and left axis) and MS (red and right axis) measurement on β-$Mg(BH_4)_2$.

stead, a multi-reaction decomposition starts at 550 K and continues till 700 K, and intermediate compounds are possibly formed [72].

In this work, neutron scattering experiments were done up to 530 K, thus below the main hydrogen release.

5.2 Experimental

Quasi-elastic neutron scattering experiments were performed on α-$Mg(BH_4)_2$ and on β-$Mg(BH_4)_2$.
Approximatively 200 mg of $Mg(^{11}BH_4)_2$ were mounted in an aluminium flat cell, yielding to calculated neutron transmission of $\sim$ 90%. The large transmission allows to minimize multiple scattering effects, although they can not be excluded at all.
In the experiments, two different wavelengths of incoming neutrons were selected: $\lambda_1 = 2.5\,\text{Å}$ yielding an energy resolution of 450 µeV (FWHM) of the elastic line and an accessible elastic momentum transfer Q from 0.5 to 4.2 Å^{-1}, the second, $\lambda_2 = 6\,\text{Å}$, with an energy resolution of 48 µeV (FWHM) and a momentum transfer from 0.2 to 2 Å^{-1}.
Both samples were measured in a range of temperatures from 11 K to 500 K: at 11 K, the measured width of the elastic peak at zero energy transfer reflects the instrumental resolution function. At higher temperatures, the quasi-elastic and inelastic signals were measured, and, at 500 K, the transition from α- to β-phase occurs.
The raw time-of-flight data were converted to the scattering function $S(Q,\omega)$ following the procedure described in section 3.6. During the analysis, detector angles of the aluminium Bragg peaks were excluded.

In order to elucidate the dynamics in both samples, the data analysis will be divided according to the sample. The first measurements were done on β-$Mg(BH_4)_2$, in order to extend work previously done [99]. Subsequently, measurements were performed on α-$Mg(BH_4)_2$ with the aim to shed some light on the dynamics of different crystal phases.

5.2.1 $\beta-Mg(BH_4)_2$

The results of QENS measurements at different temperatures are shown in figs. 5.4 and 5.5 for the two wavelengths and a chosen Q-value. With increasing temperature, a quasi-elastic broadening is observed, and its intensity rises with increasing temperature. Note, that the two incoming wavelengths λ probe different characteristic time scales and hence the observed quasi-elastic signal could be caused by different underlying motions. Besides the quasi-elastic broadening, the data probing the shorter time scales, ($\lambda = 2.5\,\text{Å}$) show distinct low energy (vibrational) inelastic peaks at $\Delta E = \pm 3.2\,\text{meV}$ at temperatures below 300 K. The energy of

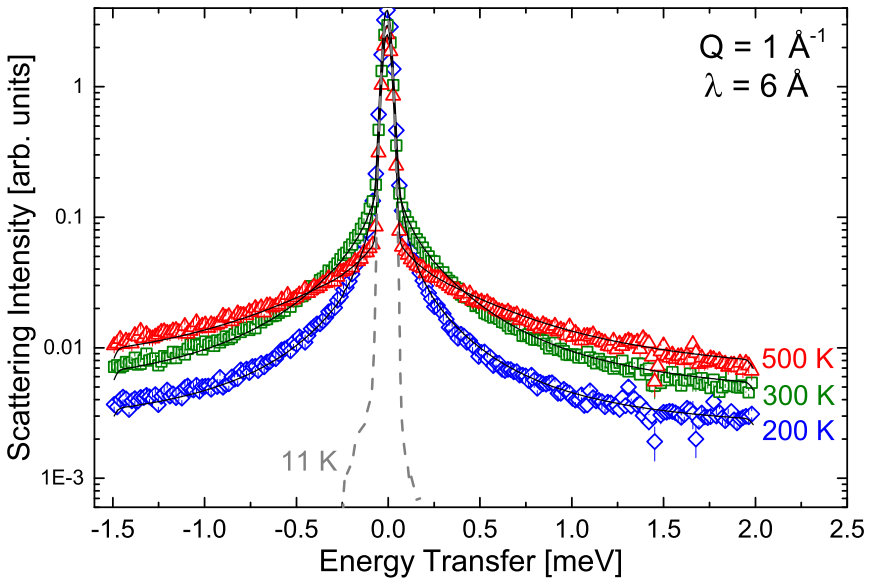

Figure 5.4: $S(Q,\omega)$ at 6 Å of $\beta-Mg(BH_4)_2$ at 11, 200, 300 and 500 K. The black solid lines represent the fit of the data according to eq. 2.56. (grey dashed line) 11 K (resolution), (blue rhombus) 200 K, (green square) 300 K, (red triangle) 500 K.

these excitations is constant for all Q. At 300 K and above, the quasi-elastic signal becomes more intense and the inelastic excitations can not be resolved in the spectra.

The first attempt to separate the vibrational and quasi-elastic signals followed the procedure proposed by Cusack et. al [130]. In the harmonic approximation, the vibrational frequency distribution (usually denoted by $g(\omega)$) is temperature independent, and the Debye-Waller factor and the Bose occupation number relate the data taken at different temperatures. Outside the quasi-elastic region, the relation between low and high temperature data is then given by:

$$\frac{S\left(Q,\omega,T\right)}{S\left(Q,\omega,T_0\right)}\frac{\mathrm{e}^{-Q^2U_{\mathrm{Vib}}(T_0)}}{\mathrm{e}^{-Q^2U_{\mathrm{Vib}}(T)}}=\frac{n\left(\omega,T\right)}{n\left(\omega,T_0\right)}\approx\frac{T}{T_0}\left[1+\frac{\hbar\omega}{2k_B}\left(\frac{1}{T_0}-\frac{1}{T}\right)\right]. \tag{5.1}$$

In the equation above, T_0 is the reference temperature where no quasi-elastic intensity is detected, in this case $T_0 = 100\,\mathrm{K}$. The last inequality is derived in the small energy transfer approximation. A plot of the left hand side of eq. 5.1 is shown in fig. 5.6, together with the linear dependence of the right hand side of eq. 5.1. The vibrational displacement U_{Vib} in eq. 5.1 is temperature dependent and the best agreement with the data is obtained for $U_{\mathrm{Vib}} = 0.0001 \times T[\mathrm{K}]\,\mathrm{Å}^2$. Clearly, at 200 K, the quasi-elastic signal falls to zero beyond $\sim 2\,\mathrm{meV}$. Above $\sim 2\,\mathrm{meV}$, the signal is described to a good approximation by the quasiharmonic temperature scaling, whereas above 300 K, the agreement with the approximation is only found for energies above $\sim 8\,\mathrm{meV}$. This is an indication of a transition in the vibrational modes that affects the quasi-elastic region. A clear separation of these two contributions is not possible and the vibrational part can not be subtracted for analysis of the quasi-elastic

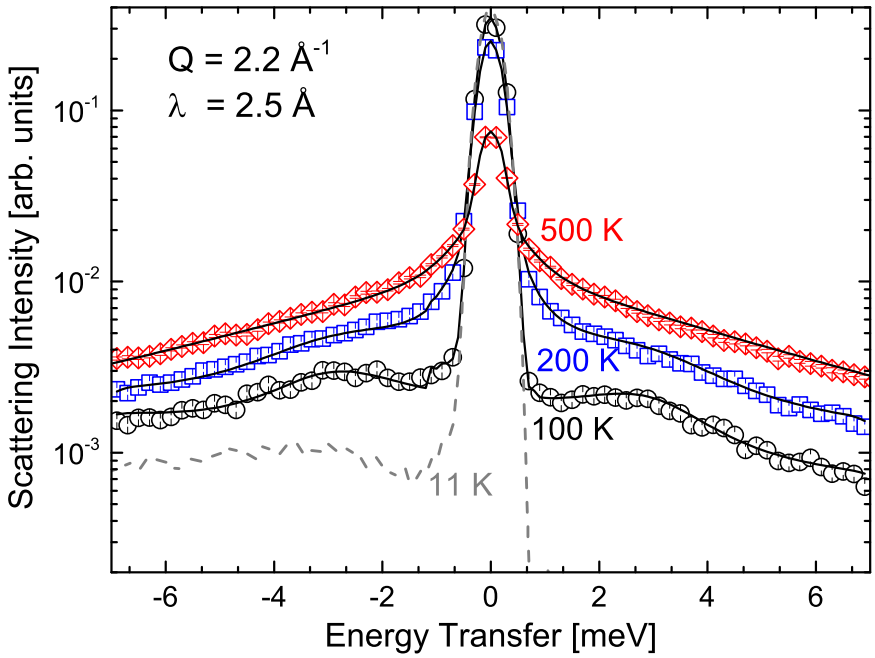

Figure 5.5: $S(Q,\omega)$ of $\beta-Mg(BH_4)_2$ measured at 2.5 Å and at 11, 100, 200 and 500 K. The black solid lines represent the fit of the data according to eq. 2.56 and 2.49. (grey line) 11 K (resolution), (blue circle) 100 K, (green square) 200 K, (red triangle) 500 K. Data sets measured at 300 and 400 K have been omitted for clarity.

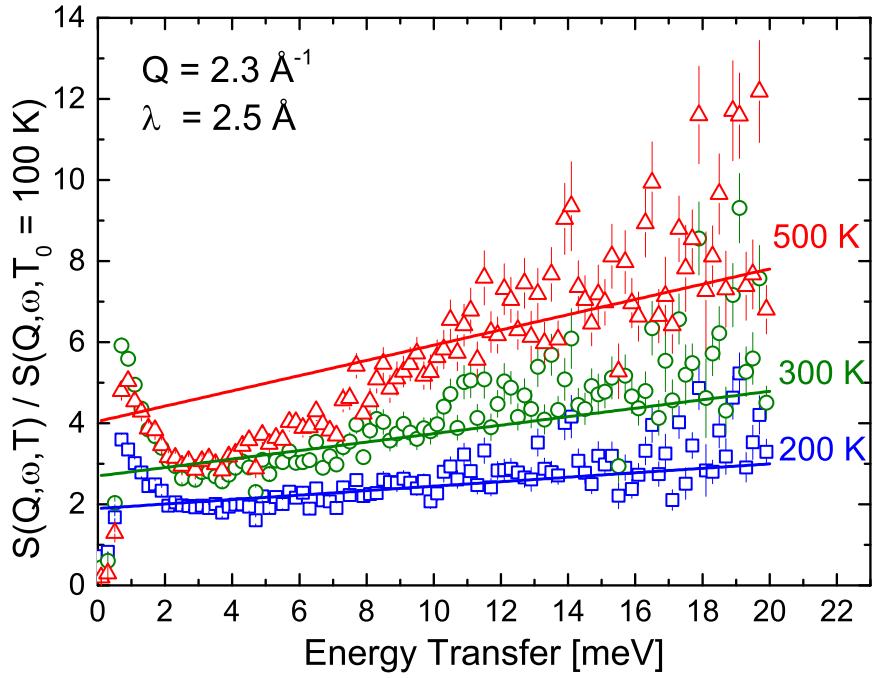

Figure 5.6: Ratio between high temperature data and low temperature data ($T_0 = 100$K) at $\lambda = 2.5$ Å: (blue squares) 200 K, (green circle) 300 K, (red triangle) 500 K. The line represents the right hand-side of eq. 5.1, using $U_{\mathrm{Vib}} = 0.0001 \times T[\mathrm{K}]\,\mathrm{Å}^2$

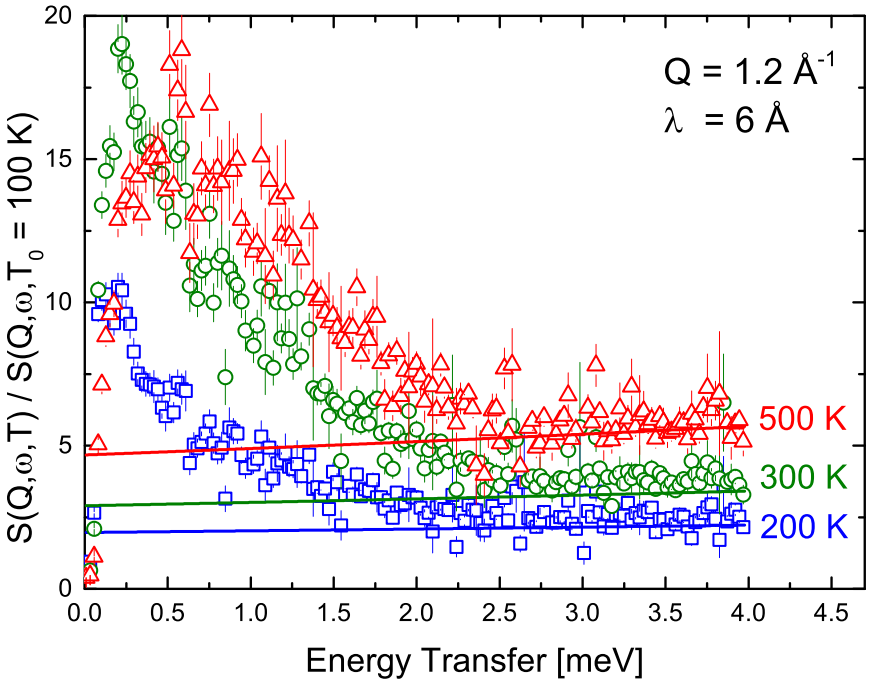

Figure 5.7: Ratio between high temperature data and low temperature data ($T_0 = 100\,\mathrm{K}$) at $\lambda = 6\,\text{Å}$: (blue squares) 200 K, (green circle) 300 K, (red triangle) 500 K. The lines represent the right hand-side of eq. 5.1, using $U_{\mathrm{Vib}} = 0.0001 \times T[\mathrm{K}]\,\text{Å}^2$

data. Therefore, a more complex approach was chosen, as outlined below.

The same analyis for the 6 Å data is shown fig. 5.7. Above $\sim 2\,\mathrm{meV}$ the quasielastic signal falls off, showing a good agreement with the right hand side of eq. 5.1 hence in this case, the vibrational part could be treated as flat background contribution.
It is important to underline that the two different wavelengths probe different time scales and therefore validity of eq. 5.1 strongly depends on the instrumental resolution setting.

5.2.1.1 Data analysis

Due to the large hydrogen incoherent scattering cross-section, the experiments almost exclusively probe hydrogen dynamics. As written above (eq. 2.69), in the incoherent approximation and for independent motions, the scattering function $S(Q,\omega)$ can be written as:

$$S(Q,\omega) = S_{\mathrm{trans}}(Q,\omega) \otimes S_{\mathrm{rot}}(Q,\omega) \otimes S_{\mathrm{vib}}(Q,\omega)\,, \tag{5.2}$$

where S_{trans}, S_{rot} and S_{vib} are the scattering functions of translational diffusion, rotational diffusion and vibrational motions, respectively. The measured intensity is related to the scattering function via a convolution with the instrument resolution function $\mathrm{Res}(Q,\omega)$. For the experimental data shown above, we suppose a combination of rotational and vibrational reorientations (i.e. no translational diffusion).

The scattering function of jump rotational processes ($S_{\rm rot}(Q,\omega)$) and vibrational scattering ($S_{\rm vib}(Q,\omega)$) are described in eqs. 2.49 and 2.56. The inelastic peaks are modelled with a damped harmonic oscillator. At low temperature, the jump rotational diffusion can be hindered, and therefore eq. 2.77 is used. Data are analysed considering both rotational and vibrational contributions, and therefore, the total scattering function is the convolution of the respective scattering functions. The derivation is done in section 2.1.2.3 and the expression of EISF and QISFs are given:

$$\begin{aligned}
\mathrm{EISF}^{\rm hind} &= D(Q)\left[p+(1-p)\,A_0(Q)\right] && (5.3)\\
\mathrm{QISF}^{\rm hind}_{L_1} &= D(Q)\left[1-A_0(Q)\right](1-p) && (5.4)\\
\mathrm{QISF}^{\rm hind}_{\mathrm{S}^{\rm inel}_{\rm vib}} &= A_0(Q)\left[1-D(Q)\right](1-p) && (5.5)\\
\mathrm{QISF}^{\rm hind}_{\mathrm{S}^{\rm inel}_{\rm vib}\otimes L_1} &= \left[1-A_0(Q)\right]\left[1-D(Q)\right](1-p)\,, && (5.6)
\end{aligned}$$

where $A_0(Q)$ is the EISF of the jump rotational dynamics and $D(Q)$ is the Debye-Waller factor. In case there are any "hindered motions", the parameter p is set to $p=0$, and the above expressions become:

$$\begin{aligned}
\mathrm{EISF} &= A_0(Q)D(Q) && (5.7)\\
\mathrm{QISF}_{L_1} &= D(Q)\left[1-A_0(Q)\right] && (5.8)\\
\mathrm{QISF}_{\mathrm{S}^{\rm inel}_{\rm vib}} &= A_0(Q)\left[1-D(Q)\right] && (5.9)\\
\mathrm{QISF}_{\mathrm{S}^{\rm inel}_{\rm vib}\otimes L_1} &= \left[1-A_0(Q)\right]\left[1-D(Q)\right]. && (5.10)
\end{aligned}$$

In order to discriminate different reorientational motions, the EISF and the QISFs can be calculated and evaluated from the fraction of elastically, quasi-elastically and inelastic scattered neutrons,

$$\mathrm{EISF}\,(Q)=\frac{I_{\rm el}(Q)}{I_{\rm el}(Q)+I_{\rm QE}(Q)+I_{\rm inel}(Q)} \qquad (5.11)$$

and

$$\mathrm{QISF}_{\rm QE/Vib}\,(Q)=\frac{I_{\rm QE/Inel}(Q)}{I_{\rm el}(Q)+I_{\rm QE}(Q)+I_{\rm inel}(Q)}. \qquad (5.12)$$

For purely rotational reorientations of the tetrahedra [BH_4], in $Mg(BH_4)_2$, around the C_2 or C_3 symmetry axis (see fig. 5.8), the factor $A_0(Q)$ is given by (in the powder average):

$$A_0\,(Q)_{\rm C_2/C_3}=\frac{1}{2}\left[1+j_0\left(\frac{2\sqrt{2}}{\sqrt{3}}\,Qr\right)\right], \qquad (5.13)$$

where $j_0(x)=\sin(x)/x$ is the zeroth-order spherical Bessel function and $r=d_{\rm B\text{–}H}$ is the bond length between boron and hydrogen atoms. For tumbling motions, among the hydrogen atoms, the EISF is

$$A_0\,(Q)_{\rm tumb}=\frac{1}{4}\left[1+3j_0\left(\frac{2\sqrt{2}}{\sqrt{3}}\,Qr\right)\right]. \qquad (5.14)$$

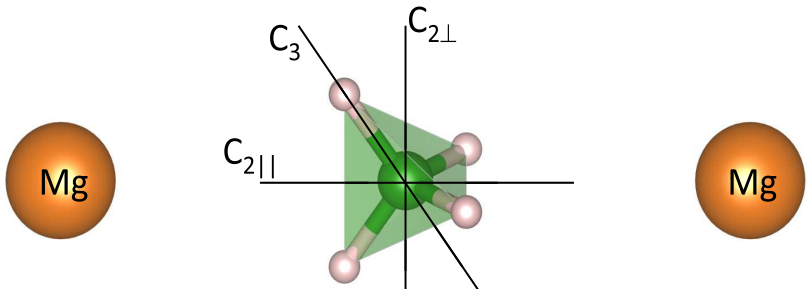

Figure 5.8: Idealized configuration of the [BH_4] units in the Mg environment. The [BH_4] unit lies almost in the line between two Mg atoms in a linear configuration. The three rotation axis are shown: the 3-fold 120° rotation axis C_3, and the 2-fold 180° rotation axes ($C_{2||}$ and $C_{2\perp}$). (large orange sphere) magnesium, (green spheres) boron, (small grey spheres) hydrogen.

Isotropic rotational diffusion is a reorientation mechanism that is not preserving the crystallographic symmetry of the tetrahedron. In fact, hydrogen atoms are visiting the surface of a sphere of radius $d_{\mathrm{B-H}}$ and the EISF results in

$$A_0(Q)_{\mathrm{iso}} = j_0^2(Qr). \tag{5.15}$$

All these models can be applied to identify and discriminate the reorientation mechanism. During the fit procedure, it is found that the spectra can well be described by the sum of the elastic contribution, a quasi-elastic single Lorentzian and a vibrational contribution (for details see table 4.1). The scattering intensities relative to $S^{\mathrm{inel}}_{\mathrm{vib}}(\omega)$ and $S^{\mathrm{inel}}_{\mathrm{vib}}(\omega) \otimes L(\omega)$ (i.e. $\mathrm{QISF}^{(\mathrm{hind})}_{\mathrm{S^{inel}_{vib}}}$ and $\mathrm{QISF}^{(\mathrm{hind})}_{\mathrm{S^{inel}_{vib}} \otimes L_1}$) could not be separated experimentally, and thus were summed to yield the following normalized intensities:

$$\begin{aligned} \mathrm{EISF} &= D(Q)\,[p + (1-p)\,A_0(Q)] && (5.16)\\ \mathrm{QISF}_{L_1} &= D(Q)\,(1-p)\,[1 - A_0(Q)] && (5.17)\\ \mathrm{QISF}_{\mathrm{Vib}} &= 1 - D(Q) && (5.18) \end{aligned}$$

These quantities describe the EISF and QISFs, and they are measured experimentally.
The data analysis will be split in two parts: data taken at longer time scale, and data at shorter time scale.

Data Analysis at $\lambda = 6$ Å In the analysis of measurements performed at $\lambda = 6$ Å, spectra are fitted up to 2 meV. As shown above, the vibrational contributions are separated from the quasi-elastic region and the scattering intensity is described as a sum of the scattering function $S_{\mathrm{rot}}(Q,\omega)$ (eq. 2.56) convoluted with the resolution function $\mathrm{Res}(Q,\omega)$ and a flat background $b(Q)$. The latter term takes into account vibrations, which time scales are much shorter than the time scale set by the instrumental energy resolution, thus resulting in a flat

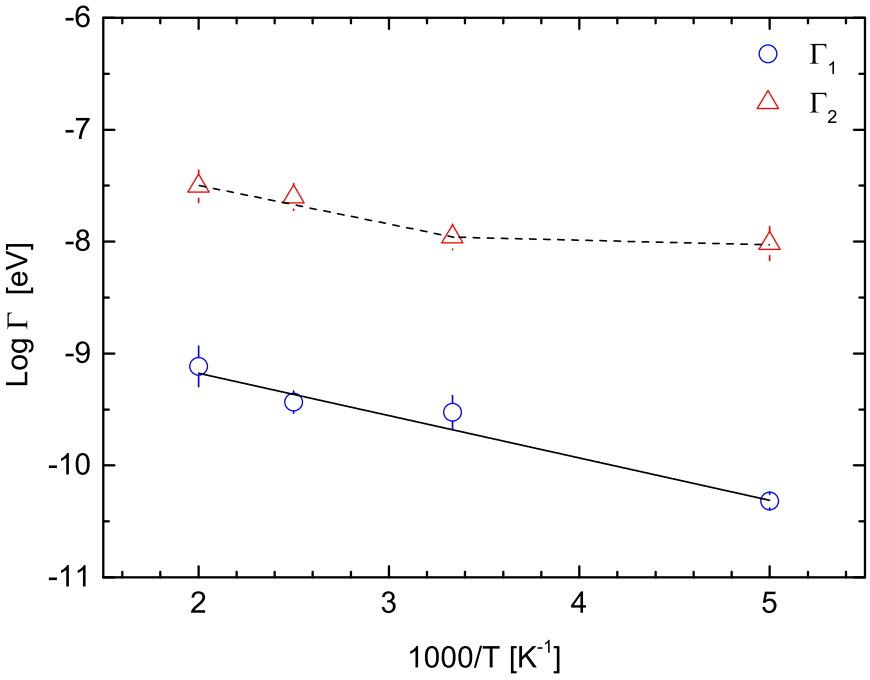

Figure 5.9: Widths Γ_1 (blue circles) and Γ_2 (red triangles) on a logarithmic scale measured at 6 Å, as function of the inverse temperature T. Γ_1 values are fitted with an Arrhenius function $\Gamma = \Gamma_0 \exp(-E_a/k_B T)$. The dashed line (guide to the eye) shows different slopes, indicating a transition phase of the faster motion Γ_2. Vertical error bars denote $\pm 1\sigma$.

background under the quasi-elastic signal.

$$S_{\text{meas}}(Q,\omega) = S_{\text{rot}}(Q,\omega) \otimes \text{Res}(Q,\omega) + b(Q) \tag{5.19}$$

In all fit functions, the correct dependence of the detailed balance factor was taken into account.

At 100 K, data do not show any quasi-elastic broadening and the increased intensity is mainly due to the vibrational dynamics increasing with temperature. At $T \geq 200\,\text{K}$, data show a clear quasi-elastic component and two Lorentzians in eq. 2.56 are necessary to describe the experimental points: the first one, with a Half Width Half Maximum (HWHM) $\Gamma_1 < 0.1\,\text{meV}$ and a second, broader one with a $\Gamma_2 > 0.3\,\text{meV}$. Both Lorentzians widths, Γ_1 and Γ_2, do not show any Q–dispersion, meaning that both are describing localized motions in space. However, the widths are increasing with temperature, indicating thermally activated motions localized in space [107, 112].

Figure 5.9 shows Γ_1 and Γ_2 as a function of the inverse temperature (on a logarithmic scale), together with the fit of the Arrhenius law:

$$\Gamma = \Gamma_0 \exp\left(-\frac{E_a}{k_B T}\right), \tag{5.20}$$

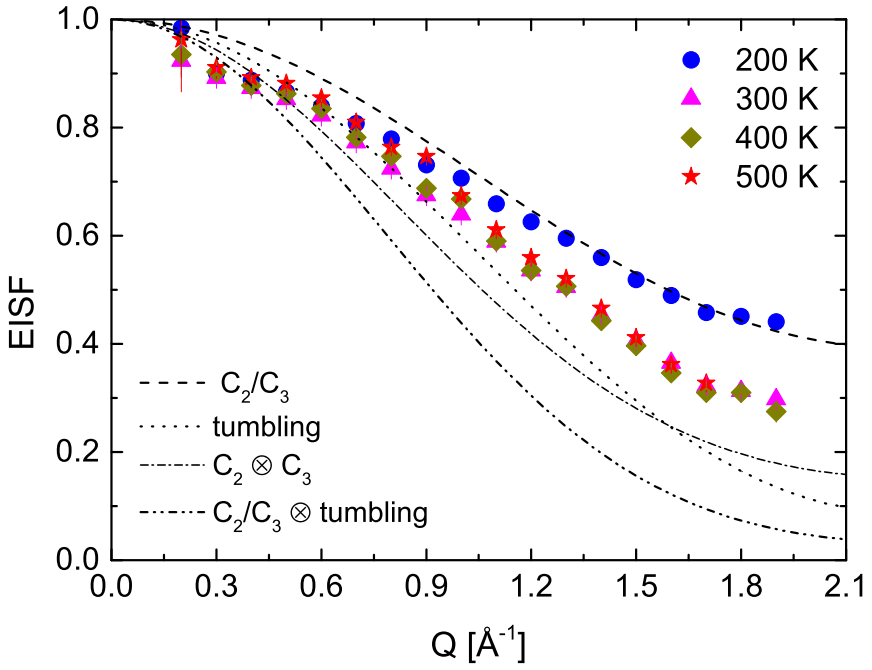

Figure 5.10: Measured EISFs at 6 Å: (blue circles) 200 K, (magenta triangles) 300 K, (yellow rhombus) 400 K, (red stars) 500 K. The dashed line represents the rotational diffusion model for C_2/C_3 rotations (eq. 5.13), whereas the dotted line represents the tumbling motions, according to eq. 5.14. The dashed-dot line is a combination of the C_2 and C_3 rotations, the dashed-dot-dot line is a combination of C_2/C_3 rotation with tumbling motions (see text for details). Is it noticeable the deviation at temperatures above 300 K from simply theoretical EISF models. Vertical error bars denote $\pm 1\sigma$.

where Γ_0 is a pre-factor, E_a is the apparent activation energy, T is temperature and k_B is the Boltzmann constant. The slower process Γ_1 shows a characteristic time scale of 5-20 ps, with an apparent activation energy of $E_a = 32 \pm 3$ meV and $\Gamma_0 = 0.22 \pm 0.03$ meV. As shown in fig. 5.9, there is an indication of a transition in the functional dependence of Γ_2 around 300 K. The shown dashed line is a guide to the eye, only. For this reason we do not attribute a single Arrhenius activation energy over the entire temperature range.

The elastic incoherent structure factor (EISF) was calculated using eq. 5.11, and the results are plotted fig. 5.10. The theoretically expected curves form of the EISF for rotations around the C_2/C_3 axis and tumbling motions are also shown. At 300 K and above, the EISF is independent on the temperature, indicating that the spatial distribution of the hydrogen atoms does not change in the probed time- and space window, however the increasing $\Gamma_{1,2}$ confirm that reorientation processes become faster with increasing temperature. The functional Q-dependence will be discussed later, in connection with the results obtained in 2.5 Å-measurements.

T [K]	$\mathbf{\Gamma}_1$ [meV]	$\mathbf{\Gamma}_2$ [meV]
100	-	-
200	0.033 ± 0.002	0.33 ± 0.05
300	0.073 ± 0.011	0.35 ± 0.04
400	0.08 ± 0.008	0.50 ± 0.06
500	0.11 ± 0.02	0.55 ± 0.08

Table 5.1: Table summarizing the widths Γ_1 and Γ_2 used to describe the data at 6 Å and at different temperatures. In addition, a $\delta(\omega)$ is used for fitting the elastic contribution at all temperatures. Data at 100 K show no quasielastic signals.

Data Analysis at $\lambda = 2.5$ Å Analysis of the data obtained at $\lambda = 2.5$ Å (see fig. 5.5) is more complex due to the observed distinct inelastic contributions close to the quasi-elastic region. A proper separation of quasi-elastic and inelastic signal is not possible, as shown in the previous section.
Spectra are described using the functions listed in table 5.2 to represent the elastic, quasi-elastic and vibrational contributions, and the results of the fits are shown in fig. 5.11 and 5.12. In the instrumental resolution function measured at 11 K (see fig. 5.5), the inelastic excitation appears in the energy-loss side of the neutron and therefore only the central peak is used as a resolution $\mathrm{Res}(Q, \omega)$ in eq. 5.2.
At 100 and 200 K, data show clearly inelastic peaks close, but still separated from the quasi-elastic region. The vibrational part is modelled by a damped harmonic oscillator (eq. 2.49) and the jump rotational part according to eq. 2.56. The starting values of the jump rotational part are taken from the 6 Å data (Γ_2) and fitted in the spectra. The values found are in agreement with 6 Å data, within 10% variation.
Above 300 K, data are do not show any distinct inelastic peaks. Most probably, a transition from an under-damped harmonic oscillator to an over-damped one took place. The scattering function of an over-damped DHO is indistinguishable from a Lorentzian shape function within the measured energy transfer range. Therefore, the inelastic contribution is described by a Lorentzian L_3, characterized by a HWHM Γ_3, distinct from the damping parameter Γ_q. Data are shown in fig. 5.12, and the damping parameter Γ_q and HWHM Γ_3 in fig. 5.13.

The quantity ω_q represents the frequency characteristic of individual $[BH_4]$, since we probe the incoherent scattering cross section of hydrogen. Given the structure of β-$Mg(BH_4)_2$, there are five different crystallographic positions of the $[BH_4]$ tetrahedron. Apparently, the lattice potentials of the crystallographic positions are very similar to each other, yielding to inelastic distinct peaks. Inelastic neutron scattering (INS) measurements on β-$Mg(BH_4)_2$ show a complex vibrational structure extending over a wide range of energies [96] . A structured low-energy band (between 3 and 38 meV) was reported and it was tentatively

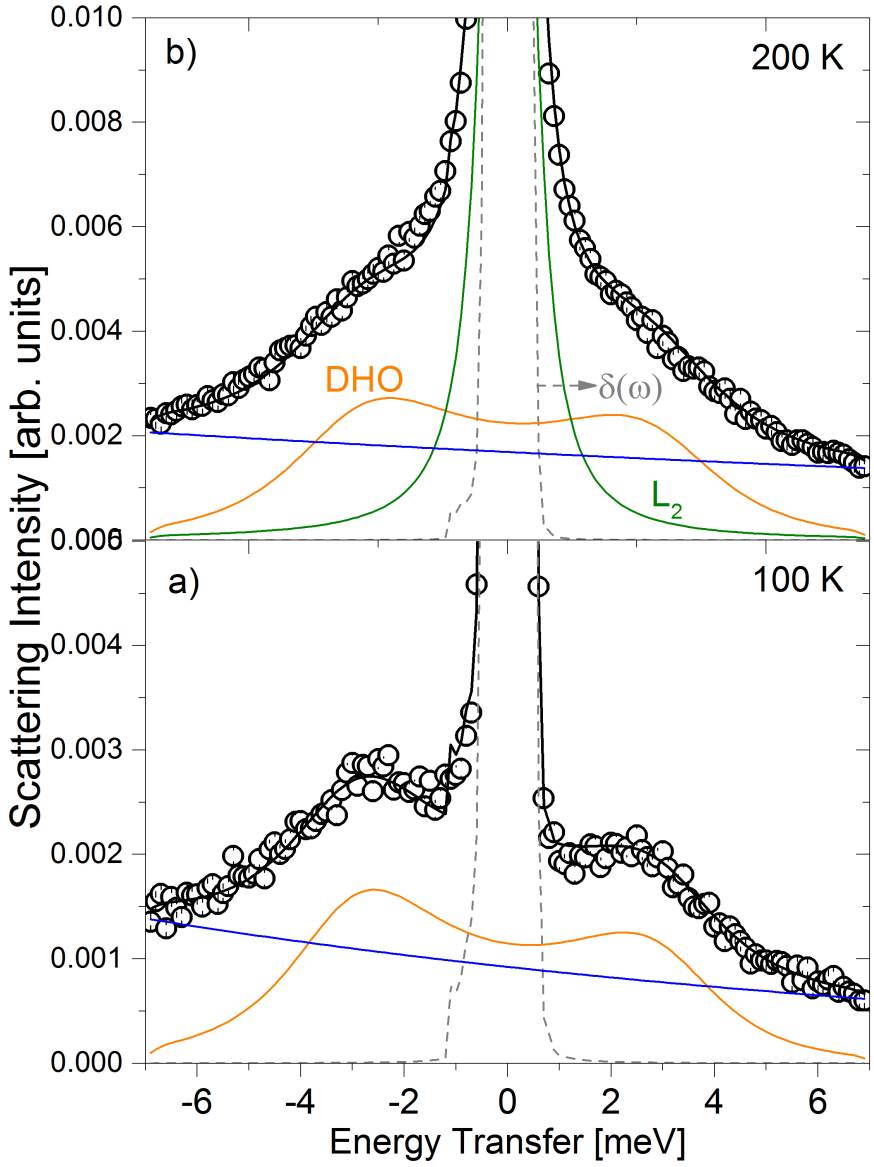

Figure 5.11: $S(Q,\omega)$ of β-$Mg(BH_4)_2$ measured at $Q = 2.1\,\text{Å}^{-1}$ at a) 100 K, and b) 200 K. Solid black lines represent the fit. In a) data are successfully described by a DHO (orange) and a background (blue) that takes into account faster vibrations. In b) data are described by a DHO, a single Lorentzian (dark green) and a background.

T [K]	**Fit functions**
100	δ + DHO + background
200	$\delta + L_2$ + DHO + background
$>$ 300 K	$\delta + L_2 + L_3$

Table 5.2: Table summarizing the fit functions used to describe data at $\lambda = 2.5$ Å at different temperatures: a δ-function is used for fitting the elastic contribution, a DHO is used to model the inelastic peaks, a background is used to model fast vibrational dynamics outside the set timescale, L_2 and L_3 represent the quasi-elastic contribution and the over-damped harmonic oscillator, respectively.

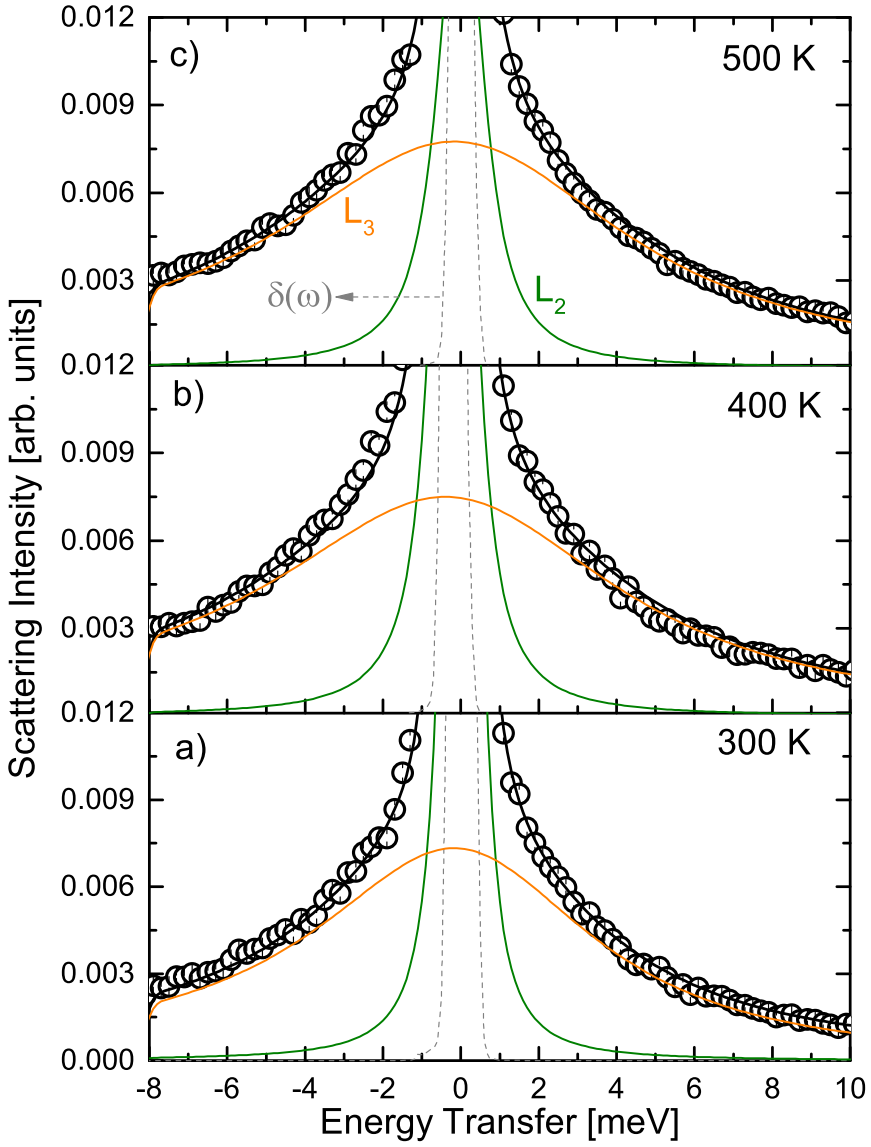

Figure 5.12: $S(Q,\omega)$ of β-$Mg(BH_4)_2$ measured at $Q = 2.1\,\text{Å}^{-1}$ at 300 (a), 400 K (b), 500 K (c). Solid black lines represent the fit. Data are described by two Lorentzians: Γ_2 (dark green) and Γ_3 (orange). The vertical error bars denote $\pm 1\sigma$.

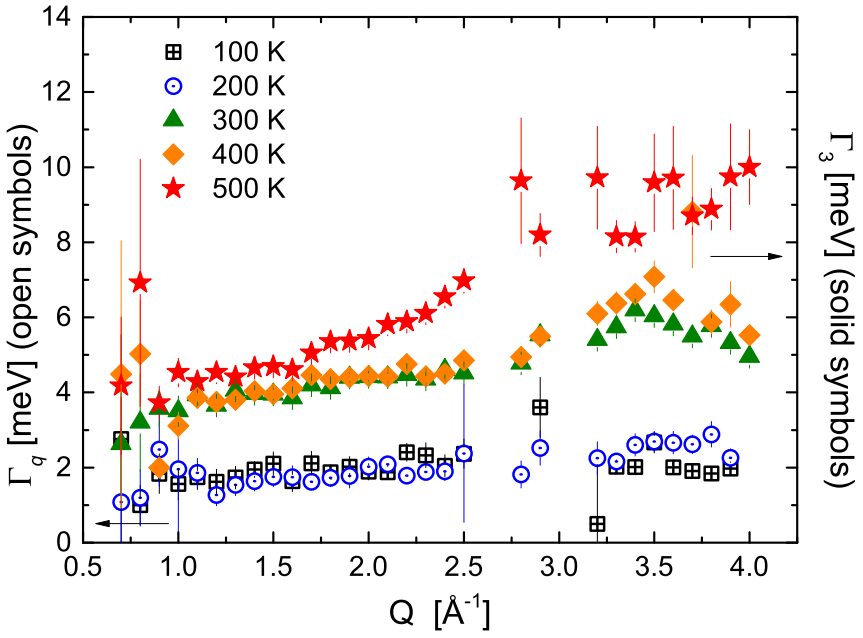

Figure 5.13: Damping Γ_q (open symbols) and HWHM Γ_3 (solid symbols) at different temperatures. On the left y-axis: (open black square) 100 K, (open blue circle) 200 K. On the right y-axis: (solid green triangle) 300 K, (solid yellow rhombus) 400 K, (solid red star) 500 K

assigned to lattice phonons. The inelastic peaks detected in this work around $\pm 3.2\,\mathrm{meV}$ are in agreement with this previous study, and thus confirming a superposition of vibrational and quasi elastic signal at low energy transfers. At higher temperatures, the vibrational diffusion becomes over-damped and it is described in our analysis by L_3. Vibrational and rotational reorientations occur on similar time scales: the characteristic frequency extracted for vibration is $\nu_{\mathrm{vib}} \sim 0.8\,\mathrm{ps}^{-1}$, which is in the same order of magnitude as rotational frequency τ_{rot}^{-1} from Γ_2.

The EISF, $\mathrm{QISF}_{\mathrm{QE}}$ and $\mathrm{QISF}_{\mathrm{Inel}}$ are calculated from the elastic, quasi-elastic and inelastic intensities, normalized to the total intensity. Results are summarized in fig. 5.14. With increasing temperature, the fraction of elastically scattered neutrons (EISF) decreases, but no oscillating behaviour characteristic of rotational reorientations around the C_2 or C_3 axis is observed. This is expected since no separation of vibrational and rotational parts is done. The solid lines in fig. 5.14 are a global fit (at each temperature) to eqs. 5.16-5.18 to extract the parameters $\langle u^2 \rangle$, p and $d_{\mathrm{B\text{-}H}}$. Due to the structureless behaviour at relatively high Q of the EISF, this information can not be obtained from the fraction of the elastically scattered neutrons alone, but the global fit procedure was necessary. For the data analysis, the quasi-elastic component is assumed to be described by C_2/C_3 reorientation (see eq. 5.13), in agreement with low temperature data collected at 6 Å and with the previously proposed reorientational mechanisms [99].

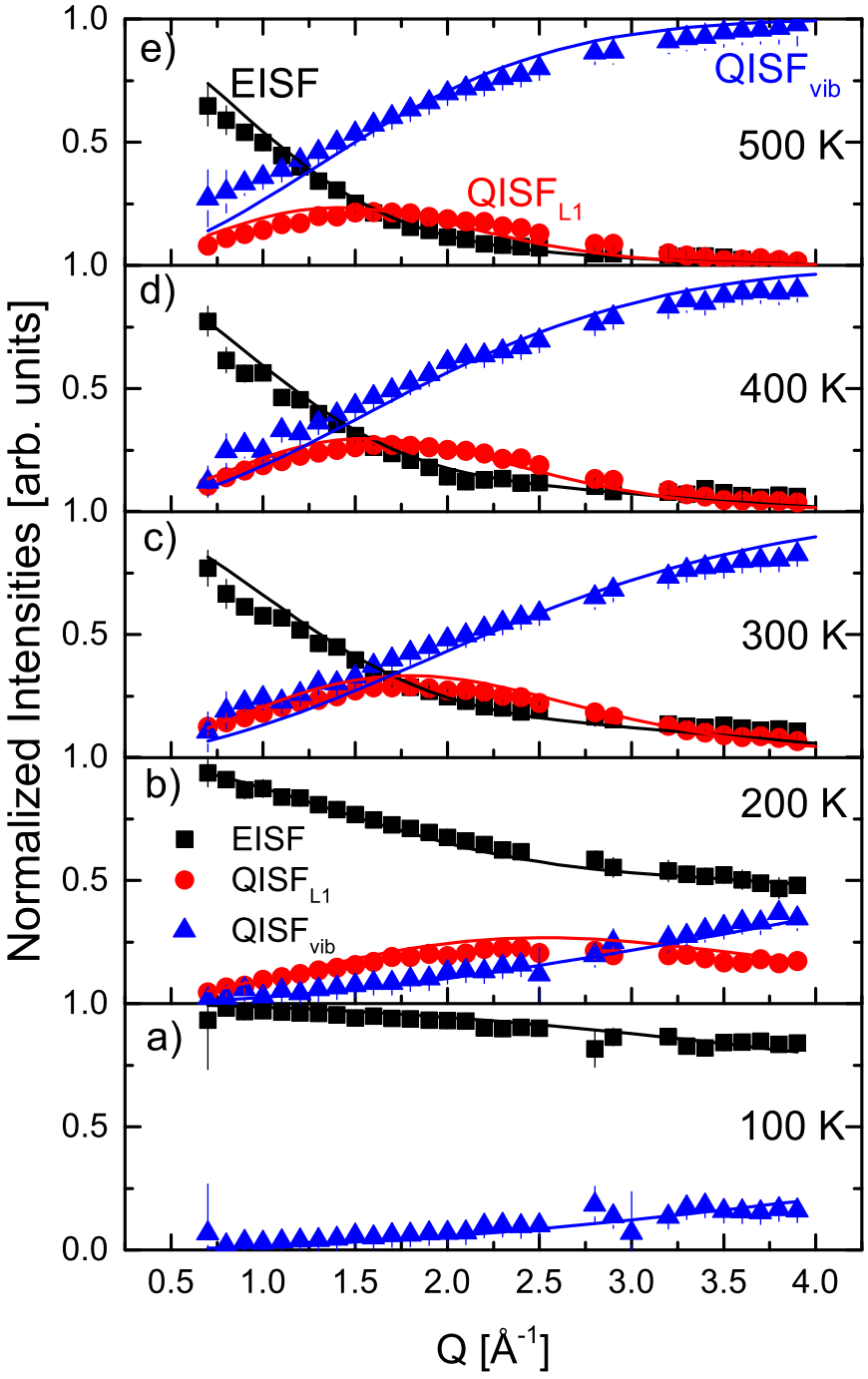

Figure 5.14: β-$Mg(BH_4)_2$: EISF (black squares), $QISF_{Vib}$ (blue triangles), $QISF_{L_1}$ (red circles) from 100 K to 500 K. Solid lines represent the fit to the data according to eqs.5.16-5.18. In a) 100 K, b) 200 K, c) 300 K, d) 400 K and e) 500 K. Vertical error bars denote $\pm 1\sigma$.

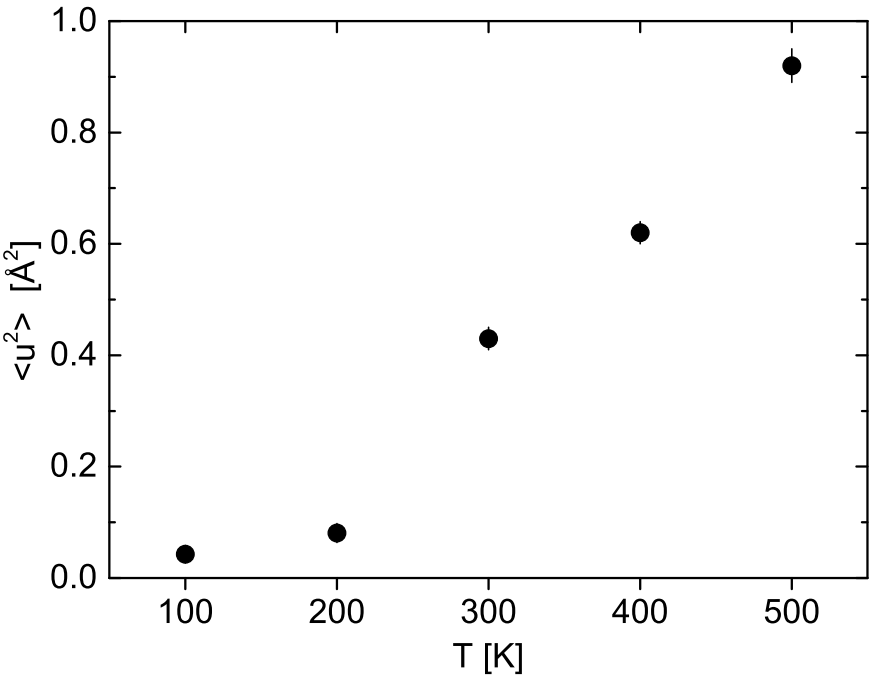

Figure 5.15: β-$Mg(BH_4)_2$: Mean square displacement $\langle u^2 \rangle$ as a function of temperature.

The agreement with the experimental data is quite satisfactory, confirming that the chosen approach for the analysis of the data allows us to extract the rotational and vibrational parts. The mean square displacement (MSD) $\langle u^2 \rangle$ and $d_{\text{B-H}}$ are show in figures 5.15 and 5.16.

5.2.1.2 Discussion

Previously, Blanchard *et al.* [99] reported three thermally activated processes in β-$Mg(BH_4)_2$ with activation energies: 39 ± 0.5, 76 ± 5 and 214 ± 4 meV from QENS data in the observation timescale of hundreds of picoseconds. In their work, the faster jump process with the lowest activation energy was attributed to the rotation around the $C_{2||}$ axis, energetically more favourable because of the BH_4 bidentate configuration with respect to the Mg ions, although its weight was rather low (15% of the QENS intensity). NMR measurements on β-$Mg(BH)_2$ [98] do not show discrete activation energies, but a broad distribution, centred around 138 ± 5 meV with a distribution width of $\Delta E_a = 36 \pm 3$ meV.
In this thesis, at longer timescales (up to ~ 16 ps, 6 Å-measurement), two reorientational processes with different time constants are detected. For the slower one, the activation energy is calculated to be $E_a = 32 \pm 1$ meV and $\Gamma_0 = 0.22 \pm 0.03$ meV, in a reasonable agreement with previous QENS and DFT calculations [99]. It is tentatively assigned to a $C_{2||}$ reorientation, energetically more favourable with respect to C_3 rotations due to the bidentate configuration between Mg and H atoms 5.8. The other process is one order of magnitude faster ($\tau^{-1} \sim 0.5 - 1$ ps^{-1}), but it shows a discontinuity around 300 K and therefore its

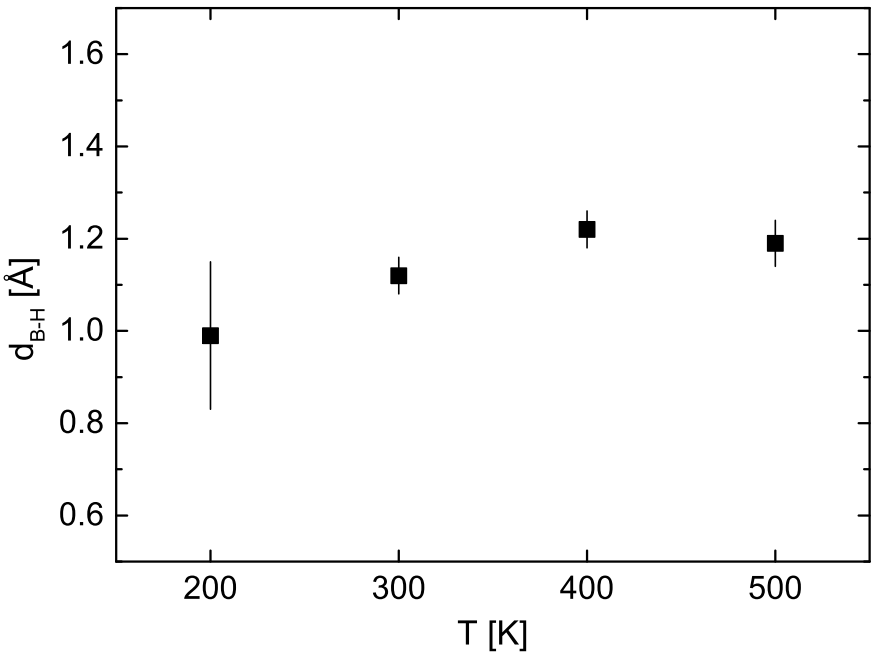

Figure 5.16: β-$Mg(BH_4)_2$: Distance between boron and hydrogen atoms as a function of temperature.

activation energy is not determined. Γ_2 is also of rotational origin, but its temperature dependence most likely reflects the transition in the vibrational part.
This transition is also visible in the EISF, where, for temperatures above 200 K, the deviation from simple reorientational motions (like C_2/C_3 rotations) becomes significant (see fig. 5.10). Other reorientation processes (like tumbling motions (eq. 5.14)) or other combinations (convolution between C_2 and C_3 rotations, or between C_2 and tumbling motions) also do not describe the measured EISF obtained at 6 Å.
Similarly, in the same temperature range, the data measured at $\lambda = 2.5$ Å show the transition from an under-damped (observed at 100 K and 200 K) to the over-damped harmonic oscillator regime (above 300 K). The damping Γ_q and the HWHM Γ_3 are plotted in fig. 5.13. At 300 K and above, the vibrational inelastic scattering overlaps with the quasi-elastic region, therefore the EISF reflects the merging of the two contributions, and a clear separation is not possible during data analysis.
The transition from the under-damped to the over-damped DHO is also reflected in the parameters extracted from the data analysis. The mean square displacement shows a step like increase from 200 K to 300 K and above (fig. 5.15). The large values of $\langle u^2 \rangle$ (fig. 5.15) differ from the harmonic contribution U_{vib} that are estimated at the beginning of this section. U_{vib} characterizes fast vibrations of single nuclei around their lattice position (Debye-Waller factor), whereas $\langle u^2 \rangle$ it is tentatively attributed to confined vibrational modes that originate from movements of the entire $[BH_4]$ units around their equilibrium position. Therefore, the MSD $\langle u^2 \rangle$ describes in first approximation, the sum of contributions of localized atom vibra-

tions and a phonon band vibrations of the host lattice. For the lattice term, it is supposed that the hydrogen atoms follow the motions of the host lattice atoms [112].

The rotational part, described by $L_2(Q,\omega)$, is detected at 200 K and above. The scattering intensity follows eq. 5.17, as shown in fig. 5.14. At 200 K, only a fraction $1-p$, with $p = 0.47 \pm 0.08$, undergoes reorientational motions, whereas at higher temperature, all BH_4 reorient and therefore in the eqs. 5.16-5.17, $p = 0$. The distances extracted are in the range of the crystallographic values measured with X-ray and neutron diffraction (fig. 5.16). From the analysis, we could assign the quasi-elastic rotational component to a C_2 reorientation mechanism.

From the analysis of the 2.5 Å data, it became obvious that vibrational modes contribute significantly to the observed intensities at low energy transfers. However, since the 6 Å data are sensitive to longer time scales, it can be expected that $\langle u^2 \rangle$ has different values. Similarly, it is supposed that the analysis of 6 Å data, especially the functional dependence of the EISF at 300 K and above, reflects the overlap of vibrational intensity with the quasi-elastic region. The limited momentum transfer Q available in the 6 Å measurements makes the analysis of the EISF and QISFs quite harsh and is therefore not attempted.

Hydrogen dynamics has been studied in several borohydride compounds in order to elucidate the connection of crystal structure and dynamics. In alkali borohydrides, like $LiBH_4$ [131, 132], $NaBH_4$ and KBH_4 [104, 133], the rotational reorientation correlated with a crystal structure transition from an ordered (low-temperature) to a disordered (high-temperature) crystal phase. In $NaBH_4$ and $LiBH_4$, hydrogen motions become faster as soon the disordered state is reached. In the disordered phase of KBH_4, the hydrogen reorientation (jump rotation around the C_4 axis) is similar to the one found in $NaBH_4$. In $LiBH_4$, the $[BH_4]$ dynamics changes from an C_3 reorientation mechanism to a disordered reorientational model involving all four H atoms, as soon as the structural transition from orthorhombic (LT) to hexagonal (HT) is approached [127]. Another mechanism in the crystal structure transition is found in $Ca(BH_4)_2$ [134], which is mainly driven by librations. Internal vibrations strongly affect the free energy, and therefore drive the crystal phase transition.
In this work, in β-$Mg(BH_4)_2$ it is observed a transition in the $[BH_4]$ dynamics, between 200 and 300 K: in the rotational part, at 300 K all $[BH_4]$ units take part in the reorientation while only hindered rotations are observed at 200 K. Additionally, a transition from under-damped to over-damped DHO is observed in that temperature range. The change in dynamics seems not to be connected to any structural phase transition. However, a study on β-$Mg(BH_4)_2$ [135] showed highly anisotropic, non-uniform thermal expansion of the lattice. Especially, the b-lattice parameter showed a maximum around 275 K, while for the a-lattice parameter

a minimum value at approximately 200 K was observed. Moreover, the authors found that the refined atomic displacements did not detectably decreased with lower temperature. Our findings suggest a strong correlation between BH_4 dynamics and the structural environment. The partial covalent character of β-$Mg(BH_4)_2$ appears to be connected with the crystal vibrational dynamics, in an intermediate position between ionic bonded borohydrides ($LiBH_4$ and $NaBH_4$) to the more covalently bonded $Ca(BH_4)_2$.

5.2.1.3 Conclusions

In this work, QENS experiments were performed on $\beta-Mg(BH_4)_2$ probing two different time scales in order to explore the hydrogen dynamics, and in particular possible reorientations of the $[BH_4]$ units. At longer time scale (up to 16 ps, 6 Å), two different rotation motions are detected. The slower one has an apparent activation energy of 32 ± 3 meV. The second reorientation motion is also assigned to a rotational reorientation around $C_{2||}$ or $C_{2\perp}$, however its temperature dependence is influenced by the underlying vibrations as it became obvious from the investigations at faster observation times. Below 300 K, a distinct DHO signal appears in the measured data whereas at 300 K and above, it overlaps with the quasi-elastic signal. A transition from an under-damped to an over-damped regime is plausible. This transition in the scattering intensity strongly affects the EISF, $QISF_{QE}$ and $QISF_{Vib}$ and the vibrational and rotational motions could only be separated in a global fitting approach. From the experimental results, on both time scales, no long range diffusion of the $[BH_4]$ units is detected. In conclusion, the whole hydrogen dynamics in the picosecond time scale is dominated by both local rotational and vibrational reorientations occurring on similar time scales.

5.2.2 $\alpha-Mg(BH_4)_2$

Data collected at $\lambda = 2.5$ Å and $\lambda = 6$ Å are shown in figs. 5.17 and 5.18, respectively, and for two values of momentum transfer Q. The sample was heated up to 500 K, where it is known to transform to the β-$Mg(BH_4)_2$ phase.

At longer time scale (6 Å-data), the quasi-elastic signal appears at 200 K and above. The resulting broadening increases as soon the temperature rises. At shorter timescale, inelastic peaks are observed, centred at energy transfer $\Delta E_1 \sim \pm 4.2$ meV and $\Delta E_2 \sim 8$ meV. In the energy loss side, the inelastic peak at ~ -8 meV is not visible due to the limited energy transfer set by the spectrometer.

The inelastic signal is still visible at 400 K. Around 470 K, the sample undergoes the structural phase transition, as shown in the DSC data (fig. 5.1) and, at 500 K, data do now show any inelastic peaks around the elastic line, but looking similar to the scattering data collected on the β phase.

These excitations have not been reported in previous studies of hydrogen dynamics in α-

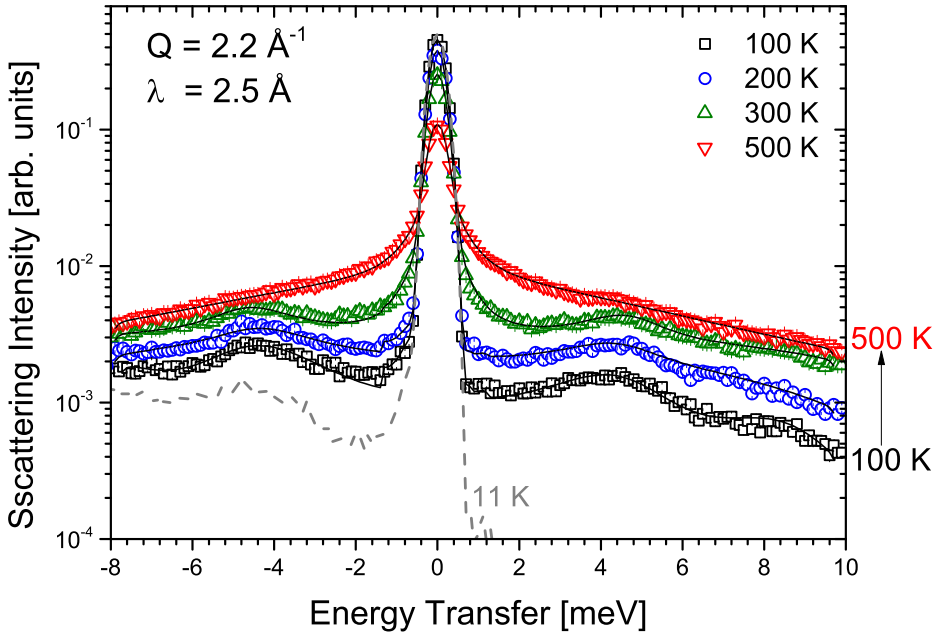

Figure 5.17: $S(Q,\omega)$ of α-$Mg(BH_4)_2$ measured at 2.5 Å and at 11, 100, 200, 400 and 500 K. The solid black lines represent the fit to the data. (gray dashed line) 11 K (resolution), (black squares) 100 K, (blue circle) 200 K, (green up triangles) 400 K and (red down triangles) 500 K. Data sets measured at 400 K have been omitted for clarity.

phase [96, 95]. Although the inelastic signal seems quite separated from the quasi-elastic region around zero energy transfer, the same procedure used in the β-phase is applied [130]. At 100 K, the signal is only originating from inelastic scattering, i.e. low energy vibrational modes. Using this approach, the ratio between low temperature data (where the only scattering is inelastic) and the high temperature data is given by (see eq. 5.1):

$$\frac{S\left(Q,\omega,T\right)}{S\left(Q,\omega,T_0\right)}\frac{\mathrm{e}^{-Q^2U_{\mathrm{Vib}}(T_0)}}{\mathrm{e}^{-Q^2U_{\mathrm{Vib}}(T)}}=\frac{n\left(\omega,T\right)}{n\left(\omega,T_0\right)}\approx\frac{T}{T_0}\left[1+\frac{\hbar\omega}{2k_B}\left(\frac{1}{T_0}-\frac{1}{T}\right)\right]. \tag{5.21}$$

Substituting $T_0 = 100\,\mathrm{K}$, the rescaling procedure for measurements performed at 6 Å and 2.5 Å are shown in figs. 5.19 and 5.20.

At 6 Å and for energy transfer larger than 2 meV, the quasi-elastic signal falls off and data show agreement with the scaling procedure with a vibrational displacement U_{Vib} in eq. 5.21, $U_{\mathrm{Vib}} = 0.0005 \times T[\mathrm{K}]\,\mathrm{Å}^2$.
At 2.5 Å, the agreement with the rescaling procedure is reached at energies greater than 10 meV and in this case the vibrational displacement follows the empirical law $U_{\mathrm{Vib}} = 0.0001 \times T[\mathrm{K}]\,\mathrm{Å}^2$. Based on these findings, data at longer time scale are analysed up to 2 meV, while data at shorter time scale up to 10 meV.

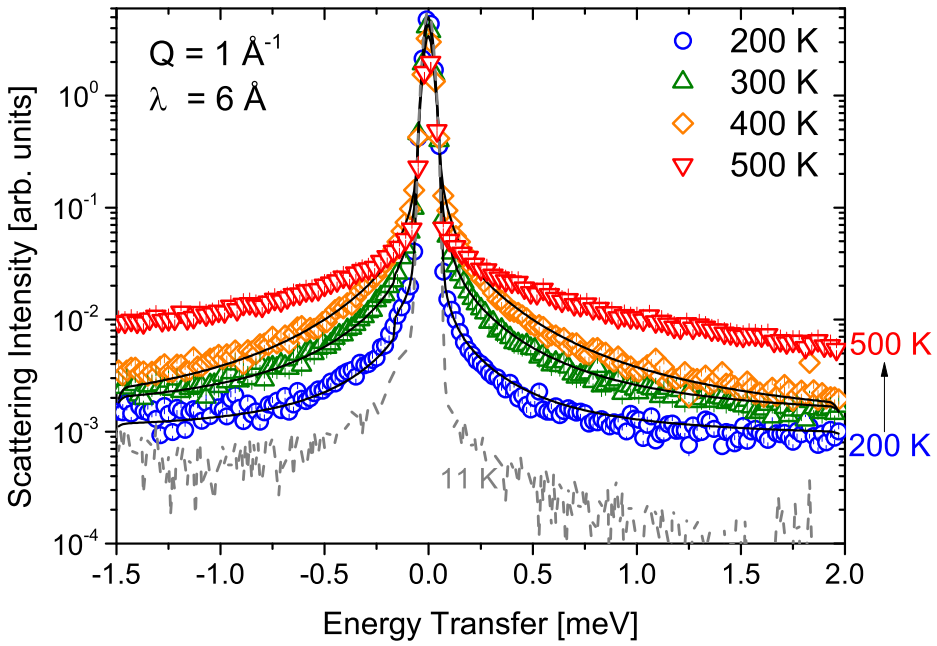

Figure 5.18: $S(Q,\omega)$ of α-$Mg(BH_4)_2$ measured at 6 Å and at 11, 200, 300, 400 and 500 K. The solid black lines represent the fit of the data according to eq. 5.22.

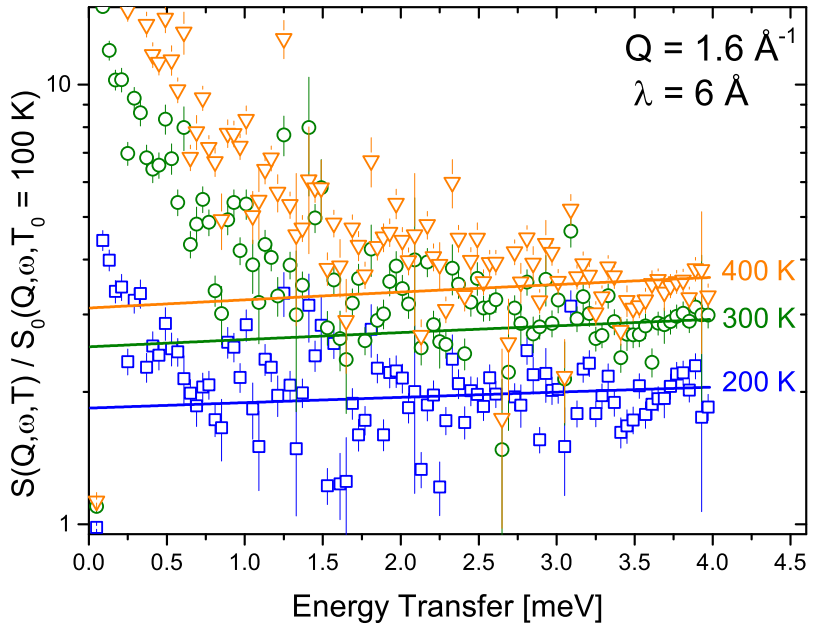

Figure 5.19: α-$Mg(BH_4)_2$: Ratio between high temperature and low temperature data (T_0 = 100K) at $\lambda = 6$ Å: (blue squares) 200 K, (green circles) 300 K, (orange down triangles) 400 K. The lines represent the right hand-side of eq. 5.21, using $U_{\mathrm{Vib}} = 0.0005 \times T[\mathrm{K}]\,\mathrm{Å}^2$.

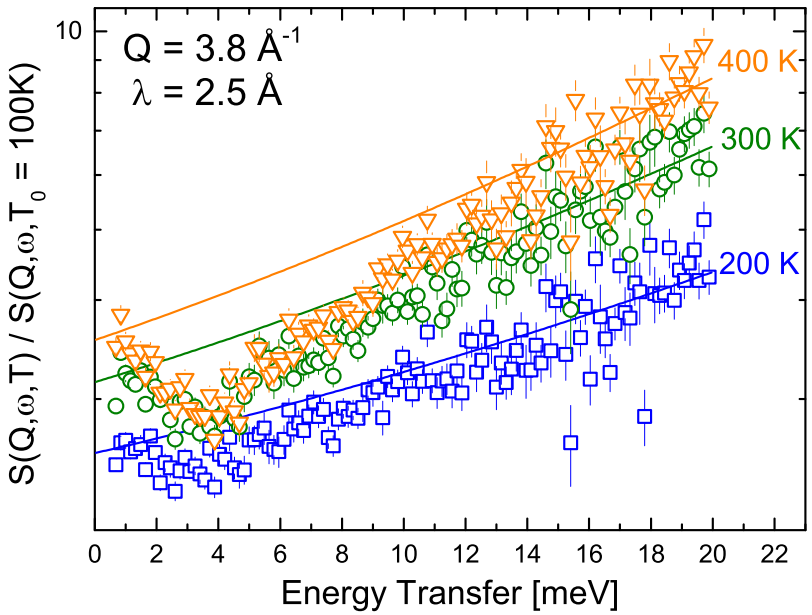

Figure 5.20: α-$Mg(BH_4)_2$: Ratio between high temperature and low temperature data ($T_0 = 100\,\mathrm{K}$) at $\lambda = 2.5\,\text{Å}$: (blue circles) 200 K, (green up triangles) 300 K, (orange rhombus) 400 K. The lines represent the right hand-side of eq. 5.21, using $U_{\mathrm{Vib}} = 0.0001 \times T[\mathrm{K}]\,\text{Å}^2$.

5.2.2.1 Data analysis

Data analysis is split in two parts, according to the observable time scale: data at $\lambda_1 = 6\,\text{Å}$ and data at $\lambda_2 = 2.5\,\text{Å}$.

Data analysis at $\lambda_1 = 6$ Å Data at 6 Å show quasi-elastic signal at 200 K and above, where the intensity is generally increasing as the temperature increases. Data are modelled with an elastic line and a sum of Lorentzians, in order to observe the reorientational dynamics of the $[BH_4]$ tetrahedra. A background $b(Q)$ is introduced to model inelastic scattering resulting from fast reorientations or vibrations, outside the observation time window determined by the instrumental resolution setting.
The scattering function reads:

$$\begin{aligned} S_{\mathrm{tot}}(Q,\omega) &= S_{\mathrm{rot}}(Q,\omega) + b(Q) = \\ &= A_0(Q)\delta(\omega) + \sum_{n>0} A_n(Q) L_n(\Gamma_n,\omega) + b(Q), \end{aligned} \tag{5.22}$$

with the constraint $\sum_{n>0} A_n(Q) = 1 - A_0(Q)$. Fit functions include the detailed balance factor, and results of the fits are shown in fig. 5.21. Data at 500 K are also analysed, in order to highlight possible differences in dynamics in the transition from α- to β-phase. Two quasi-elastic components are detected, characterized from two different half-widths-half-maximum: $L_1(Q,\omega)$ with a HWHM Γ_1, and $L_2(Q,\omega)$ with a HWHM Γ_2. Both widths show

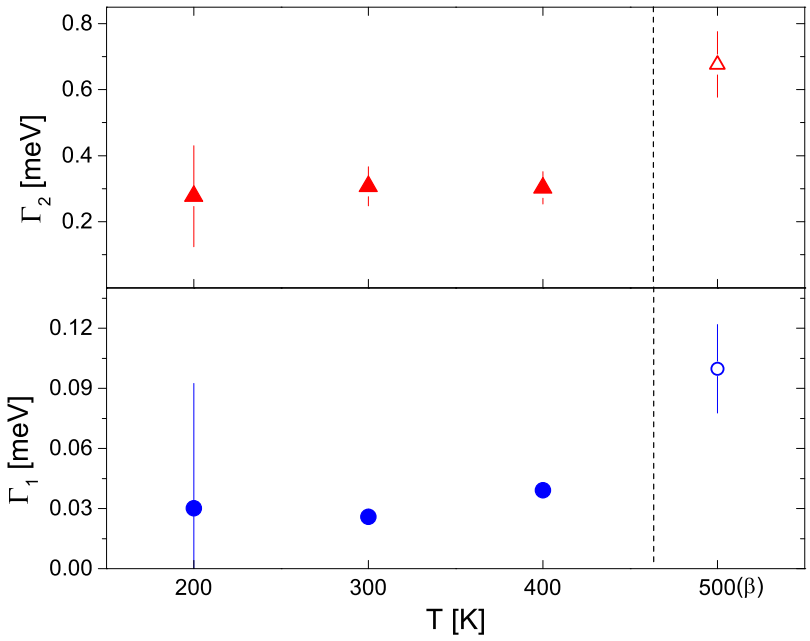

Figure 5.21: α-$Mg(BH_4)_2$: Half widths at half maximum Γ_1 and Γ_2 at different temperatures. (blue circles) Γ_1, (red triangles) Γ_2. The vertical dashed line indicates the crystal phase transition temperature. Above it, the material transforms in the β crystal phase, and therefore empty symbols are used.

any Q-dispersion, indicating a localized reorientational dynamics. Surprisingly, they do not show (within the experimental uncertainty) any temperature dependence. The graphs also contain data taken at 500 K, where the β-phase is reached. Values for Γ_1 and Γ_2 are shown in fig. 5.21 and in table 5.3.

The smaller Lorentzian $L_1(Q,\omega)$ shows a HWHM $\Gamma_1 < 0.04\,\text{meV}$, corresponding to motions in the time scale of $\sim 16\,\text{ps}$. The second Lorentzian shows a HWHM $\Gamma_2 > 0.1\text{meV}$, one order of magnitude larger than Γ_1, and therefore a dynamical process one order of magnitude faster. Plotting data in a logarithmic scale as a function of the inverse of temperature T, it is evident the absence of temperature dependence for both processes (see fig. 5.22).

The elastic and quasi-elastic incoherent structure factors, EISF and QISF respectively, can be calculated from data using eq. 2.59, and results are shown in fig. 5.23. Due to geometry of the $[BH_4]$ units, possible reorientations are rotations around the 2-fold symmetry axes $C_{2||}$ or $C_{2\perp}$, with 180° rotations, rotations around the C_3 symmetry axis (with 120° rotations), or tumbling motions where all H atoms are reorienting. As evident in fig. 5.23, none of the simple rotational motions describes properly the EISF. EISFs at lower temperature deviate from any simple model, indicating that an excess of elastic intensity is dominating. Only data at 400 K seem to be described by a C_2/C_3 rotational diffusion.

As observed for β-$Mg(BH_4)_2$, some of the rotations can be hindered, meaning that not

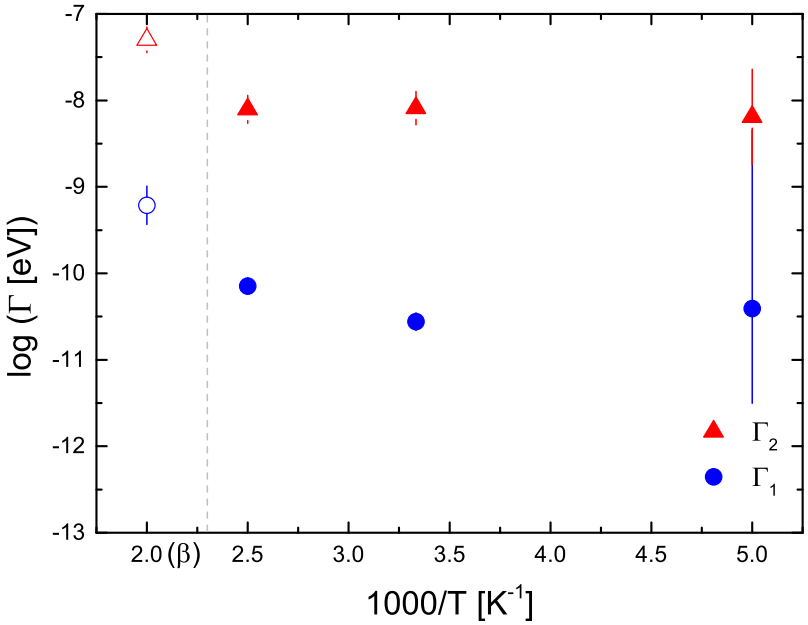

Figure 5.22: α-$Mg(BH_4)_2$: Arrhenius plot of Γ_1 and Γ_2 on a logarithmic scale. (blue circles) Γ_1, (red trainagles) Γ_2. Open symbols are from the β-phase at 500 K. Error bars correspond to $\pm 1\sigma$.

T [K]	$\mathbf{\Gamma}_1$ [meV]	$\mathbf{\Gamma}_2$ [meV]
100	-	-
200	0.030 ± 0.06	0.28 ± 0.15
300	0.026 ± 0.003	0.30 ± 0.06
400	0.039 ± 0.003	0.30 ± 0.05
500	0.100 ± 0.02	0.67 ± 0.1

Table 5.3: Table summarizing half widths at half maximum Γ_1 and Γ_2 obtained from data at 6 Å and different temperatures. In addition, a $\delta(\omega)$ is used for fitting the elastic contributions at all temperatures. Data at 100 K show no quasielastic signals. Uncertainties correspond to $\pm 1\sigma$.

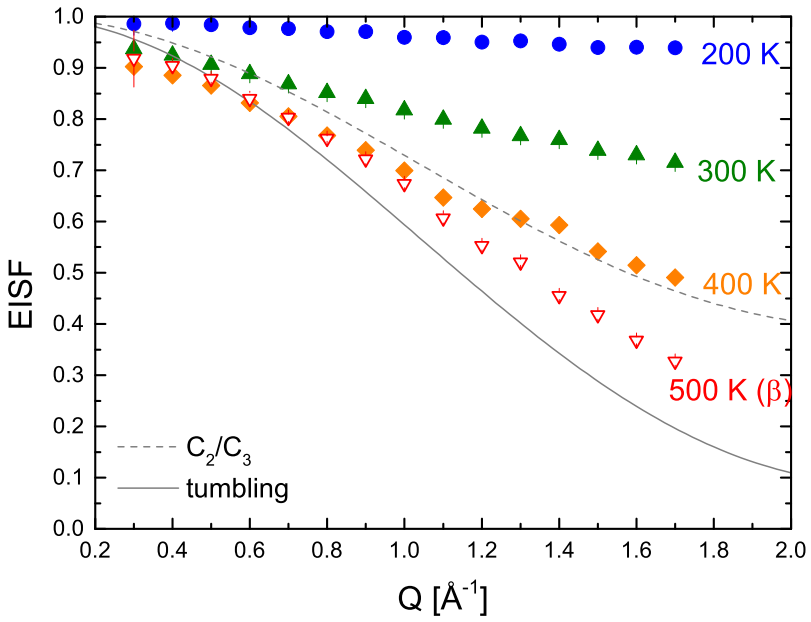

Figure 5.23: Measured EISF of α-$Mg(BH_4)_2$ at 6 Å: blue circles) 200 K, (green triangles) 300 K, (orange rhombus) 400 K, (empty red triangles) 500 K. The dashed line represents the rotational diffusion model for C_2/C_3 rotations (eq. 5.13), continuous line represents the tumbling motions, according to eq. 5.14. In both models, the distance $d_{B\text{-}H}$ is kept fixed to 1.12 Å.

all the $[BH_4]$ units are undergoing rotations. The analysis is done taking into account also the QISFs, in order to better identify the reorientational motions, as shown in fig. 5.24.

In this time scale, two motions are identified by the two Lorentzians used in the data analysis at 200 K and above. The scattering functions are indicated by $S_1(Q,\omega)$ and $S_2(Q,\omega)$. If motions are not well separated in time, a convolution of the two is necessary. A possibility to interpret the EISF would be considering the $[BH_4]$ units undergoing rotational diffusion with rotations around C_2/C_3 at the same time, whereas a fraction is not participating at all. Considering that both rotational dynamics are hindered, the scattering functions are described by:

$$S_1(Q,\omega) = p\delta(\omega) + (1-p)\left[A_0(Q)\delta(\omega) + (1-A_0(Q))L_1(Q,\omega)\right] \tag{5.23}$$

$$S_2(Q,\omega) = k\delta(\omega) + (1-k)\left[B_0(Q)\delta(\omega) + (1-B_0(Q))L_2(Q,\omega)\right] \tag{5.24}$$

Performing the convolution between these two scattering functions, it yields to (the explicit dependence from Q is omitted):

$$\begin{aligned} S(Q,\omega) &= \left[p + (1-p)A_0\right]\left[k + (1-k)B_0\right]\delta(\omega) + & (5.25)\\ &+ (1-p)(1-A_0)\left[k + (1-k)B_0\right]L_1(Q,\omega) + & (5.26)\\ &+ (1-k)(1-B_0)\left[p + (1-p)A_0\right]L_2(Q,\omega) + & (5.27)\\ &+ (1-k)(1-p)(1-A_0)(1-B_0)L_1 \otimes L_2(Q,\omega) & (5.28) \end{aligned}$$

All the factors represent the EISF and the QISFs. Summing up the last two contributions, since they are not experimentally resolved, the normalized intensities read:

$$\text{EISF} = [p + (1-p)A_0]\,[k + (1-k)B_0] \tag{5.29}$$

$$\text{QISF}_{L_1} = (1-p)(1-A_0)\,[k + (1-k)B_0] \tag{5.30}$$

$$\text{QISF}_{L_2} = (1-k)(1-B_0). \tag{5.31}$$

The parameters involved are the fractions p and k, whereas the distance $d_{\text{B-H}}$ is kept constant to the crystallographic value 1.12 Å [78]. It is possible to observe the quite satisfactory agreement at all temperatures. Parameters p and k, obtained from eq.s 5.29-5.31, are plotted in fig. 5.25. As the temperature raises, the fraction of hindered rotations decreases in both motions. At 200 K, only a small fraction of $[BH_4]$ units undergoes rotational motions described by C_2/C_3 rotations. As the temperature increases, these fractions decrease, and the EISF reflects a combination of two rotational motions.
Nevertheless, the limited momentum transfer range does not allow a proper identification of the reorientational motions, and therefore measurements at shorter time scale are performed to extend the Q-range and to confirm the dynamical reorientation of the $[BH_4]$ units.

Data analysis at $\lambda_2 = 2.5$ Å Data at shorter time scale and low temperatures show a strong presence of inelastic scattering. Two inelastic excitations are found in the energy range up to 10 meV, and persist at temperatures up to 400 K (see fig. 5.17). At 500 K, data do now show any more distinct inelastic peaks, and they look similar to data collected at the same temperature on β-$Mg(BH_4)_2$.
The quasi-elastic signal is visible from 300 K and above, although from 6 Å data a quasi-elastic contribution is already present at 200 K. At this temperature, the Lorentzian width is at the edge of the elastic resolution, therefore it is not possible to extract a clear quasi-elastic component. Although the quasi-elastic signal seems to be separated from the inelastic peaks, the exact value of the energy transfer where the two can be separated is hard to guess. Therefore, the data analysis is performed at energy transfer up to 10 meV, in order to include also the inelastic signal.

Up to 400 K, inelastic excitations are still visible and therefore two damped harmonic oscillators are used to describe the inelastic signal, the quasi-elastic is described by a Lorentzian.

At 500 K, the sample is in the β-phase, and data analysis is done as before (see section 5.2.1.1): an elastic line and two Lorentzians, the latter one labelled as $L_3(Q, \omega)$.

The first Lorentzian is ascribed to a localized dynamics, whereas the second one is ascribed to vibrational motions. The starting values for the jump rotational part are taken

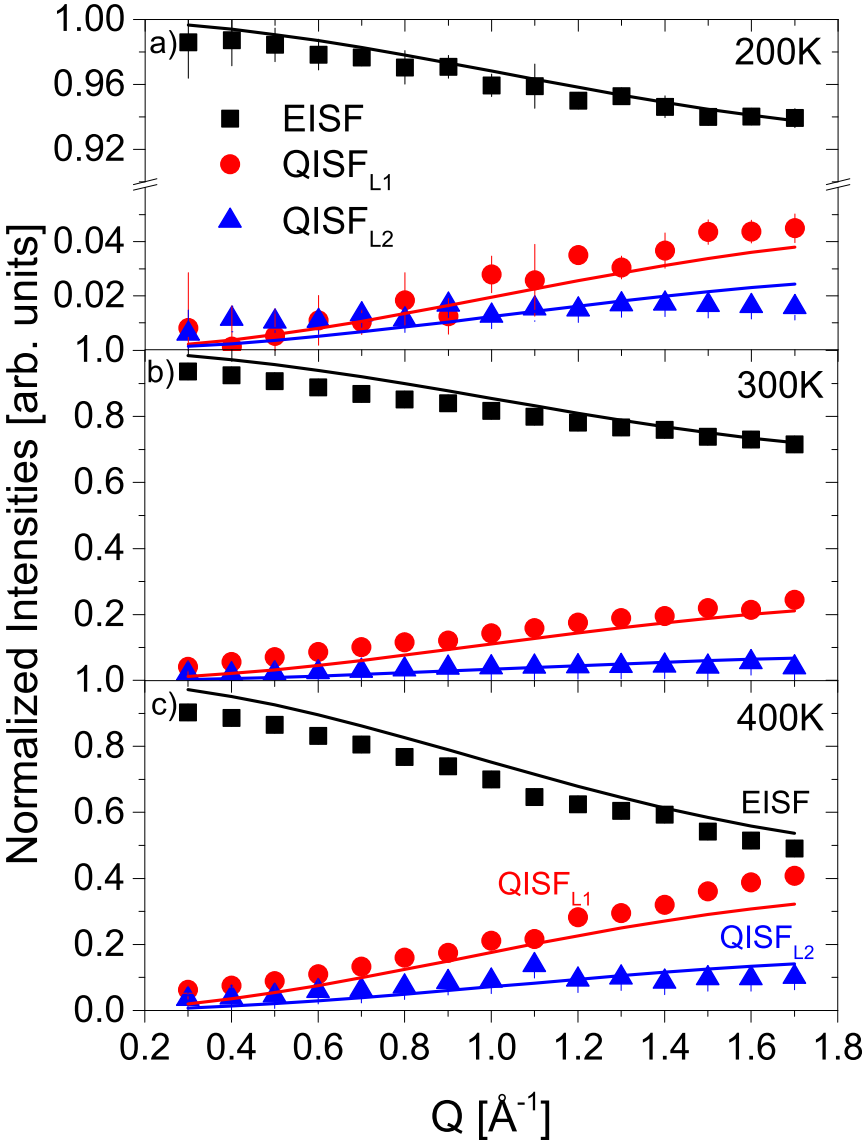

Figure 5.24: α-$Mg(BH_4)_2$: EISF and QISFs at 6 Å and at different temperatures. (black squares) EISF, (red circles) $QISF_{L_1}$, (blue triangles) $QISF_{L_2}$. Solid lines represent fit to the data according to eqs. 5.29-5.31.

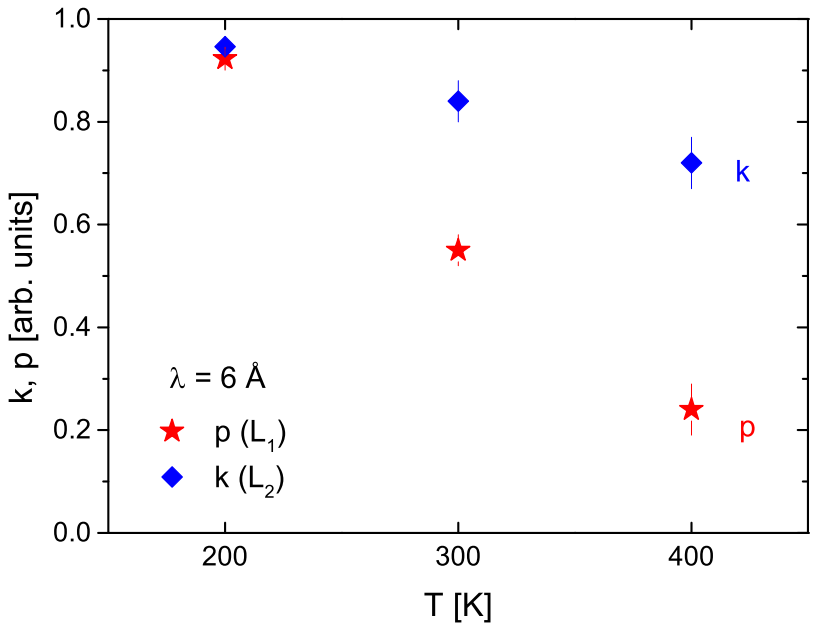

Figure 5.25: α-$Mg(BH_4)_2$. Parameters p and k derived from EISF and QISFs at 6 Å. (blue rhombus) k, (red stars) p. The parameter p corresponds to the hindered rotations described by $L_1(Q,\omega)$ in eq. 5.23, whereas k to hindered rotations described by $L_2(Q,\omega)$ in eq. 5.24.

T [K]	**Fit functions**
100 - 200	$\delta(\omega)$ + DHO_1 + DHO_2
300 - 400	$\delta(\omega)$ + DHO_1 + DHO_2 + $L(Q,\omega)$
500 (β)	$\delta(\omega)$ + $L(Q,\omega)$ + $L_3(Q\omega)$

Table 5.4: Table summarizing the fit functions used for describing the data at 2.5 Å at different temperatures.

from the 6 Å data (Γ_2) and fitted in the spectra. The values found for Γ_2 are in agreement with the 6 Å data. Spectra are fitted using the above mentioned functions, and results are shown in fig. 5.26 and 5.27. Table 5.4 summarizes the functions used at different temperatures.
In the instrumental resolution function measured at 11 K (see fig. 5.5), the inelastic excitation appears in the energy-loss side of the neutron and therefore only the central peak is used as resolution $\mathrm{Res}(Q,\omega)$.

Two damped harmonic oscillators take into account vibrations that are still separated but close to the quasi-elastic region. In order to improve the fit procedure, the frequencies ω_{q_1} and ω_{q_2} are kept fixed during the process. The quantities ω_{q_1} and ω_{q_2} represent the vibrational frequencies of individual $[BH_4]$, since the signal is mainly originating from the

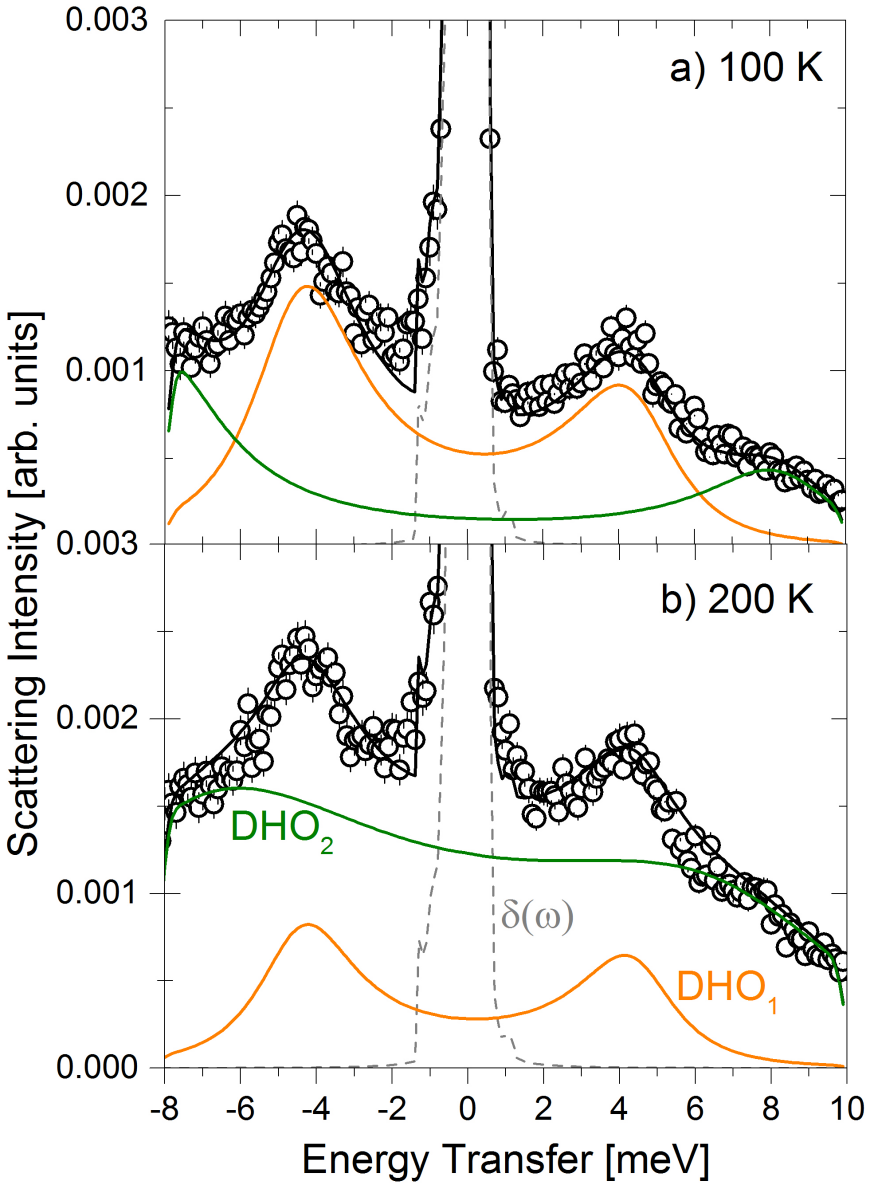

Figure 5.26: α-$Mg(BH_4)_2$: Scattering data from at $Q = 1.6\,\text{Å}^{-1}$ at a) 100 K and b) 200 K. Solid black lines represent the fit. In a) and b) data are described by two DHO (green and orange) and an elastic line $\delta(\omega)$.

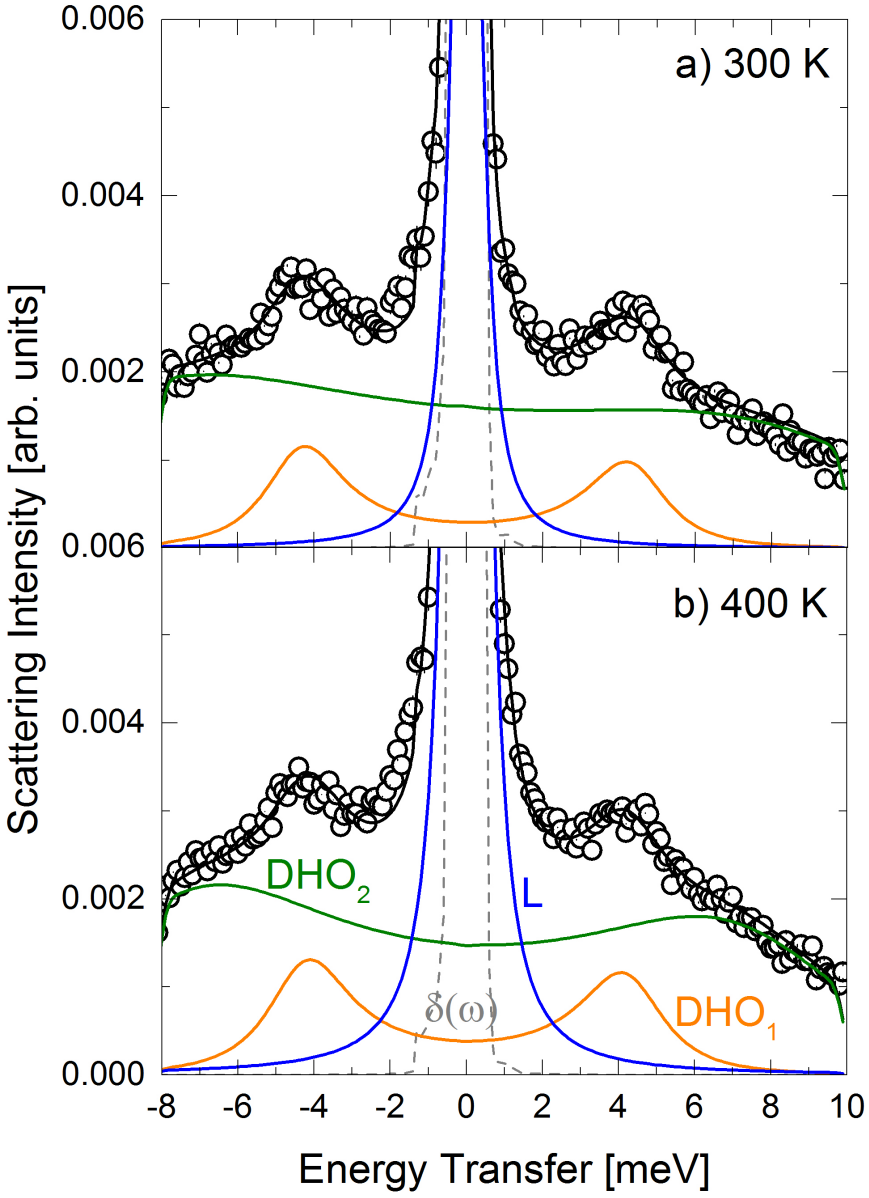

Figure 5.27: α-$Mg(BH_4)_2$: Scattering data from at $Q = 1.6\,\text{Å}^{-1}$ at a) 300 K and b) 400 K. Solid black line represent the fit. In a) and b) data are described by two DHO (green and orange), a Lorentzian (blue) and an elastic line $\delta(\omega)$.

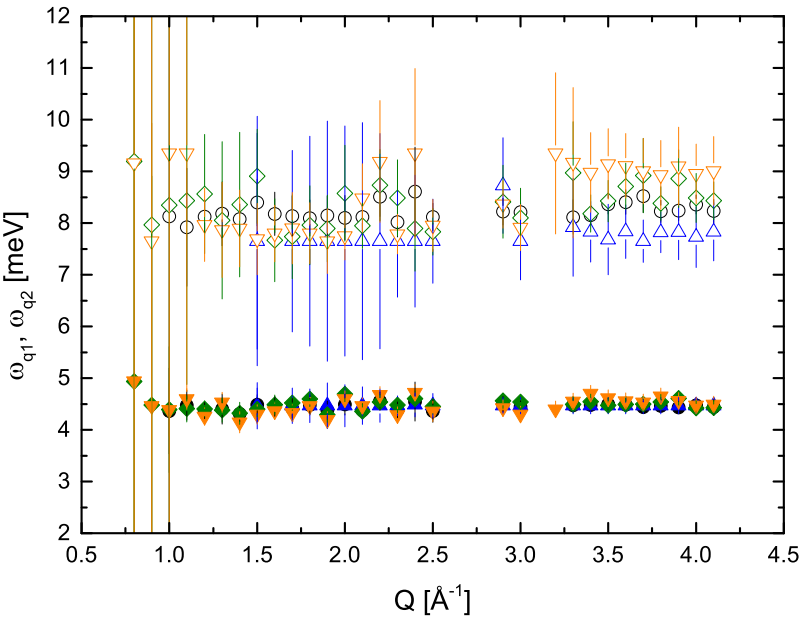

Figure 5.28: α-$Mg(BH_4)_2$: DHO vibrational frequencies ω_{q_1} (full symbols) and ω_{q_2} (empty symbols). (black squares) 100 K, (blue circles) 200 K, (green up triangles) 300 K, (orange down triangles) 400 K.

incoherent scattering cross section of hydrogen. Even though there are six different crystallographic positions of the tetrahedra, their lattice potentials are very similar to each other, and therefore the inelastic peaks remain separated.

The scattering function can not be simplified, and therefore a convolution between quasi-elastic and inelastic scattering functions is considered, with an approach similar to the β-$Mg(BH_4)_2$. The large momentum transfer available allows to clarify the nature of the reorientational dynamics, and therefore not only the EISF is taken into account, but also the QISFs. The EISF is shown in fig. 5.29. Therefore, a more complex approach is used to interpret the EISF and QISFs.

The $S_{\rm vib}(Q,\omega)$ is represented by the sum of the two harmonic oscillators, and $S_{\rm rot}(Q,\omega)$ is given by a sum of an elastic line and a Lorentzian $L(Q,\omega)$. The scattering function resulting from the convolution is, in case of hindered rotations,

$$\begin{aligned} S\left(Q,\omega\right) &= D(Q)\left[f+\left(1-f\right)A_0(Q)\right]\delta(\omega) \\ &\quad + D(Q)\left(1-f\right)\left[1-A_0(Q)\right]L(Q,\omega) + \\ &\quad + \left[f+\left(1-f\right)A_0(Q)\right]\left[1-D(Q)\right]S^{\rm inel}_{\rm vib}(Q,\omega) + \\ &\quad + \left[1-D(Q)\right]\left(1-f\right)\left[1-A_0(Q)\right]\left[S^{\rm inel}_{\rm vib}(Q,\omega)\otimes L(Q,\omega)\right], \end{aligned} \tag{5.32}$$

where $D(Q)$ is the Debye-Waller factor and f is the fraction of $[BH_4]$ units not undergoing reorientation motions. It is reasonable to assume a rotational diffusion motion around C_2/C_3

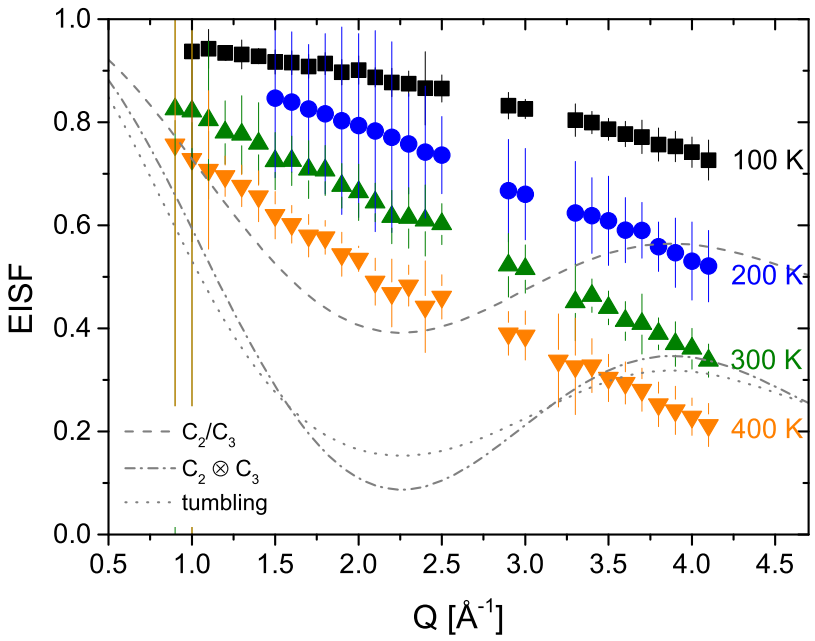

Figure 5.29: α-$Mg(BH_4)_2$: EISF calculated from eq. 5.11. (black squares) 100 K, (blue circles) 200 K, (green up triangles) 300 K, (orange down triangles) 400 K. Gray lines show some theoretical EISF models: (dashed) C_2/C_3 rotations, (dotted) tumbling motions, (dash dotted) convolution between C_2 and C_3 rotations.

axes, and therefore the expression for A_0 (and consequently for A_1) is given in the section above.

Data are fitted with a sum of a δ-function, a Lorentzian, and two damped harmonic oscillators. Experimentally, the last two terms in eq. 5.32 are not resolved, and therefore they are summed up, yielding to:

$$\mathrm{EISF} = D(Q)\,[f + (1-f)\,A_0(Q)] \tag{5.33}$$

$$\mathrm{QISF}_L = D(Q)\,(1-f)\,[1 - A_0(Q)] \tag{5.34}$$

$$\mathrm{QISF}_{\mathrm{vib}} = 1 - D\,(Q) \tag{5.35}$$

These expressions are used to fit the experimental EISF and QISFs, in a global fit procedure. The adjusting parameters are the fraction f of hindered rotational motions and the mean square displacement $\langle u^2 \rangle$. The distance of $d_{\text{B-H}}$ is kept fixed to the value 1.14 Å. Results for the fitted data and obtained parameters are shown in figs. 5.30, 5.31 and 5.32.

The QISF_L reflects the shape of a C_2/C_3 jump rotational diffusion. The fraction f of hindered rotations decreases as the temperature increases, whereas the mean square displacement $\langle u^2 \rangle$ increases. The obtained values of f are in good agreement with values found at 6 Å data, at temperatures of 300 K and 400 K (values are listed in table 5.5, where also the values of k are reported from L_2 at 6 Å). At 500 K, the fraction f is zero, and this confirms the crystal phase transition to the β-phase.

The mean square displacement $\langle u^2 \rangle$ is shown in fig. 5.31. Up to 400 K, the MSD is linearly

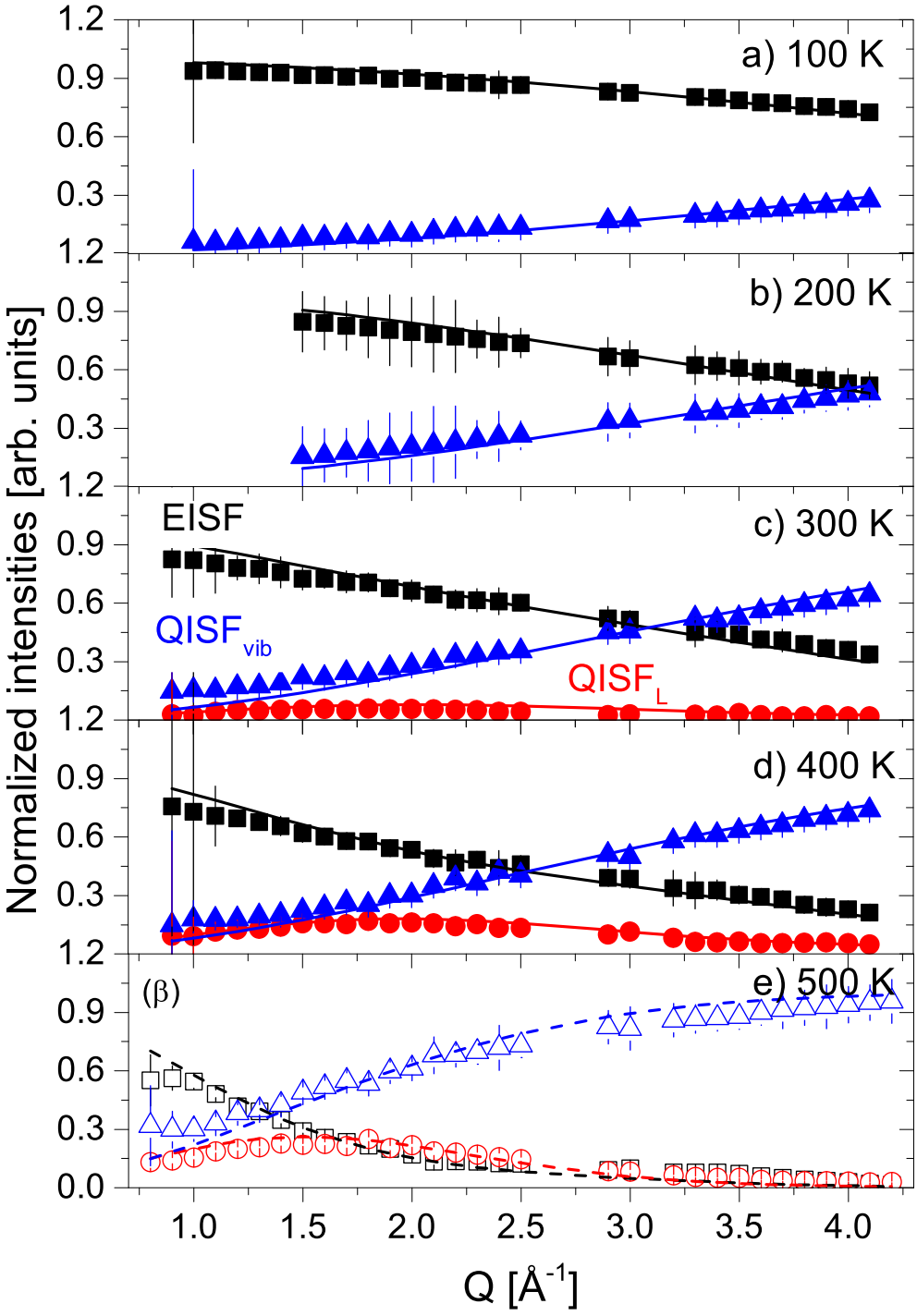

Figure 5.30: α-$Mg(BH_4)_2$: EISF (black squared), $QISF_L$ (red circles) and $QISF_{inel}$ (blue triangles) measured at 2.5 Å and at 100, 200, 300, 400 and 500 K. Solid lines represent the fit to data according to eqs. 5.33 - 5.35. The panel e) 500 K shows open symbols to distinguish between β- and α-phase.

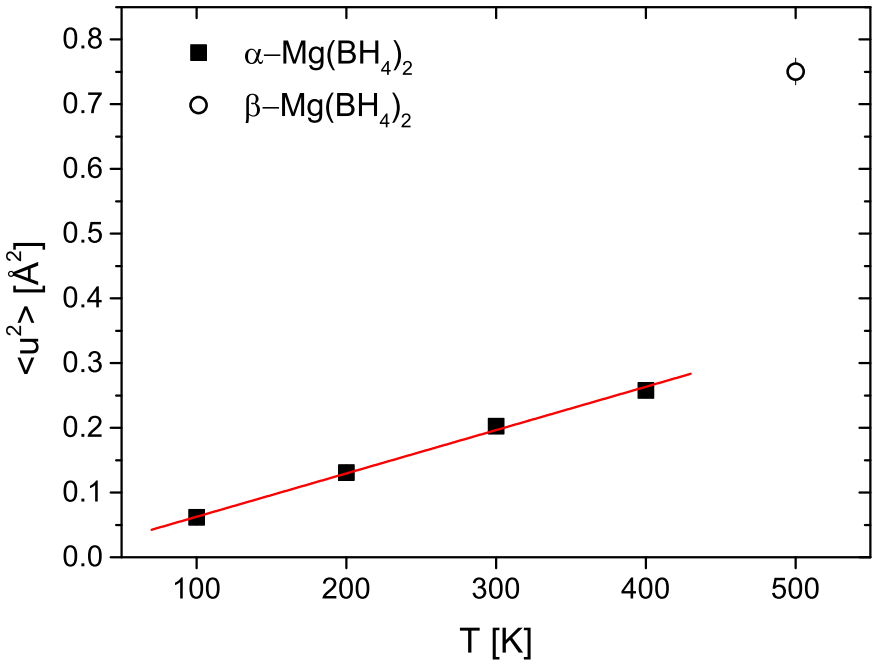

Figure 5.31: α-$Mg(BH_4)_2$: Mean square displacement $\langle u^2 \rangle$ as a function of T. The red line is a linear fit to the data, in order to extract the temperature dependence of the MSD: $\langle u^2 \rangle = (6.7 \pm 0.2) \cdot 10^{-4} \times T[\mathrm{K}]\,\mathrm{Å}^2$. Open symbols show data at 500 K, where the system is already in the β-polymorph.

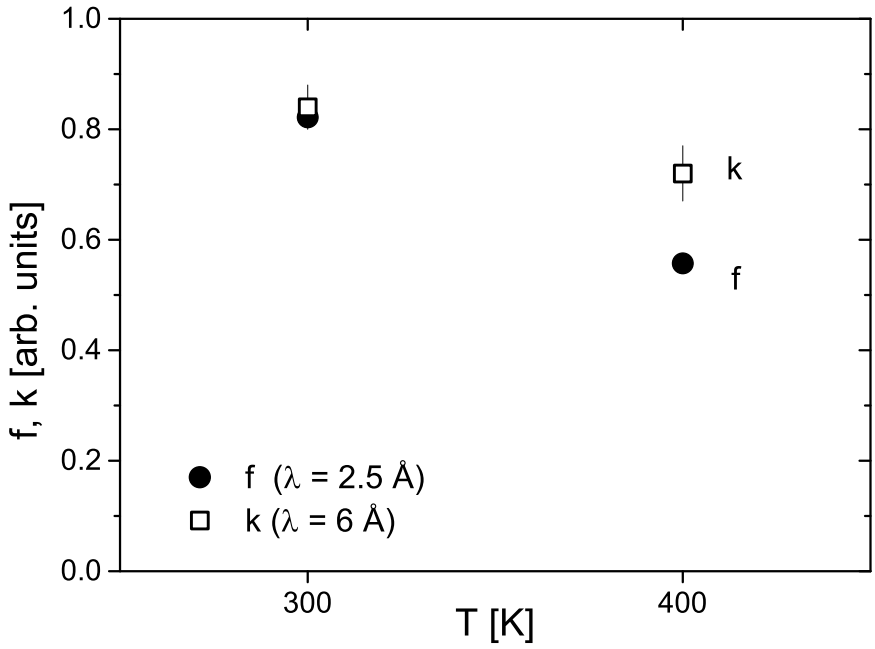

Figure 5.32: α-$Mg(BH_4)_2$: fractions f and k as a function of temperature T. (solid circles) f derived from the $L(Q,\omega)$ at 2.5 Å, (open squared) k derived from $L_2(Q,\omega)$ at 6 Å.

T [K]	**k** [L_2 at 6 Å]	**f** [L at 2.5 Å]
300	0.84 ± 0.04	0.82 ± 0.01
400	0.72 ± 0.05	0.55 ± 0.02

Table 5.5: α-$Mg(BH_4)_2$: parameters k and f, describing the fractions of hindered rotations of the $[BH_4]$ units, derived from 6 Å and 2.5 Å analysis, respectively.

increasing with temperature, as expected for harmonic crystal vibrations [106]; at 500 K, the sharp value jump reflects the structural phase transition. A linear fit (up to 400 K) shown in fig. 5.31, gives a temperature dependence

$$\langle u^2 \rangle = (6.7 \pm 0.2) \cdot 10^{-4} \times T[\mathrm{K}]\,\mathrm{\AA}^2, \tag{5.36}$$

which is rather similar to the one used in the rescaling procedure at the beginning of this subsection, $U_{\mathrm{Vib}} = 0.0001 \times T[\mathrm{K}]\,\mathrm{\AA}^2$.

5.2.2.2 Discussion

α-$Mg(BH_4)_2$ dynamics has been recently studied using Raman, Nuclear Magnetic Resonance, Infrared and inelastic neutron scattering [96, 97, 95]. NMR performed on α-phase and over a large range of temperature, showed a reorientation dynamics that was ascribed to C_2 or C_3 rotations, with three characteristic activation energies [97]. Notably, the same reorientation motions were found to have three different activation energies, well separated from each other, $E_{a1} = 116 \pm 6$ meV, $E_{a2} = 198 \pm 12$ meV, $E_{a3} = 362 \pm 5$ meV. Despite the six inequivalent crystallographic positions, it was always assumed that the local environment of the $[BH_4]$ is rather similar, as depicted in fig. 1.14. Crystallographic data show that the Mg-B-Mg is not linear, with the angle Mg-B-Mg in a range of 148°-177° [78]. A deviation from a linear configuration and the six crystallographic inequivalent $[BH_4]$, leads to a different activation energies, each one characterized by an energy distribution.

In this experiment, two processes are detected at longer observation time scale (measurements at $\lambda_1 = 6$ Å), but the widths of the quasi-elastic components do not show any Arrhenius type behaviour as a function of temperature. Moreover, the limited momentum transfer range Q does not allow a clear process identification.

Inelastic neutron scattering experiments were performed on α-$Mg(BH_4)_2$ [96, 95], but the vibrational density of states measured is not mapping inelastic scattering at low energy transfer as probed in this work. The inelastic peaks around 4.5 meV, observed in this work, can be tentatively assigned to lattice phonons, similar to β-$Mg(BH_4)_2$.

X-ray and neutron diffractions show an almost uniform thermal expansion of the lattice parameters, with a unit cell volume showing a minima around 175 K, up to the structural phase transition around $T = 490$ K. As soon as the crystal phase transition is reached, the

inelastic signal becomes strongly over-damped, and this might be related to the structural transition.

5.2.2.3 Conclusion

Quasi-elastic neutron scattering experiments were done on α-$Mg(BH_4)_2$, in order to explore the dynamics on the picosecond time scale. At longer time scale, two rotational diffusion processes are detected, possibly ascribed to C_2 or C_3 rotations. Surprisingly, these processes do not show any Arrhenius behaviour typically of thermally activated processes. From the analysis of the EISF and QISFs, both jump rotational diffusion processes are hindered. An equivalent finding of similar reorientations with distinctly different activation energies was reported from NMR measurements.
At shorter time scale, a jump rotational diffusion process is detected at 300 K and above. A sufficiently large momentum transfer range allows a clear identification of the localized dynamics, taking into account the EISF and QISF. Up to 400 K, a hindered jump rotational diffusion around the C_2 axis is detected (being energetically more favourable than C_3 rotations [97]), consistent with the measurements performed at 6 Å. The inelastic peaks detected at low temperature are energetically close to the quasi-elastic region, and they persist up to 400 K. As soon as the phase transition is reached, both quasi-elastic and inelastic dynamics strongly change: rotations are not any more hindered and the inelastic peaks are not any more visible, consistent with the β-phase.

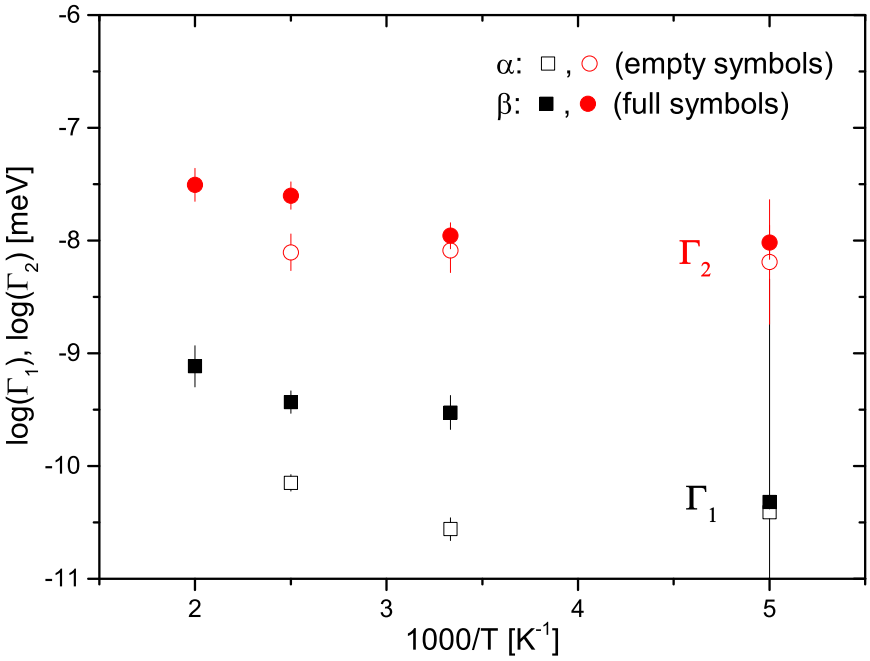

Figure 5.33: Linewidths Γ_1 and Γ_2 on a logarithmic scale measured at 6 Å and on both species, as a function of temperature. Square symbols correspond to Γ_1, round circles to Γ_2. The vertical error bars denote $\pm 1\sigma$.

5.3 General conclusions on $Mg(BH_4)_2$

Quasi-elastic measurements were performed on two polymorphs of magnesium borohydride, the α- and the β-$Mg(BH_4)_2$, on two different time scales.
At longer time scales ($\lambda = 6$ Å), two processes are identified in both α- and β-phases (see fig. 5.33).
At 200 K, both polymorphs show the same time scale dynamics, inside the experimental uncertainties. Instead, in each polymorph, the time scales associated to Γ_1 is, at least, one order of magnitude larger than the process associated to Γ_2.
Moreover, for each process, the α-polymorph shows a slower dynamics compared to the β crystal phase. In the α-polymorph both processes do not show any Arrhenius-like behaviour.

At shorter time scales ($\lambda = 2.5$ Å) and low temperatures, both species are characterized by low energy vibrational excitations very close to the quasi-elastic region. α-$Mg(BH_4)_2$ shows two inelastic peaks around 4.5 and 9 meV, whereas the β polymorph shows only one peak at a slightly lower energy, around 3.2 meV (see fig. 5.34). As soon as the temperature increases, the vibrational behaviour of the two polymorph changes: in the α-phase, peaks persists till high temperature, till the phase transition is reached at 500 K; in the β-phase, above 200 K, the vibrational signal is described by an over-damped harmonic oscillator.

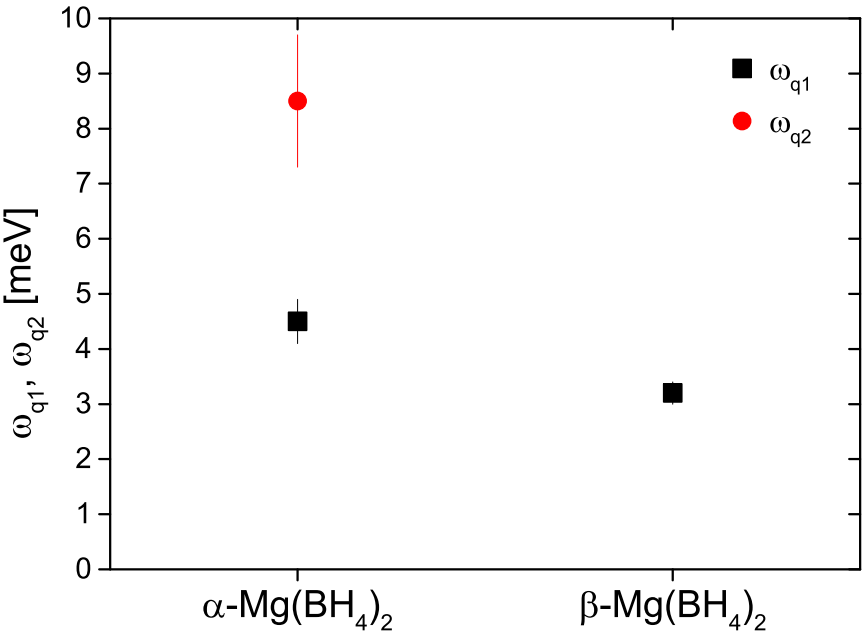

Figure 5.34: Vibrational frequencies ω_{q_1} (black squares) and ω_{q_2} (red circles) in α and β-$Mg(BH_4)_2$ at 100 K.

Therefore, the inelastic signal superimposes on the quasi-elastic signal.
A simultaneous analysis of the EISF and QISFs, and an extended available momentum transfer Q, allows a more precise identification of the reorientational processes.
In both species, reorientations are characterized by jump rotations around the symmetry axes C_2 or C_3. The identical functional form of the EISF (and therefore also of the QISFs) made the discrimination not possible with these measurements.
In β-$Mg(BH_4)_2$ and at 200 K, some motions are hindered, whereas at higher temperatures, all the tetrahedra units undergo C_2/C_3 rotations.
In α-$Mg(BH_4)_2$, instead, both jump rotations are found to be hindered in both time scales, with a significant fraction of "static" tetrahedra up to 400 K (see fig. 5.35). As soon the phase transition from α- to β-$Mg(BH_4)_2$ is reached, the hindrance disappears. The difference in the dynamical behaviour of the two polymorphs is also reflected by the mean square displacement as a function of temperature (see fig. 5.36.)
In α-$Mg(BH_4)_2$, the mean square displacement $\langle u^2 \rangle$ increases linearly with temperature. This indicates that, up to 400 K, the vibrational behaviour follows the harmonic crystal approximation. In fact, up to 400 K, the quasi-elastic and the vibrational signal can be visually distinguished.
The situation is different in β-$Mg(BH_4)_2$: the vibrational behaviour changes at temperatures above 200 K, where the double peaks inelastic signal merges in the quasi-elastic region. Therefore, the mean square displacement, extracted from a global analysis of EISF and

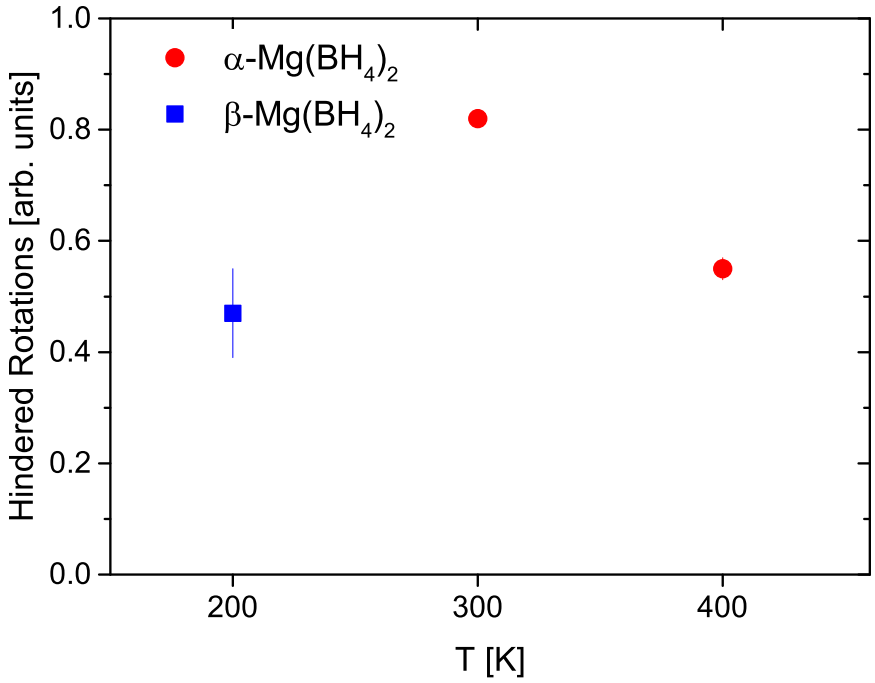

Figure 5.35: Fraction of hindered jump rotations at short time scale $\lambda = 2.5\,\text{Å}$, in α-$Mg(BH_4)_2$ (red circles) and in β-$Mg(BH_4)_2$ (blue squares).

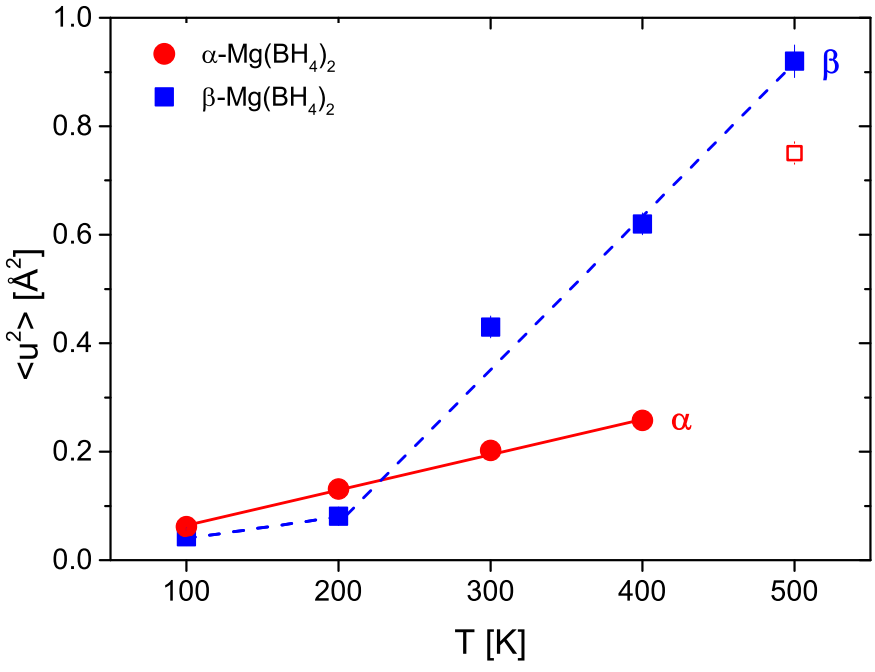

Figure 5.36: Mean square displacement $\langle u^2 \rangle$ at short time scale $\lambda = 2.5\,\text{Å}$, in α-$Mg(BH_4)_2$ (red circles) and in β-$Mg(BH_4)_2$ (blue squares). In β-$Mg(BH_4)_2$, the dotted line is a guide to the eyes. In α-$Mg(BH_4)_2$, the solid line is a linear fit of the data (see explanation in the text).

QISFs, reflects a superposition of local reorientation and vibrations of hydrogen atoms, occurring on similar time scales.

In conclusion, the two species show different dynamics: the α polymorph shows a more hindered localized rotational dynamics and a more harmonic vibrational behaviour than the β-polymorph. The increased rotational activity and the over-damped inelastic dynamics might modify the free energy landscape, and thus explaining the metastability of the β-phase at temperature below the crystal phase transition temperature.

Chapter 6

Lithium and Magnesium Borohydride mixture

Contents

6.1 Experimental

A batch of 1:1 mixture of o-$LiBH_4$ and α-$Mg(BH_4)_2$ was prepared, according to the procedure described in [28, 68]. Due to the high neutron absorption cross-section of natural boron, the isotope ^{11}B was used. The natural lithium isotope composition is instead maintained, because Li is less abundant in the stoichiometric composition of the sample.
Approximatively 160 mg of mixture were used in the neutron scattering experiment: an aluminium flat cell was used as a sample holder and oriented as in fig. 3.10. The calculated transmission was above 0.90: a scattering power of 10% ensures, up to a certain extend, a small amount of multiple scattering [120], and therefore no further data treatment has to be performed in order to remove multiple scattering contributions.
Data were collected at three different temperatures (373, 423 and 500 K), as shown in fig. 1.15 and table 6.1. The incident wavelength was $\lambda_1 = 3.5\,\text{Å}$ and the chopper frequency was $\nu_{ch} = 18000\,\text{rpm}$, leading to an elastic resolution of 200 μeV at full-width-half-maximum and a momentum transfer Q range of $0.4 - 3.0\,\text{Å}^{-1}$. The instrumental resolution was measured using a vanadium standard, with a geometry similar to the sample. Data reduction was performed according to the procedure described in section 3.6.

T [K]	**$LiBH_4$**	**$Mg(BH_4)_2$**
373	*Pnma* (ortho)	$P6_122$ (α)
423	$P6_3mc$ (hex)	$P6_122$ (α)
500	$P6_3mc$ (liquid)	*Fddd* (liquid)

Table 6.1: Crystal structure phases of the mixture as a function of temperatures at which the neutron scattering experiment has been performed.

Compound	σ_{coh} [barn]	σ_{inc} [barn]
$Li^{11}BH_4$	13.01	322.17
$Mg(^{11}BH_4)_2$	28.75	642.58
Total	41.76	964.75

Table 6.2: Coherent and incoherent scattering cross-sections of $Li^{11}BH_4$ and $Mg(^{11}BH_4)_2$. As noticeable, the incoherent scattering cross-section dominates by more than one order of magnitude compared to the coherent one. Also, the incoherent scattering power of $Mg(^{11}BH_4)_2$ is two times greater than the $Li^{11}BH_4$.

6.2 Data analysis

Measurements conducted at different temperatures are analysed and results are shown in fig. 6.1, for two particular Q values. It is noticeable, in the energy range up to $\sim 2\,\text{meV}$, that the quasi-elastic signal increases with increasing temperature, and, at the same time, the elastic peak decreases in intensity. This is an indication of a thermally activated process.
At 373 and 423 K, an inelastic peak is visible around $\sim 4.5\,\text{meV}$, whereas at 500 K it is not any more visible. Unfortunately the inelastic peak at negative energy transfers (neutron energy loss) is not covered in the experimental dynamical range. Moreover, with increasing momentum transfer Q, the inelastic peak is more pronounced. Taking into account the stoichiometric composition of the sample, the scattering cross sections per formula are calculated (see table 6.2). The hydrogen incoherent scattering cross-section is more than one order of magnitude greater than the all other elements' scattering cross-sections. As a consequence, the experiments probe mainly the hydrogen dynamics.
The scattering cross-section calculations suggest that, the signal derived from the 0.5:0.5 mixture is 1/3 originating from $Li^{11}BH_4$ and 2/3 from $Mg(^{11}BH_4)_2$, corresponding to the number of hydrogen atoms in the formula unit.
Both quasi-elastic and vibrational scattering functions can be written for $LiBH_4$ (abbreviated with subscript LBH) and $Mg(BH_4)_2$ (subscript MBH):

$$S^{\text{QE}}_{\text{LBH}}(Q,\omega) = A_0(Q)\delta(\omega) + \sum_{i\neq 0} A_i(Q) L_{\text{i-LBH}}(Q,\omega)\,, \tag{6.1}$$

$$S^{\text{QE}}_{\text{MBH}}(Q,\omega) = B_0(Q)\delta(\omega) + \sum_{i\neq 0} B_i(Q) L_{\text{i-MBH}}(Q,\omega)\,, \tag{6.2}$$

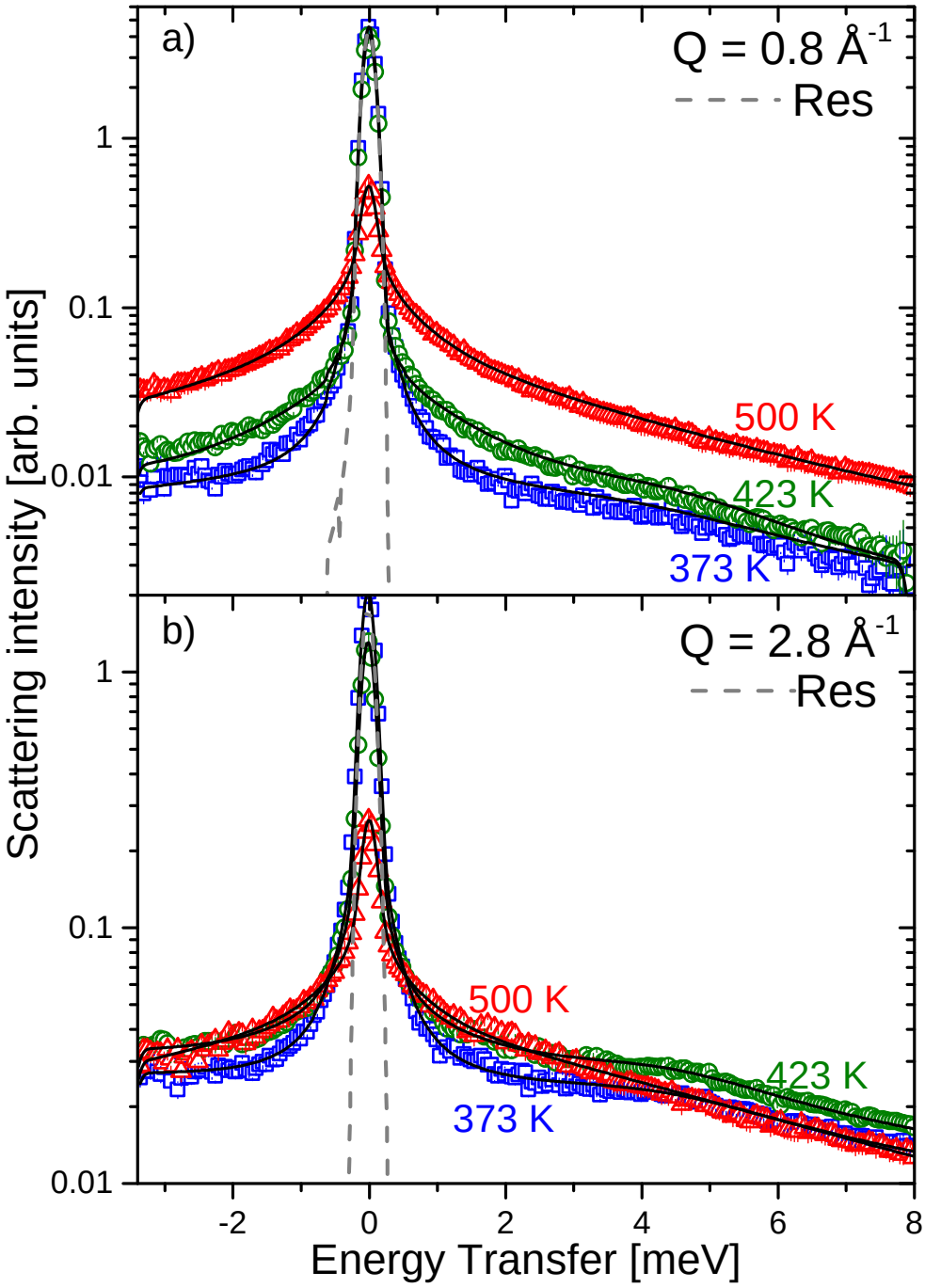

Figure 6.1: Quasi-elastic neutron scattering measurements on $0.5LiBH_4$-$0.5Mg(BH_4)_2$ at 373 K (blue squares), 423 K (green circles) and 500 K (red triangles). Dashed lines represent the vanadium measurements (instrumental resolution). Solid black lines represent the fit to the data (see text for details). In a) measurements at $Q = 0.8\,\text{Å}^{-1}$, in b) measurements at $Q = 2.8\,\text{Å}^{-1}$.

where $A_0(Q)$ and $B_0(Q)$ are the EISF of $LiBH_4$ and $Mg(BH_4)_2$, respectively. Also, between the EISFs and the QISF, the follow relationships hold:

$$A_0(Q) + \sum_{i>0} A_i(Q) = 1, \quad B_0(Q) + \sum_{i>0} B_i(Q) = 1 \tag{6.3}$$

The vibrational scattering functions are:

$$S^{\text{vib}}_{\text{LBH}}(Q,\omega) = C_0(Q)\delta(\omega) + C_1(Q)S^{\text{Inel}}_{\text{LBH}}(Q,\omega), \tag{6.4}$$

$$S^{\text{vib}}_{\text{MBH}}(Q,\omega) = D_0(Q)\delta(\omega) + D_1(Q)S^{\text{Inel}}_{\text{MBH}}(Q,\omega), \tag{6.5}$$

where, instead, the terms $C_0(Q)$ and $D_0(Q)$ are the Debye-Waller factors of each species in the mixture. Also, $C_0(Q) + C_1(Q) = 1$ and $D_0(Q) + D_1(Q) = 1$.
Therefore, taking into account the stoichiometric composition of the physical mixture, the total scattering function can be written:

$$S(Q,\omega) = \frac{1}{3}\left[S^{\text{QE}}_{\text{LBH}}(Q,\omega) \otimes S^{\text{vib}}_{\text{LBH}}(Q,\omega)\right] + \frac{2}{3}\left[S^{\text{QE}}_{\text{MBH}}(Q,\omega) \otimes S^{\text{vib}}_{\text{MBH}}(Q,\omega)\right]. \tag{6.6}$$

In the data analysis at all selected temperatures, it has been found that two Lorentzians are able to describe the quasi-elastic region of the spectra. Therefore, in eqs. 6.1 and 6.2, $i = 1$. Making the convolution explicit, we obtain:

$$\begin{aligned} S(Q,\omega) &= \frac{1}{3}\left[A_0C_0\delta(\omega) + A_1C_0L_{\text{1-LBH}} + A_0C_1S^{\text{vib}}_{\text{LBH}} + A_1C_1L_{\text{1-LBH}} \otimes S^{\text{vib}}_{\text{LBH}}\right] + \\ &+ \frac{2}{3}\left[B_0D_0\delta(\omega) + B_1D_0L_{\text{1-MBH}} + B_0D_1S^{\text{vib}}_{\text{MBH}} + B_1D_1L_{\text{1-MBH}} \otimes S^{\text{vib}}_{\text{MBH}}\right]. \end{aligned} \tag{6.7}$$

The explicit dependence on (Q,ω) in the right hand side of the above equation has been omitted for clarity. Eq. 6.7 contains all the scattering functions that contribute to the measured spectra intensity.
At each temperature, data are analysed taking into account both quasi-elastic and inelastic signals and, therefore, they are divided in three different subsections, each one corresponding to a different temperature.

6.3 Results and discussion

6.3.1 373 K

At 373 K, the sample is composed by $LiBH_4$ in the orthorhombic crystal structure and $Mg(BH_4)_2$ in the hexagonal $P6_122$ (α) crystal phase (table 6.1). At this temperature, $LiBH_4$ shows a quasi-elastic component characterized by a HWHM of ~ 0.22 meV (fig. 4.4), assigned to a reorientational motions around all the 4 tetrahedra H atoms (tumbling motions). α-$Mg(BH_4)_2$ shows a Lorentzian with HWHM of ~ 0.3 meV (table 5.3), and, between 300

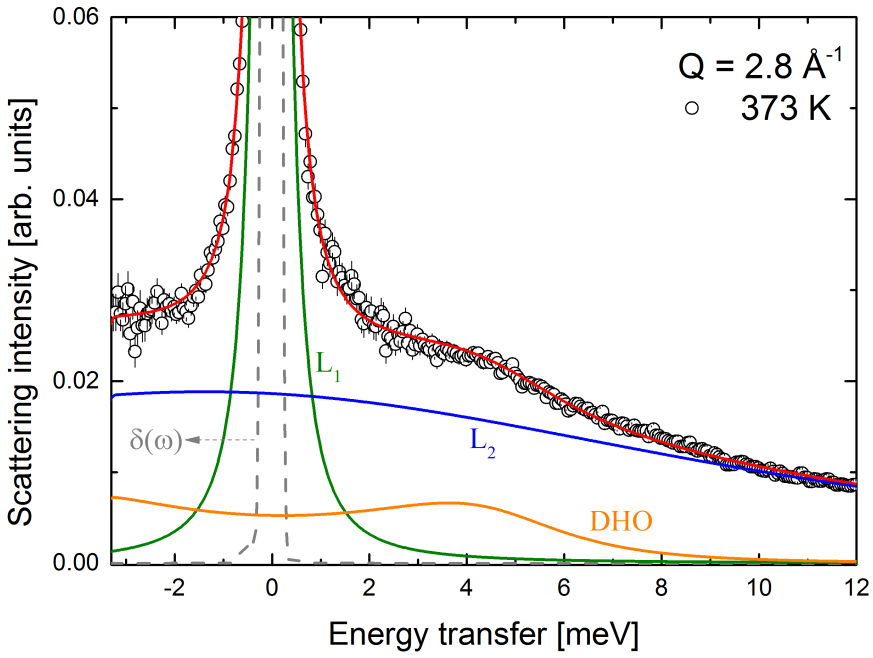

Figure 6.2: 0.5b o-Li^{11}BH$_4$ + 0.5 α-Mg(^{11}BH$_4$)$_2$: Scattering data at $Q = 2.8\,\text{Å}^{-1}$ at 373 K. Solid red line represents the fit. Data are described using an elastic line $\delta(\omega)$, a narrow Lorentzian $L_1(Q,\omega)$ (green), a damped harmonic oscillator DHO (orange) and a broad Lorentzian $L_2(Q,\omega)$ (blue).

and 400 K, it shows hindered rotation around the C_2/C_3 axis, with only 20-30% of the [BH_4] units undergoing rotational motions. The slower process is hidden in the energy resolution width.
Any attempt to fit the spectra with all functions in eq. 6.7 leads to instabilities in the numerical optimizations.

At 373 K, data are modelled with an elastic line $\delta(\omega)$, a narrow quasi-elastic Lorentzian $L_1(Q,\omega)$, a damped harmonic oscillator (DHO) and a broad Lorentzian $L_2(Q,\omega)$ in order to take into account fast vibrational motions (see fig. 6.2). All the scattering functions are convolved with the experimental resolution function and fitted to the data. Results for the different quantities are shown in fig. 6.3.

The width Γ_1 is constant in the probed Q range and therefore it is assigned to localized motions of the tetrahedra units [BH_4]. The average value is $\Gamma_1 = 0.17 \pm 0.02\,\text{meV}$.
Each component in the mixture should contribute to quasi-elastic measurements according to eq. 6.7. Instead, only one component is experimentally found. Within the instrumental resolution, the two components might not be properly resolved, and the observed Lorentzian $L_1(Q,\omega)$ reflects a combination of the two single ones.

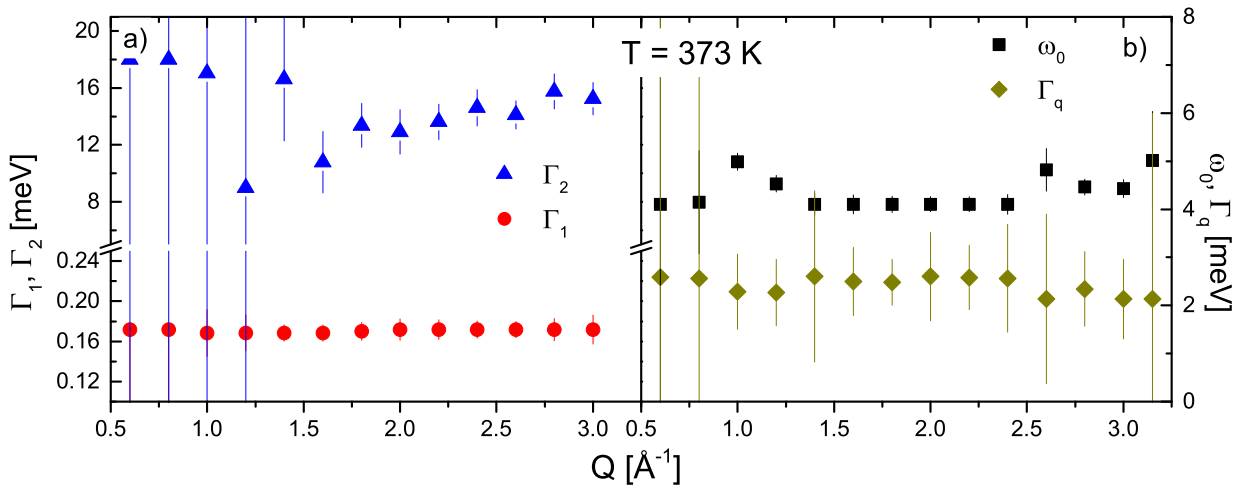

Figure 6.3: Parameters from data fit at 373 K. a) widths of $L_1(Q,\omega)$ and $L_2(Q,\omega)$. b) DHO frequency ω_0 and damping Γ_q.

The damped harmonic oscillator (eq. 2.49) is used to describe the inelastic peak and it is centred around $\omega_0 = 4.4 \pm 0.9\,\text{meV}$, a value similar to the one found in α-$Mg(BH_4)_2$ (see fig. 5.28). Therefore, the inelastic signal derived from the DHO is clearly assigned to the low energy vibration of α-$Mg(BH_4)_2$.
The width Γ_2 is two orders of magnitude bigger than Γ_1 and shows a dispersion in momentum transfer Q. Therefore, $L_2(Q,\omega)$ can be tentatively assigned to vibrational scattering from $LiBH_4$.
The elastic and quasi-elastic incoherent structure factors, EISF and QISFs, are then calculated taking into account both quasi-elastic and vibrational scattering intensities (eq. 2.59), and they are shown in fig. 6.4.

Starting from eq. 6.7, and taking into account the considerations made on the Lorentzian $L_1(Q,\omega)$, $L_{1\text{-LBH}}$ and $L_{1\text{-MBH}}$, the intensities (QISFs) can be summed up. Moreover, eq. 6.7 involves terms with the convolution of vibrational scattering functions of the two species. Experimentally, only the DHO and the broad Lorentzian $L_2(Q,\omega)$ are found. Thus, the intensities of $L_2(Q,\omega)$ and of the damped harmonic oscillators can be summed up in eq. 6.7. The respective Debye-Waller Factors (DWF) $C_0(Q)$ and $D_0(Q)$ can not be experimentally separated, and therefore only a common DWF $F_0(Q)$ is considered for both species.
The aforementioned considerations lead to the following expressions of EISF and QISF:

$$\text{EISF} = \left\{\frac{1}{3}B_0(Q) + \frac{2}{3}\left[p + (1-p)A_0(Q)\right]\right\}F_0(Q) \tag{6.8}$$

$$\text{QISF}_{L_1} = \left\{\frac{1}{3}\left[1 - B_0(Q)\right] + \frac{2}{3}(1-p)\left[1 - A_0(Q)\right]\right\}F_0(Q) \tag{6.9}$$

$$\text{QISF}_{\text{vib}} = 1 - F_0(Q). \tag{6.10}$$

$A_0(Q)$ is the EISF corresponding to hindered rotations of α-$Mg(BH_4)_2$ around C_2/C_3 axis

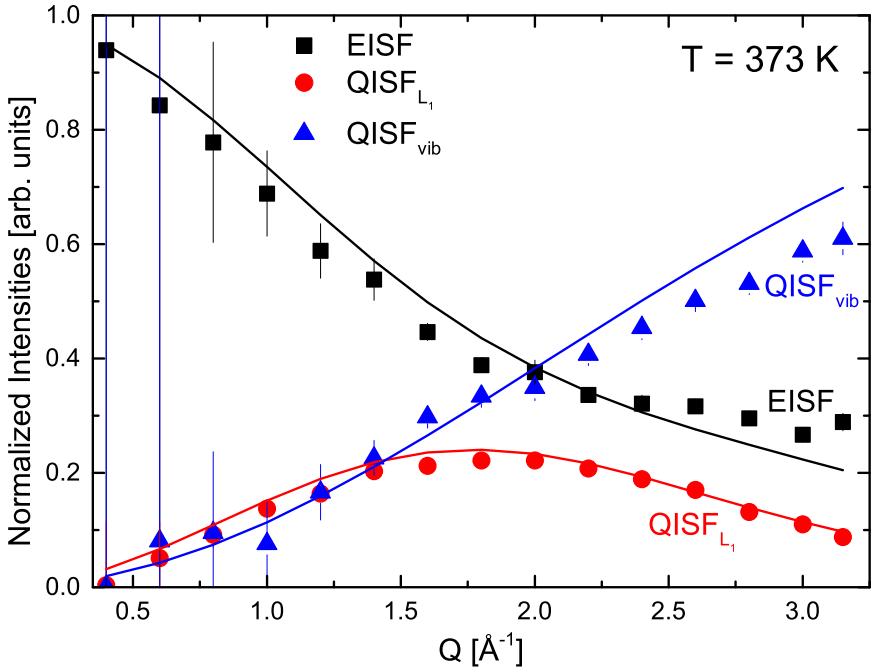

Figure 6.4: 0.5b o-Li^{11}BH$_4$ + 0.5 α-Mg(^{11}BH$_4$)$_2$: EISF (black squares), QISF$_{L_1}$ (red circles) and QISF$_{\mathrm{Vib}}$ (blue triangles) at 373 K. Solid lines represent the fit to the data according to eq.s 6.8-6.10.

and $B_0(Q)$ the one corresponding to tetrahedral jump rotations of $LiBH_4$:

$$A_0(Q) = \frac{1}{2}\left[1 + j_0\left(\frac{2\sqrt{2}}{\sqrt{3}}Qd_{\text{B-H}}\right)\right] \quad \text{and} \quad B_0(Q) = \frac{1}{4}\left[1 + 3j_0\left(\frac{2\sqrt{2}}{\sqrt{3}}Qd_{\text{B-H}}\right)\right]. \quad (6.11)$$

The expressions above are fitted globally to the normalized intensities and the results are shown in fig. 6.4. The distance between hydrogen and boron is kept fixed during the fit, $d_{\text{B-H}} = 1.21$ Å. The other parameters, i.e. the mean square displacement $\langle u^2\rangle$ and p, are let free and are globally optimised. The overall fit is quite satisfactory and it is obtained:

$$\langle u^2\rangle_{373\,\text{K}} = 0.36 \pm 0.02\,\text{Å}^2 \quad \text{and} \quad p_{373\,\text{K}} = 0.79 \pm 0.04. \quad (6.12)$$

The value of p is in agreement with previous measurements on α-Mg(BH_4)$_2$, where, nearly at the same temperature, only a fraction of 0.2-0.3 of tetrahedral units undergoes any reorientational motions (fig. 5.32). The mean square displacement of $LiBH_4$ and α-Mg(BH_4)$_2$ are, respectively, $\langle u^2\rangle_{373\,\text{K-LBH}} = 0.28 \pm 0.01$ Å^2 (see fig.4.14) and $\langle u^2\rangle_{373\,\text{K-MBH}} = 0.25 \pm 0.01$ Å^2 (using eq. 5.36).

6.3.2 423 K

At 423 K, the mixture is composed of Mg(BH_4)$_2$ still in the hexagonal $P6_122$ α crystal phase, whereas $LiBH_4$ is in the hexagonal $P6_3mc$ crystal phase. At this temperature, data are fitted with an elastic line (δ), two narrow quasi-elastic Lorentzians $L_1(Q,\omega)$ and $L_3(Q,\omega)$, a

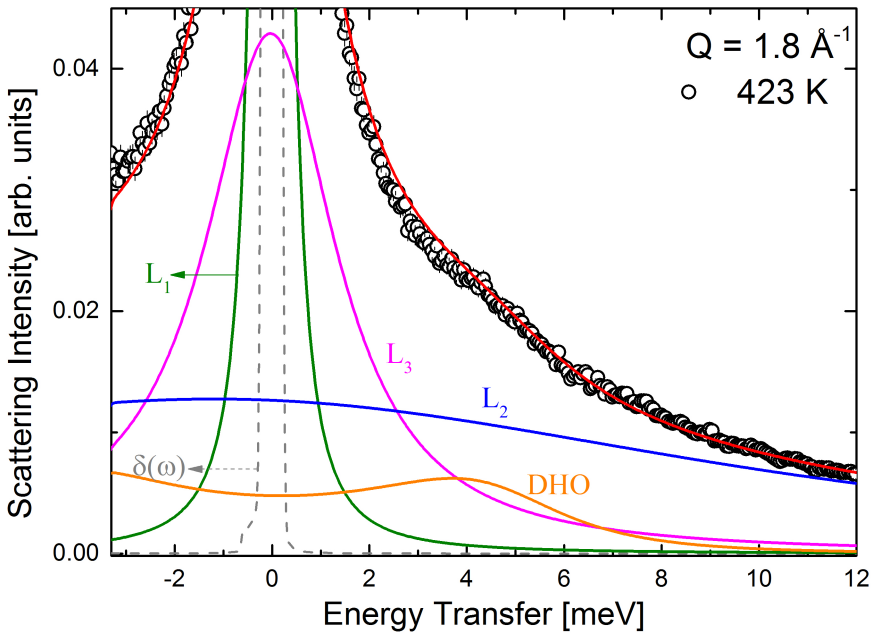

Figure 6.5: 0.5 o-Li^{11}BH$_4$ + 0.5 α-Mg(^{11}BH$_4$)$_2$: Scattering data at $Q = 1.8\,\text{Å}^{-1}$ at 423 K. Solid red line represents the fit. Data are described using a $\delta(\omega)$ line, two narrow Lorentzians (green and magenta), a damped harmonic oscillator (orange) and a broad Lorentzian (blue).

DHO and a broad Lorentzian $L_2(Q,\omega)$ to describe the vibrational contributions (see fig. 6.5).

The narrow Lorentzian $L_1(Q,\omega)$ is characterized by a HWHM $\Gamma_1 = 0.20 \pm 0.07\,\text{meV}$. Its width remains constant in the probed Q range, indicating that this quasi-elastic component describes a localized motion (see fig. 6.6). Comparing this value with the quasi-elastic components in α-Mg(BH$_4$)$_2$ (see table 5.3 and fig. 5.21), we might assign $L_1(Q,\omega)$ to rotational reorientation of the [BH$_4$] units around the C$_2$/C$_3$ axis.

The second narrow Lorentzian $L_3(Q,\omega)$ is added in order to get a satisfactory fit of the data. Moreover, the addition of this quasi-elastic component is supported by the fact that, at this temperature, the pure LiBH$_4$ shows a quasi-elastic component characterized by a HWHM of $\sim$ 1.4 meV (fig. 4.4), a value similar to the measured one $\Gamma_3 = 1.6 \pm 0.4\,\text{meV}$. At this temperature, LiBH$_4$ is already in the hexagonal HT crystal structure. In pure LiBH$_4$ this motion is assigned to a tumbling reorientation of the [BH$_4$] units.
The transition is associated to an order/disorder structural transition, and this is reflected by an enhanced localized dynamics of the [BH$_4$] units, in which the hydrogen motions are becoming faster [131, 132].

The damped harmonic oscillator is used to describe the inelastic peak and it shows the same behaviour of the DHO at 373 K. It is centred at $\omega_0 = 4.6 \pm 0.3\,\text{meV}$, with a damping

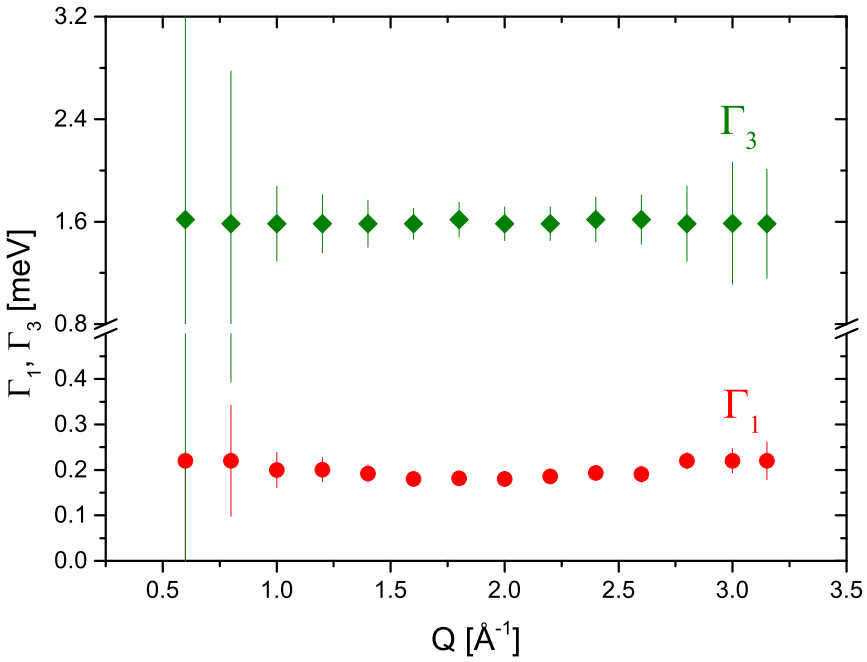

Figure 6.6: Widths Γ_1 and Γ_3 of $L_1(Q,\omega)$ and $L_3(Q,\omega)$ at 423 K. The HWHM Γ_2 is not shown.

$\Gamma_q = 2.5 \pm 0.1$ meV. Therefore, the DHO is assigned to the α-$Mg(BH_4)_2$ excitations.
The width of Lorentzian L_2 shows a similar behaviour to the one at 373 K, and it takes into account the fast vibrational part of the spectra. It is characterized by a quite broad HWHM Γ_2 (> 10 meV), which shows a dispersion in momentum transfer Q. For clarity, it has not been shown in the graph.
The EISF and QISFs are calculated in the same manner as at 373 K, and are shown in fig. 6.7. The analysis is performed using the same global approach, but now the QISFs corresponding to the Lorentzians of $LiBH_4$ and $Mg(BH_4)_2$ can be separated.

In eq. 6.7, the terms containing the vibrational scattering functions can be summed up, using a global Debye-Waller factor. Moreover, still some hindered rotations associated to α-$Mg(BH_4)_2$ are present, taken into account by the parameter p. The theoretical expression of EISF and QISFs are therefore obtained.

$$\text{EISF} = \left\{\frac{1}{3}B_0(Q) + \frac{2}{3}\left[p + (1-p)A_0(Q)\right]\right\} F_0(Q) \tag{6.13}$$

$$\text{QISF}_{L_{1\text{-MBH}}} = \frac{2}{3}(1-p)\left[1 - A_0(Q)\right] F_0(Q) \tag{6.14}$$

$$\text{QISF}_{L_{3\text{-LBH}}} = \frac{1}{3}\left[1 - B_0(Q)\right] F_0(Q) \tag{6.15}$$

$$\text{QISF}_{\text{vib}} = 1 - F_0(Q). \tag{6.16}$$

The $A_0(Q)$ and $B_0(Q)$ are the respective EISF and QISFs of α-$Mg(BH_4)_2$ and $LiBH_4$, and

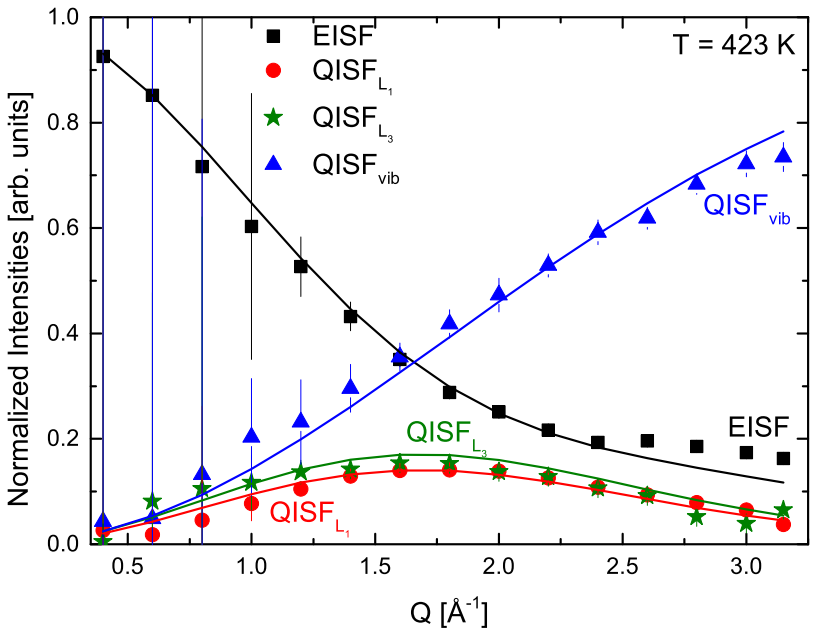

Figure 6.7: 0.5 h-Li^{11}BH$_4$ + 0.5 α-Mg(^{11}BH$_4$)$_2$: EISF (black squares), QISF$_{L_1}$ (red circles), QISF$_{L_3}$ (green stars)and QISF$_{\mathrm{Vib}}$ (blue triangles) at 423 K. Solid lines represent the fit to the data according to eq.s. 6.13-6.16

$F_0(Q)$ is the global Debye-Waller factor, as shown in eq. 6.11. During the fit procedure, the distance $d_{\text{B-H}}$ has been kept fixed to 1.21 Å.
The results of the global fit, using eq.s 6.13-6.16, are shown in fig. 6.7 and the agreement is quite satisfactory. The mean square displacement $\langle u^2 \rangle$ and the fraction p are obtained:

$$\langle u^2 \rangle_{423\,\mathrm{K}} = 0.46 \pm 0.01\ \text{Å}^2 \quad \text{and} \quad p_{423\,\mathrm{K}} = 0.34 \pm 0.03. \tag{6.17}$$

The nature of reorientational motions at 423 K are similar to the one found at 373 K, although the fraction of hindered rotations decreases and the mean square displacement increases. The closest measured value of the MSD for $LiBH_4$ and $Mg(BH_4)_2$ are at 400 K. At 403 K, pure $LiBH_4$ shows a MSD $\langle u^2 \rangle_{403\,\mathrm{K}} = 0.43 \pm 0.01$ Å^2, whereas at 400 K, $Mg(BH_4)_2$ shows a MSD $\langle u^2 \rangle_{400\,\mathrm{K}} = 0.26 \pm 0.01$ Å^2.

6.3.3 500 K

At 500 K, $LiBH_4$ is in the hexagonal high temperature crystal phase and $Mg(BH_4)_2$ in the β crystal modification. According to the phase diagram of $xLiBH_4 + (1-x)Mg(BH_4)_2$, $x = 0.5$, the sample is in a liquid state and already in the first decomposition step, as shown in fig. 1.15 [28].
While recording spectra at this temperature, a drop of total integrated intensity was observed ($\sim 30\%$), as an indication that the decomposition process has already started at 500 K.
The sample is in the liquid state and, as a first approach, data are analysed using a sum of

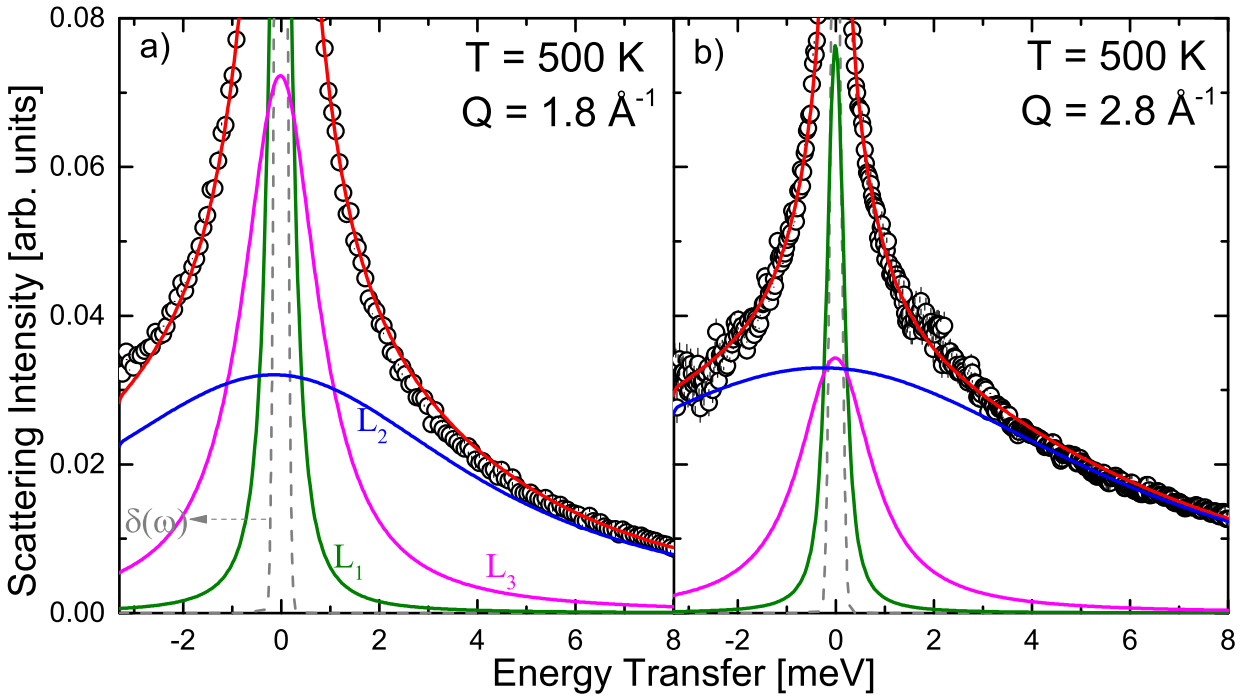

Figure 6.8: 0.5 o-Li^{11}BH$_4$ + 0.5 α-Mg(^{11}BH$_4$)$_2$: Scattering data at 500K and at a) $Q = 1.8\,\text{Å}^{-1}$ and b) $Q = 2.8\,\text{Å}^{-1}$. Solid red line represents the fit. Data have been described using a $\delta(\omega)$ line (grey dashed), two narrow Lorentzians L_1 and L_3 (green and magenta, respectively) a broad Lorentzian L_2 (blue).

Lorentzians (no elastic line). However, the results indicate that a component with the elastic line width is required. Therefore, in the fit procedure, an elastic line $\delta(\omega)$ and two Lorentzians are used. The inelastic peak at $\sim 4.5\,\text{meV}$ is not any more visible, and this in an indication of the crystal phase transition of $Mg(BH_4)_2$ [136]. Results of the fit procedure are shown in fig. 6.8. Data are quite successfully described by the proposed fit functions and values of the Lorentzians widths are reported in fig. 6.9. All three Lorentzians ($L_1(Q,\omega)$, $L_3(Q,\omega)$ and $L_2(Q,\omega)$) are not constant in the momentum range probed by the experiment. This is an indication that, at this temperature, diffusion-like processes may take place. Nevertheless, the broader Lorentzian $L_2(Q,\omega)$ shows approximately the same behaviour of the broader Lorentzian at 373 and 423 K. Therefore, $L_2(Q,\omega)$ may be assigned to vibrational motions, even if the crystal structure is not any more present in the liquid state.

Normalized intensities can be calculated following the same procedure of the two previous temperatures, and they are shown in fig. 6.10. As claimed above, the sample is already in the liquid state and the first decomposition step has already started. According to the decomposition of the single species, $Mg(BH_4)_2$ and $LiBH_4$, the following two reaction schemes

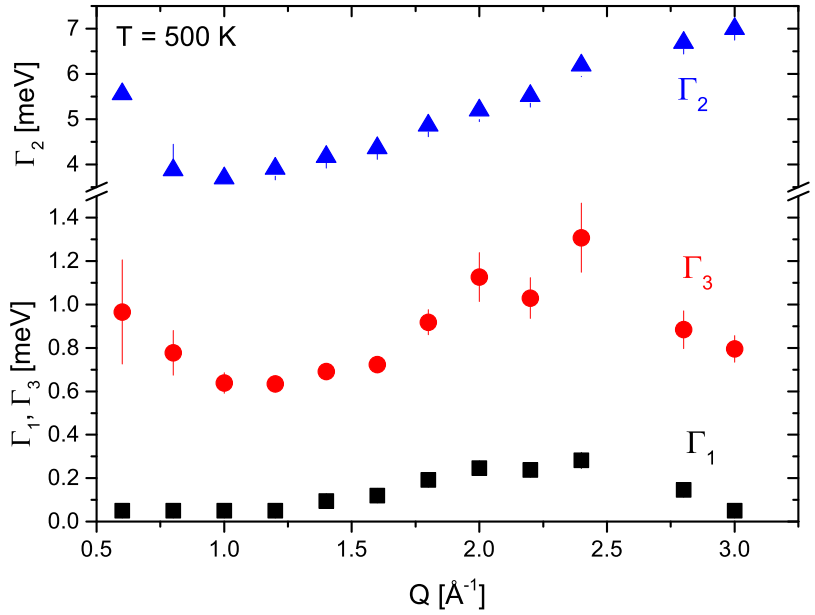

Figure 6.9: 0.5 h-Li^{11}BH$_4$ + 0.5 β-Mg(^{11}BH$_4$)$_2$. Widths of the Lorentzians $L_1(Q,\omega)$, $L_2(Q,\omega)$ ans $L_3(Q,\omega)$ at 500 K: Γ_1 (black squares), Γ_2 (blue triangles) and Γ_3 (red circles). Error bars denote $\pm 1\sigma$.

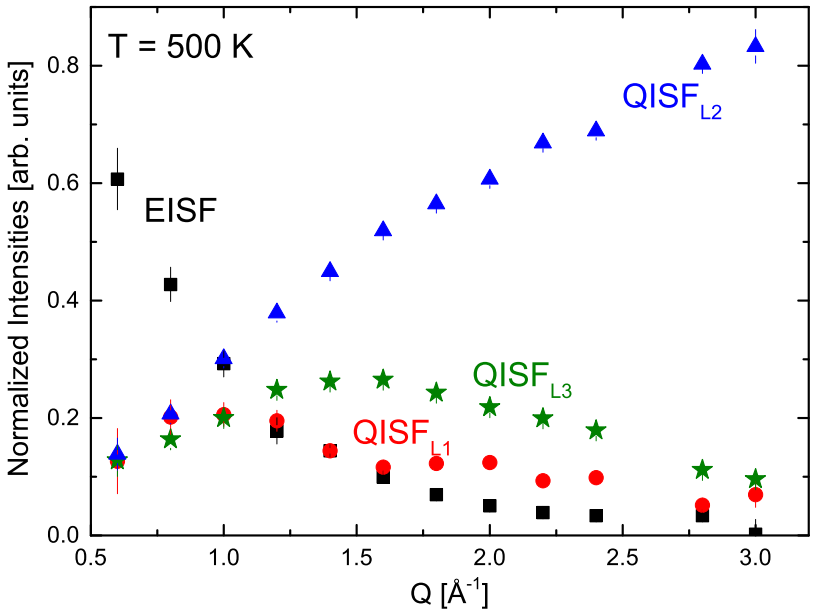

Figure 6.10: 0.5 h-Li^{11}BH$_4$ + 0.5 β-Mg(^{11}BH$_4$)$_2$. EISF (black squares), QISF$_{L_1}$ (red circles), QISF$_{L_3}$ (green stars)and QISF$_{\mathrm{Vib}}$ (blue triangles) at 500 K. Error bars denote $\pm 1\sigma$.

can be written (at up to the first decomposition step):

$$\mathrm{Mg(BH_4)_2} \longrightarrow \mathrm{MgH_2} + 2\,\mathrm{B} + 3\,\mathrm{H_2} \tag{6.18}$$

$$\mathrm{LiBH_4} \longrightarrow \mathrm{LiH} + \mathrm{B} + \frac{3}{2}\,\mathrm{H_2}. \tag{6.19}$$

In the mixture, then, it is reasonable to write:

$$\mathrm{LiBH_4} + \mathrm{Mg(BH_4)_2} \longrightarrow \mathrm{MgH_2} + \mathrm{LiH} + 3\,\mathrm{B} + \frac{9}{2}\,\mathrm{H_2} \tag{6.20}$$

In a liquid, the scattering signal is characterised by the absence of an elastic line. Nevertheless, the reaction products MgH_2 and LiH are not performing any reorientation motion, since they are solid and not undergoing in any reorientational motions. Therefore, in a quasi-elastic experiment, they would contribute to the total scattering intensity with an elastic signal. A calculation of the partial cross-sections can be performed in order to discriminate the contributions to the elastic and quasi-elastic one.

	σ_{coh} [barn]	σ_{inc} [barn]
$\mathrm{Li^{11}BH_4}$	13.01	322.17
$\mathrm{Mg(^{11}BH_4)_2}$	28.75	642.58
LiH	2.21	81.18
$\mathrm{MgH_2}$	7.13	160.6
$3\,^{11}\mathrm{B}$	16.68	0.63
$\frac{9}{2}\,\mathrm{H_2}$	15.75	722.34

In total, the LiH, MgH_2 and 3 B would give an incoherent cross sections of 242.42 barn, while the $\frac{9}{2}\,H_2$ would give 722.34 barn. Therefore, approximatively 75% of the signal would be lost, due to the H_2 gas liberation. The other 25% would be originating by LiH and MgH_2.

In the first decomposition step, TG-DSC-MS measurements show also the formation of boranes [28]. Therefore, a partial sample decomposition could be written as:

$$\mathrm{LiBH_4} + \mathrm{Mg(BH_4)_2} \longrightarrow x\,(\mathrm{LBH\text{-}MBH})_{\mathrm{liq}} + x'\mathrm{B}_x\mathrm{H}_y + x''\mathrm{LiH\text{-}MgH_{2\ (sol)}} + z\mathrm{H_{2\ (gas)}}, \tag{6.21}$$

and the sum of scattering signal of LiH and MgH_2 should not exceed 25% of the scattering intensity of $LiBH_4 + Mg(BH_4)_2$ before the decomposition step. In fact, the drop of the total intensity is due to the H_2 gas desorption, part of the sample is decomposed in LiH and MgH_2 (both solids) and part is the molten state composed of $LiBH_4 + Mg(BH_4)_2$. Therefore, the decomposition of the scattering signal as a sum of the scattering intensities of $LiBH_4$ and $Mg(BH_4)_2$ is not applicable.
A possible motion of the $[BH_4]$ units can be the diffusion inside the volume of a sphere (see eq. 2.65). On the selected time scale, the $[BH_4]$ units might undergo translational diffusion:

the lattice structure is lost [28], due to the melting , but the local environment of $[BH_4]$ might be still preserved, because the physical mixture is not totally decomposed.

The model was developed by Volino *et. al* [113], in which the scattering function is described as an expansion of a number of Lorentzians, in principle infinite (eq. 2.65):

$$S_{\text{diff}}(Q,\omega) = A_0^0(Q)\,\delta(\omega) + \sum_{(l,n)\neq(0,0)} (2l+1)\,A_n^l(Q)\,\frac{1}{\pi}\frac{\left(x_n^l\right)^2 D/a^2}{\left[\left(x_n^l\right)^2 D/a^2\right]^2+\omega^2}. \tag{6.22}$$

Lorentzians are characterized by a HWHM of $\left(x_n^l\right)^2 D/a^2$, where D is the diffusion coefficient and a is the radius of an hypothetical sphere, in which space the diffusion takes place. The EISF is

$$\text{EISF} = A_0^0(Q) = \left[\frac{3j_1(Qa)}{Qa}\right]^2. \tag{6.23}$$

Trying to model the data with more than four functions, including the elastic line, the fit procedure becomes unstable. The quasi-elastic components in eq. 6.22 are characterized by constant widths, whereas the experimental found show Q-dependencies. This discrepancy might be originated from the fact that the data should be modelled by a (theoretically) infinite series of functions, and the experimental Lorentzians L_1, L_3 and L_2 might results from a combination of different Lorentzians with different (constant) HWHMs and modulated intensities ($A_n^l(Q)$). Therefore, a direct comparison between theoretical and experimental EISF and QISFs is not possible, using a global approach as in the previous temperature data analysis.

However, taking into account the partial decomposition of the sample, the scattering function can be expressed as

$$S_{500\text{ K}}(Q,\omega) = cS_{\text{LiH-MgH2 (sol)}}(Q,\omega) + (1-c)S_{\text{LBH-MBH(liq)}}(Q,\omega), \tag{6.24}$$

where $S_{\text{LBH-MBH(liq)}}(Q,\omega)$ represents the scattering function of the molten $Mg(BH_4)_2 + LiBH_4$, and $S_{\text{LiH-MgH2 (sol)}}(Q\omega)$ the scattering function of the solid $LiH + MgH_2$. The scattering function of the liquid part can be described by a vibrational part and the localized one (eq. 6.22), whereas for the solid $LiH + MgH_2$ only a vibrational scattering function is used. Without going into the calculation details, the EISF can be derived only taking into account the elastic terms in the scattering function:

$$\text{EISF}_{500\text{ K}} = D(Q)\left[c + (1-c)\,A_0^0(Q)\right]. \tag{6.25}$$

$D(Q)$ is the Debye-Waller term and $A_0^0(Q)$ is given in eq. 6.23. Results of the fit using this model are shown in fig. 6.11. The fit gives an estimation of the radius of a spheres, in which the diffusion takes place, the mean square displacement of H atoms and the fraction c of the

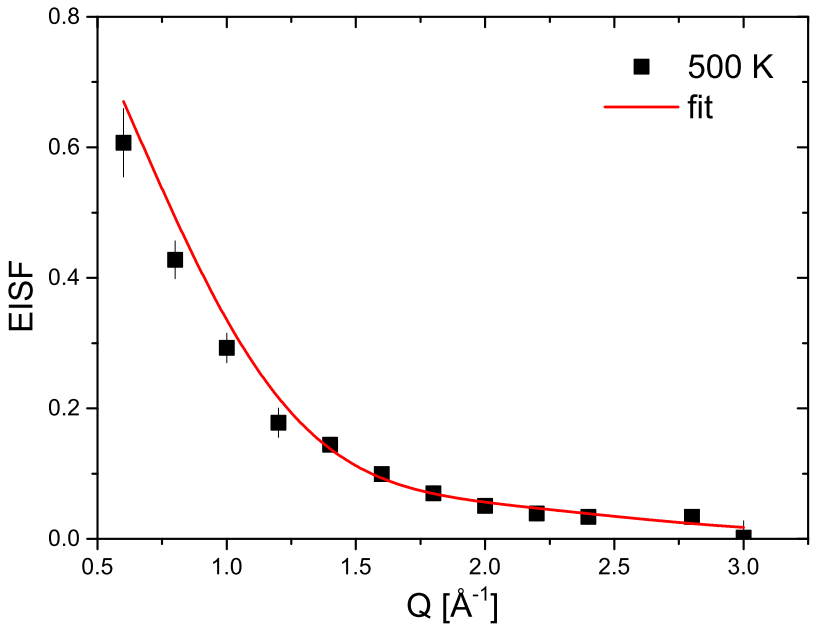

Figure 6.11: $LiBH_4 + Mg(BH_4)_2$: EISF at 500 K (black squares), together with the fit of eq. 6.25. Error bars denote $\pm 1\sigma$.

decomposition products:

$$\begin{aligned} \langle u^2 \rangle &= 0.71 \pm 0.15\,\text{Å}^2 \\ c &= 0.14 \pm 0.03 \\ a &= 2.26 \pm 0.09\,\text{Å} \end{aligned} \tag{6.26}$$

The fraction c that is extracted is quite low, indicating that the signal deriving from $LiH + MgH_2$ is rather low. Most of the scattering is originating by the diffusion of the H atoms of the molten $LiBH_4 + Mg(BH_4)_2$.
In β-$Mg(BH_4)_2$ (at 500 K, but still in the solid state), it was reported

$$\langle u^2 \rangle_{500\,\text{K}} = 0.92 \pm 0.03\,\text{Å}^2, \tag{6.27}$$

which is close to the above reported value.

Analysis of the $I(Q,t)$ Data are analysed using the intermediate scattering representation $I(Q,t)$. A Fourier transform in ω is performed for each of the spectra at constant Q and some of the intermediate scattering functions in the time domain are shown in fig. 6.12. As we can observe, the intensity of the scattering curves is generally decreasing with increasing Q. At relatively long time, each curve tends to reach a plateau, that represents the elastic incoherent structure factor, in mathematical form:

$$\text{EISF} = \lim_{t\to\infty} I(Q,t). \tag{6.28}$$

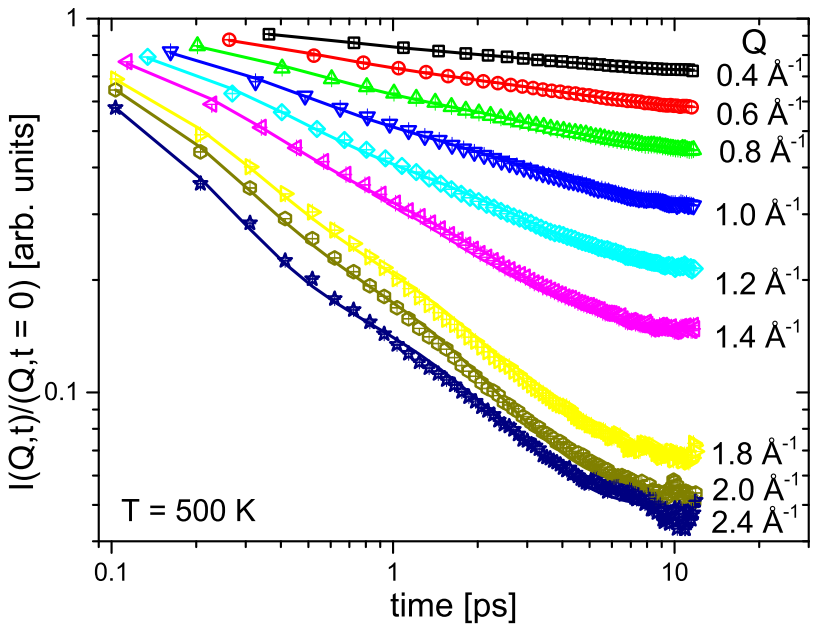

Figure 6.12: $I(Q,t)$ of $LiBH_4 + Mg(BH_4)_2$ at 500 K. Each curve correspond to a specific Q value indicated on the right side. Solid lines are the fit to the data according to eq. 6.29

Data might be described by a series of exponentials, that describe different motions taking part at different time scale. Two exponential decaying functions are sufficient to describe the data, and the intermediate scattering function can be written as:

$$I_{500K}(Q,t) = k + (1-k)\left[b\exp\left(-\frac{t}{\tau_1}\right) + (1-b)\exp\left(-\frac{t}{\tau_2}\right)\right]. \tag{6.29}$$

The parameter k represents the long time limit of the intermediate scattering function and, by definition, corresponds to the EISF. Parameters τ_1 and τ_2 are the time constants of the two different motions that are detected in the observed time scale. The dependence of τ_1 and τ_2 from the momentum transfer Q is related to the type of the motion: if the atoms are performing localized reorientations, τ_1 or τ_2 are constant over the momentum transfer range; conversely, the particle undergoes in diffusion-like motions. The parameter b represents the relative weight of the motions detected at this temperature. Most prominently, the dynamics can not be described by a superposition of $LiBH_4$ and $Mg(BH_4)_2$ dynamics, and this is only partially due to the partial sample decomposition. Therefore, the parameter b is not related to any weight of the different species in the sample.

The results of the fit are shown in figs. 6.14 and 6.13. Parameters τ_1 and τ_2 are plotted in fig. 6.14, and both are showing a Q-dependence: this suggests that the H motions are not localized. In order to extract a possible diffusion coefficient from the two detected dynamics, we plot the inverse of the time parameters versus Q^2, as shown in figs. 6.15 and 6.16, together with a linear fit. At high Q, a deviation from the linear regime is observed

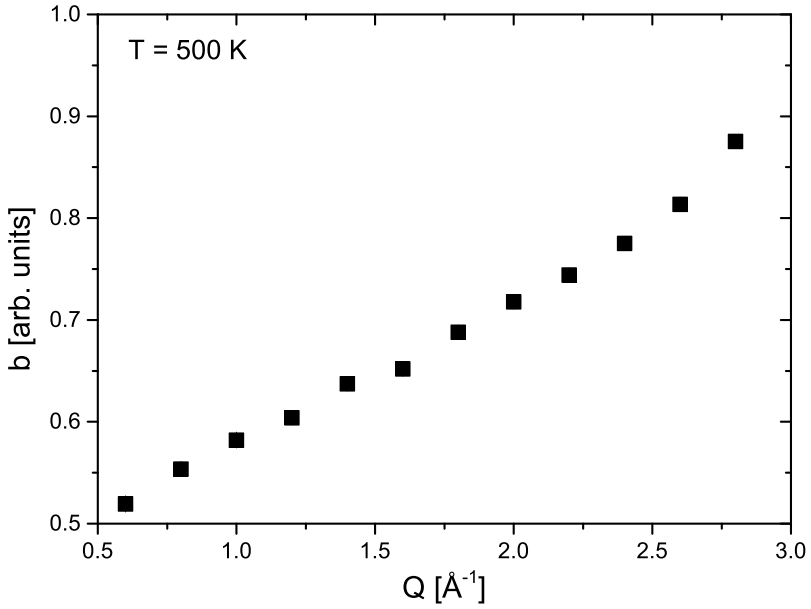

Figure 6.13: $LiBH_4 + Mg(BH_4)_2$ at 500 K: parameter b as a function of Q (see eq.6.29).

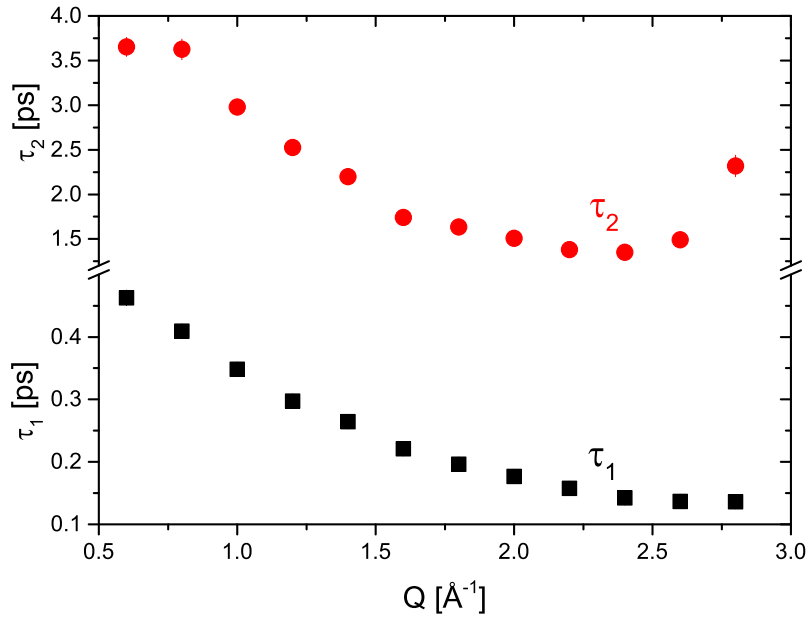

Figure 6.14: $LiBH_4 + Mg(BH_4)_2$ at 500 K. Time parameters τ_1 (black squares) and τ_2 (red circles) extracted from the data fit with eq. 6.29. Both time parameters are showing a Q dependence. Note that the maximum observation time at the selected energy resolution is ~ 3.3 ps.

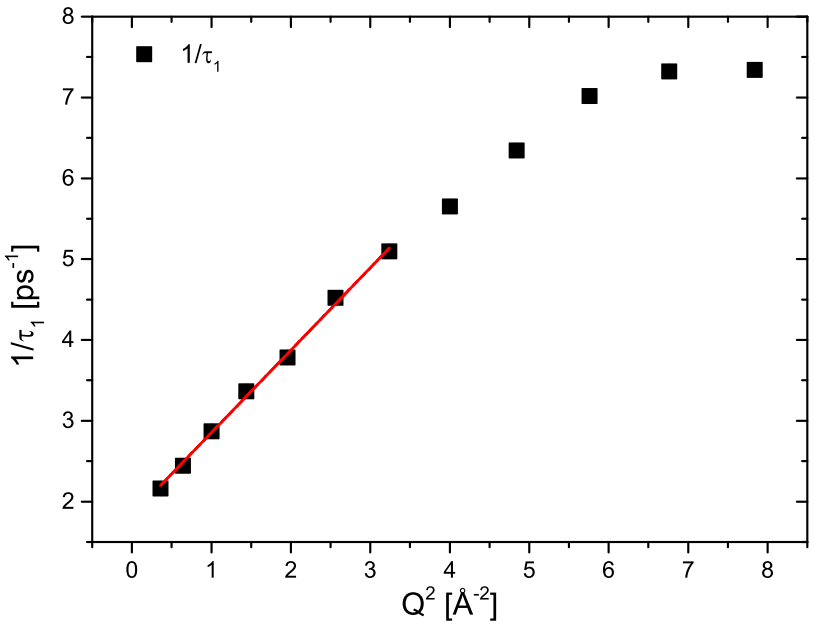

Figure 6.15: Inverse of the time parameter τ_1 plotted as a function of Q^2. The straight line is a linear fit to the data in the relatively small region of Q (see eq. 6.30). The diffusion coefficient can be extracted from the slope of the linear fit. In this case, $D_1 = (1.02 \pm 0.03) \cdot 10^{-4} \frac{\mathrm{cm}^2}{\mathrm{s}}$.

in both quantities. This is somehow expected, because motions are spatially restricted, as shown above. However, at low Q, a linear dependence is always valid, independent of the diffusion mechanism [107, 137]. Therefore, data are fitted with a linear function only in the low momentum transfer region. The diffusion coefficient is related to the time constant trough the following relation:

$$\frac{1}{\tau_i} = D_i Q^2, \text{ with } i = 1, 2. \tag{6.30}$$

From the slope of the linear fits, we can extract two different self-diffusion coefficients:

$$D_1 = (1.02 \pm 0.03) \cdot 10^{-4} \frac{\mathrm{cm}^2}{\mathrm{s}}, \qquad D_2 = (1.28 \pm 0.09) \cdot 10^{-5} \frac{\mathrm{cm}^2}{\mathrm{s}}. \tag{6.31}$$

The self-diffusion coefficient in $LiBH_4$ was already measured up to 723 K, above the melting point at 550 K [64]. In that work, an Arrhenius-like temperature dependence was found:

$$D = D_0 \exp\left(-\frac{E_\mathrm{a}}{k_\mathrm{B} T}\right), \text{ with } E_\mathrm{a} = 88 \pm 15\,\mathrm{meV} \quad D_0 = (3.1 \pm 1) \cdot 10^{-4} \frac{\mathrm{cm}^2}{\mathrm{s}} \tag{6.32}$$

Substituting $T = 500\,\mathrm{K}$, we obtain a diffusion coefficient $D_{500\,\mathrm{K}} = (4 \pm 2) \cdot 10^{-5} \frac{\mathrm{cm}^2}{\mathrm{s}}$, a value not far from D_2 obtained in this work. Therefore, it is possible to assign the self-diffusion coefficient D_2 to the $[BH_4]$ units in the liquid $LiBH_4 + Mg(BH_4)_2$. The other diffusion coefficient is one order of magnitude bigger than D_2.

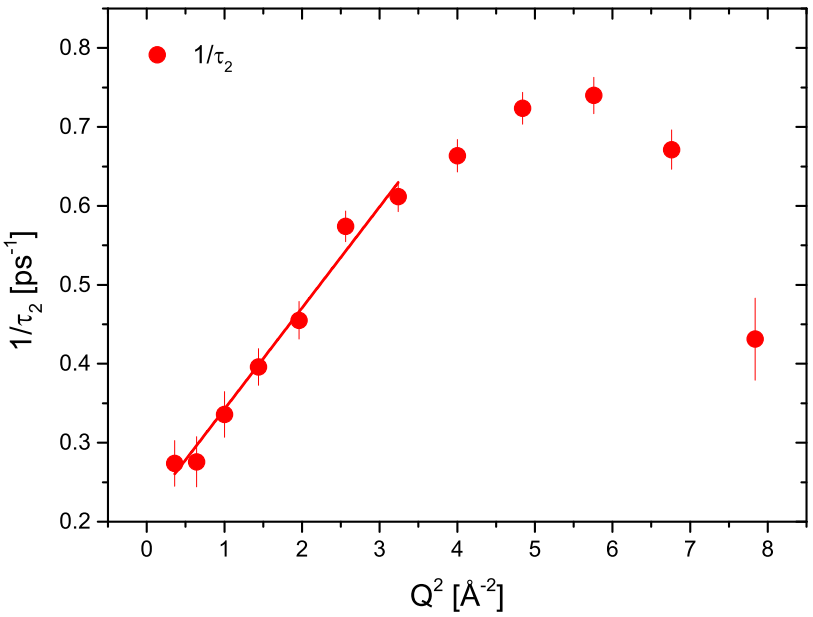

Figure 6.16: Inverse of the time parameter τ_2 plotted as a function of Q^2. The straight line is a linear fit to the data in the relatively small region of Q (see eq. 6.30). The diffusion coefficient can be extracted from the slope of the linear fit. In this case $D_2 = (1.28 \pm 0.09) \cdot 10^{-5} \frac{\mathrm{cm}^2}{\mathrm{s}}$.

In fig. 6.17, the EISF derived from $I(Q,t)$ is plotted together with the EISF calculated as the ratio of the elastic line and the total intensity derived from $S(Q,\omega)$. The agreement is quite satisfactory, although in the low Q region some discrepancies are evident.%. The parameters obtained from the fit to the data are:

$$\begin{aligned} \langle u^2 \rangle &= 0.53 \pm 0.11\,\text{Å}^2 \\ c &= 0.14 \pm 0.03 \\ a &= 1.96 \pm 0.03\,\text{Å} \end{aligned} \tag{6.33}$$

Parameters extracted are in a good agreement with the ones extracted from the EISF measured as the ratio between the elastic line and the total intensity 6.27. A comparison is plotted in fig. 6.18.

6.3.4 373 K - back measurements

After the measurements at 500 K, the sample was cooled down to 373 K, in order to verify the reversible crystal phase transition from β-($Fddd$) to α-($P6_122$) of magnesium borohydride. The scattering signal is 30 % lower of the measurements performed at the same temperature when the experiments started, due to the hydrogen decomposition process at 500 K.
According to the decomposition scheme, the sample contains, in addition to $LiBH_4$ and $Mg(BH_4)_2$, the decomposition products.

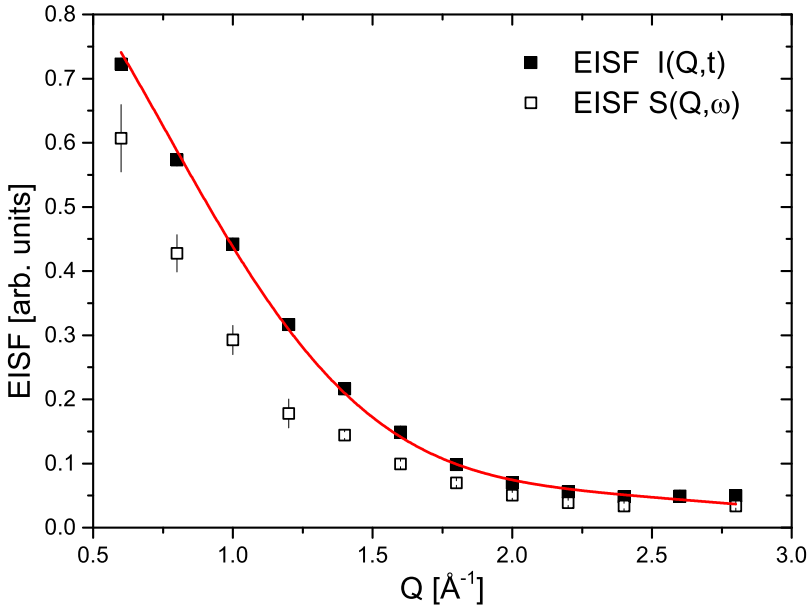

.

Figure 6.17: EISF derived from the parameter k in eq. 6.29 (black squares). The empty symbols represent the EISF calculated from the ratio between the elastic and the total scattering intensity of $S(Q,\omega)$ (see fig.6.11). The solid line is the fit to the data with eq. 6.25

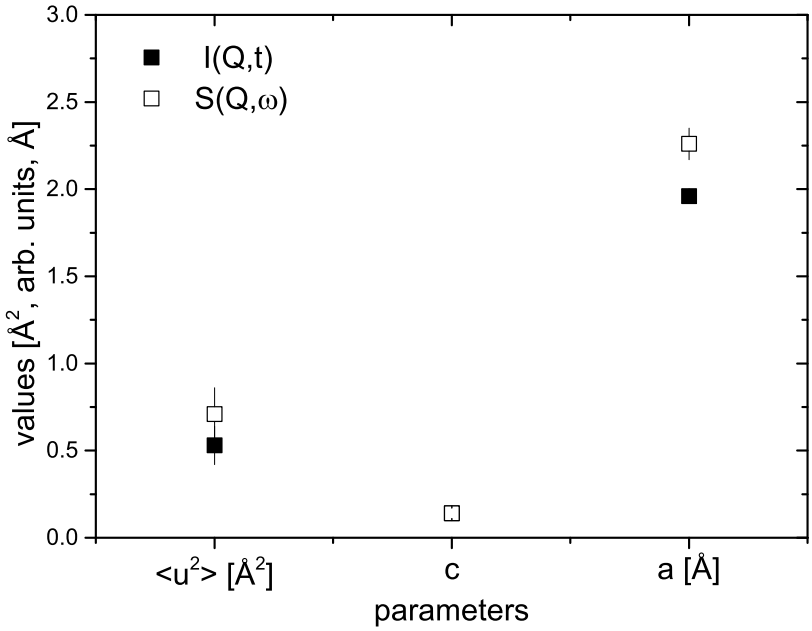

Figure 6.18: Parameters obtained from the analysis of the EISF derived from $I(Q,t)$ (full symbols) and the EISF derived from the ratio between the elastic line and the total scattering intensity (empty symbols). The model used to fit the EISF is described in eq. 6.25.

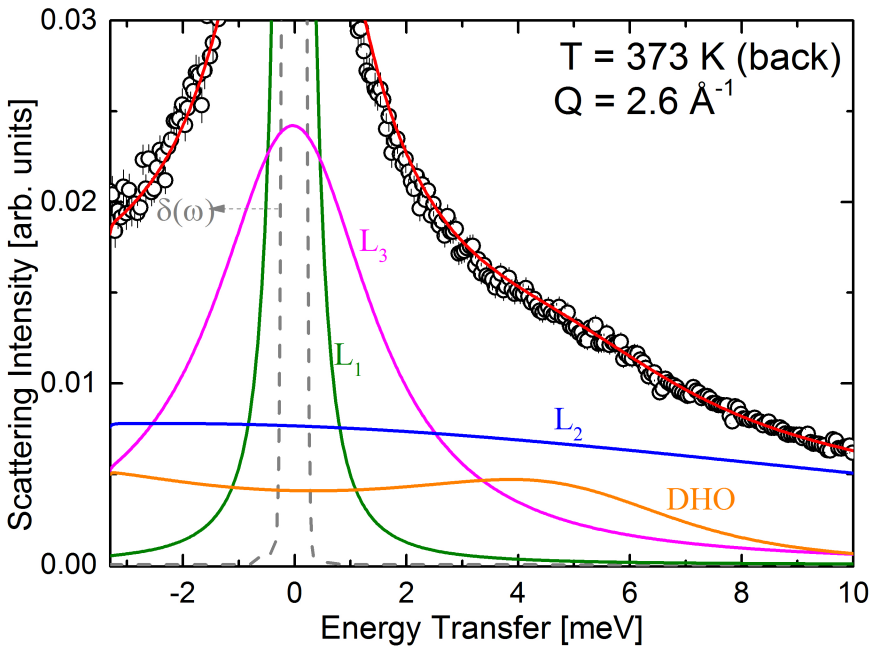

Figure 6.19: Scattering data at 373 K (back measurements) and at $Q = 2.6\,\text{Å}^{-1}$. Solid red line represents the fit. Data are described using a $\delta(\omega)$ line (grey dashed), two narrow Lorentzians (green and magenta) a DHO (orange) and a broad Lorentzian (blue).

Data were analysed using three Lorentzians, an elastic line and a damped harmonic oscillator. Results are quite satisfactory, as shown in fig. 6.19.

We can observe that the inelastic peak at $\sim 4.5\,\text{meV}$ is again visible and, as mentioned before, it can be assigned to vibrational motions of the $[BH_4]$ units in α-$Mg(BH_4)_2$. Lorentzians widths can be extracted and both are constant in the explored momentum transfer Q, with $\Gamma_1 = 0.19 \pm 0.03\,\text{meV}$ and $\Gamma_3 = 1.6 \pm 0.2\,\text{meV}$ (see fig. 6.20). At this temperature, both $LiBH_4$ and $Mg(BH_4)_2$ are expected to be in the orthorhombic and hexagonal crystal phases, respectively. The valued of Lorentzian widths Γ_1 and Γ_3 are similar to Γ_1 and Γ_3 at 423 K (assigned to α-$Mg(BH_4)_2$ and to HT-$LiBH_4$, respectively). Data are shown in fig. 6.21. As we can observe, EISF and QISFs are similar to the one measured at 423 K (see fig. 6.7), but the analysis is not performed due to the presence of the decomposition products in the sample.

6.4 Conclusions

The eutectic mixture $0.5LiBH_4$+$0.5Mg(BH_4)_2$ was studied by quasi-elastic neutron scattering in the picosecond time scale. Below the melting point, the hydrogen dynamics is the superposition of the dynamics of the single constituent phases, $LiBH_4$ and α-$Mg(BH_4)_2$: $LiBH_4$ undergoes tumbling rotations, with the $[BH_4]$ units reorienting among all symmetry

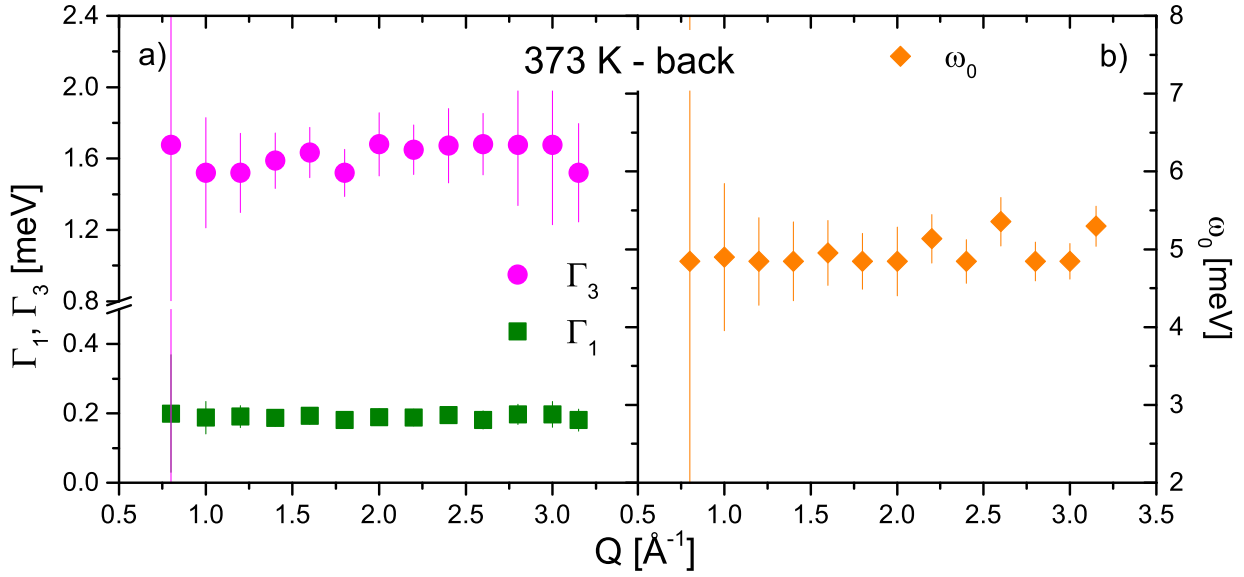

Figure 6.20: Parameter from data fit at 373 K - back measurements. a) widths of $L_1(Q,\omega)$ and $L_3(Q,\omega)$. b) DHO frequency ω_0 and damping Γ_q.

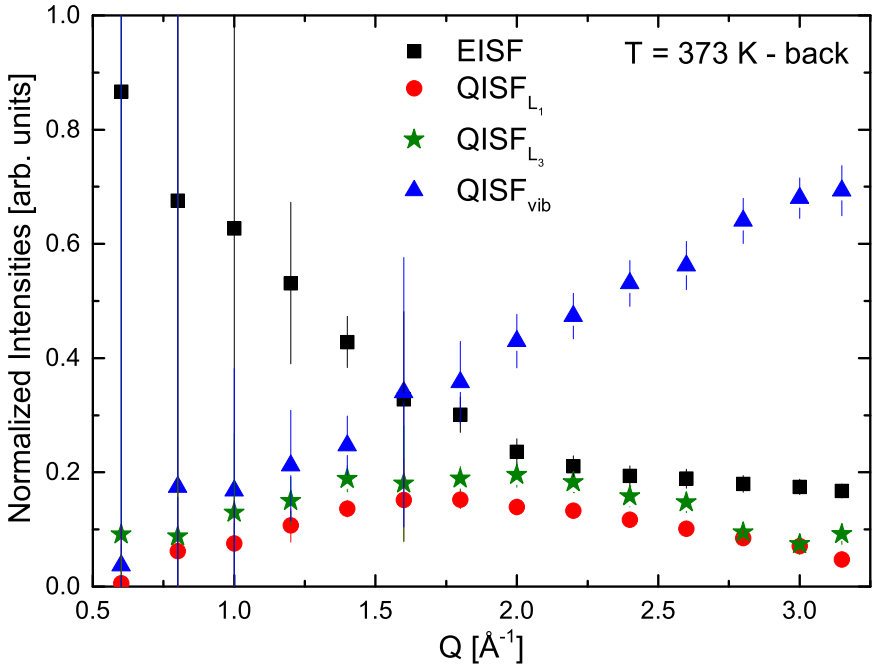

Figure 6.21: EISF (black squares), QISF$_{L_1}$ (red circles), QISF$_{L_3}$ (green stars) and QISF$_{\text{Vib}}$ (blue triangles) at 373 K (back measurements).

axes, and $Mg(BH_4)_2$ undergoes hindered rotational dynamics with the $[BH_4]$ units performing rotations along the C_2/C_3 axis. At 423 K, the fraction of hindered rotations is still more than 30%.

At the melting point, the mixture is in the liquid state and the dynamics changes. The dynamics can not be described as a superposition of the single constituent phases' dynamics, due to the partial sample decomposition.
The partial decomposition leads to a formation of lithium and magnesium hydrides, which are still solid at 500 K, and, at the same time, a loss of scattering signal of roughly 30 %. The analysis in the intermediate scattering function representation allows a better identification of the dynamics taking place in the liquid phase. The $[BH_4]$ units undergo isotropic diffusion, but spatially restricted. Two different relaxation times are observed, and two self-diffusion coefficients are extracted. The lower one is $D_2 = (1.28 \pm 0.09) \cdot 10^{-5} \frac{\mathrm{cm}^2}{\mathrm{s}}$, similar to the diffusion coefficient previously reported in liquid $LiBH_4$, and it can be tentatively assigned to $[BH_4]$ units diffusive dynamics. The faster one is one order of magnitude bigger ($D_1 = (1.02 \pm 0.03) \cdot 10^{-4} \frac{\mathrm{cm}^2}{\mathrm{s}}$).

The experiment also probes the reversibility of the crystal phase transition in $Mg(BH_4)_2$, and it is confirmed by the analysis of the inelastic excitation around $\sim 4.5\,\mathrm{meV}$ at 373 K, assigned to α-$Mg(BH_4)_2$.

Chapter 7

General discussion and conclusions

Contents

7.1 Hydrogen dynamics on the picosecond time scale

In this thesis, the hydrogen dynamics in $LiBH_4$, $Mg(BH_4)_2$ and $LiBH_4 + Mg(BH_4)_2$ was investigated on the picosecond time scale. The main goal was to get further insight to the hydrogen dynamics in the alkaline and earth alkaline borohydrides in their different structural modifications and to study the influence of the electronegativity of the cation on the hydrogen dynamics, especially in view of the reported correlation between cation electronegativity and borohydride stability [*reference*]. Measurements were performed at the cold neutron time-of-flight spectrometer TOFTOF (Forschungs-Neutronenquelle Heinz Maier-Leibnitz (FRM II) [116]).

The materials under study have a hydrogen content which might be of interest for use as storage materials in mobile applications. Unfortunately, the harsh conditions for dehydrogenation and hydrogenation prevent direct applications. Beside studies on destabilization and on sorption properties, basic studies on structure and hydrogen dynamics are essential to fully understand, characterize and optimize the materials. In this framework, the hydrogen dynamics in the picosecond time scale and across a wide range of temperatures was studied.

The large momentum transfer explored by TOFTOF, together with a good energy resolution, played a crucial role in the determination of the reorientation mechanisms in all compounds studied in this thesis. The high signal-to-noise ratio made possible the measurements of low energy inelastic excitations close to the quasielastic region. At high temperatures, both signal are superimposed, thus the measured $S(Q, \omega)$ were analysed considering

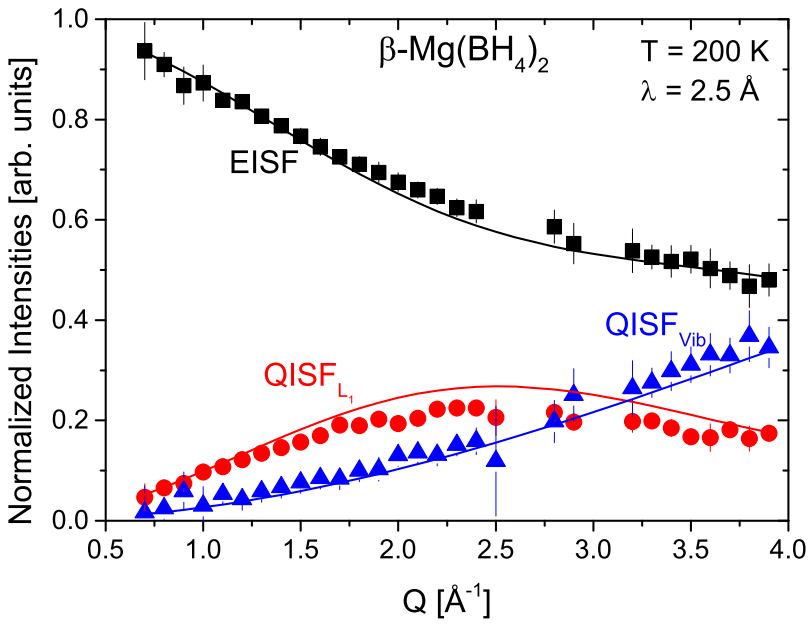

Figure 7.1: Normalized intensities of β-$Mg(BH_4)_2$, measured at 2.5 Å and at 200 K. EISF (black squares), $QISF_{L_1}$ (red circles), $QISF_{L_{inel}}$ (blue triangles). Solid lines represent the fit to the data with the full expressions of EISF and QISFs, in a global optimization procedure (see section 2.1.2.3).

the elastic, quasielastic and inelastic contributions in the low energy transfer regime, and the elastic and quasielastic incoherent structure factors were evaluated. From a global analysis of these factors, a detailed description of localized motions and the lattice vibrational part was obtained (fig. 7.1).

In all three materials, common and different characteristics are found. These will be reviewed in the following sections, comparing different quantities in different materials.

7.1.1 Localized dynamics

- In $LiBH_4$, the dynamics was investigated below and above the crystal phase transition at 381 K. The global analysis of the EISF and QISFs allowed a clear mechanism identification of the $[BH_4]$ units local reorientations. At 343 K, uni-axial C_3 rotations were observed, with one hydrogen atom fixed and the other three rotating in a circle, with 120Â° jump rotations. At 373 K, i.e. close to the crystal phase transition, the $[BH_4]$ units are undergoing tumbling motions, where all four H atoms exchange the position. Therefore, rotations around all four C_3 symmetry axis might occur, without any fixed H atom. At 403 K, all four C_3 axes contribute to the rotations, but three H atoms rotate quasi-free around one specific C_3 axis [126].
  Notably, $LiBH_4$ shows a change in localized dynamics already below the crystal phase transition, and it can be concluded that this acts as a precursor of the crystal phase

transition.

- In α-$Mg(BH_4)_2$, the localized dynamics was investigated on two different time scales, in order to observe dynamics up to 16 ps. The crystal structure shows different $[BH_4]$ sites in the unit cell, and rotations around a C_2 or C_3 axis of the $[BH_4]$ units are observed. Up to 400 K, not all rotations are activated, showing a significant portion of hindered rotations. This can be attributed to the different crystallographic positions of the $[BH_4]$ (not equivalent) which apparently has a large impact on the local dynamics in this polymorph. Moreover, no change in the local dynamics is observed as the phase transition is approached, in contrast to the findings for $LiBH_4$. Above the phase transition ($T > 490\,K$), a strong change in the vibrational part becomes obvious.

- In β-$Mg(BH_4)_2$, the localized dynamics is similar to the one observed in the α-polymorph, but it shows a different degree of activation: above 200 K, no hindered rotations are detected. Furthermore, a change in the vibrational dynamics was observed between 200 K and 300 K, without any crystal structure transition. However, the thermal expansion coefficients of the lattice parameters also reflect a transition in this temperature range[135].
  In conclusion, differences between α- and β-$Mg(BH_4)_2$ are in the vibrational dynamics and in the degree of activation of rotational motions. There is no indication that a change in localized $[BH_4]$ rotations triggers the phase transition, but, similar to $Ca(BH_4)_2$, the vibrational dynamics drives the structural phase transition.

7.1.2 Vibrational dynamics

In all compounds, low lying vibrational modes were detected in the range $3 - 9\,meV$, energetically close to and overlapping with the QENS signal. In the data evaluation, these excitations were described by damped harmonic oscillators (see fig 7.3), and the total scattering intensity was taken into account in the calculation of the normalized intensities.
From the global analysis, the mean square displacement of hydrogen atoms was obtained and mapped across the crystal phases transitions (see fig 7.2). The frequency of the lowest inelastic contribution decreases in the order $LiBH_4$ - α-$Mg(BH_4)_2$ - β-$Mg(BH_4)_2$. In all compounds, the frequency does not show any dependence on temperature, however in $LiBH_4$ and β-$Mg(BH_4)_2$, a transition from an under-damped to an over-damped harmonic oscillator is observed. The Debye-Waller factor, DWF, increases with temperature, and its temperature dependent increase reflects the change in the inelastic mode, from under-damped to over-damped, observed in $LiBH_4$ and β-$Mg(BH_4)_2$. Conversely, α-$Mg(BH_4)_2$ shows a linear dependence of the DWF with temperature.

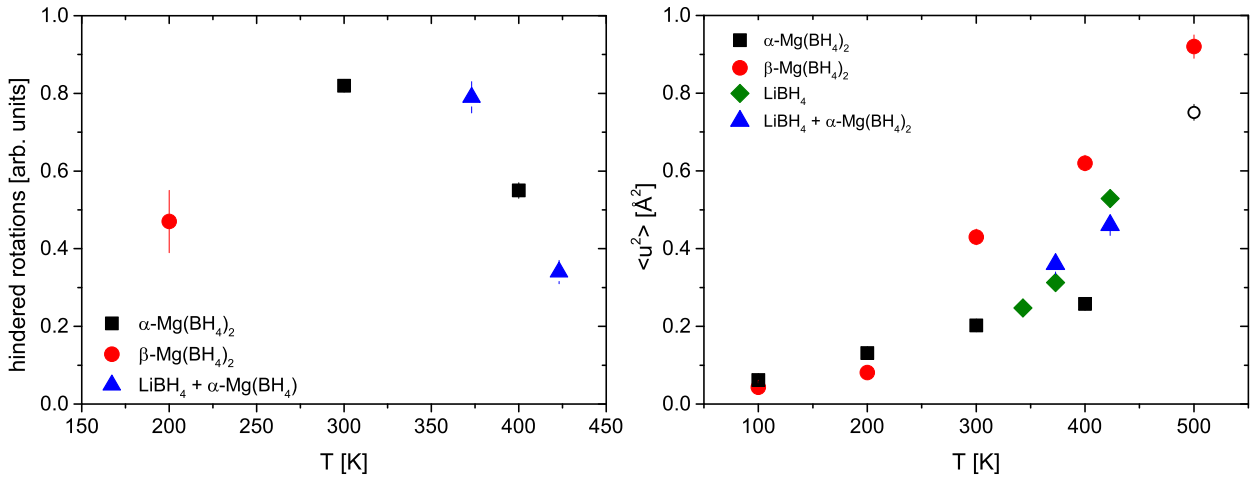

Figure 7.2: Left: fraction of hindered rotations in $Mg(BH_4)_2$ and in $LiBH_4$ + $Mg(BH_4)_2$, as a function of temperature. **Right:** mean square displacements obtained by the global analysis of the normalized scattering intensities as a function of temperature. (see text for details).

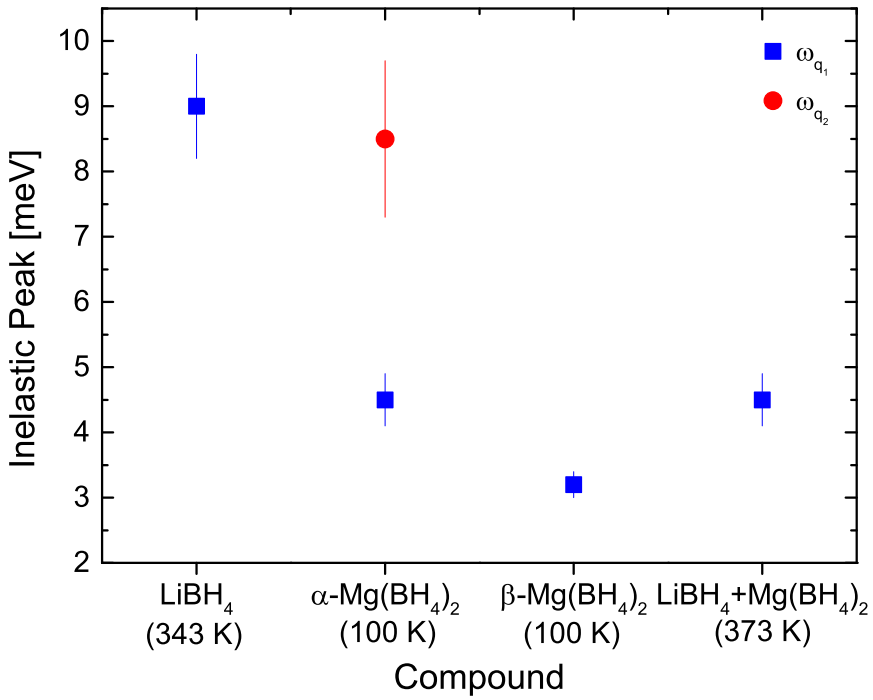

Figure 7.3: Vibrational frequencies of the damped harmonic oscillator(s) used to describe the inelastic excitations in the QENS spectra.

7.2 Conclusions and Future perspectives

In this thesis, fundamental aspects of $LiBH_4$, $Mg(BH_4)_2$ and $LiBH_4$+$Mg(BH_4)_2$ have been studied, and the conclusions are briefly summarised.

- An extensive study of the low energy excitation in borohydride materials has been carried out at the time-of-flight spectrometer TOFTOF. Lattice vibrations in the low energy transfer range were observed for the first time in $LiBH_4$, α- and β-$Mg(BH_4)_2$. They superimpose the quasielastic signal originating from the $[BH_4]$ reorientations. Therefore, an innovative data analysis was developed in order to evaluate both vibrational and quasielastic signals. A convolution of rotational and vibrational scattering functions was performed, and the normalized intensities (EISF and QISFs) were calculated. These quantities were directly compared with the experimentally measured ones, in a simultaneous analysis of the elastic and quasielastic incoherent structure factors. Using this approach, not only information on the reorientations of the $[BH_4]$ units were obtained (e.g. fractions of hindered rotations), but also information on the vibrational dynamics, and in particular on the mean square displacement of the hydrogen atoms [136].

- The cation electronegativity (χ_P) is strongly connected to the $[BH_4]$ dynamics. In $LiBH_4$, where the electronic charge density between $[BH_4]^-$ and Li^+ is well separated, the reorientational dynamics of the $[BH_4]$ units evolves with temperature, changing its nature across the crystal phase transition. The local $[BH_4]$ rotations thus drive the structural phase transition.
  In $Mg(BH_4)_2$, where there is a less pronounced charge density separation between the hydrogen and the cation, the rotation symmetry of the $[BH_4]$ units remains unchanged over the entire temperature range studied. Moreover, it is the same in both polymorphs, but the two crystal phases differ in the degree of activation of these localized motions. The bidentate orientation of the $[BH_4]$ units towards the Mg^{2+} cation yields to a chain-like structure $\cdots BH_4\text{-}Mg\text{-}BH_4 \cdots$, which, presumably, are the origin of low energy lattice excitations. [136].

- Lattice vibrations in the low energy transfer range were observed for the first time in $LiBH_4$, α- and β-$Mg(BH_4)_2$. They are ascribed to translational modes of the $[BH_4]$ units. Remarkably, the two polymorphs of $Mg(BH_4)_2$ studied here, show significant differences in the low energy lattice dynamics. α-$Mg(BH_4)_2$ displays a pronounced harmonic behaviour, with a higher vibrational energy compared to the β-polymorph. This is also reflected in the mean square displacement of the hydrogen atoms. The low energy dynamics modifies the free energy landscape of the crystal structure, and therefore the stability of the compound.

- The mixture of $LiBH_4$ and $Mg(BH_4)_2$, in the 1:1 ratio, is characterized, below the melting point, by a superposition of the dynamics of the single constituent phases. The dynamics can be decomposed in the dynamics of the compounds in a 1:2 ratio, according to relative hydrogen content of the pure compounds. Above the melting point, two diffusive processes are found. These finding confirm the physical mixture of the two constituents, and from a dynamical point of view, no indication for a new compound was found.

The study of hydrogen dynamics in borohydrides could be extended to other compounds dedicated to hydrogen storage, e.g. calcium borohydride or to eutectic mixtures of complex hydrides [138]. Measurements close to the temperature of hydrogen release could yield insights on the processes and reaction pathways related to the hydrogen desorption. Destabilization strategies include the modification of the structure, leading to a modification of the vibrational dynamics at low energies. This could be a key point of a successful implementation of these materials in the storage applications.

Appendices

Appendix A

Vibrational scattering function

The normalization of the self correlation function, imposes that the incoherent scattering function $S_{\text{inc}}(Q,\omega)$ is also properly normalized. In case of vibrations, this results in:

$$\int_{-\infty}^{+\infty} S_{\text{vib}}\left(Q,\omega\right)\mathrm{d}\omega = 1. \tag{A.1}$$

The vibrational scattering function is characterized by an elastic line $\delta(\omega)$, multiplied by a factor $D(Q)$, the so-called Debye-Waller factor. In isotropic approximation, we can write it as:

$$D(Q) = \exp(-2W(Q)) = \exp\left(-\frac{\langle u^2\rangle Q^2}{3}\right). \tag{A.2}$$

The term $\langle u^2\rangle$ is the averaged nuclear mean squared displacement. The vibrational scattering function can be separated in two terms, one elastic and one inelastic

$$S_{\text{vib}}\left(Q,\omega\right) = D(Q)\delta\left(\omega\right) + kS_{\text{vib}}^{\text{inel}}\left(Q,\omega\right), \tag{A.3}$$

where k is a constant to be determined. Due to the normalization condition (see eq. A.1), the constant k is just $1 - D(Q)$. Therefore, the vibrational scattering function is:

$$S_{\text{vib}}\left(Q,\omega\right) = D(Q)\delta\left(\omega\right) + \left[1 - D(Q)\right]S_{\text{vib}}^{\text{inel}}\left(Q,\omega\right). \tag{A.4}$$

If we factorize $D(Q)$ in the equation above, we obtain:

$$\begin{aligned} S_{\text{vib}}\left(Q,\omega\right) &= D(Q)\left\{\delta\left(\omega\right) + \left[D^{-1}(Q) - 1\right]S_{\text{vib}}^{\text{inel}}\left(Q,\omega\right)\right\} = & \text{(A.5)}\\ &= \mathrm{e}^{-\frac{\langle u^2\rangle Q^2}{3}}\left[\delta\left(\omega\right) + \left(\mathrm{e}^{\frac{\langle u^2\rangle Q^2}{3}} - 1\right)S_{\text{vib}}^{\text{inel}}\left(Q,\omega\right)\right]. & \text{(A.6)}\end{aligned}$$

For small values of $\langle u^2\rangle Q^2$, we can use the Taylor expansion of $\mathrm{e}^x \simeq 1 + x + x^2/2 + O(x^3)$, and therefore, setting $x = \langle u^2\rangle Q^2/3$, we obtain:

$$1 - \mathrm{e}^{-\frac{\langle u^2\rangle Q^2}{3}} = \mathrm{e}^{-\frac{\langle u^2\rangle Q^2}{3}}\left[\langle u^2\rangle Q^2/3 + \frac{1}{2}(\langle u^2\rangle Q^2/3)^2 + \dots\right]. \tag{A.7}$$

The terms in the square brackets are representing the one-phonon scattering, the second the two-phonon scattering, etc. Disregarding the second term, and re-arranging the eq. A.6, we can write, introducing the density of states $Z(\omega)$ in order to describe S_{vib},

$$S_{\text{vib}}^{+1} \simeq \mathrm{e}^{-\frac{\langle u^2\rangle Q^2}{3}}\left[\delta(\omega) + \frac{Z(\omega)}{\omega}Q^2\left[n(\omega) + 1\right]\right], \tag{A.8}$$

a similar expression that is find in textbook for neutron scattering [106, 139].

Appendix B

List of Publications

- M. Philipp, K. Kryakos, **L. Silvi**, W. Lohstroh, W. Petry, K. Krüger, M. C. Papadakis, and P. Müller-Buschbaum, "From Molecular Dehydration to Excess Volumes of Phase-Separating PNIPAM Solutions", J. Phys. Chem. B, 2014, 118 (15), 4253-4260.

- **L. Silvi**, E. Röhm, M. Fichtner, W. Petry, and W. Loshtroh, "Hydrogen dynamics in Mg(BH4)2 on the picosecond timescale", Phys. Chem. Chem. Phys., 2016, 18, 14323-14332

- K. Kryakos, M. Philipp, **L. Silvi**, W. Lohstroh, W. Petry, P. Müller-Buschbaum, and M. C. Papadakis, "Solvent Dynamics in Solutions of PNIPAM in Water/Methanol Mixtures–A Quasi-Elastic Neutron Scattering Study", Phys. Chem. Chem. Phys., 2016, 18, 14323-14332

Acknowledgement

At the end of this work, I would like to acknowledge many people that took part in this journey. The results in this thesis would have not been achieved without contributions, in various forms, from a large number of people.
First, I would like to thank Prof. Dr. Winfried Petry, for giving me the opportunity to do my PhD at the Technische Universität München and at the Forschungs-Neutronenquelle Heinz Maier-Leibnitz (FRM II), and the opportunity to become a member of the E13 Lehrstuhl für Funktionelle Materialien at the Physik Department.
I would like to thank my supervisor, Dr. Wiebke Lohstroh: Thank you for your availability, firmness and patience in the key moments of this thesis, for giving me priceless advices, for having an open ear for me all the time, and for supporting me during the experiments and data analysis. I really thank you.
I would like to thank Prof. Alessandro Paciaroni, for the helpful discussions about science and experiments on neutron scattering. Thanks to Dr. Humphrey Morhenn, to Juan Francisco Mora Cardozo and Sandro Szabó for sharing the office at the FRM II.
A special thanks goes to my family, for having supported me all the time and for encouraging me to go on. Without you, this could have never been possible.
A big thanks to the "holidays group" for being really good friends and for the support given to me during the whole time: Juliana, Kaye, Adam, Adrian, Maite, Bene and Ettore. A big hug and thanks goes to "The pacchetto fisici on the world" for being the resort of PhD students (and not only) and to my hometown friends (Luca, Alessandro, Eros).
Thanks also to Giuseppe, Marialucia and Agnese (non ci sono abbastanza parole per ringraziarvi).
A special thanks goes to Antonella, Simona, Maddalena, Vivi, Ines, Manuchar, Jerome and Bob (sorry guys, ladies first!), for not only being colleagues, but also really good friends and for sharing this journey.
Thanks to Gerhard, Andreas, Omar, Eugenio and, of course, Ettore for supporting, listening, and encouraging me.
Thanks to Linda, Michaela and Eckart, for having made me feel "home" when I arrived in München for the first time.
It is impossible to thank all the people I have met during these five years, and I just say to all of them: thank you.

Luca

References

[1] Department of Economic Social Affairs Population Division (2015) United Nations. World population prospects: The 2015 revision, volume i: Comprehensive tables (st/esa/ser.a/379). https://esa.un.org/unpd/wpp/Download/Standard/Population/, 2015. [Online; accessed 21-December-2016]. (Cited on page 4.)

[2] BP. Statistical review of world energy june 2016. http://www.bp.com/en/global/corporate/energy-economics/statistical-review-of-world-energy.html, 2016. [Online; accessed 21-December-2016]. (Cited on page 4.)

[3] FrameWork Convention on Climate Change United Nations. Kyoto protocol to the united nations framework convention on climate change. http://unfccc.int/kyoto_protocol/items/2830.php, 1998. [Online; accessed 21-December-2016]. (Cited on page 4.)

[4] BMWi. Offshore-windenergie. http://www.erneuerbare-energien.de/EE/Redaktion/DE/Downloads/bmwi_de/offshore-windenergie.pdf?__blob=publicationFile&v=2, 2015. [Online; accessed 21-December-2016]. (Cited on page 5.)

[5] Andreas Züttel, Arndt Remhof, Andreas Borgschulte, and Oliver Friedrichs. Hydrogen: the future energy carrier. *Philosophical Transactions of the Royal Society of London A: Mathematical, Physical and Engineering Sciences*, 368(1923):3329–3342, 2010. (Cited on page 5.)

[6] Andreas Züttel, Andreas Borgschulte, and Louis Schlapbach. *Hydrogen as a Future Energy Carrier*. John Wiley & Sons, 2008. (Cited on pages 5 and 9.)

[7] Michael Hirscher. *Handbook of Hydrogen Storage*. Wiley-VCH Verlag GmbH & Co. KGaA, 2010. (Cited on pages 7, 12 and 16.)

[8] Johannes Töpler and Jochen Lehmann. *Hydrogen and Fuel Cell*. Springer Berlin Heidelberg, 2016. (Cited on page 9.)

[9] Daniel Teichmann, Wolfgang Arlt, Peter Wasserscheid, and Raymond Freymann. A future energy supply based on Liquid Organic Hydrogen Carriers (LOHC). *Energy Environ. Sci.*, 4:2767–2773, 2011. (Cited on page 9.)

[10] DOE. Types of fuel cells. http://energy.gov/eere/fuelcells/types-fuel-cells, 2015. [Online; accessed 21-December-2016]. (Cited on page 10.)

[11] Darren P. Broom. *Hydrogen Storage Materials*. Springer London, 2011. (Cited on page 11.)

[12] Craig E. Buckley, Ping Chen, Bart A. van Hassel, and Michael Hirscher. Hydrogen-based Energy Storage (IEA-HIA Task 32). *Applied Physics A*, 122(2):1–2, 2016. (Cited on page 11.)

[13] IEA. Hydrogen production and storage. http://ieahia.org/PUBLICATIONS,-REPORTS-PRESENTATIONS/Technical-Reports/Task-17-Reports.aspx, 2006. [Online; accessed 21-December-2016]. (Cited on page 11.)

[14] DOE. Target explanation document:onboard hydrogen storage for light-duty fuel cell vehicles. http://energy.gov/eere/fuelcells/doe-technical-targets-onboard-hydrogen-storage-light-duty-vehicles, 2016. [Online; accessed 21-December-2016]. (Cited on page 11.)

[15] Borislav Bogdanović and Manfred Schwickardi. Ti-doped alkali metal aluminium hydrides as potential novel reversible hydrogen storage materials. *Journal of Alloys and Compounds*, 253-254:1 – 9, 1997. (Cited on page 14.)

[16] Elsa Callini, Zuleyha Özlem Kocabas Atakli, Bjørn C. Hauback, Shin-ichi Orimo, Craig Jensen, Martin Dornheim, David Grant, Young Whan Cho, Ping Chen, Bjørgvin Hjörvarsson, Petra de Jongh, Claudia Weidenthaler, Marcello Baricco, Mark Paskevicius, Torben R. Jensen, Mark E. Bowden, Thomas S. Autrey, and Andreas Züttel. Complex and liquid hydrides for energy storage. *Applied Physics A*, 122(4):1–22, 2016. (Cited on pages 14, 16 and 19.)

[17] Line H. Rude, Thomas K. Nielsen, Dorthe B. Ravnsbaek, Ulrike Bösenberg, Morten B. Ley, Bo Richter, Lene M. Arnbjerg, Martin Dornheim, Yaroslav Filinchuk, Flemming Besenbacher, and Torben R. Jensen. Tailoring properties of borohydrides for hydrogen storage: A review. *physica status solidi (a)*, 208(8):1754–1773, 2011. (Cited on page 14.)

[18] Hai-Wen Li, Yigang Yan, Shin-ichi Orimo, Andreas Züttel, and Craig M. Jensen. Recent Progress in Metal Borohydrides for Hydrogen Storage. *Energies*, 4(1):185, 2011. (Cited on pages 14 and 17.)

[19] Lyci George and Surendra K. Saxena. Structural stability of metal hydrides, alanates and borohydrides of alkali and alkali- earth elements: A review. *International Journal of Hydrogen Energy*, 35(11):5454 – 5470, 2010. 3rd Argentinean and 2nd Latin American Congress in Hydrogen and Sustainable Energy Sources. (Cited on page 14.)

[20] I.P. Jain, Pragya Jain, and Ankur Jain. Novel hydrogen storage materials: A review of lightweight complex hydrides. *Journal of Alloys and Compounds*, 503(2):303 – 339, 2010. (Cited on page 14.)

[21] Y. Nakamori, H.-W. Li, M. Matsuo, K. Miwa, S. Towata, and S. Orimo. Development of metal borohydrides for hydrogen storage. *Journal of Physics and Chemistry of Solids*, 69(9):2292 – 2296, 2008. Study of Matter Under Extreme Conditions 2007Study of Matter Under Extreme Conditions 2007. (Cited on page 14.)

[22] Shinichi Orimo, Yuko Nakamori, Jennifer R. Eliseo, Andreas Züttel, and Craig M. Jensen. Complex Hydrides for Hydrogen Storage. *Chemical Reviews*, 107(10):4111–4132, 2007. PMID: 17848101. (Cited on page 14.)

[23] Yuko Nakamori, Kazutoshi Miwa, Akihito Ninomiya, Haiwen Li, Nobuko Ohba, Shinichi Towata, Andreas Züttel, and Shinichi Orimo. Correlation between thermodynamical stabilities of metal borohydrides and cation electronegativites: First-principles calculations and experiments. *Phys. Rev. B*, 74:045126, Jul 2006. (Cited on pages 15, 17 and 22.)

[24] Zbigniew Łodziana and Michiel J. van Setten. Binding in alkali and alkaline-earth tetrahydroborates: Special position of magnesium tetrahydroborate. *Phys. Rev. B*, 81:024117, Jan 2010. (Cited on pages 15 and 17.)

[25] Donald J. Siegel, C. Wolverton, and V. Ozoliņš. Thermodynamic guidelines for the prediction of hydrogen storage reactions and their application to destabilized hydride mixtures. *Phys. Rev. B*, 76:134102, Oct 2007. (Cited on page 16.)

[26] Kyle Jay Michel and Vidvuds Ozoliņš. Recent advances in the theory of hydrogen storage in complex metal hydrides. *MRS Bulletin*, 38:462–472, 6 2013. (Cited on page 16.)

[27] Zhan-Zhao Fang, Xiang-Dong Kang, Ping Wang, Hai-Wen Li, and Shin-Ichi Orimo. Unexpected dehydrogenation behavior of $LiBH_4/Mg(BH_4)_2$ mixture associated with the in situ formation of dual-cation borohydride. *Journal of Alloys and Compounds*, 491(1-2):L1 – L4, 2010. (Cited on pages 17 and 27.)

[28] Elisa Gil Bardají, Zhirong Zhao-Karger, Nancy Boucharat, Angeloclaudio Nale, Michiel J. van Setten, Wiebke Lohstroh, Eva Röhm, Michele Catti, and Maximilian Fichtner. $LiBH_4$-$Mg(BH_4)_2$: A Physical Mixture of Metal Borohydrides as Hydrogen Storage Material. *The Journal of Physical Chemistry C*, 115(13):6095–6101, 2011. (Cited on pages 17, 27, 131, 140, 143 and 144.)

[29] Zhirong Zhao-Karger, Raiker Witter, Elisa Gil Bardají, Di Wang, Daniel Cossement, and Maximilian Fichtner. Altered reaction pathways of eutectic $LiBH_4$-$Mg(BH_4)_2$ by nanoconfinement. *J. Mater. Chem. A*, 1:3379–3386, 2013. (Cited on page 17.)

[30] Ji Youn Lee, Dorthe Ravnsbaek, Young-Su Lee, Yoonyoung Kim, Yngve Cerenius, Jae-Hyeok Shim, Torben R. Jensen, Nam Hwi Hur, and Young Whan Cho. Decomposition Reactions and Reversibility of the $LiBH_4$-$Ca(BH_4)_2$ Composite. *The Journal of Physical Chemistry C*, 113(33):15080–15086, 2009. (Cited on page 17.)

[31] H. Wang, H.J. Lin, W.T. Cai, L.Z. Ouyang, and M. Zhu. Tuning kinetics and thermodynamics of hydrogen storage in light metal element based systems - A review of recent progress. *Journal of Alloys and Compounds*, 658:280 – 300, 2016. (Cited on page 17.)

[32] H. I. Schlesinger and Herbert C. Brown. Metallo Borohydrides. III. Lithium Borohydride. *Journal of the American Chemical Society*, 62(12):3429–3435, 1940. (Cited on page 18.)

[33] O. Friedrichs, F. Buchter, A. Borgschulte, A. Remhof, C.N. Zwicky, Ph. Mauron, M. Bielmann, and A. Züttel. Direct synthesis of $Li[BH_4]$ and $Li[BD_4]$ from the elements. *Acta Materialia*, 56(5):949 – 954, 2008. (Cited on page 18.)

[34] A. Züttel, P. Wenger, S. Rentsch, P. Sudan, Ph. Mauron, and Ch. Emmenegger. $LiBH_4$ a new hydrogen storage material. *Journal of Power Sources*, 118(1-2):1 – 7, 2003. Scientific Advances in Fuel Cell Systems. (Cited on page 18.)

[35] Philippe Mauron, Florian Buchter, Oliver Friedrichs, Arndt Remhof, Michael Bielmann, Christoph N. Zwicky, and Andreas Züttel. Stability and Reversibility of $LiBH_4$. *The Journal of Physical Chemistry B*, 112(3):906–910, 2008. PMID:18088111. (Cited on page 18.)

[36] S. Orimo, Y. Nakamori, G. Kitahara, K. Miwa, N. Ohba, S. Towata, and A. Züttel. Dehydriding and rehydriding reactions of $LiBH_4$. *Journal of Alloys and Compounds*, 404-406:427 – 430, 2005. Proceedings of the 9th International Symposium on Metal-Hydrogen Systems, Fundamentals and Applications (MH2004)The International Symposium on Metal-Hydrogen Systems, Fundamentals and Applications, {MH2004}. (Cited on page 18.)

[37] Shin-Ichi Orimo, Yuko Nakamori, Nobuko Ohba, Kazutoshi Miwa, Masakazu Aoki, Shin-ichi Towata, and Andreas Züttel. Experimental studies on intermediate compound of LiBH4. *Applied Physics Letters*, 89(2), 2006. (Cited on page 18.)

[38] Son-Jong Hwang, Jr. Robert C. Bowman, Joseph W. Reiter, Job Rijssenbeek, Grigorii L. Soloveichik, Ji-Cheng Zhao, Houria Kabbour, and Channing C. Ahn. NMR Confirmation for Formation of $[B_{12}H_{12}]^{2-}$ Complexes during Hydrogen Desorption from Metal Borohydrides. *The Journal of Physical Chemistry C*, 112(9):3164–3169, 2008. (Cited on page 18.)

[39] John J. Vajo, , Sky L. Skeith, and Florian Mertens. Reversible Storage of Hydrogen in Destabilized $LiBH_4$. *The Journal of Physical Chemistry B*, 109(9):3719–3722, 2005. PMID: 16851415. (Cited on page 18.)

[40] Gagik Barkhordarian, Thomas Klassen, Martin Dornheim, and Rüdiger Bormann. Unexpected kinetic effect of MgB_2 in reactive hydride composites containing complex borohydrides. *Journal of Alloys and Compounds*, 440(1-2):L18 – L21, 2007. (Cited on page 18.)

[41] Frederick E. Pinkerton, Martin S. Meyer, Gregory P. Meisner, Michael P. Balogh, , and John J. Vajo. Phase Boundaries and Reversibility of $LiBH_4/MgH_2$ Hydrogen Storage Material. *The Journal of Physical Chemistry C*, 111(35):12881–12885, 2007. (Cited on page 18.)

[42] Young Whan Cho, Jae-Hyeok Shim, and Byeong-Joo Lee. Thermal destabilization of binary and complex metal hydrides by chemical reaction: A thermodynamic analysis. *Calphad*, 30(1):65 – 69, 2006. (Cited on page 18.)

[43] Seon-Ah Jin, Jae-Hyeok Shim, Young Whan Cho, Kyung-Woo Yi, Oleg Zabara, and Maximilian Fichtner. Reversible hydrogen storage in $LiBH_4$-Al-LiH composite powder. *Scripta Materialia*, 58(11):963 – 965, 2008. (Cited on page 18.)

[44] Jun Yangs, Andrea Sudik, and C. Wolverton. Destabilizing $LiBH_4$ with a Metal (M = Mg, Al, Ti, V, Cr, or Sc) or Metal Hydride (MH_2 = MgH_2, TiH_2, or CaH_2). *The Journal of Physical Chemistry C*, 111(51):19134–19140, 2007. (Cited on page 18.)

[45] F.E. Pinkerton and M.S. Meyer. Reversible hydrogen storage in the lithium borohydride-calcium hydride coupled system. *Journal of Alloys and Compounds*, 464(1-2):L1 – L4, 2008. (Cited on page 18.)

[46] Ming Au and Arthur Jurgensen. Modified Lithium Borohydrides for Reversible Hydrogen Storage. *The Journal of Physical Chemistry B*, 110(13):7062–7067, 2006. PMID: 16571023. (Cited on page 19.)

[47] J. Kostka, W. Lohstroh, M. Fichtner, and H. Hahn. Diborane Release from $LiBH_4$/Silica-Gel Mixtures and the Effect of Additives. *The Journal of Physical Chemistry C*, 111(37):14026–14029, 2007. (Cited on page 19.)

[48] Z.Z. Fang, P. Wang, T.E. Rufford, X.D. Kang, G.Q. Lu, and H.M. Cheng. Kinetic- and thermodynamic-based improvements of lithium borohydride incorporated into activated carbon. *Acta Materialia*, 56(20):6257 – 6263, 2008. (Cited on page 19.)

[49] Yao Zhang, Wan-Sheng Zhang, Ai-Qin Wang, Li-Xian Sun, Mei-Qiang Fan, Hai-Liang Chu, Jun-Cai Sun, and Tao Zhang. nanoparticles supported by disordered mesoporous

carbon: Hydrogen storage performances and destabilization mechanisms. *International Journal of Hydrogen Energy*, 32(16):3976 – 3980, 2007. TMS06: Symposium on Materials in Clean Power Systems. (Cited on page 19.)

[50] Adam F. Gross, John J. Vajo, Sky L. Van Atta, , and Gregory L. Olson. Enhanced Hydrogen Storage Kinetics of $LiBH_4$ in Nanoporous Carbon Scaffolds. *The Journal of Physical Chemistry C*, 112(14):5651–5657, 2008. (Cited on page 19.)

[51] Arndt Remhof, Philippe Mauron, Andreas Züttel, Jan Peter Embs, Zbigniew Łodziana, A. J. Ramirez-Cuesta, Peter Ngene, and Petra de Jongh. Hydrogen Dynamics in Nanoconfined Lithiumborohydride. *The Journal of Physical Chemistry C*, 117(8):3789–3798, 2013. (Cited on page 19.)

[52] Peter Ngene, Philipp Adelhelm, Andrew M. Beale, Krijn P. de Jong, and Petra E. de Jongh. $LiBH_4$/SBA-15 Nanocomposites Prepared by Melt Infiltration under Hydrogen Pressure: Synthesis and Hydrogen Sorption Properties. *The Journal of Physical Chemistry C*, 114(13):6163–6168, 2010. (Cited on page 19.)

[53] Nina Verdal, Terrence J. Udovic, John J. Rush, Xiangfeng Liu, Eric H. Majzoub, John J. Vajo, and Adam F. Gross. Dynamical Perturbations of Tetrahydroborate Anions in $LiBH_4$ due to Nanoconfinement in Controlled-Pore Carbon Scaffolds. *The Journal of Physical Chemistry C*, 117(35):17983–17995, 2013. (Cited on pages 19, 77, 80 and 81.)

[54] C. Li, P. Peng, D.W. Zhou, and L. Wan. Research progress in $LiBH_4$ for hydrogen storage: A review. *International Journal of Hydrogen Energy*, 36(22):14512 – 14526, 2011. Fuel Cell Technologies: {FUCETECH} 2009. (Cited on page 19.)

[55] Adem Tekin, Riccarda Caputo, and Andreas Züttel. First-Principles Determination of the Ground-State Structure of $LiBH_4$. *Phys. Rev. Lett.*, 104:215501, May 2010. (Cited on page 19.)

[56] S. A. Shevlin, C. Cazorla, and Z. X. Guo. Structure and Defect Chemistry of Low- and High-Temperature Phases of $LiBH_4$. *The Journal of Physical Chemistry C*, 116(25):13488–13496, 2012. (Cited on page 19.)

[57] J-Ph. Soulié, G. Renaudin, R. Černý, and K. Yvon. Lithium boro-hydride $LiBH_4$: I. Crystal structure. *Journal of Alloys and Compounds*, 346(1-2):200 – 205, 2002. (Cited on pages 19, 20 and 82.)

[58] Yaroslav Filinchuk, Dmitry Chernyshov, Andriy Nevidomskyy, and Vladimir Dmitriev. High-Pressure Polymorphism as a Step towards Destabilization of $LiBH_4$. *Angewandte Chemie International Edition*, 47(3):529–532, 2008. (Cited on page 19.)

[59] Yaroslav Filinchuk, Dmitry Chernyshov, and Radovan Černý. Lightest Borohydride Probed by Synchrotron X-ray Diffraction: Experiment Calls for a New Theoretical Revision. *The Journal of Physical Chemistry C*, 112(28):10579–10584, 2008. (Cited on pages 19, 20 and 83.)

[60] F. Buchter, Z. Łodziana, Ph. Mauron, A. Remhof, O. Friedrichs, A. Borgschulte, A. Züttel, D. Sheptyakov, Th. Strässle, and A. J. Ramirez-Cuesta. Dynamical properties and temperature induced molecular disordering of $LiBH_4$ and $LiBD_4$. *Phys. Rev. B*, 78:094302, Sep 2008. (Cited on pages 19 and 22.)

[61] R. Gremaud, A. Züttel, A. Borgschulte, A.J. Ramirez-Cuesta, K. Refson, and D. Colognesi. Origin of the large anharmonicity in the phonon modes of $LiBH_4$. *Chemical Physics*, 427:22 – 29, 2013. Advances and frontiers in chemical spectroscopy with neutrons. (Cited on pages 19 and 80.)

[62] Tung Tsang and T. C. Farrar. Nuclear Magnetic Relaxation Studies of Internal Rotations and Phase Transitions in Borohydrides of Lithium, Sodium, and Potassium. *The Journal of Chemical Physics*, 50(8):3498–3502, 1969. (Cited on page 19.)

[63] Arndt Remhof, Zbigniew Łodziana, Pascal Martelli, Oliver Friedrichs, Andreas Züttel, Alexander V. Skripov, Jan Peter Embs, and Thierry Strässle. Rotational motion of BH_4 units in $M BH_4$ ($M = \mathrm{Li, Na, K}$) from quasielastic neutron scattering and density functional calculations. *Phys. Rev. B*, 81:214304, Jun 2010. (Cited on page 19.)

[64] Pascal Martelli, Arndt Remhof, Andreas Borgschulte, Philippe Mauron, Dirk Wallacher, Ewout Kemner, Margarita Russina, Flavio Pendolino, and Andreas Züttel. BH_4^- Self-Diffusion in Liquid $LiBH_4$. *The Journal of Physical Chemistry A*, 114(37):10117–10121, 2010. PMID: 20806929. (Cited on pages 19 and 148.)

[65] Motoaki Matsuo, Yuko Nakamori, Shin-ichi Orimo, Hideki Maekawa, and Hitoshi Takamura. Lithium superionic conduction in lithium borohydride accompanied by structural transition. *Applied Physics Letters*, 91(22), 2007. (Cited on page 22.)

[66] Samantha K. Callear, E. Anne Nickels, Martin O. Jones, Motoaki Matsuo, Shin-Ichi Orimo, Peter P. Edwards, and William I. F. David. Order and disorder in lithium tetrahydroborate. *Journal of Materials Science*, 46(2):566–569, 2010. (Cited on page 22.)

[67] J. Lang, A. Gerhauser, Y. Filinchuk, T. Klassen, and J. Huot. Differential Scanning Calorimetry (DSC) and Synchrotron X-ray Diffraction Study of Unmilled and Milled $LiBH_4$: A Partial Release of Hydrogen at Moderate Temperatures. *Crystals*, 2(1):1, 2012. (Cited on page 22.)

[68] Krzysztof Chłopek, Christoph Frommen, Aline Léon, Oleg Zabara, and Maximilian Fichtner. Synthesis and properties of magnesium tetrahydroborate, $Mg(BH_4)_2$. *J. Mater. Chem.*, 17:3496–3503, 2007. (Cited on pages 22, 25, 89 and 131.)

[69] H.-W. Li, K. Kikuchi, Y. Nakamori, N. Ohba, K. Miwa, S. Towata, and S. Orimo. Dehydriding and rehydriding processes of well-crystallized $Mg(BH_4)_2$ accompanying with formation of intermediate compounds. *Acta Materialia*, 56(6):1342 – 1347, 2008. (Cited on page 22.)

[70] T. Matsunaga, F. Buchter, P. Mauron, M. Bielman, Y. Nakamori, S. Orimo, N. Ohba, K. Miwa, S. Towata, and A. Züttel. Hydrogen storage properties of $Mg(BH_4)_2$. *Journal of Alloys and Compounds*, 459(1-2):583 – 588, 2008. (Cited on page 22.)

[71] Grigorii L. Soloveichik, Yan Gao, Job Rijssenbeek, Matthew Andrus, Sergei Kniajanski, Robert C. Bowman Jr., Son-Jong Hwang, and Ji-Cheng Zhao. Magnesium borohydride as a hydrogen storage material: Properties and dehydrogenation pathway of unsolvated $Mg(BH_4)_2$. *International Journal of Hydrogen Energy*, 34(2):916 – 928, 2009. (Cited on pages 22 and 25.)

[72] Nobuko Hanada, Krzysztof Chłopek, Christoph Frommen, Wiebke Lohstroh, and Maximilian Fichtner. Thermal decomposition of $Mg(BH_4)_2$ under He flow and H_2 pressure. *J. Mater. Chem.*, 18:2611–2614, 2008. (Cited on pages 22, 25, 90 and 92.)

[73] Godwin Severa, Ewa Rönnebro, and Craig M. Jensen. Direct hydrogenation of magnesium boride to magnesium borohydride: demonstration of >11 weight percent reversible hydrogen storage. *Chem. Commun.*, 46:421–423, 2010. (Cited on page 22.)

[74] Mark Paskevicius, Mark P. Pitt, Colin J. Webb, Drew A. Sheppard, Uffe Filsø, Evan MacA. Gray, and Craig E. Buckley. In-Situ X-ray Diffraction Study of γ-$Mg(BH_4)_2$ Decomposition. *The Journal of Physical Chemistry C*, 116(29):15231–15240, 2012. (Cited on page 22.)

[75] Yaroslav Filinchuk, Bo Richter, Torben R. Jensen, Vladimir Dmitriev, Dmitry Chernyshov, and Hans Hagemann. Porous and Dense Magnesium Borohydride Frameworks: Synthesis, Stability, and Reversible Absorption of Guest Species. *Angewandte Chemie International Edition*, 50(47):11162–11166, 2011. (Cited on pages 22, 25 and 31.)

[76] W. I. F. David, S. K. Callear, M. O. Jones, P. C. Aeberhard, S. D. Culligan, A. H. Pohl, S. R. Johnson, K. R. Ryan, J. E. Parker, P. P. Edwards, C. J. Nuttall, and A. Amieiro-Fonseca. The structure, thermal properties and phase transformations of the cubic polymorph of magnesium tetrahydroborate. *Phys. Chem. Chem. Phys.*, 14:11800–11807, 2012. (Cited on page 22.)

[77] Jae-Hyuk Her, Peter W. Stephens, Yan Gao, Grigorii L. Soloveichik, Job Rijssenbeek, Matthew Andrus, and Ji-Cheng Zhao. Structure of unsolvated magnesium borohydride $Mg(BH_4)_2$. *Acta Crystallographica Section B*, 63(4):561–568, Aug 2007. (Cited on pages 22 and 23.)

[78] Radovan Filinchuk, Yaroslav andČerný and Hans Hagemann. Insight into $Mg(BH_4)_2$ with Synchrotron X-ray Diffraction: Structure Revision, Crystal Chemistry, and Anomalous Thermal Expansion. *Chemistry of Materials*, 21(5):925–933, 2009. (Cited on pages 22, 23, 115 and 124.)

[79] Bing Dai, David S. Sholl, and J. Karl Johnson. First-Principles Study of Experimental and Hypothetical $Mg(BH_4)_2$ Crystal Structures. *The Journal of Physical Chemistry C*, 112(11):4391–4395, 2008. (Cited on page 25.)

[80] A. Bil, B. Kolb, R. Atkinson, D. G. Pettifor, T. Thonhauser, and A. N. Kolmogorov. van der Waals interactions in the ground state of $Mg(BH_4)_2$ from density functional theory. *Phys. Rev. B*, 83:224103, Jun 2011. (Cited on page 25.)

[81] Riccarda Caputo, Arkadiusz Kupczak, Wieslawa Sikora, and Adem Tekin. Ab initio crystal structure prediction by combining symmetry analysis representations and total energy calculations. An insight into the structure of $Mg(BH_4)_2$. *Phys. Chem. Chem. Phys.*, 15:1471–1480, 2013. (Cited on page 25.)

[82] V. Ozolins, E. H. Majzoub, and C. Wolverton. First-Principles Prediction of a Ground State Crystal Structure of Magnesium Borohydride. *Phys. Rev. Lett.*, 100:135501, Mar 2008. (Cited on page 25.)

[83] J Voss, J S Hummelshøj, Z Łodziana, and T Vegge. Structural stability and decomposition of $Mg(BH_4)_2$ isomorphs-an ab initio free energy study. *Journal of Physics: Condensed Matter*, 21(1):012203, 2009. (Cited on page 25.)

[84] Xiang-Feng Zhou, Artem R. Oganov, Guang-Rui Qian, and Qiang Zhu. First-Principles Determination of the Structure of Magnesium Borohydride. *Phys. Rev. Lett.*, 109:245503, Dec 2012. (Cited on page 25.)

[85] Junzhi Yang, Xuanzhou Zhang, Jie Zheng, Ping Song, and Xingguo Li. Decomposition pathway of $Mg(BH_4)_2$ under pressure: Metastable phases and thermodynamic parameters. *Scripta Materialia*, 64(3):225 – 228, 2011. (Cited on page 25.)

[86] Michiel J. van Setten, Gilles A. de Wijs, Maximilian Fichtner, and Geert Brocks. A Density Functional Study of α-$Mg(BH_4)_2$. *Chemistry of Materials*, 20(15):4952–4956, 2008. (Cited on page 25.)

[87] Yigang Yan, Hai-Wen Li, Hideki Maekawa, Masakazu Aoki, Tatsuo Noritake, Mitsuru Matsumoto, Kazutoshi Miwa, Shin ichi Towata, and Shin ichi Orimo. Formation Process of $[B_{12}H_{12}]^{2-}$ from $[BH_4]^-$ during the Dehydrogenation Reaction of $Mg(BH_4)_2$. *MATERIALS TRANSACTIONS*, 52(7):1443–1446, 2011. (Cited on page 25.)

[88] Elisa Gil Bardají, Nobuko Hanada, Oleg Zabara, and Maximilian Fichtner. Effect of several metal chlorides on the thermal decomposition behaviour of α-$Mg(BH_4)_2$. *International Journal of Hydrogen Energy*, 36(19):12313 – 12318, 2011. (Cited on page 26.)

[89] Z.G. Zhang, H. Wang, J.W. Liu, and M. Zhu. Thermal decomposition behaviors of magnesium borohydride doped with metal fluoride additives. *Thermochimica Acta*, 560(0):82 – 88, 2013. (Cited on page 26.)

[90] Rebecca J. Newhouse, Vitalie Stavila, Son-Jong Hwang, Leonard E. Klebanoff, and Jin Z. Zhang. Reversibility and Improved Hydrogen Release of Magnesium Borohydride. *The Journal of Physical Chemistry C*, 114(11):5224–5232, 2010. (Cited on page 26.)

[91] Yuen S. Au, Yigang Yan, Krijn P. de Jong, Arndt Remhof, and Petra E. de Jongh. Pore Confined Synthesis of Magnesium Boron Hydride Nanoparticles. *The Journal of Physical Chemistry C*, 118(36):20832–20839, 2014. (Cited on page 26.)

[92] Maximilian Fichtner, Zhirong Zhao-Karger, Jianjiang Hu, Arne Roth, and Peter Weidler. The kinetic properties of $Mg(BH_4)_2$ infiltrated in activated carbon. *Nanotechnology*, 20(20):204029, 2009. (Cited on page 26.)

[93] Satoshi Hino, Jon Erling Fonneløp, Marta Corno, Olena Zavorotynska, Alessandro Damin, Bo Richter, Marcello Baricco, Torben R. Jensen, Magnus H. Sørby, and Bjørn C. Hauback. Halide Substitution in Magnesium Borohydride. *The Journal of Physical Chemistry C*, 116(23):12482–12488, 2012. (Cited on page 26.)

[94] Olena Zavorotynska, Abdelouahab El-Kharbachi, Stefano Deledda, and Bjørn C. Hauback. Recent progress in magnesium borohydride $Mg(BH_4)_2$: Fundamentals and applications for energy storage. *International Journal of Hydrogen Energy*, 41(32):14387 – 14403, 2016. (Cited on page 26.)

[95] Hans Hagemann, Vincenza D'Anna, Jean-Philippe Rapin, Radovan Černy, Yaroslav Filinchuk, Ki Chul Kim, David S. Sholl, and Stewart F. Parker. New fundamental experimental studies on α-Mg(BH4)2 and other borohydrides. *Journal of Alloys and Compounds*, 509, Supplement 2:S688 – S690, 2011. Proceedings of the 12th International Symposium on Metal-Hydrogen Systems, Fundamentals and Applications (MH2010). (Cited on pages 26, 109 and 124.)

[96] A. Giannasi, D., L. Ulivi, M. Zoppi, A. J. Ramirez-Cuesta, E. G. Bardají, E. Röhm, and M. Fichtner. High Resolution Raman and Neutron Investigation of $Mg(BH_4)_2$ in an Extensive Temperature Range. *The Journal of Physical Chemistry A*, 114(8):2788–2793, 2010. PMID: 20141188. (Cited on pages 26, 100, 109 and 124.)

[97] Alexander V. Skripov, Alexei V. Soloninin, Olga A. Babanova, Hans Hagemann, and Yaroslav Filinchuk. Nuclear Magnetic Resonance Study of Reorientational Motion in α-$Mg(BH_4)_2$. *The Journal of Physical Chemistry C*, 114(28):12370–12374, 2010. (Cited on pages 26, 124 and 125.)

[98] Alexei V. Soloninin, Olga A. Babanova, Alexander V. Skripov, Hans Hagemann, Bo Richter, Torben R. Jensen, and Yaroslav Filinchuk. NMR Study of Reorientational Motion in Alkaline-Earth Borohydrides: β and γ Phases of $Mg(BH_4)_2$ and α and β Phases of $Ca(BH_4)_2$. *The Journal of Physical Chemistry C*, 116(7):4913–4920, 2012. (Cited on pages 26 and 105.)

[99] D. Blanchard, J. B. Maronsson, M. D. Riktor, J. Kheres, D. Sveinbjørnsson, E. Gil Bardají, A. Léon, F. Juranyi, J. Wuttke, K. Lefmann, B. C. Hauback, M. Fichtner, and T. Vegge. Hindered Rotational Energy Barriers of BH4- Tetrahedra in β-$Mg(BH_4)_2$ from Quasielastic Neutron Scattering and DFT Calculations. *The Journal of Physical Chemistry C*, 116(2):2013–2023, 2012. (Cited on pages 27, 92, 103 and 105.)

[100] D. Colognesi, L. Ulivi, M. Zoppi, A.J. Ramirez-Cuesta, A. Orecchini, A.J. Karkamkar, M. Fichtner, E. Gil Bardají, and Z. Zhao-Karger. Hydrogen-storage materials dispersed into nanoporous substrates studied through incoherent inelastic neutron scattering. *Journal of Alloys and Compounds*, 538:91 – 99, 2012. (Cited on page 27.)

[101] Xiangfeng Liu, David Peaslee, T. Patrick Sheehan, and Eric H. Majzoub. Decomposition Behavior of Eutectic $LiBH_4$-$Mg(BH_4)_2$ and Its Confinement Effects in Ordered Nanoporous Carbon. *The Journal of Physical Chemistry C*, 118(47):27265–27271, 2014. (Cited on page 27.)

[102] Payam Javadian and Torben R. Jensen. Enhanced hydrogen reversibility of nanoconfined $LiBH_4$-$Mg(BH_4)_2$. *International Journal of Hydrogen Energy*, 39(18):9871 – 9876, 2014. (Cited on page 27.)

[103] Yaroslav Filinchuk, Dmitry Chernyshov, and Vladimir Dmitriev. Light metal borohydrides: crystal structures and beyond. *Z. Kristallogr.*, 10:649–659, 2008. (Cited on page 31.)

[104] Olga A. Babanova, Alexei V. Soloninin, Adolf P. Stepanov, Alexander V. Skripov, and Yaroslav Filinchuk. Structural and Dynamical Properties of $NaBH_4$ and KBH_4:

NMR and Synchrotron X-ray Diffraction Studies. *The Journal of Physical Chemistry C*, 114(8):3712–3718, 2010. (Cited on pages 31 and 107.)

[105] Radovan Černý, Yaroslav Filinchuk, Hans Hagemann, and Klaus Yvon. Magnesium Borohydride: Synthesis and Crystal Structure. *Angewandte Chemie International Edition*, 46(30):5765–5767, 2007. (Cited on page 31.)

[106] S.W. Lovesey. *Theory of Neutron Scattering from Condensed Matter*. Number 2 in International series of monographs on physics. Clarendon Press, 1986. (Cited on pages 33, 44, 124 and 163.)

[107] M. Bée. *Quasielastic Neutron Scattering*. Adam Hilger, 1988. (Cited on pages 33, 50, 68, 98 and 148.)

[108] Varley F. Sears. Neutron scattering lengths and cross sections. *Neutron News*, 3(3):26–37, 1992. (Cited on page 38.)

[109] Léon Van Hove. Correlations in Space and Time and Born Approximation Scattering in Systems of Interacting Particles. *Phys. Rev.*, 95:249–262, Jul 1954. (Cited on page 39.)

[110] B. Fåk and B. Dorner. Phonon line shapes and excitation energies. *Physica B: Condensed Matter*, 234(0):1107–1108, 1997. Proceedings of the First European Conference on Neutron Scattering. (Cited on page 44.)

[111] B Fåk and B Dorner. On the interpretation of phonon line shapes and excitation energies in neutron scattering experiments. Technical report, ILL, 1992. ILL Report No. 92FA008S. (Cited on pages 44 and 78.)

[112] R. Hempelmann. *Quasielastic Neutron Scattering and Solid State Diffusion*. Oxford science publications. Clarendon Press, 2000. (Cited on pages 48, 50, 98 and 107.)

[113] F. Volino and A.J. Dianoux. Neutron incoherent scattering law for diffusion in a potential of spherical symmetry: general formalism and application to diffusion inside a sphere. *Molecular Physics*, 41(2):271–279, 1980. (Cited on pages 49 and 144.)

[114] A. A. Maradudin and P. A. Flinn. Anharmonic Contributions to the Debye-Waller Factor. *Phys. Rev.*, 129:2529–2547, Mar 1963. (Cited on page 50.)

[115] RE Lechner. Tof-tof spectrometers at pulsed neutrons sources and at steady-state reactors. In *Proc. Workshop on Neutron Scattering for SNQ, Maria Laach*, pages 202–223. Jül, 1984. (Cited on page 56.)

[116] Tobias Unruh, Jürgen Neuhaus, and Winfried Petry. The high-resolution time-of-flight spectrometer TOFTOF. *Nuclear Instruments and Methods in Physics Research Section*

A: Accelerators, Spectrometers, Detectors and Associated Equipment, 580(3):1414 – 1422, 2007. (Cited on pages 59, 60, 64 and 155.)

[117] MLZ. Experimental facilities - Heinz Maier-Leibnitz Zentrum, 2013. (Cited on page 59.)

[118] H. Aschauer, A. Fleischmann, C. Schanzer, and E. Steichele. Neutron guides at the FRM-II. *Physica B: Condensed Matter*, 283(4):323 – 329, 2000. (Cited on page 59.)

[119] H. H. Paalman and C. J. Pings. Numerical Evaluation of X-Ray Absorption Factors for Cylindrical Samples and Annular Sample Cells. *Journal of Applied Physics*, 33(8):2635–2639, 1962. (Cited on page 68.)

[120] V.F. Sears. Slow-neutron multiple scattering. *Advances in Physics*, 24(1):1–45, 1975. (Cited on pages 68 and 131.)

[121] Alexander V. Skripov, Alexei V. Soloninin, Yaroslav Filinchuk, and Dmitry Chernyshov. Nuclear Magnetic Resonance Study of the Rotational Motion and the Phase Transition in LiBH4. *The Journal of Physical Chemistry C*, 112(47):18701–18705, 2008. (Cited on page 77.)

[122] John Tomkinson and Thomas C. Waddington. Inelastic neutron scattering from the alkali metal borohydrides and calcium borohydride. *J. Chem. Soc., Faraday Trans. 2*, 72:528–538, 1976. (Cited on page 80.)

[123] Michael R. Hartman, John J. Rush, Terrence J. Udovic, Robert C. Bowman Jr., and Son-Jong Hwang. Structure and vibrational dynamics of isotopically labeled lithium borohydride using neutron diffraction and spectroscopy. *Journal of Solid State Chemistry*, 180(4):1298 – 1305, 2007. (Cited on page 80.)

[124] A. Borgschulte, A. Jain, A. J. Ramirez-Cuesta, P. Martelli, A. Remhof, O. Friedrichs, R. Gremaud, and A. Züttel. Mobility and dynamics in the complex hydrides LiAlH4 and LiBH4. *Faraday Discuss.*, 151:213–230, 2011. (Cited on page 80.)

[125] S. Gomes, H. Hagemann, and K. Yvon. Lithium boro-hydride LiBH4: II. Raman spectroscopy. *Journal of Alloys and Compounds*, 346(1-2):206 – 210, 2002. (Cited on page 80.)

[126] Nina Verdal, Terrence J. Udovic, and John J. Rush. The Nature of BH_4^- Reorientations in Hexagonal $LiBH_4$. *The Journal of Physical Chemistry C*, 116(1):1614–1618, 2012. (Cited on pages 81, 82 and 156.)

[127] Nina Verdal, Terrence J. Udovic, John J. Rush, Hui Wu, and Alexander V. Skripov. Evolution of the Reorientational Motions of the Tetrahydroborate Anions in Hexagonal

$LiBH_4$-LiI Solid Solution by High-Q Quasielastic Neutron Scattering. *The Journal of Physical Chemistry C*, 117(23):12010–12018, 2013. (Cited on pages 81 and 107.)

[128] H. Hagemann, Y. Filinchuk, D. Chernyshov, and W. van Beek. Lattice anharmonicity and structural evolution of $LiBH_4$: an insight from Raman and X-ray diffraction experiments. *Phase Transitions*, 82(4):344–355, 2009. (Cited on page 88.)

[129] Philippe C. Aeberhard, Keith Refson, and William I. F. David. Molecular dynamics investigation of the disordered crystal structure of hexagonal $LiBH_4$. *Phys. Chem. Chem. Phys.*, 15:8081–8087, 2013. (Cited on page 88.)

[130] S. Cusack and W. Doster. Temperature dependence of the low frequency dynamics of myoglobin. Measurement of the vibrational frequency distribution by inelastic neutron scattering. *Biophysical Journal*, 58(1):243 – 251, 1990. (Cited on pages 93 and 109.)

[131] Alexander V. Skripov, Alexei V. Soloninin, Yaroslav Filinchuk, and Dmitry Chernyshov. Nuclear Magnetic Resonance Study of the Rotational Motion and the Phase Transition in $LiBH_4$. *The Journal of Physical Chemistry C*, 112(47):18701–18705, 2008. (Cited on pages 107 and 138.)

[132] Nina Verdal, Terrence J. Udovic, and John J. Rush. The Nature of BH_4^- Reorientations in Hexagonal $LiBH_4$. *The Journal of Physical Chemistry C*, 116(1):1614–1618, 2012. (Cited on pages 107 and 138.)

[133] Nina Verdal, Michael R. Hartman, Timothy Jenkins, Daniel J. DeVries, John J. Rush, and Terrence J. Udovic. Reorientational Dynamics of $NaBH_4$ and KBH_4. *The Journal of Physical Chemistry C*, 114(21):10027–10033, 2010. (Cited on page 107.)

[134] A. Borgschulte, R. Gremaud, A. Züttel, P. Martelli, A. Remhof, A. J. Ramirez-Cuesta, K. Refson, E. G. Bardají, W. Lohstroh, M. Fichtner, H. Hagemann, and M. Ernst. Experimental evidence of librational vibrations determining the stability of calcium borohydride. *Phys. Rev. B*, 83:024102, Jan 2011. (Cited on page 107.)

[135] Yaroslav Filinchuk, Radovan Černý, and Hans Hagemann. Insight into $Mg(BH_4)_2$ with Synchrotron X-ray Diffraction: Structure Revision, Crystal Chemistry, and Anomalous Thermal Expansion. *Chemistry of Materials*, 21(5):925–933, 2009. (Cited on pages 107 and 157.)

[136] Luca Silvi, Eva Röhm, Maximilian Fichtner, Winfried Petry, and Wiebke Lohstroh. Hydrogen dynamics in β-$Mg(BH_4)_2$ on the picosecond timescale. *Phys. Chem. Chem. Phys.*, 18:14323–14332, 2016. (Cited on pages 141 and 159.)

[137] Tasso Springer and Dieter Richter. 10. hydrogen in metals. In David L. Price and Kurt Sköld, editors, *Neutron Scattering*, volume 23, Part B of *Methods in Experimental Physics*, pages 131 – 186. Academic Press, 1987. (Cited on page 148.)

[138] Mark Paskevicius, Morten B. Ley, Drew A. Sheppard, Torben R. Jensen, and Craig E. Buckley. Eutectic melting in metal borohydrides. *Phys. Chem. Chem. Phys.*, 15:19774–19789, 2013. (Cited on page 160.)

[139] G.L. Squires. *Introduction to the Theory of Thermal Neutron Scattering*. Cambridge University Press, 2012. (Cited on page 163.)